



UNIVERSITÀ DEGLI STUDI DI UDINE

---

DOTTORATO DI RICERCA IN  
INGEGNERIA CIVILE, ARCHITETTURA E TERRITORIO  
XXIX CICLO

*Tesi di Dottorato*

***DEVELOPMENT OF A FINITE VOLUME MODEL SUITABLE FOR  
STUDYING RIVERINE AND COASTAL MORPHODYNAMICS***

Supervisore  
***Prof. Ing. Marco Petti***

Dottorando  
***Ing. Francesco Lubrano***

---

2017



*A Eleonora,  
per aver sempre creduto in me più di ogni altro.*

*Alla mia famiglia,  
per avermi spronato quando pensavo che non ce l'avrei fatta.*



# Sommario

La comprensione della dinamica dei sedimenti è di primaria importanza nella gestione delle aree costiere e fluviali. L'evoluzione morfologica di tali regioni, infatti, ha un forte impatto sia sull'equilibrio ambientale che su attività economiche quali ad esempio la navigazione o il turismo.

In letteratura, tale fenomeno è stato ampiamente studiato e dibattuto, e un numero rilevante di diverse teorie è stato proposto, sia di natura analitica che sperimentale, valide alternativamente per sedimenti granulari o sedimenti coesivi.

Uno degli strumenti più utili nello studio del trasporto solido è la modellazione morfodinamica, che accoppia il problema idrodinamico al problema del trasporto solido stesso e all'evoluzione morfologica del bacino in esame.

Sebbene diversi modelli numerici siano già stati presentati in letteratura, spesso hanno diversi limiti: alcuni sono codici commerciali, risultando troppo costosi per molti degli scopi tecnici e scientifici che possono avere. Altri sono basati su ipotesi troppo restrittive per descrivere adeguatamente aree complesse, come ad esempio le lagune, dove la transizione asciutto-bagnato riveste un ruolo di primaria importanza, o non sono in grado di considerare contemporaneamente fenomeni tipici delle aree costiere, come l'effetto del moto ondoso, l'instabilità delle sponde e l'effetto delle correnti secondarie.

Allo scopo di ottenere una visione generale del problema del trasporto solido in ambiente fluviale e costiero, nel presente lavoro è stato sviluppato e descritto un nuovo modello morfodinamico. Sono stati perseguiti due principali obiettivi: ridurre il più possibile il numero dei parametri di calibrazione e avere la possibilità di confrontare diverse delle teorie disponibili per la risoluzione del trasporto solido.

In questa tesi si pone l'attenzione innanzitutto al problema del calcolo dello stress al fondo. In secondo luogo vengono illustrati numerosi studi, teorici e sperimentali, riguardanti il trasporto solido. Infine, viene descritto il modello morfodinamico e viene presentata la sua validazione.



# Summary

Comprehension of sediment dynamics is peculiar in riverine and coastal management. In fact morphological evolution has a strong influence not only in the environmental equilibrium but also in the economic activities like navigation or tourism.

In literature, this problem has been widely studied and debated, and a great number of experimental and analytical theories have been proposed, valid either for granular or cohesive sediments.

One of the most useful instruments available in sediment transport study is morphodynamic modelling, which couples the hydrodynamic problem with the sediment transport problem, taking into consideration the basin's morphological evolution.

Although different numerical models have been presented in literature, they often have several limits. Some of them are in fact commercial codes and result too much expensive for many scientific and technical purposes. Others are based on too much restrictive hypothesis and can't thus describe adequately complex areas, such as lagoons, where wet-dry transition play an important role. Still others are not able to consider together phenomena typical of coastal areas, like wave effects, slope avalanching and secondary flow effects.

In order to get a general overview of the river and coastal morphodynamic problem, in the present work a new morphodynamic model has been developed and described.

Two main purposes are reached: the former is to reduce, as much as possible, calibration parameters; the latter is the possibility to compare several theoretical approaches available in literature for the sediment transport problem.

This work is structured as follows. The first part is dedicated to the discussion of the bed shear stress computation problem. In the second part, different theoretical and experimental studies in sediment transport are illustrated. In the last part, the morphodynamic model is presented, described and validated.



# Contents

<b>Sommario</b>	<b>I</b>
<b>Summary</b>	<b>III</b>
<b>Contents</b>	<b>V</b>
<b>Introduction</b>	<b>1</b>
<b>1 The bed shear stress</b>	<b>3</b>
1.1 The shear stress in real fluid . . . . .	3
1.1.1 Some definitions . . . . .	3
1.1.2 Viscosity . . . . .	5
1.1.3 Turbulent flow for a current: the Reynolds Equations. . . . .	6
1.1.4 The Reynolds equation in presence of oscillatory flows . . . . .	8
1.1.5 The mixing length model . . . . .	9
1.1.6 Wall bounded shear flow and boundary layer . . . . .	12
1.2 Currents, waves: computation of the bed shear stress . . . . .	17
1.2.1 Currents . . . . .	18
1.2.2 Waves . . . . .	20
1.3 The bed shear stress under combined current and waves . . . . .	22
1.3.1 Bijker (1967) . . . . .	22
1.3.2 Grant and Madsen (1979) . . . . .	24
1.3.3 Fredsøe (1984) . . . . .	26
1.3.4 Van Rijn (1993) . . . . .	30
1.3.5 Soulsby (1993-1997) . . . . .	31
<b>2 Principles of sediment transport</b>	<b>37</b>
2.1 Sediment properties . . . . .	38
2.1.1 Granular Sediments . . . . .	38
2.1.2 Cohesive sediments . . . . .	39
2.2 Granular sediment transport . . . . .	40
2.2.1 Threshold of motion . . . . .	41
2.2.2 Bed load . . . . .	45
2.2.3 Suspended load . . . . .	49
2.3 Cohesive sediment transport . . . . .	57
2.3.1 Settling velocity for cohesive sediments . . . . .	59
2.3.2 Erosion . . . . .	60
2.3.3 Deposition . . . . .	62
2.4 Bottom morphological evolution . . . . .	65

<b>3</b>	<b>The morphodynamic model</b>	<b>69</b>
3.1	The hydrodynamic module . . . . .	70
3.1.1	The mathematical scheme . . . . .	70
3.1.2	The numerical solution . . . . .	74
3.2	The sediment transport module . . . . .	88
3.2.1	Computation of granular sediment transport . . . . .	89
3.2.2	Computation of cohesive sediment transport . . . . .	95
3.2.3	Some consideration about input parameters in DAM_SED . . . . .	97
3.3	The morphological module . . . . .	98
3.3.1	The Morphological factor . . . . .	99
3.4	Secondary factors for morphological evolution . . . . .	100
3.4.1	Secondary flow . . . . .	100
3.4.2	Avalanching . . . . .	102
<b>4</b>	<b>Model validation: laboratory tests</b>	<b>105</b>
4.1	Migration of a trench in a flume . . . . .	106
4.1.1	Trench Migration under steady current . . . . .	106
4.1.2	Trench Migration under Current and waves . . . . .	111
4.2	Bi-dimensional dam-break over an erodible bed . . . . .	116
4.3	Hydrodynamics of a curved channel under steady flow . . . . .	119
4.4	Channel bend evolution under unsteady flow . . . . .	121
	<b>Conclusions</b>	<b>129</b>
	<b>Symbols</b>	<b>133</b>
	<b>Bibliography</b>	<b>145</b>

# Introduction

The sediment dynamics in riverine and coastal regions plays an important role not only for the environmental equilibrium, but also for human activities.

In fact, morphological changes due to erosional and deposition processes can be relatively fast. In a few months or years, for example, a channel can be filled, a river meander can migrate or a beach can be strongly eroded: such phenomena often have negative effects on navigation, port management, tourism and all connected economic sectors.

Also dredging operations, required to contrast the filling processes, need adequate locations for the disposal of sediments: deposition areas have to be sufficiently stable and protected from current flows and waves, in order to avoid material resuspension.

The importance of a correct understanding of environmental morphodynamics, comprehensive of morphological evolution and sediment transport, is demonstrated, amongst other, by similar examples.

Sediment transport is the movement of solid particles due to the mutual effect of different factors. On one hand, the motion is generated by water flow, caused by the presence of currents, waves, or both of them: the knowledge of hydrodynamic field is thus fundamental in solving sediment transport problem. On the other, physical, chemical and mechanical sediment properties have a great influence on how water flow picks them up from the bottom, how they move and distribute along water depth and how they are finally deposited. Therefore, a correct and complete knowledge of geological and geotechnical characteristics of grains or transported particles is equally important.

Morphological evolution is strictly related to sediment transport, as it directly depends on how and where sediments are eroded or deposited.

In literature, a great number of theoretical approaches and experimental formulas have been presented in order to evaluate sediment transport load and morphological evolution (see for example theories summarized in [44, 59, 60]). Such formulas have been generally obtained from laboratory analysis, under ideal conditions and, for example, 1-dimensional hydrodynamic field (e.g. a laboratory channel). Thus, a direct application of similar theories to real study cases can result difficult to be done, while approximations would generally be excessive.

For this reason, alternative instruments have been developed, in order to provide a better overview of sediment dynamics with a more optimized use of theoretical and experimental approaches. One of the most widely adopted is the morphodynamic model.

Morphodynamic models are numerical models which associate and couple the hydrodynamic problem, the sediment transport problem and the morphological problem. A wide number of different depth-averaged models have been proposed and discussed. Some of them are commercial codes (e.g. [10]), which generally result very expensive and just a few research laboratories or engineering societies use them for scientific or design purposes. Others are license-free and they can be therefore easily obtained from their developers, but they are generally simpler and not easily applicable in complex problems, such as river

floods events or, for example, tide excursion on salt marshes (e.g. [17]). Moreover, it is very difficult to have a complete scientific description of commercial and license-free codes, and, for this reason, it is difficult to fully understand how they work and speculate on which they are based.

In the light of these considerations, in the present work an alternative morphodynamic model is presented and validated. The model is based on the hydrodynamic code developed by the hydraulic laboratory of University of Udine, and is designed to fit typical coastal morphodynamic problems: rivers, estuaries, lagoons, coastal areas and similar regions.

The model is a 2D depth-averaged, finite volume code and its design would achieve two main purposes: to limit, as much as possible, the number of input and calibration parameters and the possibility to apply and to compare a conspicuous number different theories and approaches in the main parts of morphodynamic problem: the computation of bed shear stress and the evaluation of sediment load.

The thesis is divided in 4 chapters. The first chapter is a theoretical and practical focus on the the bed shear stress computation, from hydrodynamic considerations for real fluids to the evaluation of bed shear stress under currents alone, waves alone and currents and waves. In the last case, different theories on how currents and waves interact are proposed and discussed.

The second chapter is a quick overview on sediment transport problem. In particular, granular sediment transport and cohesive sediment transport are described and several approaches are here summarized.

The third chapter describes the numerical model, considering the hydrodynamic module, the sediment transport module and the morphological module.

Finally, in the fourth chapter model the validation is illustrated: in particular, several applications to laboratory and numerical tests are described and compared with experimental data.

# Chapter 1

## The bed shear stress

### 1.1 The shear stress in real fluid

One of the most important factors which influence sediment transport is bed shear stress. Bed shear stress is the resistance to the water flow exerted by the bottom. It is caused by two main factors: the viscosity of water and the presence of turbulence.

The viscosity is a property of the fluid which causes an internal stress opposing fluid deformation during the flow. It takes place, for example, in presence of boundaries. In fact, due to the interaction with the boundaries (like the bottom or, more generally, the solid walls), the fluid have 0-velocity relative to them.

Also turbulence is caused by interactions between the fluid and the boundaries: if enough kinetic energy is present, the motion of the fluid particles is irregular and fluctuant. The consequent collision between them and with the boundary generates eddies and internal additional stress.

Viscosity and presence of turbulence (when flow conditions generate it) are topic characteristics of a *real fluid*.

In hydrodynamics, also *inviscid fluid* is defined, which does not have viscosity: in this case, no shear stress are generated. However, in environmental hydraulics and in particular for morphodynamic problems where the bed shear stress plays a key role, water can't be considered as an inviscid fluid.

Bed shear stress is always consequence of water motion, which can exist due to two main causes: currents and waves. They can act alone or, often in coastal environment, together. In this chapter, the theoretical concepts useful in the computation of current and wave bed shear stress are briefly illustrated and discussed.

#### 1.1.1 Some definitions

In order to discuss the problem of bed shear stress some declarations and definitions are required.

We consider the space  $(x, y, z)$  where, in particular,  $(x, y)$  is the horizontal plane and  $z$  the vertical coordinate. The components of vectorial variables are identified by the pedice  $x$ ,  $y$  or  $z$ . For example, for a generic vector  $\vec{a}$ , we have

$$\vec{a} = (a_x, a_y, a_z) \quad (1.1)$$

In order to analyse phenomena acting on different time scales, it is useful to define two average operators: the *moving average* and the *phase average*.

The moving average of a variable  $a(t)$  is the average on a localised region in time with period  $T_m$ . In particular,

$$\langle a(t) \rangle = \frac{1}{T_m} \int_t^{t+T_m} a(t^*) dt^* \quad (1.2)$$

where  $\langle \cdot \rangle$  operator indicates the moving average.

In presence of an oscillatory flow with period  $T_w$ , it is then possible to define the phase average of  $a(t)$  as

$$\acute{a}(t) = \frac{1}{N} \sum_{j=1}^N a(t + jT_w) \quad (1.3)$$

where  $\acute{\cdot}$  is the phase average operator and  $N$  the number of periods on which phase average is done.

The *periodic component* of the variable is thus

$$\tilde{a}(t) = \frac{1}{N} \sum_{j=1}^N a(t + jT_w) - \langle a(t) \rangle. \quad (1.4)$$

Finally, we define fluctuating component of  $a$  as

$$a'(t) = a(t) - \langle a(t) \rangle - \tilde{a}(t). \quad (1.5)$$

In absence of an oscillatory flow, only fluctuating and moving averaged components are considered.

In order to apply these operators to hydrodynamic problems, some considerations about  $T_m$  and  $T_w$  are needed.

The scope of using a moving average on an environmental (and, particularly, coastal) hydrodynamic problem is to analyse the behaviour of a flow without taking account high frequency fluctuations (which are generated by turbulence) and, if present, gravity waves. For this reason,  $T_m$  should be considered the time scale of main flow variations, while the period  $T_w$  of phase average should be the gravity wave period, which generally is much shorter. In the same way, the time scale of fluctuations  $T_{turb}$  is much shorter than  $T_w$ . A sketch of this perspective is given in Figure 1.1. Thus, the following relation is assumed valid:

$$T_m \gg T_w \gg T_{turb} \quad (1.6)$$

Thus, from previous definitions we have

$$\langle \tilde{a} \rangle = \langle a' \rangle = \acute{\tilde{a}} = 0 \quad (1.7)$$

and

$$\langle \langle a \rangle \tilde{b} \rangle = \langle \langle a \rangle b' \rangle = \langle \tilde{a} b' \rangle = \langle \widetilde{\langle a \rangle b'} \rangle = \widetilde{\langle a \rangle b'} = \widetilde{\tilde{a} b'} = 0. \quad (1.8)$$

Moreover, it is easy to demonstrate that

$$\langle ab \rangle = \langle a \rangle \langle b \rangle + \langle a' b' \rangle + \langle \tilde{a} \tilde{b} \rangle \quad (1.9)$$

and, finally,

$$\widetilde{\tilde{a} \tilde{b}} = \tilde{a} \tilde{b} - \langle \tilde{a} \tilde{b} \rangle \quad (1.10)$$

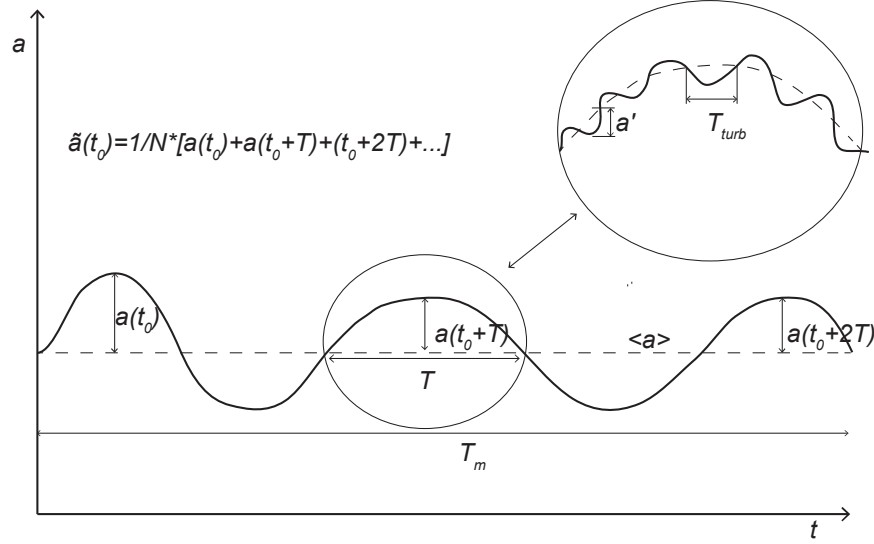


Figure 1.1: Sketch of time scales in coastal problem.

### 1.1.2 Viscosity

Viscosity is defined as the ratio between the stress intensity and related fluid strain:

$$\tau_{lam} = \mu (\dot{\gamma}) \dot{\gamma} \quad (1.11)$$

where  $\mu (\dot{\gamma})$  is the dynamic viscosity and, for example,  $\dot{\gamma} = \frac{du_x}{dz}$  for a 2DV shear flow while, in a more general perspective,  $\dot{\gamma}_{ij} = \left( \frac{\partial u_i}{\partial x_j} + \frac{\partial u_j}{\partial x_i} \right)$ , with  $x_i, x_j = x, y, z$ .

Relationship between shear stress and strain rate is said rheological model: it can take a wide variety of forms, as illustrated in Figure 1.2.

When  $\mu$  is independent from  $\dot{\gamma}$ , fluid is said *Newtonian*. If  $\mu$  increases when increase  $\dot{\gamma}$  then the fluid is said *dilatant* and, conversely, when  $\mu$  decreases, increasing  $\dot{\gamma}$ , fluid is said *pseudoplastic*. Finally, when fluid behaves like a solid under a threshold value of  $\tau_{lam}$  and as a Newtonian fluid when  $\tau_{lam}$  exceeds that value, it is said *Bingham plastic* (or *viscoplastic*). All these rheologies can be described by the model

$$\tau_{lam} = \tau_{threshold} + \mu_n \left( \frac{du_x}{dz} \right)^n \quad (1.12)$$

where  $\tau_{threshold}$ ,  $\mu_n$  and  $n$  are property of the fluid. This generalized rheology is said *Herschel-Bulkely* model.

All models here quickly described can be relevant in mixtures of suspended sediments and water. In particular considering cohesive sediments, high material concentration can have a strong influence on the rheology of the resulting fluid. However, in this thesis, all considerations are done under hypothesis of Newtonian fluid, which is the typical rheology of clean water. This assumption greatly simplifies the problem and is adequate in developing a numerical model useful in complex real cases, which is the aim of our work. In fact, too complex physical schemes would be too heavy to be applied wide domains, where a great number of computational cells is required and computational time is a relevant factor in problem solution.

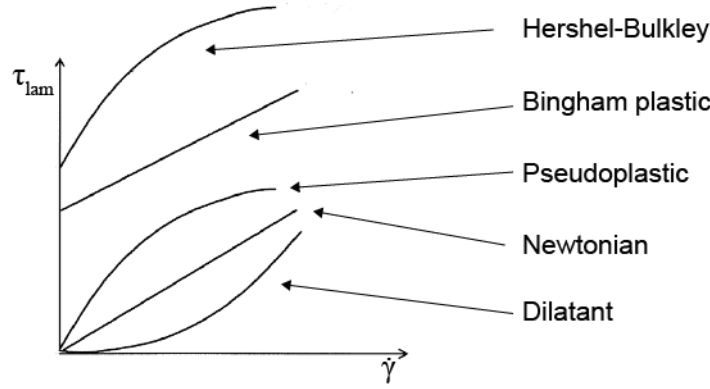


Figure 1.2: Rheological Models.

### 1.1.3 Turbulent flow for a current: the Reynolds Equations.

Consider an incompressible real fluid: the equations of motion (respectively, the continuity equation and the momentum equations) are

$$\frac{\partial u_x}{\partial x} + \frac{\partial u_y}{\partial y} + \frac{\partial u_z}{\partial z} = 0 \quad (1.13)$$

$$\frac{\partial u_x}{\partial t} + u_x \frac{\partial u_x}{\partial x} + u_y \frac{\partial u_x}{\partial y} + u_z \frac{\partial u_x}{\partial z} = -\frac{1}{\rho} \left( \frac{\partial \sigma_{xx}}{\partial x} + \frac{\partial \tau_{xy}}{\partial y} + \frac{\partial \tau_{xz}}{\partial z} \right) \quad (1.14)$$

$$\frac{\partial u_y}{\partial t} + u_x \frac{\partial u_y}{\partial x} + u_y \frac{\partial u_y}{\partial y} + u_z \frac{\partial u_y}{\partial z} = -\frac{1}{\rho} \left( \frac{\partial \tau_{yx}}{\partial x} + \frac{\partial \sigma_{yy}}{\partial y} + \frac{\partial \tau_{yz}}{\partial z} \right) \quad (1.15)$$

$$\frac{\partial u_z}{\partial t} + u_x \frac{\partial u_z}{\partial x} + u_y \frac{\partial u_z}{\partial y} + u_z \frac{\partial u_z}{\partial z} = g - \frac{1}{\rho} \left( \frac{\partial \tau_{zx}}{\partial x} + \frac{\partial \tau_{zy}}{\partial y} + \frac{\partial \sigma_{zz}}{\partial z} \right) \quad (1.16)$$

where  $\rho$  is the water density,  $g$  the gravitational acceleration,  $u_i$  the velocity components and  $\sigma_{ii}$  and  $\tau_{ij}$  are components of the stress tensor, with  $i, j = x, y, z$ . Under the hypothesis of Newtonian fluid, the stress tensor components becomes

$$\begin{aligned} \sigma_{ii} &= p - 2\mu S_{ii} \\ \tau_{ij} &= -2\mu S_{ij} \end{aligned} \quad (1.17)$$

where  $S_{ij} = \frac{1}{2} \left( \frac{\partial u_i}{\partial x_j} + \frac{\partial u_j}{\partial x_i} \right)$  is the strain tensor.

Substituting (1.17) into (1.14), the  $x$ -direction Navier-Stokes equation in is obtained:

$$\frac{\partial u_x}{\partial t} + u_x \frac{\partial u_x}{\partial x} + u_y \frac{\partial u_x}{\partial y} + u_z \frac{\partial u_x}{\partial z} = -\frac{1}{\rho} \frac{\partial p}{\partial x} + \nu \left( \frac{\partial^2 u_x}{\partial x^2} + \frac{\partial^2 u_x}{\partial y^2} + \frac{\partial^2 u_x}{\partial z^2} \right) \quad (1.18)$$

where  $\nu = \mu/\rho$  is the kinematic viscosity.

In order to describe a turbulent flow in a current, for which is not feasible to analyze the problem at all points in space and time, Reynolds suggested to decompose quantities in moving mean quantities and fluctuating quantities, coherently with definitions (1.2) and (1.5). In particular, the components of velocity  $\vec{u}$  can be rewritten as

$$(u_x, u_y, u_z) = (\langle u_x \rangle + u'_x, \langle u_y \rangle + u'_y, \langle u_z \rangle + u'_z) . \quad (1.19)$$

By definition, the mean value of fluctuating velocities is zero:

$$\langle u'_i(t) \rangle = \frac{1}{T_m} \int_t^{t+T_m} (u_i(t^*) - \langle u_i(t^*) \rangle) dt^* \equiv 0. \quad (1.20)$$

In the same way, pressure can be divided into its components:  $p = \langle p \rangle + p'$ .

Considering Reynolds decomposition to the motion equation in  $x$ -direction, it becomes

$$\begin{aligned} & \frac{\partial (\langle u_x \rangle + u'_x)}{\partial t} + (\langle u_x \rangle + u'_x) \frac{\partial (\langle u_x \rangle + u'_x)}{\partial x} + \\ & (\langle u_y \rangle + u'_y) \frac{\partial (\langle u_x \rangle + u'_x)}{\partial y} + (\langle u_z \rangle + u'_z) \frac{\partial (\langle u_x \rangle + u'_x)}{\partial z} = \\ & - \frac{1}{\rho} \frac{\partial (\langle p \rangle + p')}{\partial x} + \nu \left( \frac{\partial^2 (\langle u_x \rangle + u'_x)}{\partial x^2} + \frac{\partial^2 (\langle u_x \rangle + u'_x)}{\partial y^2} + \frac{\partial^2 (\langle u_x \rangle + u'_x)}{\partial z^2} \right). \end{aligned} \quad (1.21)$$

The mean flow problem is then obtained applying  $\langle \cdot \rangle$  operator in terms of the equation (1.21). In all linear terms, fluctuation component of the averaged term is vanishing. In non linear terms, from equation (1.9) (without consider oscillatory term), we can write

$$\langle u_i u_j \rangle = \langle u_i \rangle \langle u_j \rangle + \langle u'_i u'_j \rangle. \quad (1.22)$$

Thus, developing the momentum equation, we obtain

$$\begin{aligned} & \frac{\partial \langle u_x \rangle}{\partial t} + \langle u_x \rangle \frac{\partial \langle u_x \rangle}{\partial x} + \langle u_y \rangle \frac{\partial \langle u_x \rangle}{\partial y} + \langle u_z \rangle \frac{\partial \langle u_x \rangle}{\partial z} \\ & + \langle u'_x \frac{\partial u'_x}{\partial x} \rangle + \langle u'_y \frac{\partial u'_x}{\partial y} \rangle + \langle u'_z \frac{\partial u'_x}{\partial z} \rangle = \\ & - \frac{1}{\rho} \frac{\partial \langle p \rangle}{\partial x} + \nu \left( \frac{\partial^2 \langle u_x \rangle}{\partial x^2} + \frac{\partial^2 \langle u_x \rangle}{\partial y^2} + \frac{\partial^2 \langle u_x \rangle}{\partial z^2} \right) \end{aligned} \quad (1.23)$$

where, the terms  $u'_j \frac{\partial u'_x}{\partial x_j}$ , thanks to the continuity equation, can be written as

$$\sum_j^{x,y,z} \langle u'_j \frac{\partial u'_x}{\partial x_j} \rangle = \sum_j^{x,y,z} \frac{\partial \langle u'_j u'_x \rangle}{\partial x_j}. \quad (1.24)$$

These factors (as observed also in [50]) are analogous to the terms  $\langle u_j \rangle \frac{\partial \langle u_i \rangle}{\partial x_j}$  and represent the mean of the momentum transport caused by the turbulent fluctuations. If  $u'_i$  and  $u'_j$  were uncorrelated, there would not be turbulent momentum transfer, but experience shows that such transfer has a key role in turbulent motion. Terms in (1.24) are the divergence of a stress: thanks to Reynolds decomposition, turbulence effect is perceived as stress acting on the mean flow. Rearranging (1.23) and putting all stress together, we obtain the *Reynolds Equation* in  $x$ -direction:

$$\begin{aligned} & \frac{\partial \langle u_x \rangle}{\partial t} + \sum_j^{x,y,z} \langle u_j \rangle \frac{\partial \langle u_x \rangle}{\partial x_j} = - \frac{1}{\rho} \frac{\partial \langle p \rangle}{\partial x} + \nu \frac{\partial^2 \langle u_x \rangle}{\partial x_j^2} - \sum_j^{x,y,z} \frac{\partial \langle u'_j u'_x \rangle}{\partial x_j} \\ & \frac{\partial \langle u_x \rangle}{\partial t} + \sum_j^{x,y,z} \langle u_j \rangle \frac{\partial \langle u_x \rangle}{\partial x_j} = - \sum_j^{x,y,z} \frac{1}{\rho} \frac{\partial}{\partial x_j} (\langle \sigma_{ij} \rangle + \tau_{xj}^{Re}) \end{aligned} \quad (1.25)$$

where  $\tau_{xj}^{Re} = \rho \langle u'_x u'_j \rangle$  are Reynolds Stress Tensor components and, as usual,  $j = x, y, z$ .

Generalizing to the 3D problem, the Reynolds Stress Tensor is characterized by six unknown independent components, added to the other unknowns (components  $\langle u_i \rangle$  and  $\langle p \rangle$ ). In order to solve the system, variables must be reduced and Reynolds stress needs to be related to the mean flow variables. This is said *closure problem of turbulence*. Many authors have attempted to find a relation between  $\tau_{ij}$  and  $S_{ij} = \frac{1}{2} \left( \frac{\partial u_i}{\partial x_j} + \frac{\partial u_j}{\partial x_i} \right)$ , in order to obtain a form for turbulent stresses similar to that of the viscous stresses  $2\mu S_{ij}$ . In subsection 1.1.5 one of the main theories about relations between  $\tau_{ij}^{Re}$  and  $S_{ij}$  is presented.

### 1.1.4 The Reynolds equation in presence of oscillatory flows

In order to evaluate the effect of an oscillatory flow combined with a current, Nielsen [29] proposed to derive Reynolds equations (1.25) considering also a periodic component with period equal to the wave period  $T_w$ . Coherently with definition (1.4), we can define in  $xz$ -plane the oscillatory component flow along  $z$  as

$$\tilde{u}_i(t, z) = \frac{1}{N} \sum_{k=1}^N u_i(z, t + kT_w) - \langle u_i(t, z) \rangle. \quad (1.26)$$

The velocity vector can be thus divided into mean, periodic and fluctuant components, becoming

$$(u_x, u_y, u_z) = (\langle u_x \rangle + \tilde{u}_x + u'_x, \langle u_y \rangle + \tilde{u}_y + u'_y, \langle u_z \rangle + \tilde{u}_z + u'_z). \quad (1.27)$$

Let us develop the momentum equation for a 2DV case of combined wave and current flow, where we take into account mean, oscillatory and turbulent components. The wave is developed in  $(x, z)$  plane and the mean flow has just  $x$ -component non-vanishing. In  $x$ -direction we obtain

$$\begin{aligned} & \frac{\partial (\langle u_x \rangle + \tilde{u}_x + u'_x)}{\partial t} + \\ & (\langle u_x \rangle + \tilde{u}_x + u'_x) \frac{\partial (\langle u_x \rangle + \tilde{u}_x + u'_x)}{\partial x} + (\tilde{u}_z + u'_z) \frac{\partial (\langle u_x \rangle + \tilde{u}_x + u'_x)}{\partial z} = \\ & - \frac{1}{\rho} \frac{\partial (\langle p \rangle + \tilde{p} + p')}{\partial x} + \nu^2 \nabla^2 (\langle u_x \rangle + \tilde{u}_x + u'_x). \end{aligned} \quad (1.28)$$

where  $\nabla^2$  is Laplace operator.

If the steady component of mean flow problem is considered, deleting all trivial terms equation 1.28 reduces to the form

$$\begin{aligned} \langle u_x \rangle \frac{\partial \langle u_x \rangle}{\partial x} + \langle u_z \rangle \frac{\partial \langle u_x \rangle}{\partial z} + \langle \tilde{u}_x \frac{\partial \tilde{u}_x}{\partial x} \rangle + \langle \tilde{u}_z \frac{\partial \tilde{u}_z}{\partial x} \rangle + \\ \langle u'_x \frac{\partial u'_x}{\partial x} \rangle + \langle u'_z \frac{\partial u'_x}{\partial x} \rangle = - \frac{1}{\rho} \frac{\partial \langle p \rangle}{\partial x} + \nu^2 \nabla^2 \langle u_x \rangle. \end{aligned} \quad (1.29)$$

Moreover, by the continuity equation, we know that

$$\frac{\partial (\langle u_x \rangle + \tilde{u}_x + u'_x)}{\partial x} + \frac{\partial (\langle u_z \rangle + \tilde{u}_z + u'_z)}{\partial z} = 0. \quad (1.30)$$

It is thus possible to rearrange equation (1.29) adding the following vanishing terms:

$$\langle u_x \rangle \left( \frac{\partial \langle u_x \rangle}{\partial x} + \frac{\partial \langle u_z \rangle}{\partial z} \right) + \tilde{u}_x \left( \frac{\partial \tilde{u}_x}{\partial x} + \frac{\partial \tilde{u}_z}{\partial z} \right) + u'_x \left( \frac{\partial u'_x}{\partial x} + \frac{\partial u'_z}{\partial z} \right). \quad (1.31)$$

In this way, such equation becomes:

$$\begin{aligned} \frac{\partial \langle u_x \rangle^2}{\partial x} + \frac{\partial \langle \tilde{u}_x \rangle^2}{\partial x} + \frac{\partial \langle \tilde{u}_x \tilde{u}_z \rangle}{\partial z} \\ + \frac{\partial \langle u'_x \rangle^2}{\partial x} + \frac{\partial \langle u'_x u'_z \rangle}{\partial z} = -\frac{1}{\rho} \frac{\partial \langle p \rangle}{\partial x} + \nu^2 \nabla^2 \langle u_x \rangle \end{aligned} \quad (1.32)$$

As discussed above, vertical momentum transfer terms are the vertical derivatives of shear stress components. In this case the mean component shear stress is thus:

$$\langle \tau_{xz} \rangle = \rho \nu \frac{\partial \langle u_x \rangle}{\partial z} - \rho \langle u'_x u'_z \rangle - \rho \langle \tilde{u}_x \tilde{u}_z \rangle. \quad (1.33)$$

An analogous expression can be derived for phase averaged shear stress, applying the phase average operator to the equation (1.28) and making use of continuity equation. Phase averaged shear stress is:

$$\tilde{\tau}_{xz} = \rho \nu \frac{\partial \langle u_x \rangle}{\partial z} - \rho \langle u_x \rangle \tilde{u}_z - \rho \widetilde{u'_x u'_z} - \rho \widetilde{u'_x u'_z}. \quad (1.34)$$

Equations (1.33) and (1.34) are useful to understand (from a qualitative point of view) how waves and current interact from a dynamic point of view: in mutual presence of waves and current, both steady component of shear stress (which directly influences the current) and phase averaged component (which acts on the waves) are influenced by steady and periodic components of the flow. As we will see in next sections, this is particularly important in evaluation of bed shear stress under waves and current.

Generally, oscillatory terms  $\rho \langle \tilde{u}_x \tilde{u}_z \rangle$  and  $\rho \widetilde{u'_x u'_z}$  are dominant, except very close to the bed: turbulent fluctuations have no great importance in oscillatory boundary layer processes (as discussed in [29]).

From now, we will omit the operator  $\langle \cdot \rangle$ , and all quantities, if not specified otherwise, have to be considered moving averaged in time.

### 1.1.5 The mixing length model

Consider a steady (uniform) shear flow in  $x$  direction with  $\frac{\partial u_x}{\partial z} > 0$  (Figure 1.3) and suppose a moving point starting from a level  $z = 0$  at time  $t = 0$  and passing to level  $z = l$  at time  $t = t_l$ , without losing its momentum traveling. The momentum per unit volume is therefore  $M_0 = \rho u_x(0, 0)$  and the momentum deficit of the moving point at  $z = l$  will be

$$\Delta M = \rho [u_x(l, t_l) - u_x(0, 0)] + \rho [u'_x(l, t_l) - u'_x(0, 0)]. \quad (1.35)$$

Contributions of turbulence to the momentum deficit can be neglected; moreover, equation (1.35) may be expanded in Taylor series and approximated by

$$\Delta M = \rho z \frac{\partial u_x}{\partial z} = \rho l \frac{\partial u_x}{\partial z} \quad (1.36)$$

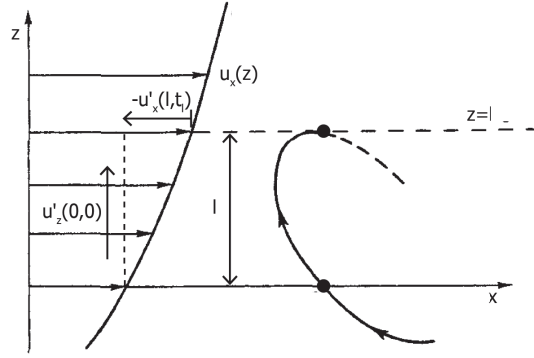


Figure 1.3: Transport of momentum by turbulent motion, [50].

Under our hypothesis, there would not be momentum transfer between moving point and its environment. Thus,  $u_z$  would remain constant and  $z$  would continue to increase. This is not realistic: in fact, we expect that correlation between  $u_z$  and  $z$  decreases when  $z$  increase: we assume the two variables to become uncorrelated at values of  $z$  comparable with a transverse length scale  $l$ , called *mixing length*.

Inspiring from kinetic theory of gases, Prandtl assumed that mixing length-related momentum deficit corresponds to the root mean square of the fluctuating velocity in  $x$ -direction  $u'_{xrm}$ . In this way, equation (1.36) becomes:

$$u'_{xrm} = \sqrt{\langle u_x'^2 \rangle} = l \frac{\partial u_x}{\partial z}. \quad (1.37)$$

In order to evaluate turbulent stress, contribution of vertical fluctuant velocity  $u'_z$  is needed too. It is defined as *correlation coefficient between  $u'_x$  and  $u'_z$*  the expression

$$c_{xz} = \frac{\langle u'_x u'_z \rangle}{u'_{xrm} u'_{zrm}} \quad (1.38)$$

where  $u'_{zrm}$  is the root mean square of the  $z$ -direction fluctuating velocity. As pointed out by Rouse [38], since in accordance with their definitions means of  $u'_x$  and  $u'_z$  must be 0, the mean product have a finite magnitude only if the magnitude of  $u'_x$  is to some extent related to the magnitude of  $u'_z$ . Consider the moving point in Figure 1.3: due to a vertical velocity fluctuation  $u'_z$ , the point is transported into a zone of somewhat higher velocity. The correspondent low velocity fluid transported will tend to decelerate the fluid in high velocity zone, causing here a  $x$  fluctuation  $-u'_x$ .

Moreover, consider continuity equation applied to fluctuation velocities:

$$\frac{\partial u'_x}{\partial x} + \frac{\partial u'_z}{\partial z} = 0. \quad (1.39)$$

Far from the boundary, it is probable that eddies fluctuations are approximately spherical and limited by the mixing length. Thus, given  $O$  the order of magnitude of a certain quantity, it is possible to write that

$$O(x) \simeq O(z) \simeq l. \quad (1.40)$$

For this reason, by continuity equation it must result that

$$O(u'_x) \simeq -O(u'_z). \quad (1.41)$$

From these considerations, it is demonstrable that the correlation coefficient is negative and its order of magnitude is approximately 1:

$$c_{xz} \simeq -1. \quad (1.42)$$

The total shear stress, is then:

$$\tau_{xz} = \tau_{lam} + \tau_{xz}^{Re} = -\mu \frac{du_x}{dz} + \rho \langle u'_x u'_z \rangle = \mu \frac{du_x}{dz} + \rho l^2 \left( \frac{\partial u_x}{\partial z} \right)^2. \quad (1.43)$$

The ratio between turbulent and viscous stress is defined *Reynolds number*. Considering Prantl stress we have:

$$\frac{\tau^{Re}}{\mu \frac{\partial u_x}{\partial z}} = \frac{\nu_T}{\nu} = \frac{l^2 \frac{\partial u_x}{\partial z}}{\nu} \approx \frac{u'_{xrm} l}{\nu} = Re_l. \quad (1.44)$$

In most cases, the viscous stress may be neglected with respect to Reynolds stress and  $Re_l$  is very large. In facts, turbulent momentum transport tends to be much more effective than molecular transport and the dependence of the mean on the Reynolds number is generally small, except in regions where  $l$  is of the same order of magnitude of  $\frac{\nu}{u'_{xrm}}$ .

Consider a uniform 2DV shear flow near a rigid wall in  $x$ -direction. In particular,  $u_z = 0$ , and  $\frac{\partial p}{\partial x} = \frac{\partial u_x}{\partial x} = 0$  (Figure 1.4).

In order to solve the problem the choice of the mixing length is of great importance for problem solution. The presence of a wall constrains the turbulent motion and, under a certain value  $z$ , eddy dimension and momentum transfer are restricted to distances smaller than  $z$  itself. Tennekes and Lumley [50] observed that, in order to guarantee a coherent dimension of the mixing length, this should be proportional to  $z$ . The most simple formulation imposes a constant proportional factor:

$$l = \kappa z \quad (1.45)$$

where  $\kappa$  is the *constant of Von Karman* and is demonstrated to be approximately equal to 0.4.

Consider the region very close to the wall, for which  $z \leq \delta$  where  $\delta$  is the so called *boundary layer*. Here, mixing length  $l$  is approximately 0 and  $u'_x \simeq u'_z \simeq 0$ . For this reason the flow is considered laminar and the shear stress is approximately constant and it is possible to write

$$\tau_{xz} = \tau_b \quad (1.46)$$

where  $\tau_b$  is the bed shear stress.

Let us define the *friction velocity*  $u_*$  as

$$u_* = \sqrt{-\frac{\tau_b}{\rho}}. \quad (1.47)$$

At  $z = \delta$  turbulent stress is considered greater than laminar stress. From equation (1.43), assuming  $\tau(\delta) \simeq \tau_b$ , we obtain

$$u_*^2 = \kappa^2 z^2 \left( \frac{\partial u_x}{\partial z} \right)^2. \quad (1.48)$$

Solving (1.48), a logarithmic distribution of  $u_x$  in  $z$  direction is obtained:

$$\frac{u_x}{u_*} = \frac{1}{\kappa} \ln z + const. \quad (1.49)$$

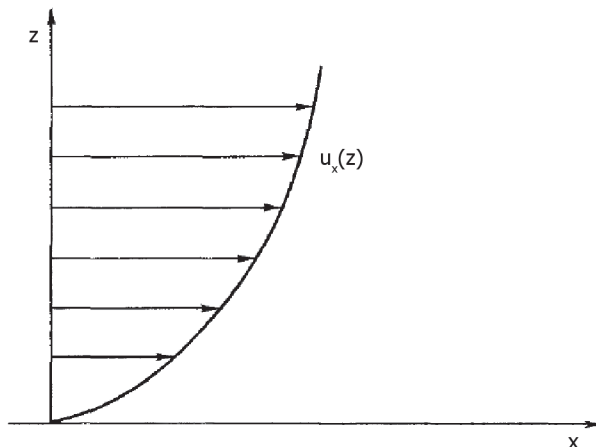


Figure 1.4: Turbulent flow near a rigid wall [50].

where integration constant can be determined applying by the so called *no slip condition*. In particular,  $u_x = 0$  for a given level  $z_0$  very close to the boundary. Thus, equation (1.49) becomes

$$\frac{u_x}{u_*} = \frac{1}{\kappa} \ln \frac{z}{z_0}. \quad (1.50)$$

### 1.1.6 Wall bounded shear flow and boundary layer

Is said boundary layer, the region of the flow in immediate vicinity of a bounding surface, called *wall*, where the effects of fluid viscosity and interactions between fluid and wall become significant.

Boundary-layer flow is characterized by the mutual presence of different length scales in the physical problem.

Consider in facts the region very close to the wall. Viscosity of the fluid enforces the no slip condition, which is a typical viscous constrain. In case no rough elements are present at the wall (*smooth wall*), viscous-dominated characteristic length of the order of  $\nu/v'$ , being  $v'$  the order of magnitude of fluctuating velocity ( $v' \simeq O(u'_{xrm})$ ). In case the wall is characterized by a macroscopical roughness, characteristic length of the viscous-dominated zone becomes typically the wall roughness height  $\varepsilon$  (*rough wall*).

However, at large Reynolds number, the thickness of the boundary layer  $\delta$  results to be much larger than  $\nu/v'$  or  $\varepsilon$  and it is thus characterized by a different length scale, which acts simultaneously that of viscous-dominated zone.

Because of the much smaller size, the viscous-dominated length scale is supposed not to influence the entire flow in the boundary layer but just a narrow region in the immediate vicinity of the wall. This region is called *surface layer* (or wall layer) and has an asymptotic behaviour for  $\delta v'/\nu \rightarrow \infty$  or  $\delta/\varepsilon \rightarrow \infty$ . The rest of the flow, dominated by phenomena with  $\delta$  length scale, is said *outer layer* or *core region*.

If we consider a boundary layer in which the turbulence is driven by Reynolds stresses, the scaling length should be  $\delta$ , which is the typical size of large eddies. In this case, the gradient of velocity  $\frac{\partial u_x}{\partial x}$  has to be of order of  $\frac{w}{\delta}$  where  $w$  is the scaling velocity for the

Reynolds stresses. The differential similarity law gives

$$\frac{\partial u_x}{\partial z} = \left(\frac{w}{\delta}\right) f\left(\frac{z}{\delta}\right) \quad (1.51)$$

and, integrating,

$$u_x - u_{x0} = -\left(\frac{w}{\delta}\right) \int f\left(\frac{z}{\delta}\right) dz = wF\left(\frac{z}{\delta}\right) \quad (1.52)$$

where  $u_{x0}$  is the velocity outside the boundary layer and  $z$  the coordinate across it. It is demonstrable that self-preservation of turbulence can be obtained only if  $w \ll u_{x0}$ . It is important to notice that a similar law does not apply to the flow near the surface: in fact a velocity defect of order  $w$  can not meet the no slip condition because  $u - u_{x0} \sim w \neq u_{x0} \gg w$ . For this reason, a dynamically distinct surface layer has to exist, in which there is a very steep velocity gradient, able to satisfy the boundary condition.

In order to solve the problem, we choose the approach proposed by Tennekes and Lumley [50] and we consider a turbulent uniform flow in  $x$ -direction of a 2DV channel of depth  $h$  (see Figure 1.4). The flow is assumed to be plane (2DV) and steady. The only non-vanishing derivative in  $x$  direction is  $\frac{\partial p}{\partial x}$ , where  $p$  is the mean pressure, which drives the flow against the shear stress at the walls. The boundary layer momentum equations of motion in  $x$  and  $z$  directions are

$$0 = -\frac{1}{\rho} \frac{\partial p}{\partial x} - \frac{d}{dz} \langle u'_x u'_z \rangle + \nu \frac{d^2 u_x}{dz^2} \quad (1.53)$$

$$0 = -\frac{1}{\rho} \frac{\partial p}{\partial z} - \frac{d}{dz} \langle u_z'^2 \rangle. \quad (1.54)$$

Because of the dimensions of boundary layer, influence of gravity  $g$  is considered negligible. Integrating (1.54) with bottom boundary condition, we obtain

$$p/\rho + u_z'^2 = p_0/\rho \quad (1.55)$$

where  $p_0$  is the pressure at  $z = 0$ . Derivative of  $p$  in  $x$ -direction is thus equal to derivative of  $p_0$  (which is a function of  $x$  only, while  $u_z'^2$  is assumed to be independent from  $x$ ). Thus, integrating from  $z = 0$  equation (1.53) and coherently with definition of friction velocity  $u_*$ , we obtain

$$0 = -\frac{z}{\rho} \frac{dp_0}{dx} - \langle u'_x u'_z \rangle + \nu \frac{du_x}{dz} - u_*^2. \quad (1.56)$$

At the free surface the total shear stress (both viscous and turbulent contributions) must be 0: from (1.56) we thus obtain

$$u_*^2 = -\frac{h}{\rho} \frac{dp_0}{dx} \quad (1.57)$$

where  $h$  is the water depth.

Substituting in (1.56) it is easy to demonstrate that

$$\tau_{xz}(z) = \rho u_*^2 \left(1 - \frac{z}{h}\right) = \tau_b \left(1 - \frac{z}{h}\right). \quad (1.58)$$

The equation (1.58) can be expressed in two different non-dimensional forms which help to focus separately on the effect of turbulent stresses and viscous stresses.

First of all, we can consider  $u_*^2$  as the proper scaling factor for the turbulence term, because viscous stresses are expected to be much smaller at large Reynolds number. Also

$\frac{du_x}{dz}$  should be scaled with  $\frac{u_*}{h}$ , coherently with dynamic scales of turbulence. For this reason it is possible to write

$$-\frac{\langle u'_x u'_z \rangle}{u_*^2} + \frac{\nu}{u_* h} \frac{d(u_x/u_*)}{d(z/h)} = 1 - \frac{z}{h}. \quad (1.59)$$

This particular non-dimensional form suppresses the viscous stresses when  $Re_* = u_* h/\nu$  is large. This can not be valid near the wall, where the stress is purely viscous.

An alternative non-dimensional form of (1.58) which does not vanishing viscous term for large Reynolds number can be obtained absorbing  $Re_*$  in the  $z$  scale:

$$-\frac{\langle u'_x u'_z \rangle}{u_*^2} + \frac{d(u_x/u_*)}{d(zu_*/\nu)} = 1 - \frac{\nu}{hu_*} \frac{u_* z}{\nu} \quad (1.60)$$

Let us consider asymptotic behavior of equations (1.59) and (1.60). If  $Re_* \rightarrow \infty$  and  $z/h \sim 1$ , from (1.59) it is possible to write

$$\frac{\langle u'_x u'_z \rangle}{u_*^2} = 1 - \frac{z}{h}. \quad (1.61)$$

This equation can't represent the flow where  $z/h \rightarrow 0$ : the above mentioned *core region* can be defined as the region where the flow is described by this equation.

Finally, if  $Re_* \rightarrow \infty$  and  $yu_*/\nu \sim 1$ , (1.60) becomes

$$-\frac{\langle u'_x u'_z \rangle}{u_*^2} + \frac{d(u_x/u_*)}{d(zu_*/\nu)} = 1. \quad (1.62)$$

The part of the flow governed by such equation is the *surface layer*.

This two-layer scheme of the flow requires special attention in the region where the two descriptions occur simultaneously (in other words, limits  $z/h \rightarrow 0$  and  $zu_*/\nu \rightarrow \infty$  can be taken at the same time). Here, the length scale  $\nu/w$  is probably too small to control the flow and  $\delta$  is too large, while the best length scale able to describe the dynamic of the flow may be  $z$ , while the turbulence intensity is represented by  $w$ . This region is called *inertial sublayer* and is expected to be characterized by a logarithmic velocity profile, coherently with Prantl theory and assumptions done. In fact:

$$\frac{\partial u_x}{\partial z} \alpha \frac{w}{z} \mapsto \frac{u}{w} = \alpha_1 \ln z + \alpha_2 \quad (1.63)$$

where  $\alpha_1$  and  $\alpha_2$  are numerical coefficients.

### Smooth wall

Considering a smooth wall, there is no roughness  $\varepsilon$  as an additional parameter. In the surface layer, as illustrated, the flow is described by equation (1.62) and there is no explicit dependence on variables except on  $\frac{u_* z}{\nu}$ . We may expect the solution of this equation to be

$$\frac{u_x}{u_*} = f_1 \left( \frac{u_* z}{\nu} \right) \quad (1.64)$$

and

$$-\frac{\langle u'_x u'_z \rangle}{u_*^2} = f_2 \left( \frac{u_* z}{\nu} \right). \quad (1.65)$$

These relations, called *law of the wall*, need as only boundary conditions to satisfy  $f_1(0) = f_2(0) = 0$ . In particular,  $f$  and  $g$  describe respectively the influence on laminar and turbulent stresses in the surface layer.

Nevertheless, in the core region, equation (1.61) describes how the Reynolds stress varies along  $z$ . It is easily demonstrable that in core region  $\frac{du_x}{dz} \sim \frac{u_*}{h}$  [50]. Hence, far from the surface layer, we can state without loss of generality that

$$\frac{du_x}{dz} = \frac{u_*}{h} \frac{df_3(z/h)}{d(z/h)} \quad (1.66)$$

where  $f_3$  is an unknown function of order 1. Integrating along  $z$  from the free surface, we obtain

$$\frac{(u_x - u_{xh})}{u_*} = f_3(z/h) \quad (1.67)$$

with  $u_{xh}$  the mean velocity at the free surface. This evidences that the similarity law for the core region is a *velocity-defect law* (of course not applicable for  $z/h \rightarrow 0$ ).

As described above, in the inertial sublayer, characteristics of surface layer and core region are simultaneously valid. In surface layer, from (1.64) we can write

$$\frac{du_x}{dz} = \frac{u_*^2}{\nu} \frac{df_1}{d\left(\frac{u_*z}{\nu}\right)}. \quad (1.68)$$

Hence, in inertial sublayer we can equal the two formulations of derivative of velocity and we obtain

$$\frac{u_*}{h} \frac{df_3}{d(z/h)} = \frac{u_*^2}{\nu} \frac{df_1}{d\left(\frac{u_*z}{\nu}\right)}. \quad (1.69)$$

We define  $\eta_a = z/h$  and  $z^+ = \frac{u_*z}{\nu}$ . Equation (1.69) can be rewritten as

$$\eta_a \frac{df_3}{d\eta_a} = z^+ \frac{df_1}{dz^+} = \frac{1}{\kappa} \quad (1.70)$$

where  $\kappa$  is Von Karman constant. The presence of the same constant for both the derivatives is coherent with the variables  $\eta_a$  and  $z^+$ , which are independent from other parameters. Von Karman was one of the first to derive the logarithmic velocity profile from similarity arguments. Solving, we obtain the functions  $f_1$  and  $f_3$  in the inertial sublayer:

$$f_1(z^+) = \frac{1}{\kappa} \ln z^+ + const \quad (1.71)$$

$$f_3(\eta) = \frac{1}{\kappa} \ln \eta_a + const \quad (1.72)$$

which are valid for  $\eta_a \ll 1$  and  $z^+ \gg 1$ . From (1.66), (1.68), (1.72) and (1.71) we obtain the velocity distribution in the inertial sublayer as

$$\frac{(u_x - u_{xh})}{u_*} = \frac{1}{\kappa} \ln \eta_a + \beta \quad (1.73)$$

and

$$\frac{u_x}{u_*} = \frac{1}{\kappa} \ln z^+ + \alpha \quad (1.74)$$

where  $\alpha$  and  $\beta$  are integrating constants. Is thus obtained by substitution the *logarithmic friction law*:

$$\frac{u_{xh}}{u_*} = \frac{1}{\kappa} \ln Re_* + \alpha - \beta \quad (1.75)$$

which determines  $u_{xh}$  if the gradient of  $p$  and the the water depth are known.

Finally, let us consider the part of the flow very close to the wall, inside the surface layer. It is demonstrable that for  $z^+ \leq 5$ , Reynolds stress contribution to  $u_*$  is quite small. In this area turbulence cannot sustain itself. Here, we have not a steady laminar flow, but fluctuations do not contribute much to the total stress. This region is called *viscous sublayer* and, considering (1.62) neglecting Reynolds stress, must be characterized by a linear velocity profile  $u_x/u_* = z^+$ .

### Rough Wall

In the case of rough wall, the surface layer is characterized by two characteristic lengths:  $\varepsilon$  and  $\nu/u_*$ . The ratio of them is defined as the roughness Reynolds number  $Re_\varepsilon = \varepsilon u_*/\nu$ . We thus expect that in the surface layer the law of the wall can be written as

$$\frac{u_x}{u_*} = f_4 \left( \frac{z}{\varepsilon}, Re_\varepsilon \right). \quad (1.76)$$

Matching it with the velocity defect law (1.67), the logarithmic velocity profile in the inertial sublayer becomes [50]

$$\frac{u_x}{u_*} = \frac{1}{\kappa} \ln \frac{z}{\varepsilon} + f_5 (Re_\varepsilon) \quad (1.77)$$

Consider a new alternative non-dimensional form of the equation (1.58):

$$-\frac{\langle u'_x u'_z \rangle}{u_*^2} + Re_\varepsilon^{-1} \frac{d(u_x/u_*)}{d(z/\varepsilon)} = 1 - \frac{z}{\varepsilon} \frac{\varepsilon}{h}. \quad (1.78)$$

From equation (1.78), it is demonstrable that in case  $Re_\varepsilon \rightarrow \infty$ , shear stress tends to the Reynolds stress and  $f_4 (Re_\varepsilon)$  is independent of  $Re_\varepsilon$ . In this limit, we obtain the rough wall velocity profile:

$$\frac{u_x}{u_*} = \frac{1}{\kappa} \ln \frac{z}{\varepsilon} + const. \quad (1.79)$$

In this conditions, inertial sublayer loses his sense (no viscous contributions are acting on the flow), and core regin is assumed to cover the entire water flow. Because  $z = 0$  is not accurately known (for the irregularity of the wall due to the roughness), the virtual origin of the velocity profile is absorbed in the definition of  $\varepsilon$ : in case of rough turbulent flow it is generally assumed that  $u_x = 0$  for  $z = z_0 = \frac{\varepsilon}{30}$ .

The friction law, finally, is thus written as

$$\frac{u_x(z)}{u_*} = \frac{1}{\kappa} \ln \frac{z}{z_0} \quad (1.80)$$

which corresponds to Prandtl velocity profile and describes the so called fully turbulent flow.

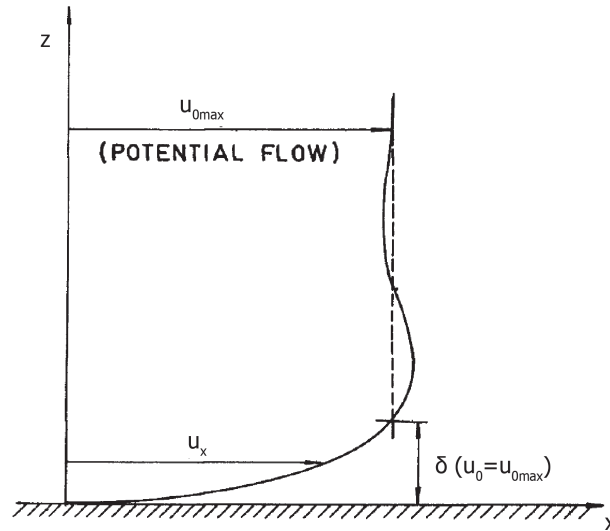


Figure 1.5: “Overshoot” in wave boundary layer[21].

### The boundary layer in oscillatory flows

The wave boundary layer is the layer close to the bottom where the wave-induced water motion is noticeably affected by the boundary [29]. On smooth bed, wave boundary layer is generally very thin (from a few millimetres on solid bed to a few centimetres on sandy flat bed). In presence of bed forms however it could be much thicker, reaching a height of about 50 cm under field conditions.

In case of simple harmonic flow, the bottom velocity close to the boundary layer is  $u_0(t) = u_{0max} \sin(\omega t)$  (where  $u_{0max}$  is the maximum bottom velocity amplitude outside the boundary layer,  $\omega = 2\pi/T_w$ , with  $T_w$  the wave period and  $t$  the time), the behavior of boundary layer and shear stress is related to the type of flow.

In laminar conditions, shear stress is simple harmonic and generally leads  $u_0$  by  $45^\circ$ , but in turbulent flow the variation in time is more complicated [29].

Another characteristic of the oscillatory boundary layer is the “overshoot” near the bed (Figure 1.5): at particular elevations, the velocity amplitude exceeds the value of the free stream value  $A\omega$ , where  $A$  is the wave semi-orbital excursion close to the boundary layer.

As illustrated by Nielsen[29], with his experiments, Sleath studied deeply shear stresses and related quantities for turbulent oscillatory flows. He observed that the total stress was about factor ten larger than periodic Reynolds stress, defined as

$$\tau^{RE}(z, t) = -\rho \widetilde{(u'_x u'_z)}. \quad (1.81)$$

The latter is thus “mere spectator” to the oscillatory boundary layer processes and is totally overshadowed by the analogous contribution  $-\rho \tilde{u}_x \tilde{u}_z$ .

Further details on wave boundary layer and calculation of bed shear stress are presented in subsection 1.2.2. Finally, Nielsen treated thoroughly this topic in his monograph [29].

## 1.2 Currents, waves: computation of the bed shear stress

One of the main hydrodynamic factors that influence morphodynamics in rivers and coastal environments are currents and waves. These give rise to a shear stress between the fluid

and the bottom. As we will describe in the next chapters, this bed shear stress can be sufficiently high to move sediments from the bed, giving rise to a morphological changes. In the present section, concepts described previously will be applied to currents and waves, with particular attention to the combination of these factors.

### 1.2.1 Currents

In environmental hydraulics problems, it is often accepted to consider the fluid characterized by a turbulent flow. Under this condition, coherently with equations (1.74) and (1.79), the velocity distribution over the vertical coordinate is logarithmic. Defining  $\beta_M$  as

$$\beta_M = \frac{1}{U^2 A_s} \int_{A_s} u_x^2 dA_s \quad (1.82)$$

where  $U$  is the depth-averaged velocity in  $x$ -direction and  $A_s$  the cross section, under turbulent flow hypothesis it is fairly equal to 1. Hence, we can consider  $u_x(x, z) \cong U(x)$  over the depth. This assumption lets the problem be much easier to be solved. Continuity and momentum equations of depth-averaged flow are said *shallow water equations*.

Consider a volume of flowing fluid in an open channel. In particular, the channel is supposed to be rectilinear and the flow 1D in  $x$ -direction (Figure 1.6); the bed slope is considered small and  $U$  can be approximated with the streamline velocity  $U_s$ . Under steady conditions, momentum equation becomes

$$-\rho g A_s \Delta h - \tau_{bc} B \Delta x = \rho A_s U \frac{dU}{dx} \Delta x \quad (1.83)$$

where  $g$  the gravitational acceleration,  $\Delta h$  the piezometric head loss,  $B$  the wetted perimeter and  $\tau_{bc}$  the current bed shear stress.

The latter term is then

$$\tau_{bc} = -\rho g R \frac{d}{dx} \left( h_p + \frac{U^2}{2g} \right) \quad (1.84)$$

where  $R$  is the *hydraulic radius* and  $h_p + \frac{U^2}{2g}$  is the *total load*. We define the grade of the total load as  $j = -\frac{d}{dx} \left( h_p + \frac{U^2}{2g} \right)$ . We can then write

$$\tau_{bc} = \rho g R j = \gamma_w R j \quad (1.85)$$

and, if the flow is uniform, it reduces to

$$\tau_{bc} = \gamma_w R i_f \quad (1.86)$$

where  $i_f$  is the bed slope. Equation (1.86) is valid under uniform flow condition, but it is in general of great importance in the computation of bed shear stress and, in particular, in development of bed shear stress calculation formulas.

### Bed resistance formulas

From dimensional analysis and by the use of Buckingham theorem, it is demonstrated that the bed resistance can be expressed as

$$\tau_{bc} B = \rho U^2 h \phi_b \left( Re, \frac{\varepsilon}{h} \right) \quad (1.87)$$

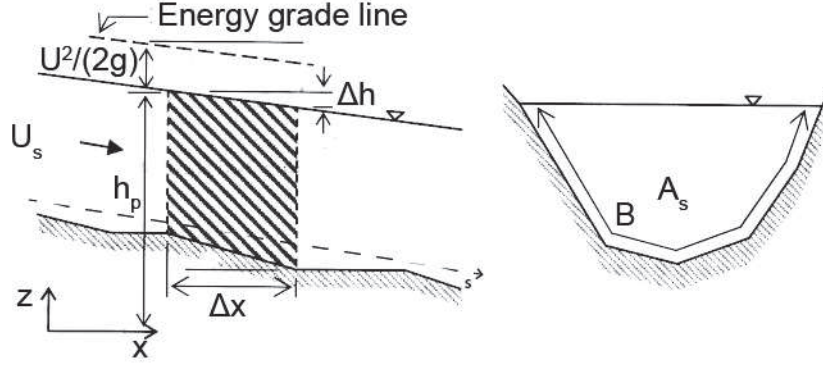


Figure 1.6: Scheme of a 1D channel in x-direction [26].

where  $h$  is the water depth and  $\phi_b \left( Re, \frac{\varepsilon}{h} \right)$  a non-dimensional function. Comparing equations (1.86) and (1.87), keeping in mind that  $R$ ,  $B$  and  $h$  are strictly related, we can write without loss of generality

$$i_f = \frac{\lambda \left( Re, \frac{\varepsilon}{h} \right) U^2}{4R} \quad (1.88)$$

and

$$\tau_{bc} = \lambda \left( Re, \frac{\varepsilon}{h} \right) \frac{\rho}{8g} U^2 \quad (1.89)$$

where  $\lambda \left( Re, \frac{\varepsilon}{h} \right)$  is said *Darcy-Weisbach friction factor*.

An analogous expression for current bed shear stress is

$$\tau_{bc} = \frac{1}{2} \rho f_c U^2 \quad (1.90)$$

where  $f_c$  is a generic current friction factor. This particular form, as we will see later, is useful in comparison between current and waves bed shear stress, where the definition of a similar friction factor is of common use.

Again, current bed shear stress can be considered as a drag stress. In this case the expression is of the type

$$\tau_{bc} = \rho C_D U^2 \quad (1.91)$$

where  $C_D$  is the drag coefficient. In case of fully turbulent flow, from the rough wall law (1.79) it is demonstrable that

$$C_D = \left[ \frac{\kappa}{1 + \ln(z_0/h)} \right]^2 \quad (1.92)$$

where  $h$  is the water depth. This particular approach, proposed also by Soulsby [44, 45], is useful for evaluation of global bottom roughness when calibrated friction factors or roughness parameters are used.

An alternative approach in calculation of bed resistance is proposed by Chezy. From equation (1.88) the velocity can be obtained by

$$U = \sqrt{\frac{8}{\lambda}} \sqrt{g} \sqrt{Ri_f} = \chi \sqrt{Ri_f} = C_{chez} \sqrt{Rg} i_f \quad (1.93)$$

where  $\chi$  is the *adimensional Chezy coefficient* and  $C_{chez}$  is the *dimensional Chezy coefficient*. Let us underline that, in particular,

$$C_{chez} = \frac{U}{u_*} = \frac{1}{\Omega} \int_{\Omega} \frac{u_x}{u_*} d\Omega \quad (1.94)$$

and is thus related to the velocity distribution over the depth ( $C_{chez} = C_{chez}(Re, \varepsilon/R, f)$ ).

Several formulas are presented in literature for the calculation of  $C_{chez}$  and  $\chi$ . The most famous of them have been obtained experimentally and cover the range of fully turbulent flow. In particular, we remember Gauckler-Strickler formula. In this case,  $\chi$  is considered equal to:

$$\chi = k_s R^{\frac{1}{6}} \quad (1.95)$$

where  $k_s$  is Gauckler-Strickler roughness parameter. This formula is largely used in field studies: in this case the velocity can be written as

$$U = k_s R^{\frac{2}{3}} i_f^{\frac{1}{2}} = \frac{1}{n} R^{\frac{2}{3}} i_f^{\frac{1}{2}} \quad (1.96)$$

where  $n$ , which is totally equivalent to  $k_s$ , is said *Manning coefficient*.

## 1.2.2 Waves

The first studies about bed shear stress evaluation under wave field were done in the sixties.

Jonsson [21] was the first to study the evolution of the stress under waves. He suggested to compute it as

$$\tau_{bw} = \frac{1}{2} f_w \rho U_{1m}^2 \quad (1.97)$$

where  $\tau_{bw}$  is the wave maximum shear stress and  $f_w$  the *wave friction factor*.  $U_{1m}$  is the maximum bottom velocity amplitude, computed using the linear wave theory. In particular,

$$U_{1m} = \frac{\pi H}{T} \frac{1}{\sinh(kh)} \quad (1.98)$$

where  $k$  is wave number,  $H$  wave height and  $h$  the water depth.

In order to calculate  $f_w$  Jonsson solved the boundary layer equation, distinguishing between laminar, smooth turbulent and rough turbulent condition. In the presence of a regular wave, the boundary layer equation can be written as

$$\frac{\partial u_x}{\partial t} = \frac{\partial (U_{1m} \sin(\omega t))}{\partial t} + \nu \frac{\partial^2 u_x}{\partial z^2} - \frac{\partial u'_x u'_z}{\partial z} \quad (1.99)$$

In the case of a laminar flow, the equation (1.99) is reduced to

$$u_x(z) = U_{1m} \left[ \sin(\omega t) - \exp\left(-\frac{\pi z}{2\delta}\right) \sin\left(\omega t - \frac{\pi z}{2\delta}\right) \right] \quad (1.100)$$

where  $\delta = \sqrt{\frac{\pi}{4} \nu T}$  is the thickness of the boundary layer. Considering *wave Reynolds number*  $Re_w$  as  $\frac{U_{1m} A_{1m}}{\nu}$  ( $A_{1m}$  being the bottom semi-orbital excursion with linear theory), the layer thickness becomes

$$\frac{\delta}{A_{1m}} = \frac{\pi}{\sqrt{2Re_w}} \quad (1.101)$$

Solving under laminar condition, the maximum bed shear stress is analytically given by

$$\tau_{bw} = \rho \frac{\pi}{\sqrt{2}} \frac{\nu U_{1m}}{\delta}. \quad (1.102)$$

It should be noticed that, comparing equations (1.102) and (1.97), friction factor can be rewritten as

$$f_w = \frac{2}{Re_w} \quad (1.103)$$

which is consistent with results obtained by the author in different experimental campaigns.

In case of rough turbulent condition, Jonsson proposed the following expressions to calculate  $\delta$  e  $f_w$ :

$$30 \frac{\delta}{\varepsilon} \log \left( 30 \frac{\delta}{\varepsilon} \right) = 1.2 \frac{A_{1m}}{\varepsilon} \quad (1.104)$$

$$\frac{1}{4\sqrt{f_w}} + \log \frac{1}{4\sqrt{f_w}} = -0.08 + \log \left( \frac{A_{1m}}{\varepsilon} \right) \quad (1.105)$$

where  $\varepsilon$  is Nikuradse's roughness.

Other expressions of equation (1.105) can be obtained by experimental fitting. For example, Jonsson proposed

$$f_w = \frac{0.0604}{\log^2 \frac{22\delta}{\varepsilon}} \quad (1.106)$$

while Swart [47] (Figure 1.7 ) suggested equation

$$f_w = \exp \left[ 5.213 \left( \frac{\varepsilon}{A_{1m}} \right)^{0.194} - 5.977 \right] \quad (1.107)$$

with an upper limit of 0.3 (suggested by Jonsson too). Swart formula for  $f_w$  is widely used in evaluation of wave bed shear stress.

Finally, in smooth turbulent flow condition, Jonsson used the same approach followed for rough turbulent condition, imposing, as Nikuradse roughness, the value

$$\varepsilon = \frac{\nu}{0.3u_{*w}}, \quad (1.108)$$

where  $u_{*w} = \sqrt{\tau_{wmax}/\rho}$ .

This formula is coherent with experimental observations. The friction factor can be thus computed as

$$\frac{1}{4\sqrt{f_w}} + 2 \log \frac{1}{4\sqrt{f_w}} = \log Re_w - 1.55 \quad (1.109)$$

or by the use of explicit relation

$$f_w = 0.09 Re_w^{-0.2}. \quad (1.110)$$

Several authors have proposed different approaches in order to evaluate wave friction factors and it may change significantly passing from a theory to another. It is not the intention of the present work to describe and discuss many different theories about wave-alone shear stress. However, in the next section, wave-current bed shear stress problem will be presented and different theoretical and engineering approaches will be illustrated. In fact, the combination of waves and current is a topic problem in coastal morphodynamics.

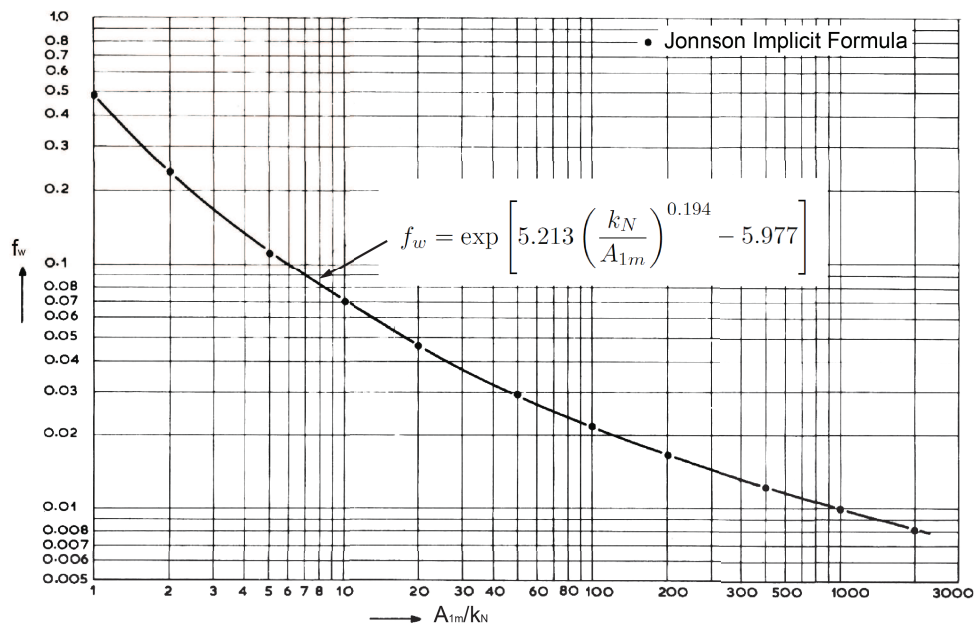


Figure 1.7: Wave friction factor in rough turbulent regime: comparison between equations (1.105) - dots - and (1.107) - filled line - (Swart [47]).

### 1.3 The bed shear stress under combined current and waves

The wave-current bed shear stress problem has been widely discussed during last decades. Several models has been proposed. Some of them are characterized by accurate mathematical and physical considerations: the most famous are Grant and Madsen [16] and Fredsøe [13] models, which will be described later in this section. Others are based on simpler mathematical schemes and on experimental data and are generally widely use in engineering problems (see for example Bijker model [4] and Van Rijn model [59]). Finally, during MAST sessions (Marine Science and Technology Programme), a regression model, able to reproduce many different previous theoretical models, has been presented by Soulsby et al. [45]. Soulsby proposed afterwards a simpler easy-to-use formula based on experimental data, in which just 2 parameters are required [44]. The latter is widely used in coastal hydraulic and morphodynamic models.

In this section, some of the most important wave-current bed shear stress models are presented and discussed.

#### 1.3.1 Bijker (1967)

One of the first studies in wave current bed shear stress computation has been presented by Bijker [4]. Bijker proposed quite a simple approach, based on Prandtl mixing length model and on superposition between currents and wave dynamic effects. In particular, he considered the limit of viscous sublayer, as illustrated in Figure 1.8.

Let us consider current bed shear stress. Outside the viscous sublayer, according to Prandtl, bed shear stress can be computed as

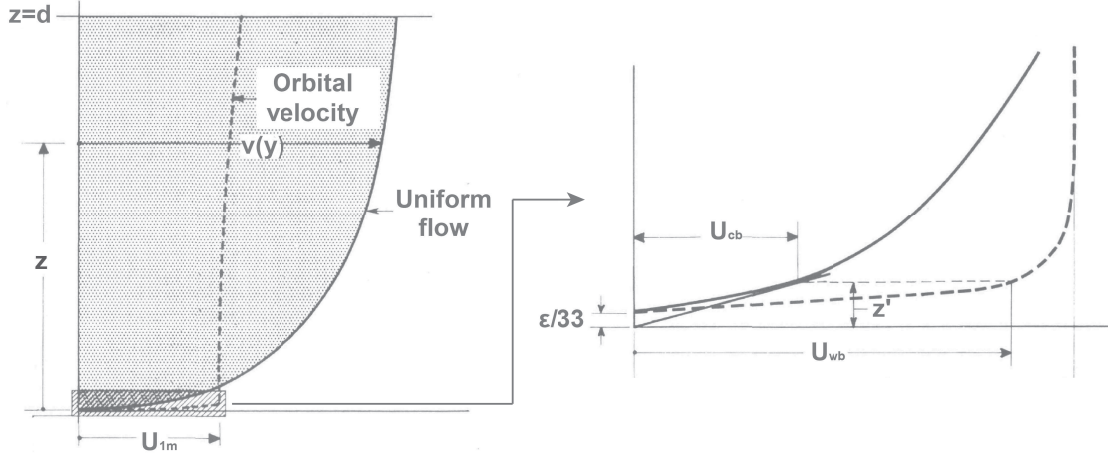


Figure 1.8: Velocity distribution of currents and wave in Bijker model (modified from [4]).

$$\tau_{bc} = \rho l^2 \left( \frac{\partial u_x(z)}{\partial z} \right)^2 \Big|_{z=0} \quad (1.111)$$

where  $l$ , close to the bed, is considered  $l = \kappa z$ . Thus, coherently with the equation (1.79) we obtain

$$u_x(z) = \frac{u_*}{\kappa} \ln \frac{z}{z_0} \quad (1.112)$$

where  $z_0 = \frac{\epsilon}{33}$  is the distance above the bed where the velocity, according to its distribution, is equal to 0. In the viscous sublayer, the derivative of velocity  $\left( \frac{\partial u_x(z)}{\partial z} \right)$  is constant. Bijker called  $z'$  the height where are valid both viscous sublayer and turbulent core laws, considering it the height of the viscous sublayer.

At  $z'$ , because from the derivative of the velocity in the viscous sublayer, we have

$$\left( \frac{\partial u_x(z)}{\partial z} \right) = \left( \frac{\partial u_x(z)}{\partial z} \right)_b = \frac{u_x(z')}{z'}. \quad (1.113)$$

Thus, deriving equation (1.112) and comparing with equation (1.113) we obtain

$$u_x(z') = \frac{u_*}{\kappa} \quad (1.114)$$

and thus the value of  $z'$  is:

$$z' = \frac{e\epsilon}{33}. \quad (1.115)$$

where  $e$  is Neper number. We define  $U_{bc} = u(z')$ . Using Chezy formula it is equal to

$$U_{bc} = \frac{u_*}{\kappa} = \frac{\sqrt{g}}{\kappa C}. \quad (1.116)$$

With regards to wave maximum orbital velocity at height  $z' U_{bw}$ , Bijker considered it a fraction of  $U_{1m}$  (the bottom maximum orbital velocity under linear wave theory), because  $z'$  is assumed to be inside wave boundary layer:  $U_{bw} = p_b U_{1m}$ . Wave shear stress is assumed to be generated by  $U_{bw}$ , with an analogous relation to (1.113). In this way

$$\tau_{bw} = \rho u_{w*}^2 = \rho \kappa^2 U_{bw}^2 = \rho \kappa^2 p_b^2 U_{1m}^2 \sin^2 \omega t \quad (1.117)$$

where  $u_{w*}$  is wave friction velocity. Using the Jonnson definition of wave friction factor  $f_w$ . Bijker rewrite  $\tau_{bw}$  as

$$\tau_{bw} = \frac{1}{2} \rho f_w U_{1m}^2 \sin^2 \omega t \quad (1.118)$$

and suggested to use the Swart formula for the calculation of wave friction factor. From equations (1.117) and (1.118) we can obtain the fraction  $p$ :

$$p_b = \frac{1}{\kappa} \sqrt{\frac{f_w}{2}}. \quad (1.119)$$

Consider  $\phi'$  to be the angle between the wave front and the current. For the superposition principle, total bottom velocity module  $U_b$  at height  $z'$  becomes (Figure 1.9)

$$U_b = \sqrt{U_{bc}^2 + p_b^2 U_{1m}^2 + 2U_{bc} p U_{1m} \sin \phi'}. \quad (1.120)$$

If we develop the wave-current bed shear stress  $\tau_{wc}$  by the use of Prandtl law (1.111) and equation (1.113), and we consider its component parallel to the current, we can easily observe that wave field enforce it of a component  $\tau_{par}$ . The wave period-averaged value of  $\tau_{par}$  has been numerically developed by Bijker, who wrote it in the form

$$\frac{\tau_{par}}{\tau_{bc}} = a_b + b_b \left( \xi \frac{U_{1m}}{U_{bc}} \right)^{c_b} \quad (1.121)$$

where  $\xi = \frac{p\kappa C}{\sqrt{g}} = C \sqrt{\frac{f_w}{2g}}$ . Considering in particular the range  $0^\circ < \phi' < 20^\circ$ , Bijker obtained the following numerical results for coefficients  $a_b, b_b, c_b$ :

$$\frac{\tau_{par}}{\tau_{bc}} = 0.75 + 0.45 \left( \xi \frac{U_{1m}}{U_{bc}} \right)^{1.13}. \quad (1.122)$$

A similar expression can be obtained for the component  $\tau_{perp}$  of the increment of bed shear stress perpendicular to the current. Total wave current bed shear stress is thus calculated as

$$\tau_{wc} = \tau_{bc} \left( 1 + \frac{1}{2} \xi^2 \frac{U_{1m}^2}{U_{bc}^2} \right). \quad (1.123)$$

Bijker model is maybe first relevant wave-current bed shear stress model: it is easy to use and thus practical in engineering problem. Despite the strong simplifications of this model, it is still widely used in coastal engineering.

### 1.3.2 Grant and Madsen (1979)

Grant and Madsen [16] proposed a wave current bed shear stress model which take into account non-linear interactions between waves and current. They assumed eddy viscosity to be linear close to the bottom, but with different laws outside and inside wave boundary layer. They hence considered two different turbulent scales outside and inside the wave boundary layer.

Eddy viscosity, which is described by a relation of the type  $\nu_T = \kappa u_* z$ , is discontinuous for  $z = \delta$ , where  $\delta$  is the wave boundary layer thickness. Inside the wave boundary layer the dynamic effect of the wave is taken into account, while outside boundary layer waves

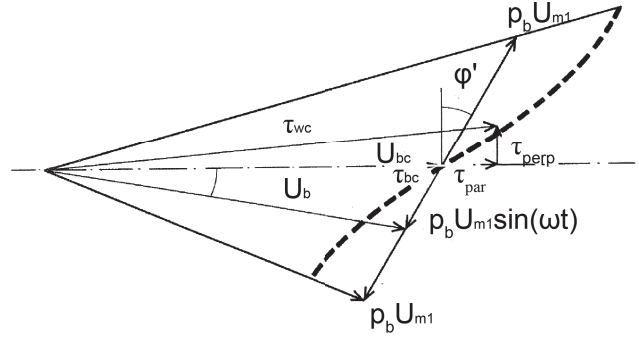


Figure 1.9: Velocity and bed shear stress geometric scheme (modified from [4])

are described by the potential theory and shear stress is related just to the resulting steady current. Thus, steady velocity profile is composed by two logarithmic laws, which intersect at  $z = \delta$ .

Bottom bed shear stress is computed as

$$\vec{\tau}_{wc} = \frac{1}{2} \rho f_{wc} (u_x^2 + u_y^2) \left[ \frac{u_x}{\sqrt{u_x^2 + u_y^2}}, \frac{u_y}{\sqrt{u_x^2 + u_y^2}} \right] \quad (1.124)$$

where  $u_x$  and  $u_y$  the resulting velocity component at a generic height  $a$  close to the bottom. It is adopted the convention that  $x$ -axis is always the direction of wave propagation. Thus,  $u_x^2$  and  $u_y^2$  can be expressed as

$$u_x^2 = \left( \sin(\omega t) + \frac{|u|}{|U_{1m}|} \cos \phi \right) |U_{1m}| \equiv g_x |U_{1m}| \quad (1.125)$$

$$u_y^2 = \left[ \frac{|u|}{|U_{1m}|} \cos \phi \right] |U_{1m}| \equiv g_y |U_{1m}| \quad (1.126)$$

where  $|u|$  is the module of steady current at height  $a$  and  $\phi$  the angle between waves and current. The averaged bed shear stress over wave period has a magnitude of

$$|\tau_m| = \frac{1}{2} \rho f_{wc} V_2 |U_{1m}|^2 \quad (1.127)$$

with

$$V_2 = \left( \frac{1}{2} \right) \left\{ \left[ \int_{-\theta_*}^{\pi+\theta_*} G d\theta - \int_{\pi+\theta_*}^{2\pi-\theta_*} G d\theta \right]^2 + \left[ \int_0^{2\pi} G d\theta \right]^2 \right\}^{1/2} \quad (1.128)$$

and

$$G = (g_x^4 + g_y^2 g_y^2)^{1/2} \quad (1.129)$$

where  $\theta_*$  is the phase  $\omega t_*$  which let us to distinguish between the fraction of the period and positive bed shear stress in  $x$ -direction. Expression of  $V_2$  can be approximated as

$$V_2 = \frac{2}{\pi} \left( \frac{|u|}{|U_{1m}|} \right) (4 - 3 \sin^2 \phi)^{1/2}. \quad (1.130)$$

Maximum bed shear stress, responsible of velocity distribution inside the wave boundary layer, is demonstrable to be

$$|\tau_{max}| = \frac{1}{2} f_{wc} \rho \left[ 1 + \left( \frac{|u|}{|U_{1m}|} \right)^2 + 2 \left( \frac{|u|}{|U_{1m}|} \right) \cos \phi \right] U_{1m}^2 = \frac{1}{2} f_{wc} \rho \alpha_{gm} U_{1m}^2. \quad (1.131)$$

From  $\tau_m$  and  $\tau_{max}$  we obtain, respectively,  $u_{*c}$  and  $u_{*wc}$ . The eddy viscosity is thus:

$$\begin{cases} \nu_T = \kappa u_{*wc} z & z < \delta_w \\ \nu_T = \kappa u_{*c} z & z > \delta_w \end{cases}. \quad (1.132)$$

Developing the solution for both wave motion and steady current, it is possible to obtain the apparent roughness  $\varepsilon_a$  (which consider wave motion effects on the current) and the wave-current friction factor  $f_{wc}$ . From them, steady and oscillatory velocity distribution is obtained inside and outside the wave boundary layer. Apparent roughness formula is

$$\frac{\varepsilon_a}{\varepsilon} = \left[ 24 \frac{|u_{wc*}|}{|u_{c*}|} \left( \frac{|A_{1m}|}{k_N} \right) \right]^{1 - \frac{|u_{c*}|}{|u_{wc*}|}} \quad (1.133)$$

$$\begin{aligned} \left[ 0.097 \left( \frac{\varepsilon}{|A_{1m}|} \right)^{0.5} \frac{K}{f_{wc}^{3/4}} \right]^2 + 2 \left[ 0.097 \left( \frac{\varepsilon}{|A_{1m}|} \right)^{0.5} \frac{K}{f_{wc}^{3/4}} \right] \left[ \frac{V_2}{2\alpha^{1/4}} \right] \cos \phi \\ = \frac{\alpha^{3/4}}{4} - \frac{V_2^2}{4\alpha^{1/2}} \end{aligned} \quad (1.134)$$

with

$$K = \frac{1}{2\xi_0^{1/2}} \frac{1}{\sqrt{Ker^2 2\xi_0^{1/2} + Kei^2 2\xi_0^{1/2}}} \quad (1.135)$$

where  $\xi_0 = \frac{\varepsilon}{30l_{gm}}$ ,  $l_{gm} = \frac{\kappa|u_{wc*}|}{\omega}$ ,  $Ker$  e  $Kei$  are Kelvin functions of zeroth order.

Grant and Madsen model is quite interesting for its approach to the problem and for the elegance of the mathematical solution (further details are available in their article [16]), but it is quite complex to apply in practical cases and it seems not to be thus useful in engineering problems. Another invariant eddy viscosity model has been proposed also by Van Kestern and Bakker [53]: further details are available in literature.

### 1.3.3 Fredsøe (1984)

Fredsøe [13] proposed another theoretical model in which is studied bed shear stress through the solution of integrated momentum equation inside the boundary layer. In particular, Fredsøe studied the evolution of quantities along the wave period, with particular regard to the thickness of boundary layer  $\delta$  and to the friction velocity  $u_*$ . Coherently with Jonnson, he considered the friction factor to be connected with the maximum bed shear stress.

First hypothesis of Fredsøe was on the turbulent time scale: he considered it small with respect to the wave period and, thus, single wave periods (and semi-periods too) are independent each other.

Consider the integrated momentum equation inside the boundary layer:

$$-\rho \int_{z_0}^{\delta+z_0} \frac{\partial}{\partial t} (u_0 - u_x) dz = \int_{z_0}^{\delta+z_0} \frac{\partial \tau}{\partial z} dz = -\tau_b. \quad (1.136)$$

where  $u_0$  is velocity at the boundary layer limit ( $z = \delta + z_0$ ) and  $z_0$ , as usual, is equal to  $\frac{\varepsilon}{30}$ . Fredsøe assumed the flow to be fully turbulent in the wave boundary layer (velocity is hence described by velocity distribution of equation (1.112)).

Let us consider at first the wave-alone motion. Author defined the adimensional parameter  $Z_F$  as:

$$Z_F = \frac{u_0}{u_*} \kappa \quad (1.137)$$

where  $u_0 = U_{1m} \sin(\omega t)$ .

It is easy to notice that, considering equations (1.112) and (1.137),

$$Z_F = \ln \left[ \frac{\delta + \frac{\varepsilon}{30}}{\frac{\varepsilon}{30}} \right]. \quad (1.138)$$

Wave boundary layer thickness is hence dependent exclusively on  $Z_F$  and is equal to

$$\delta = \frac{\varepsilon}{30} (e^{Z_F} - 1). \quad (1.139)$$

Solving equation (1.136) we thus obtains:

$$-u_*^2 = -\delta \frac{du_0}{dt} + \frac{1}{\kappa} \frac{du_*}{dt} \frac{\varepsilon}{30} [e^{Z_F} (Z_F - 1) + 1]. \quad (1.140)$$

It should be noticed that

$$\frac{dZ_F}{dt} = \frac{Z_F}{u_0} \frac{du_0}{dt} - \frac{Z_F}{u_*} \frac{du_*}{dt}, \quad (1.141)$$

and equation (1.140) can be rewritten as

$$\frac{dZ_F}{dt} = \frac{\left[ \frac{30}{\varepsilon} \kappa^2 u_0 - Z_F (e^{Z_F} - Z_F - 1) \right] \frac{1}{u_0} \frac{du_0}{dt}}{e^{Z_F} (Z_F - 1) + 1}. \quad (1.142)$$

Equation (1.142) must be solved numerically. Fredsøe proposed to substitute variable  $t$  with the adimensional variable  $\omega t$ . In this way he obtained:

$$\frac{dZ_F}{d(\omega t)} = \frac{[\beta_F \sin(\omega t) - Z_F (e^{Z_F} - Z_F - 1)] \frac{1}{u_0} \frac{du_0}{d(\omega t)}}{e^{Z_F} (Z_F - 1) + 1} \quad (1.143)$$

where  $\beta_F = \frac{30\kappa^2 U_{1m}}{\varepsilon \omega} = 30\kappa^2 \frac{A}{\varepsilon}$ . The solution is illustrated in Figure 1.10.

Theoretical expression of wave friction factor, obtained from maximum bed shear stress (using equation (1.97)) can be approximated [14] by :

$$f_w = 0.04 \left( \frac{A_{1m}}{\varepsilon} \right)^{-\frac{1}{4}} \quad \frac{A_{1m}}{\varepsilon} > 50 \quad (1.144)$$

$$f_w = 0.4 \left( \frac{A_{1m}}{\varepsilon} \right)^{-\frac{3}{4}} \quad \frac{A_{1m}}{\varepsilon} < 50 \quad (1.145)$$

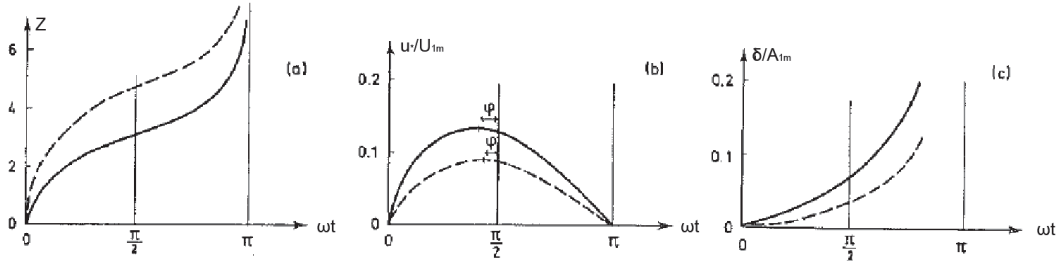


Figure 1.10: Variation in  $Z$ ,  $u_*/U_{1m}$  and  $\delta/a$  for  $A_{1m}/\varepsilon = 10$  - continuous line - and  $A_{1m}/\varepsilon = 100$  - dotted line - [13].

while, similarly, average wave boundary layer thickness can be obtained by

$$\frac{\delta}{\varepsilon} = 0.09 \left( \frac{A_{1m}}{\varepsilon} \right)^{0.82} \quad (1.146)$$

A similar approach can be applied to wave-current condition. Assuming fully turbulent flow, Fredsøe distinguished between steady and oscillating components. Inside the wave boundary layer, both these components are characterized by a logarithmic velocity distribution and, globally, the resulting velocity distribution is assumed to be the typical fully turbulent distribution given by

$$\frac{u_x(z)}{u_{*0}} = \frac{1}{\kappa} \ln \frac{z}{\frac{\varepsilon}{30}} \quad z < \delta \quad (1.147)$$

Outside the boundary layer, the oscillating component is described by the regular wave theory, while the steady component  $u_{xc}(z)$  is assumed to be described by different logarithmic distribution written as

$$\frac{u_{xc}(z)}{u_{*c}} = \frac{1}{\kappa} \ln \frac{z}{\frac{\varepsilon_a}{30}} \quad z > \delta \quad (1.148)$$

where  $\varepsilon_a$  is an apparent roughness, which take into account the effects of the wave motion on the steady current, as the wave boundary layer acts as a larger roughness element. It should be noticed that, for hypothesis of the author, two friction factors have been defined:  $u_{*0}$ , related to the boundary layer, and  $u_{*c}$ , related to the steady component outside the wave boundary layer.

Fredsøe, in order to solve the problem, imposed as boundary condition the continuity of velocity at the top of the wave boundary layer ( $z = \delta + \frac{\varepsilon}{30}$ ):

$$\left[ \frac{u_{*c}}{\kappa} \ln \left( \frac{\delta + \frac{\varepsilon}{30}}{\frac{\varepsilon}{30}} \right) \right]^2 = \left[ \frac{u_{*0}}{\kappa} \ln \left( \frac{\delta + \frac{\varepsilon}{30}}{\frac{\varepsilon}{30}} \right) + U_{1m} \sin(\omega t) \cos \phi \right]^2 + [U_{1m} \sin(\omega t) \sin \phi]^2 \quad (1.149)$$

where  $\phi$  is the angle between waves and current. As for the previous case of wave-alone condition, Fredsøe defined

$$Z_F = \frac{u_0}{u_{*res}} \kappa \quad (1.150)$$

where

$$\frac{1}{u_{*res}} = \frac{u_{*c} \cos \phi}{u_{*c}^2 - u_{*0}^2} + \sqrt{\frac{u_{*0}^2 \cos^2 \phi}{(u_{*c}^2 - u_{*0}^2)^2} + \frac{1}{u_{*c}^2 - u_{*0}^2}}. \quad (1.151)$$

It is useful to be noticed that, because of its definition and imposed boundary condition,

$$Z_F = \ln \left( \frac{\frac{\varepsilon}{30} + \delta}{\frac{\varepsilon}{30}} \right) = \frac{u_0}{u_{*res}} \kappa = \frac{u_x \left( \frac{\varepsilon}{30} + \delta \right)}{u_*} \kappa = \frac{u_{xc} \left( \frac{\varepsilon}{30} + \delta \right)}{u_{*0}} \kappa \quad (1.152)$$

while equation (1.139) is still valid. Consider  $\gamma$  the angle of resulting velocity (and bed shear stress). From trigonometry (see Figure 1.11), it is easy to demonstrate that

$$\cos \gamma = \frac{u_0 \kappa \cos \phi + u_{*0} Z_F}{u_* Z_F} \quad (1.153)$$

$$\sin \gamma = \frac{u_{*res}}{u_*} \sin \phi. \quad (1.154)$$

The calculation of  $Z_F$  is obtained considering the direction perpendicular to the current. The momentum equation (1.136) becomes

$$-u_* u_{*res} + \frac{\varepsilon}{30} (e^{Z_F} - 1) \frac{du_0}{dt} = \frac{\varepsilon}{30} [e^{Z_F} (Z_F - 1) + 1] \frac{du_{*res}}{dt}. \quad (1.155)$$

Noticing finally that  $\frac{du_{*res}}{dt} = \frac{u_*}{u_{0w}} \frac{du_{0w}}{dt} - \frac{u_{*res}}{Z_F} \frac{dZ_F}{dt}$ , we obtain the differential equation

$$\frac{dZ_F}{dt} = \frac{Z_F (1 + Z_F - e^{Z_F})}{e^{Z_F} (Z_F - 1) + 1} \frac{1}{u_0} \frac{du_0}{dt} + \frac{30\kappa}{\varepsilon} \frac{\sqrt{\kappa^2 u_0^2 + Z_F^2 u_{*0}^2 + 2Z_F \kappa u_{*0} \cos \gamma}}{e^{Z_F} (Z_F - 1) + 1} \quad (1.156)$$

which can be solved numerically.

Parallel to the current, momentum equation inside the boundary layer is

$$\int_{\frac{k_N}{30}}^{\delta + \frac{k_N}{30}} \rho \frac{d}{dt} (u_x \cos \gamma - u_0 \cos \phi) dz = -\tau_b \cos \gamma + \tau_{wc} \quad (1.157)$$

where  $\tau_{wc}$  corresponds to the bed shear stress at the top of the boundary layer. Averaging over the wave period, left-hand side of equation (1.157) becomes 0. The averaged wave current shear stress  $\overline{\tau_{wc}}$  is then

$$\overline{\tau_{wc}} = \rho u_{*c} = \frac{1}{T} \int_0^T \tau_b \cos \gamma dt = \frac{1}{T} \rho \int_0^Y u_* \cos \gamma dt. \quad (1.158)$$

Apparent roughness is obtained from velocity profile inside and outside the mean boundary layer thickness ( $\delta_m = \frac{1}{2} (\delta (\omega t = \frac{\pi}{2}) + \delta (\omega t = \frac{3\pi}{2}))$ ). Its analytical formula is

$$\frac{\varepsilon_a}{\varepsilon} = \left( \frac{30\delta_m}{\varepsilon} \right)^{1 - \frac{u_{*0}}{u_*}}. \quad (1.159)$$

Solution of Fredsøe model requires an iterative approach. From a starting value of  $u_{*0}$  it is possible to solve equations (1.156), (1.139) and (1.149). Then, from (1.158),  $u_{*c}$  and  $u_{xc}(\delta)$  are obtained and, finally,  $u_{*0}$  can be corrected by equation (1.152). Finally, let us consider

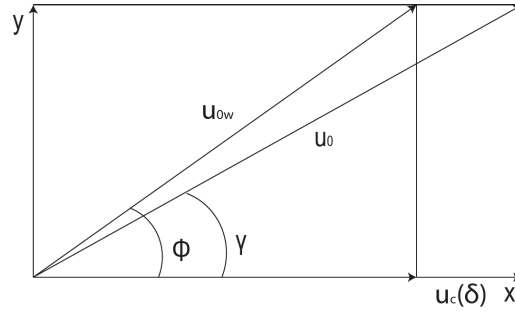


Figure 1.11: Definition sketch of angles and velocities for Fredsøe model [13].

the current friction factor, which, from equation (1.90), can be computed as  $f_c = 2 \left( \frac{u_{*c}}{U} \right)^2$  where  $U$  is depth averaged current velocity. In the presence of strong a current, the friction factor value approaches the case of a pure current flow, while for weak current  $f_c$  increases to a high value, which tends to

$$\sqrt{\frac{2}{f_c}} \rightarrow \frac{1}{\kappa} \ln \left( \frac{h}{\delta} - 1 \right) \quad (1.160)$$

where  $h$  is water depth.

### 1.3.4 Van Rijn (1993)

Van Rijn is nowadays a leading expert in coastal morphodynamics. In his studies, he developed different practical formulas and numerical models for evaluation of sediment transport, as we will discuss in next chapters. The value of his work is the simplicity of the approaches he proposed, which are quite useful in practical problems.

In the calculation of wave current bed shear stress, he proposed a mathematical scheme similar to that of Fredsøe, with a 2-layer logarithmic velocity distribution: the lowest of them is influenced by the effective roughness  $\varepsilon$  while the highest by an apparent roughness  $\varepsilon_a$  [59]. He considered the first layer thick as 3 times the wave boundary layer. In particular, in 1DV case steady-velocity distribution is

$$u_x(z) \frac{U \ln \left( \frac{30z}{\varepsilon_a} \right)}{-1 + \ln \left( \frac{30d}{\varepsilon_a} \right)} = \quad z \geq \delta \quad (1.161)$$

$$u_x(z) = \frac{U_\delta \ln \left( \frac{30z}{\varepsilon} \right)}{\ln \left( \frac{30h}{\varepsilon} \right)} \quad z < \delta \quad (1.162)$$

with  $U_\delta = u_x(\delta)$  and  $U$  is the depth-averaged velocity.

From the velocity profile (1.161) it is possible to compute the friction velocity in current direction:

$$u_{*wc} = \frac{\kappa U}{-1 + \ln \left( \frac{30h}{\varepsilon_a} \right)} \quad (1.163)$$

and, averaging over wave period, the mean bed shear stress in current direction

$$\tau_{wc} = \frac{\rho \kappa^2 U^2}{\left[-1 + \ln\left(\frac{30h}{\varepsilon_a}\right)\right]^2} = \frac{1}{8} \rho \lambda_{wc} U^2. \quad (1.164)$$

where  $\lambda_{wc} = \frac{8\kappa^2}{\left[-1 + \ln\left(\frac{30h}{\varepsilon_a}\right)\right]^2} = 0.24 \left[\ln\left(\frac{12h}{\varepsilon_a}\right)\right]^{-2}$  is the wave current Darcy-Weissbach-form friction factor.

In the 2DH case, Van Rijn suggested to consider bed shear stress in  $x$  and  $y$  directions as

$$\tau_{wc,x} = \frac{1}{8} \rho \lambda_{wc} |U| U \quad (1.165)$$

$$\tau_{wc,y} = \frac{1}{8} \rho \lambda_{wc} |U| V \quad (1.166)$$

where  $U$  and  $V$  are the two components of the depth-averaged velocity, which has module  $|U| = \sqrt{U^2 + V^2}$ .

The apparent roughness  $\varepsilon_a$  depends on  $U_{1m}$ , on wave period  $T$  and on the angle between waves and current  $\phi$ . Van Rijn considered period influence to be negligible and, from experimental analysis, proposed the following formula:

$$\frac{\varepsilon_a}{\varepsilon} = \exp\left(\gamma \frac{U_{1m}}{|U|}\right). \quad (1.167)$$

Here,  $\gamma$  coefficient depends on  $\phi$  and can be computed as  $\gamma = 0.8 + \phi - 0.3\phi^2$  where  $\phi$  is considered to be in radians. This formula is a regression function from experimental data.

Van Rijn didn't consider the value of maximum bed shear stress. Further details are available in his book [59].

### 1.3.5 Soulsby (1993-1997)

There is a great number of mathematical models for the calculation of wave-current bed shear stress presented in literature: in this chapter just some of the most important have been described. As discussed above, some of them can be difficult to apply in real study cases because of the type or the number of variables they need and the choose between one of them can be difficult to do. Just in 1991, MAST G6M group (Coastal Morphodynamic problems) compiled a list of 21 different models and several new models have appeared since then. An important contribution to this problem has been offered by that group, in particular by Soulsby et al [45]. In order to compare some of these models they studied a universal regression formula, able to represent, using a set of calibration parameters, all considered models. Soulsby focused on 2 particular values of the wave-current bed shear stress: the time-mean bed shear stress  $\tau_m$  and the maximum bed shear stress  $\tau_{max}$  (from now, "wc" subscript will be omitted).

In particular, the time-mean bed shear stress is supposed to be responsible of the current velocity and the diffusion of suspended sediment (in the upper part of the flow), while maximum bed shear stress determines threshold of motion and entertainment of sediment. The primary purpose of the model is to consider nonlinear enhancement, which relates  $\tau_m$  and  $\tau_{max}$  to wave-alone and current-alone bed shear stresses (respectively  $\tau_{bc}$  and  $\tau_{bw}$ : see Figure 1.12).

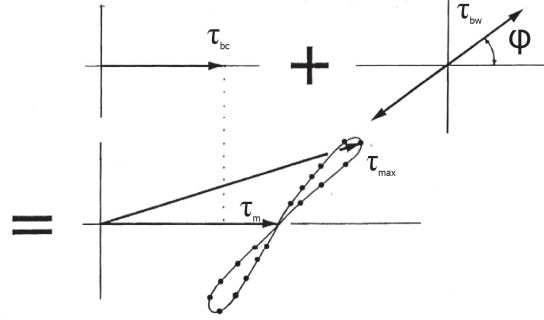


Figure 1.12: Sketch of bed shear stresses [45].

All results are presented in form of non-dimensional parameters

$$y_s = \frac{\tau_m}{\tau_{bc} + \tau_{bw}} \quad (1.168)$$

$$Y_s = \frac{\tau_{max}}{\tau_{bc} + \tau_{bw}} \quad (1.169)$$

which are difficultly confused with space coordinates of the problem. Parameters  $y_s$  and  $Y_s$  are plotted against  $x_s = \frac{\tau_c}{\tau_c + \tau_w}$ .

$\tau_{bc}$  is calculated as a drag stress and  $\tau_{bw}$  using Jonsson formula (1.97).

The functions chosen for  $y$  and  $Y$  calculations are in the forms

$$y_s = x_s [1 + b_s x_s^{p_s} (1 - x_s)^{q_s}] \quad (1.170)$$

$$Y_s = 1 + a_s x_s^{m_s} (1 - x_s)^{n_s} \quad (1.171)$$

where  $a, m, n, b, p, q$  are fitting coefficients. The first three of them, responsible for  $Y$  and so for the maximum bed shear stress, are given by

$$a_s = \left( a_1 + a_2 |\cos \phi|^I \right) + \left( a_3 + a_4 |\cos \phi|^I \right) \log_{10} (f_w / C_D) \quad (1.172)$$

where  $\phi$  is wave-current angle,  $f_w$  wave friction factor and  $C_D$  drag coefficient. Similar expressions are used for  $m$  and  $n$ .

The last three coefficients are instead similarly given by an equation like

$$b_s = \left( b_1 + b_2 |\cos \phi|^J \right) + \left( b_3 + b_4 |\cos \phi|^J \right) \log_{10} (f_w / C_D). \quad (1.173)$$

The number of independent fitting parameter are thus 13 for  $\tau_m$  and 13 for  $\tau_{max}$ .

In Figure 1.13-a, the trend of  $y$  and  $Y$  against  $x$  are plotted for 8 different models: Bijker [4] -B67-, Fredsøe [13] -F84- and Grant and Madsen [16] -GM79- have already been discussed in this chapter, while for Van Kestern and Bakker [53] -VKB84-, Huyng-h-Thahn and Temperville [20] -HT91-, Myrhaug and Slaattelid [28] -MS90-, Christoffersen and Jonsson [7] -CJ85- and David, Soulsby and King [8] -DSK88- further details are available in literature. Observing  $y$  trend, it is possible to recognize three main behaviours: the first is that of models of Fredøe F84, HT91 and DSK88, the second one is that of Bijker B67 and VKB84 and the last one is that of Grant and Madsen GM79, MS90 and CJ85.

Let us consider Figure 1.13-b. Here, Fredsøe model has been analysed using Soulsby approach: both  $y$  and  $Y$  are plotted for several values of  $\phi$ . Let us underline that while  $\tau_{max}$  is strongly influenced by the wave direction,  $\tau_m$  have a much weaker influence from it.

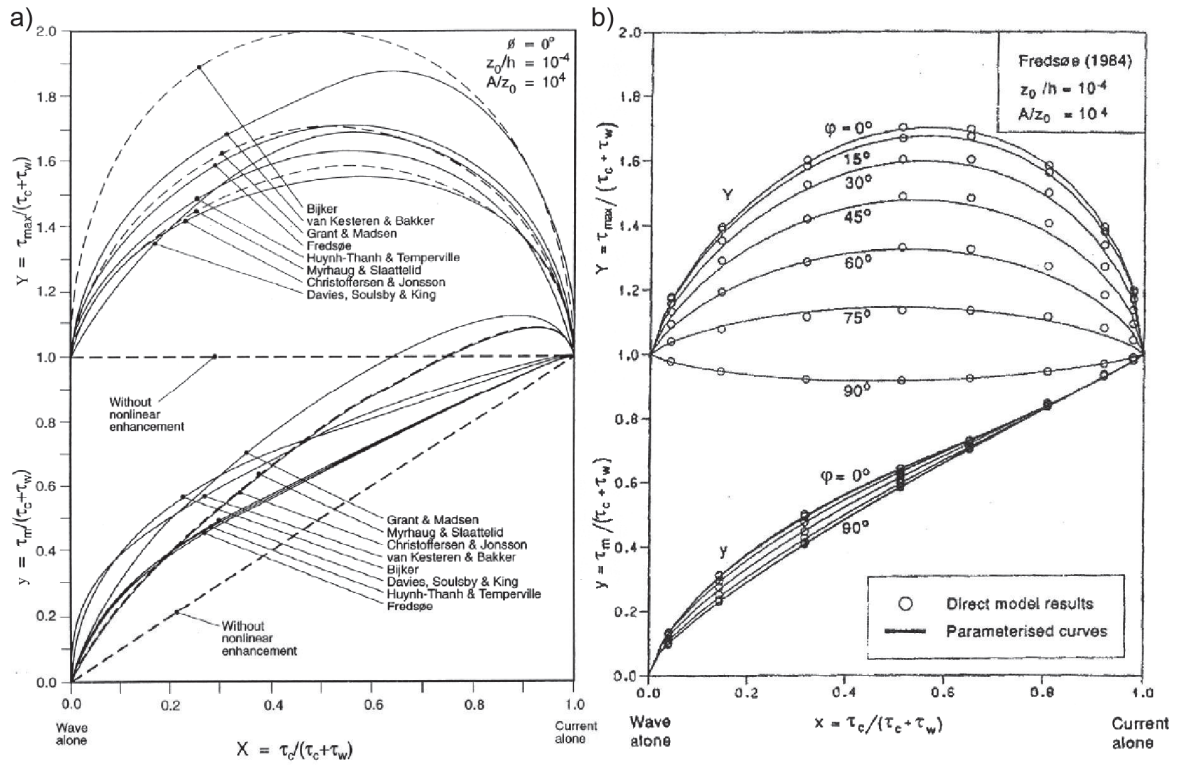


Figure 1.13: a) Comparison of the trend of  $y$  and  $Y$  between different theoretical models. b) Analysis of Fredsøe Model using Soulsby et al. approach, comparison of  $y$  and  $Y$  trends changing wave current angle [45].

In 1997, Soulsby [44] applied his 13-parameters  $\tau_m$  regression formula to a experimental data set. In this way, he obtained a set of coefficients (said “DATA13”) optimized on the data set (said “DATA13”) and, thus, able to fit significantly better than each other model available experimental data.

Afterwards, he proposed a new optimization based on just two non vanishing coefficients said “DATA2”, which seems to fit data almost as good as best of theoretical models. The latter approach reduces to the equation

$$\tau_m = \tau_{bc} \left[ 1 + 1.2 \left( \frac{\tau_{bw}}{\tau_{bc} + \tau_{bw}} \right)^{3.2} \right]. \quad (1.174)$$

In DATA2, as evident from the equation,  $\tau_m$  is independent of wave current direction. This is coherent with Figure 1.13-b, as discussed above.

Because of the lack of a sufficient number of data, Soulsby didn’t apply a similar approach for the computation of maximum bed shear stress. Thus, in DATA13 and DATA2 methods, maximum bed shear stress is obtained as a vector addition between  $\tau_m$  and  $\tau_w$  (as sketched in Figure 1.12):

$$\tau_{max} = \sqrt{(\tau_m + \tau_{bw} \cos \phi)^2 + (\tau_{bw} \sin \phi)^2}. \quad (1.175)$$

This last methods are particularly easy to use in practical problems and numerical models, where a theoretical model can be very heavy to be applied. For this reason, in particular for DATA2, its use is really common in morphodynamic models and it is currently considered a reference in wave current bed shear stress computation.

### Some considerations about DATA2 and DATA13 methods.

DATA2 and DATA13 models, as said, can result very useful for practical purposes because of their simplicity. However, it is important to have a clear idea of how they work and difference between them and theoretical models. In Figure 1.14 and 1.15 comparison between DATA2, DATA13 and some of above mentioned theoretical models is illustrated: in particular have been considered Bijker model, Grant and Madsen model and Fredøe model. Three wave current angles have been studied:  $0^\circ$  (waves parallel to the current flow),  $45^\circ$  and  $90^\circ$  (waves orthogonal to the current). From a first look, it is evident that DATA2 and DATA13 schemes are not always accurate and sometimes give results that are not coherent with theoretical models.

With regards to DATA13, if the wave current angle is close to 0 and environment is current-dominated ( $x \geq 0.5$ ), the mean bed shear stress demonstrates to be affected by a relevant error. This is not to be considered a mistake in Soulsby formula, but a consequence of the available experimental data on which regression parameters have been optimized. In fact, no many data were available in that particular dynamic conditions at the time Soulsby calculated these coefficients. Anyway, this problems seems to reduce significantly increasing  $\phi$ .

In DATA2, the independence of the formula from wave current direction lets the scheme not to have a similar problem: thus, generally, DATA2 can be considered more reliable than DATA13.

Finally, both DATA2 and DATA13 calculate maximum bed shear stress as vector addition of mean bed shear stress and wave bed shear stress, as illustrated above. In Figure 1.15, difference between them and other models is clear:  $\tau$  is generally underestimated. This is caused by the fact that similar calculation of maximum bed shear stress can't take into account of all nonlinear interaction between waves and current. Similarly, also Bijker model, which doesn't consider at all nonlinear interactions, seems to overestimate considerably maximum bed shear stress.

For this reasons, DATA2 ad DATA13 should be considered a really useful instrument for wave current bed shear stress computation, because the absence of complex mathematical algorithms and the independence of them from particular dynamic hypothesis let similar approaches to be particularly suited for the implementation in numerical modelling. However, the limits illustrated above should be always remembered in the analysis of numerical results.

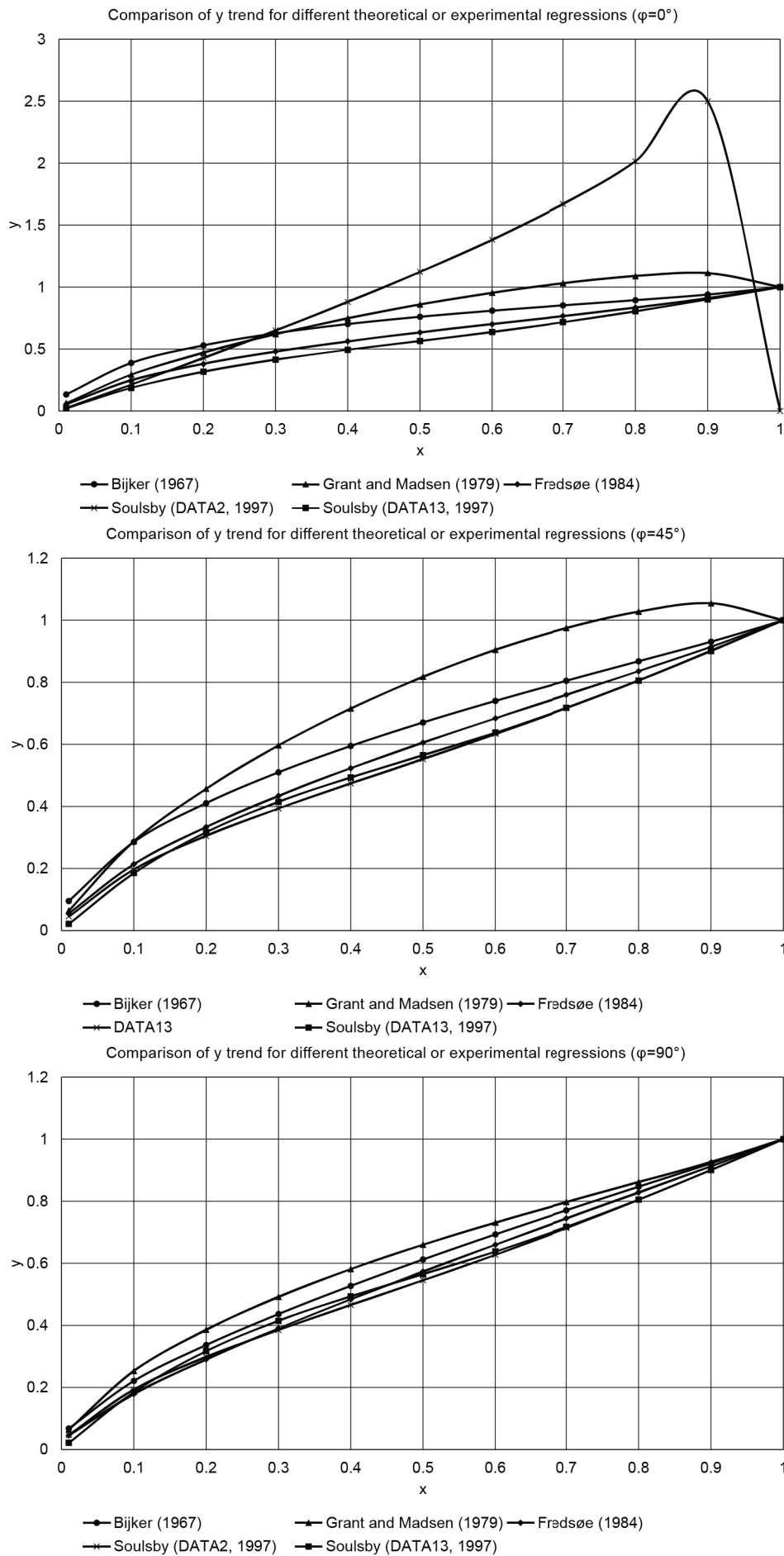


Figure 1.14: Comparison of trend of the y in different wave current directions.

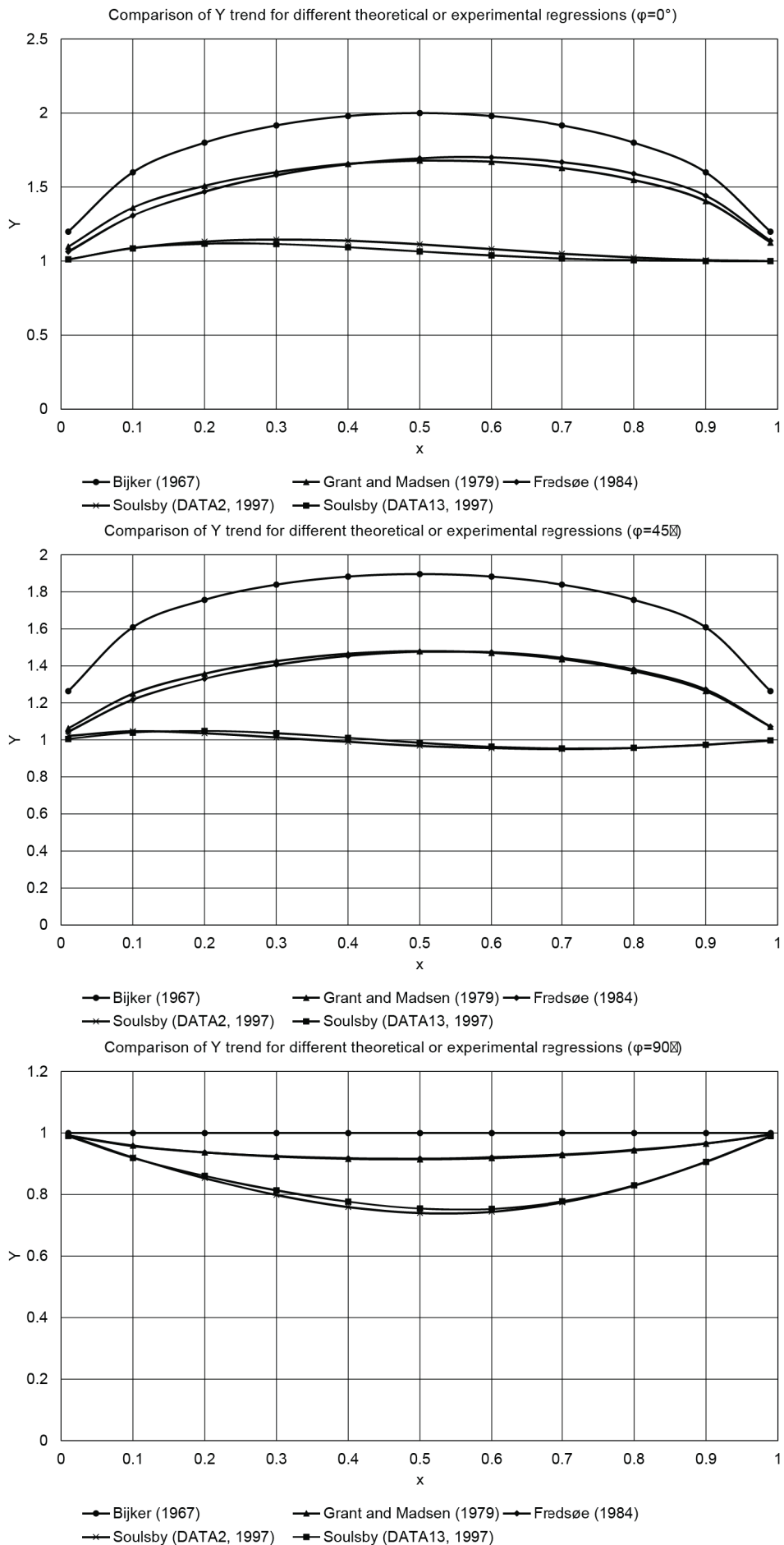


Figure 1.15: Comparison of the trend of Y in different wave current directions.

## Chapter 2

# Principles of sediment transport

Sediment transport, as pointed out by Ashish Mehta [26], is an observational science. The mechanics of this phenomenon is in fact quite impossible to be described in detail: number of variables is too high to develop an adequate analytical solution to the problem. However, in literature a great number of sediment transport studies is available, generally supported by experimental analysis. Moreover, some really simple physical schemes help to understand, from a global point of view, the dynamics of sediment transport, resulting useful for a comprehension of morphodynamic evolution in real environments.

In order to get a very first classification of sediment transport problem, it is fundamental to distinguish between *granular* and *cohesive* sediments.

Granular sediments are characterized by grains with a diameter greater than  $60\ \mu\text{m}$ . Their dynamics is dominated by the grain weight and the geometry and by the drag capacity of the flow. Granular sediment transport can be described by two main mechanisms: *bed sediment transport* and *suspended sediment transport*. In the first case, grains move by rolling and jumping in a layer close to the bottom: this mechanism is typical of heavier sediments, which can't be maintained in suspension by the flow. In the latter, sediments involve all the water volume: the flow is in fact able to sustain grain's weight and sediments following a particular concentration distribution along the depth. When grains deposit, they form a network structure, with a resistance depending on internal friction angle which will not change significantly in time because no consolidation processes are involved.

Cohesive sediments have a diameter smaller than  $60\ \mu\text{m}$ , which lets the particles ("grains" is not a proper definition) interact through an electrochemical inter molecular attraction force, called cohesion. Cohesion has great influence in sediments behaviour: the particles tend to bind together forming flocks and, for very high concentrations, layers, which changes significantly the dynamics of falling process. For presence of cohesion, the stress needed to pick up sediments is greater than the stress needed to allow sediments to remain suspended. Cohesive sediment dynamics is mainly influenced by the mass concentration (in particular considering settling velocity) and bulk properties of the bed admixture, which have a great influence on the erosion rate.

Considering the transport mechanism, due to their weight cohesive particles are generally suspended. However, a complete analysis of cohesive sediment dynamics would be much more complex, in particular at high concentrations: in this case hydrodynamics is in fact strongly affected by interaction with suspended material.

Anyway, in the present work only low-concentration suspended transport is considered: in this way, the global sediment behaviour can be easily modelled also in complex wide areas, without spending excessive computational time.

With regards to cohesive deposits, their geotechnical properties are strongly influenced by consolidation processes: consequent water expulsion has indeed great influence on their resistance.

Granular and cohesive sediments can be present together and interact each other, forming mixtures. It is not our intention to consider how cohesive and granular sediments can influence each other and they are considered here to be always independent. Further details about sand mud mixtures are available in Mitchener and Torfs [27] and in Van Ledder thesis [54].

In the present chapter, an overview on fundamentals about granular and cohesive sediment transport is offered, with particular attention to theories and approaches that have been applied in the numerical model developed.

## 2.1 Sediment properties

### 2.1.1 Granular Sediments

The unit particle of granular sediment transport is *grain*. Grains are classified according to their diameter into *clay, silts, sands, granules, pebbles, cobbles and boulders* [44]. In table 2.1 a summary of sediment classes and respective diameters is available. In sediment transport granules, pebbles, cobbles and boulders are considered *gravel* and difficultly involve coastal and estuarine environments. Thus, in these areas sand is the most common granular sediment class. Finally clay and silts are globally considered as *mud* and are treated as cohesive sediment.

Natural sands always contain a mixture of grain sizes and generally the size distribution is studied by sieving the material using a set of sieves with meshes decreasing in size. In this way a cumulative curve of the percentage of mass passing at each sieve is obtained. The notation  $d_n$  is used to indicate the diameter for which  $n\%$  is finer. Generally, sediment transport formulas involve  $d_{50}$  (diameter for which 50% of the material is finer) and  $d_{90}$  (diameter for which 90% of the material is finer). In Figure 2.1, an example of grain-size distribution is shown.

Another important property of granular sediments is the *density*. In Europe, sands are mainly composed by quartz, with a density  $\rho_s$  usually close to  $2650 \text{ kg/m}^3$ . Shells can be present in sands with a different percentage and have a typical density of 2400, while other minerals can reach also a lower density, like for example coal ( $1400 \text{ kg/m}^3$ ). One more important property is grain shape: sands grains are usually roughly spherical (ratio between major and minor axis is not usually greater than 2), but shells can be much more flat and irregular. Generally, sediments with different density or shape behave hydraulically like an equivalent quartz grain of a different (generally smaller) diameter. Thus, it is useful to consider an equivalent quartz grain for granular sediment transport.

Deposits of sand at the bottom are mixture of sand and water and are considered to be saturated. In order to study them, 4 more parameters are needed: *porosity*  $n_{por}$ , *angle of repose*  $\Phi_i$  and *residual angle*  $\Phi_r$ .

Porosity is the ratio between volume of water and the volume of mixture in granular deposits. Angle of repose (or angle of initial yield) is the steepest angle to the horizontal which guarantees grains equilibrium. It is a geotechnical parameter that, for non-cohesive sediments, depends on the shape, the sorting and the packing of grains. It is demonstrated to increase with bed concentration. Angle of repose is important in calculation of slope effect on sediment transport, and generally, its value is close to  $32^\circ$  (Soulsby, [44]) but can

Class	Subclass	Diameter $d$ (mm)
Mud	Clay	<0.004
	Silt	0.004-0.06
Sand	-	0.06-2
Gravel	Granule	2-4
	Pebble	4-65
	Cobble	65-250
	Boulder	>250

Table 2.1: Summary of Sediment classes by grain dimensions.

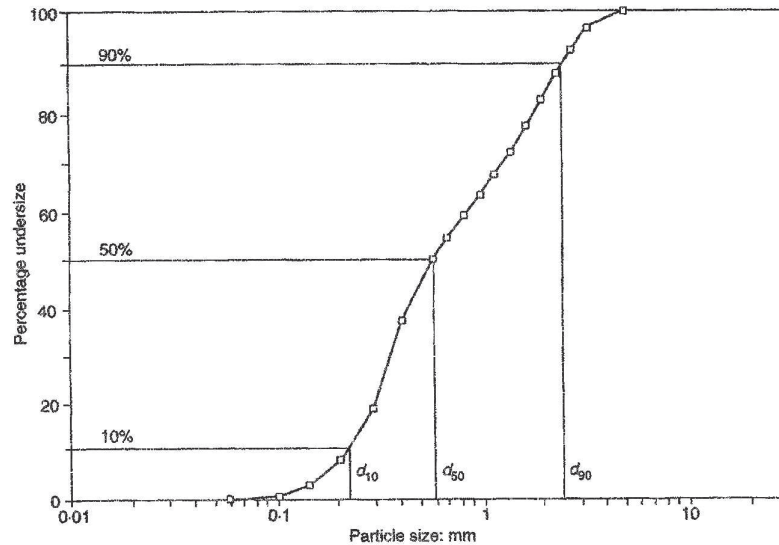


Figure 2.1: Example of grain-size distribution [44].

also exceed  $40^\circ$ - $45^\circ$  [22].

Residual angle is the final slope after shearing has taken place. This is less than  $\Phi_i$ : a typical value for natural sands is  $28^\circ$ .

Finally, the granular *volume concentration*  $c_{gran}$  is defined as ratio between volume of grains and the volume of water: from it, *mass concentration*  $c_{M,gran} = \rho_s c_{gran}$  is easily obtained.

### 2.1.2 Cohesive sediments

In sediment transport, materials with a grain diameter lower than  $60 \mu\text{m}$  are considered cohesive sediments. Although only clay particles are characterized by cohesion, both limes and clay are involved, as specify in table 2.1. In literature, mixtures of clay and lime (with a certain percentage of water) are considered as a unique material called *mud*. Also organic material, if present, plays an important role contributing to the cohesive properties.

The behaviour of cohesive sediments depends directly on the bulk properties of the mixture. The particle size of sediment ( $d_{50,coes}$ ) loses much of his influence, conversely to what happens for grain sediments. Generally, just a small percentage of fine material is sufficient to let the sediments have cohesive properties. Considering the sediment bed, bulk properties can be described by several variables, often connected each other: the cohesive *volume concentration*  $c_{coes}$  and the *density of cohesive particles*  $\rho_{coes}$ , which are defined as in

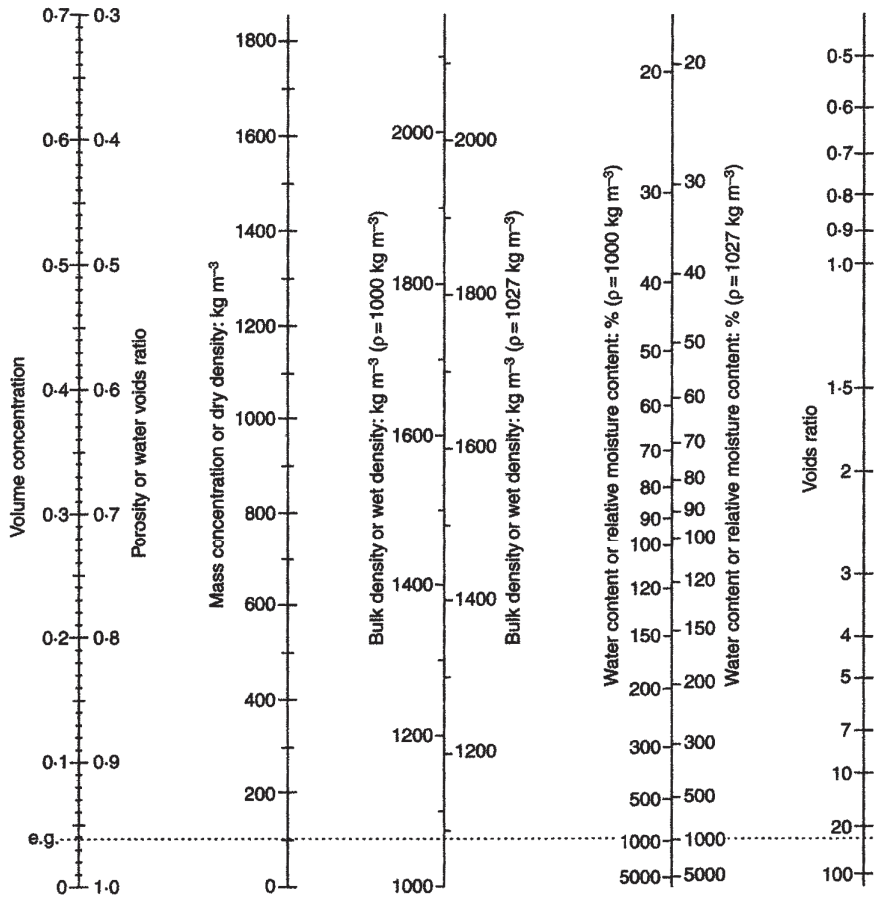


Figure 2.2: Conversion between some of main bulk measures for sediment beds [64].

granular sediments, the *bulk density*  $\rho_b = \rho(1 - c_{coes}) + \rho_{coes}c_{coes}$ , which is the density of the mud (ratio between mass of mixture and volume of mixture), the *dry density*  $c_{M,coes} = \rho_{coes}c_{coes}$ , defined as the *mass concentration*. In Figure 2.2 a schematic conversion between some of main bulk sediment properties is illustrated.

## 2.2 Granular sediment transport

The granular sediment transport is the most studied and analysed typology of sediment transport. The problem has been treated for several decades and is still discussed in literature. A great number of theories and approaches are available and, in general, they can be roughly divided in two main categories: *equilibrium approach* and *non-equilibrium approach*.

Equilibrium approach considers the sediment load corresponding to the local transport capacity:

$$q_s = q_{s,eq}. \quad (2.1)$$

where  $q_s$  is sediment transport load and  $q_{eq}$  is maximum sediment transport that instantaneous hydrodynamic conditions can guarantee (equilibrium load).

In this case a sudden change on hydrodynamics corresponds to a sudden change on the sediment load and morphological evolution is related to spatial variability of equilibrium

load:

$$z_b(x, y, t) = f(\nabla q_{s,eq}(x, y, t)) \quad (2.2)$$

where  $\nabla$  is space gradient.

Basing on equilibrium hypothesis, no additional conditions on transported sediments availability are imposed at boundaries: equilibrium load is in fact always guaranteed in inflow and outflow sections.

Instead, non-equilibrium approach studies the distribution and the propagation of sediments on the flow. In particular, the aim of the problem is the computation of sediment concentration in the domain by solving a proper advective-diffusive equation. In this case, the sediment transport problem is focused on the computation of the source-sink term of the advective-diffusive equation, which represents the erosion or deposition rate. The following relations are thus assumed:

$$z_b(x, y, t) = f(c_{gran}(x, y, z, t), c_{b,eq}(x, y, t)) \quad (2.3)$$

where  $c_{gran}$  is the volume concentration (obtained by the advective-diffusive equation) and  $c_{b,eq}$  is the bottom equilibrium volume concentration.

In the present section, the problem of the threshold of motion is discussed and different theories and approaches for granular bed and suspended load are presented, focusing on those implemented in the numerical model we are going to present in this thesis.

### 2.2.1 Threshold of motion

Let us consider a single grain resting on a horizontal granular bottom. The particle will begin moving when instantaneous fluid force on the particles will be just larger than the resisting force, acted by the submerged weight and the friction with the bottom. A really simplify scheme is sketched in Figure 2.3: on a single grain four main forces are instantaneously acting: a drag force  $F_D$  by the fluid, a friction force  $F_R$  due to the interaction with the bottom, the submerged weight  $G$  and a lifting force  $F_L$ , generated by the pressure difference along the surface of the particle. If we consider momentum equilibrium of the grain with respect to the point of contact  $P$ , we have movement when

$$F_D a_1 + F_L a_3 \geq G a_2. \quad (2.4)$$

An alternative definition of the repose angle  $\Phi_i$  is here considered. Repose angle is considered as the angle between the line through the particle centre and the point of contact and the line through the particle centre normal to the bed surface [59]. From this definition, it is easily demonstrated that (Figure 2.3)

$$\tan \Phi_i = \frac{a_2}{\sqrt{b_2^2 - a_2^2}}. \quad (2.5)$$

Assuming for simplicity lift force much smaller than submerged weight, equation (2.4) can be thus rewritten as

$$F_D \geq \alpha_1 G \tan \Phi_i \quad (2.6)$$

where  $\alpha_1 = \frac{b_2}{b_1 + b_2}$  and  $\Phi_i$  is the angle of repose.

The drag force depends on the water velocity at particle centre  $u_f$  and on the particle normal surface with respect to the water flow (proportional to  $d^2$ ).  $u_f$  is demonstrated to be

related to the friction velocity  $u'_*$ , which is said *skin-friction* friction velocity and depends on grains diameter. A general formulation of drag force is thus

$$F_D = \alpha_2 \rho d^2 u'^2_* \quad (2.7)$$

where  $\alpha_2$  is demonstrated to be depending on local Reynolds number and on the shape. The lift force, here neglected, depends on the same variables of the drag force, and is therefore taken automatically in account by empirical coefficients that will be introduced. For this reason, equation (2.6) can be considered sufficiently general.

The submerged particle weight  $G$  is

$$G = \alpha_3 (\rho_s - \rho) g d^3 \quad (2.8)$$

where  $\alpha_3$  depends on the shape of the grain.

From these considerations, we can reach the following expression for the threshold of motion of a grain:

$$\frac{u'^2_*}{(s-1)gd} \geq \alpha_4 (\alpha_1, \alpha_2, \alpha_3) \tan \Phi_i \quad (2.9)$$

where  $s = \frac{\rho_s}{\rho} \cdot \frac{u'^2_*}{(s-1)gd} = \theta$  is defined as *mobility Shields parameter* and  $\alpha_4 (\alpha_1, \alpha_2, \alpha_3) \tan \Phi_i = \theta_{cr}$  is said *critical Shields parameter*. The latter depends on the hydraulic conditions near the bed (expressed by the Reynolds number  $Re_* = \frac{u_* d}{\nu}$ ), on the shape of the grain and on its position with respect to other grains. It is immediate to reformulate mobility Shields parameter as a function of the stress acting on the grain, called *skin friction bed shear stress*: in fact, from the definition of friction velocity,  $\theta$  can be written as

$$\theta = \frac{\tau'_b}{(\rho_s - \rho) g d} \quad (2.10)$$

where  $\tau'_b$  is the skin friction bed shear stress, related to the grain geometry. Shields in 1936 [40] had performed experiments to determine  $\theta_{cr}$  as a function of the correspondent  $u_{*,cr}$  and, thus,  $Re_*$ . In Figure 2.4 the Shields curve, which represents critical shear stress as a function of  $Re_*$ , is shown.

It should be noted that the function  $\theta_{cr}(Re_*)$  can't be explicit: in fact, both  $\theta_{cr}$  and  $Re_*$  depends on  $u_{*,cr}$ . For this reason, it results not much practical. An alternative independent variable, *the dimensionless particle diameter*  $D_*$ , has been defined in order to obtain an explicit formulation of  $\theta_{cr}$ .  $D_*$  is defined as:

$$D_* = \left[ \frac{(s-1)g}{\nu^2} \right]^{(1/3)} d_{50}. \quad (2.11)$$

Van Rijn suggests the following function for the calculation of  $\theta_{cr}(D_*)$ :

$$\left\{ \begin{array}{ll} \theta_{cr} = 0.24 D_*^{-1} & 1 < D_* \leq 4 \\ \theta_{cr} = 0.14 D_*^{-0.64} & 4 < D_* \leq 10 \\ \theta_{cr} = 0.04 D_*^{-0.1} & 10 < D_* \leq 20 \\ \theta_{cr} = 0.013 D_*^{0.29} & 20 < D_* \leq 150 \\ \theta_{cr} = 0.055 & D_* > 150 \end{array} \right. \quad (2.12)$$

Soulsby and Whitehouse [46] proposed later the following continuous formula for critical state:

$$\theta_{cr} = \frac{0.30}{1 + 1.2 D_*} + 0.055 [1 - \exp(-0.020 D_*)]. \quad (2.13)$$

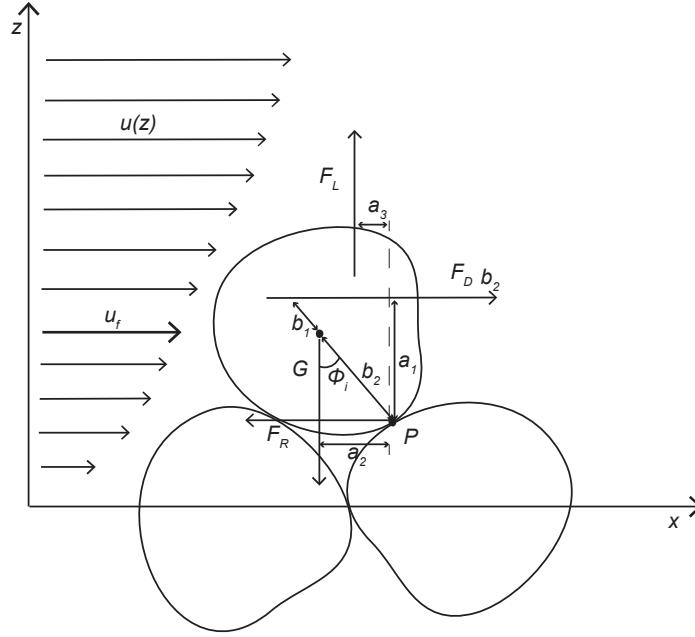


Figure 2.3: Sketch of forces acting on a grain.

As evidenced by Figure 2.5, Soulsby curve for critical state is overlaid to Shields curve for high values of  $D_*$  but seems to be much closer to experimental data for low values of the adimensional diameter. This function has been performed for the calculation of critical state in the numerical model presented in this work.

An alternative way to evaluate the critical state for the threshold of motion is to consider a critical depth-averaged velocity. Van Rijn proposed an expression for critical velocity, derived from critical bed shear stress by the use of Chezy equation. The final expression is:

$$U_{cr} = 5.75 [(s - 1) g d_{50}]^{0.5} \theta_{cr}^{0.5} \log \left( \frac{12h}{\varepsilon'} \right) \quad (2.14)$$

where  $\varepsilon'$  is the grain related roughness, or the effective roughness for a flat bed.

In the present analysis, bed slope effect has not been considered yet. With respect to the flow direction, there can be parallel and/or perpendicular slope. In order to take into account both this factors, two coefficients are available, obtained by solving force equilibrium along the slope.

The first of them is *Schoklitch factor*  $k_\beta$ , which is the ratio between the critical fluid force on a sloping bed  $F_{D,cr,\beta}$  and the critical value on an horizontal bed  $F_{D,cr,o}$ . From easy geometrical considerations it reduces to

$$k_\beta = \frac{F_{D,cr,\beta}}{F_{D,cr,o}} = \frac{\sin(\Phi_i - \beta)}{\sin \Phi_i} \quad (2.15)$$

where  $\Phi_i$  is the angle of repose and  $\beta$  the longitudinal slope of the bed.

The latter is *Leiner factor*  $k_\gamma$ , defined as the ratio between the critical fluid force on a transversely sloping bed  $F_{D,cr,\gamma}$  and that on an horizontal bed. Also  $k_\gamma$  is obtained by solving the force equilibrium and the final expression is

$$k_\gamma = \frac{F_{D,cr,\gamma}}{F_{D,cr,o}} = \cos \gamma \left( 1 - \frac{\tan^2 \gamma}{\tan^2 \Phi} \right)^{0.5} \quad (2.16)$$

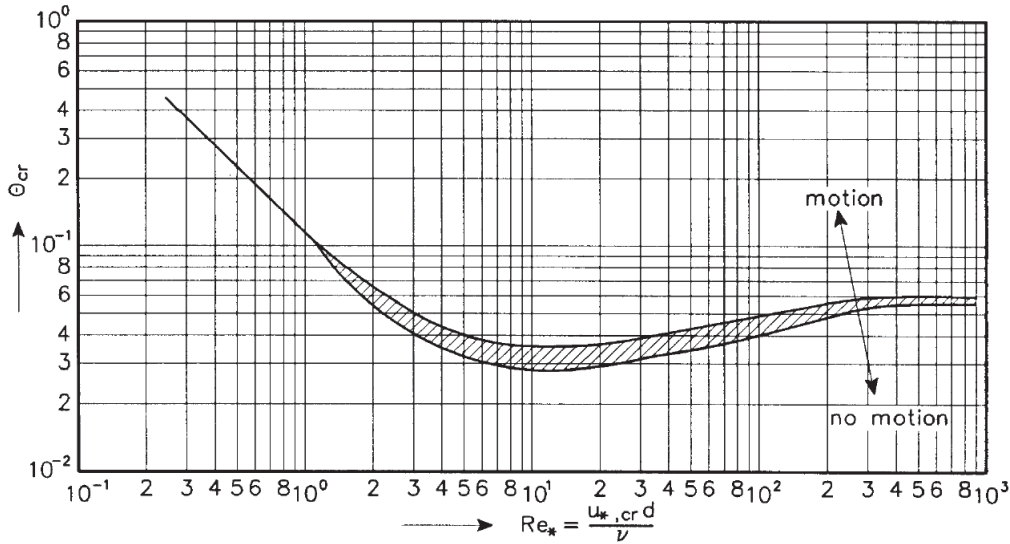


Figure 2.4: Threshold of motion: Shields curve [59].

where  $\gamma$  is the transverse slope of the bed.

Thus, for a combination of longitudinal and transverse bed slopes, the critical bed shear stress can be computed as

$$\tau_{b,cr} = k_\beta k_\gamma \tau_{b,cr,o}. \quad (2.17)$$

### The skin friction over the bed

In studying granular sediment transport, it is important to understand how water flow moves grains and, in particular, which is the stress which drag them causing the motion. Nikuradse introduced the concept of effective sand roughness height  $\varepsilon$  to simulate the height of an arbitrary roughness element of the bottom boundary. On a movable bed,  $\varepsilon$  can be divided in two main components: the *grain roughness*  $\varepsilon'$ , generated by the skin friction forces, and the *form roughness*  $\varepsilon''$ , generated by the bed forms and, more generally, by macroscopical geometry on the bed. In the same way, bed shear stress  $\tau_b$  can be divided into grain-related bed shear stress  $\tau_b'$  and form-related bed shear stress  $\tau_b''$ .

With particular regards to the grain-related bed shear stress, it can be considered as the stress caused by the grains to the flow and, thus, the stress with which water flow acts on the grains causing their movement. Generally, considering granular sediment transport, the threshold of motion is strictly related to the grain-related bed shear stress and not to the effective shear stress, which instead regulates directly hydrodynamics.

The evaluation of  $\varepsilon'$  is generally related to the grain diameter. Experimental results show that it is mainly related to the largest particles of the top layer of the bed [59], and the more relevant diameter seems therefore to be  $d_{90}$ . Van Rijn suggested for grain roughness a value of 3-5  $d_{90}$ , coherently with other authors he cited in his book. Nielsen [29, 30] proposed a granular roughness equal to  $2.5d_{50}$ . This formulation has the advantage to relate the grain roughness to the mean diameter, which is the diameter class easiest to be provided. Let us note that, if on a flat bed  $\varepsilon = \varepsilon' = 2.5d_{50}$ , then  $\varepsilon/12$  becomes  $d_{50}/30$ , and equation (2.14) becomes coherent with the classical velocity distribution for a rough turbulent flow, where typical value of  $z_0$  is  $\varepsilon/30$ .

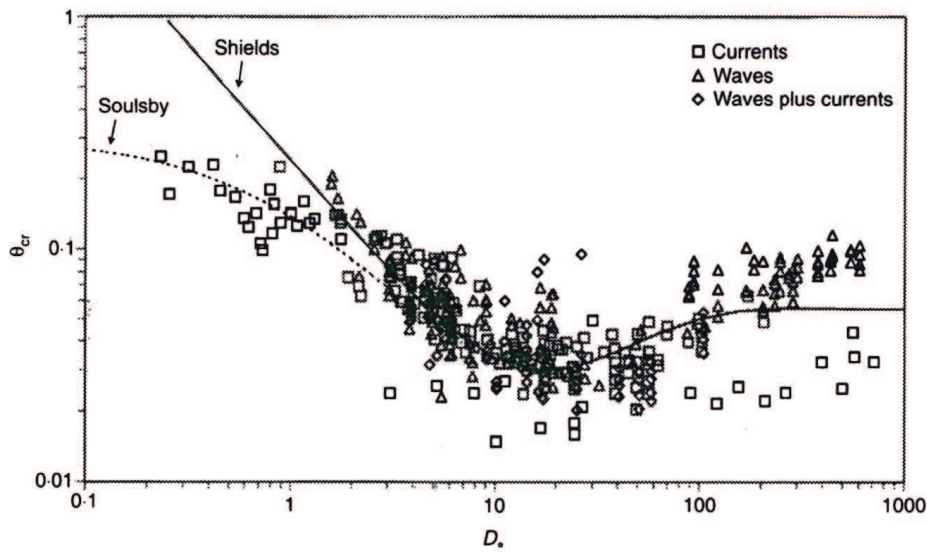


Figure 2.5: Comparison between Soulsby and Shields curves [44].

### 2.2.2 Bed load

Bed sediment transport consists on rolling, salting and sliding of particles in the very first layer above the bed. It is dominant mode in presence of heavy or large particles or in case of low regime, in which movement of grains is strictly limited by the effect of gravity and turbulence has not great influence on it.

The *bed load* can be defined as the product of the bed particle concentration, the particle velocity and the bed layer thickness:

$$q_{sb} = c_{b,gran} u_b \delta_b \quad (2.18)$$

where  $q_{sb}$  is the volume bed load for unit width,  $c_b$  the bed volume concentration,  $u_b$  the velocity of the particles and  $\delta_b$  the bed layer thickness.

Generally, bed load is computed using empirical equilibrium formulas and several of them are presented in literature. In this case, thus

$$q_{sb} = q_{sb,eq} \quad (2.19)$$

where  $q_{sb,eq}$  is the equilibrium bed load for unit width. The hypothesis of equilibrium bed load is usually accepted because of the dynamics of bed sediment transport. The saltation motion of particles, which represents the most typical bed load motion, has a characteristic height of 1-10 particle diameter and a characteristic length of about 10-20 diameters. For this reason, time scale of bed load process is small enough to assume an instantaneous adaptation of the bed load to the hydrodynamic conditions and an unlimited sediment availability.

Many of bed load formulas relate bed load to the excess of Shields parameter with respect to the critical Shields parameter. We define the *dimensionless bed-shear stress parameter*  $T$  as

$$T = \frac{\theta' - \theta_{cr}}{\theta_{cr}} = \frac{\tau'_b - \tau_{b,cr}}{\tau_{b,cr}} \quad (2.20)$$

where  $\tau_{b,cr}$  is the critical bed shear stress, corresponding to  $\theta_{cr}$ .

Because of the aim of the present work, almost all formulations here presented consider both current flow and waves effects. The only one developed exclusively for current-alone conditions is Meyer-Peter and Müller model, which is of great importance from an historical point of view, being the result of one of the first extensive studies on both uniform bed and particle mixtures.

An important author who has widely contributed to coastal sediment transport problem is Van Rijn. In his works, he proposed several formulas, valid in current-alone conditions and in wave-current conditions. In the last case, he studied both instantaneous and wave period-averaged bed load. Finally, another relevant author who considers bed load under wave-current conditions is Soulsby, whose model is based on Nielsen previous studies. Moreover, Van Rijn and Soulsby proposed a review of the original Van Rijn current-alone model, able to consider wave effect. Many other formulas are presented in literature, but are not discussed here because not implemented in our numerical model.

### Meyer-Peter Müller

Meyer-Peter and Müller had carried out an important laboratory study in a flume, considering both uniform and mixed materials with diameters from 0.4 mm to 29 mm, a water depth from 0.1 m to 1.2 m and a bed slope from 0.0004 to 0.02. They obtained the following formula for the bed load transport:

$$\frac{q_{sb,eq}}{\sqrt{(s-1)gd_m^3}} = 8(\theta - 0.047)^{1.5}. \quad (2.21)$$

Here,  $d_m$  is the mean particle diameter, defined as the weighted averaged diameter of bed sediments. However, equation (2.21) is weakly dependent on particle diameter and median diameter  $d_{50}$  can be used.

The factor 0.047 can be considered as a critical mobility Shields parameter, and can therefore be substituted with the value obtain using (2.12) or (2.13).

### Van Rijn

First sediment transport formulas proposed by Van Rijn has been published in a set of three articles in 1984 [55, 56, 57]: here, bed load, suspended load and bed-form effects in current-alone environment have been widely discussed. Considering bed load, Van Rijn analysed 130 flume experiments in low regime, observing the bed volume concentration  $c_{b,gran}$  to be related with  $T$  by the following relation:

$$\frac{c_{b,gran}}{c_{0,gran}} = 0.18 \frac{T}{D_*} \quad (2.22)$$

where  $c_{0,gran}$  is the maximum volumetric concentration, assumed to be 0.65. Similarly, he studied relation between saltation height and particle velocity and  $T$  obtaining the formulas

$$\frac{\delta_b}{d_{50}} = 0.3D_*^{0.7}T^{0.5} \quad (2.23)$$

and

$$\frac{u_b}{\sqrt{(s-1)gd_{50}}} = 1.5T^{0.6}. \quad (2.24)$$

From these relations he developed a first formula for the bed load computation, which is

$$\begin{cases} q_{sb,eq} = 0.053 (s-1)^{0.5} g^{0.5} d_{50}^{1.5} D_*^{-0.3} T^{2.1} & T < 3 \\ q_{sb,eq} = 0.1 (s-1)^{0.5} g^{0.5} d_{50}^{1.5} D_*^{-0.3} T^{1.5} & T \geq 3 \end{cases} \quad (2.25)$$

The second expression of (2.25) has been proposed because the first one, which is the original equation, seems to over-predict transport rate for  $T \geq 3$ .

A simpler formulation of the equation (2.25) has been proposed by Van Rijn assuming  $u_b = 7u'_*$ . In this way bed load reduces to

$$q_{sb,eq} = 0.25 d_{50} u'_* D_*^{-0.3} T^{1.5}. \quad (2.26)$$

Finally, one more approximated equation has been proposed [59], based on independent variables  $U$ ,  $U_{cr}$ ,  $h$  and  $d_{50}$ . The bed load in this case results

$$q_{sb,eq} = 0.005 U h \left( \frac{U - U_{cr}}{\sqrt{(s-1) g d_{50}}} \right) \left( \frac{d_{50}}{h} \right)^{1.2}. \quad (2.27)$$

Afterwards, equation (2.26) has been modified in 1993 in order to take into account the effect of the waves on the bed load transport. In particular, Van Rijn defined a calibration factor  $\alpha = 1 - (H_s/h)^{0.5}$ , where  $H_s$  is the significant wave height, and considered as bed shear stress the mean wave-current grain-related bed shear stress. Hence, the bed load becomes

$$q_{sb,eq} = 0.25 \alpha d_{50} \left( \frac{\tau'_{wc}}{\rho} \right)^{0.5} D_*^{-0.3} \left( \frac{\tau'_{wc} - \tau_{b,cr}}{\tau_{b,cr}} \right)^{1.5} \quad (2.28)$$

and is the first relevant wave current bed load formula proposed by Van Rijn.

In 2001, Van Rijn et al. reviewed this criterion proposing two more equations for instantaneous and averaged bed load in wave current conditions [61].

Considering instantaneous volume bed load, Van Rijn suggested an expression similar to (2.26) and (2.28), which is

$$q_{sb,eq} = \psi d_{50} \left( \frac{\tau'_{wc}}{\rho} \right)^{0.5} D_*^{-0.3} \left( \frac{\tau'_{wc} - \tau_{b,cr}}{\tau_{b,cr}} \right)^{\eta} \quad (2.29)$$

where  $\psi$  and  $\eta$  are calibration coefficients and  $\tau'_{wc}$  is the instantaneous grain-related bed shear stress. From flume tests, authors suggested to use  $\psi = 0.5$  and  $\eta = 1$ . The equation can be used also in non-linear wave conditions (for example in case of breaking waves), which however are not treated in the present work. The second method is an approximation of the first one and focuses on averaged bed load transport over the wave period. The equation (2.29) reduces to

$$q_{sb,eq} = 0.006 w_{s,gran} d_{50} \left( \frac{U_{eff}^2}{(s-1) g d_{50}} \right)^{0.5} \left( \frac{(U_{eff} - U_{cr})^2}{(s-1) g d_{50}} \right)^{0.7} \quad (2.30)$$

where  $U_{eff} = \sqrt{U^2 + U_{on}^2}$  is the effective velocity due to waves and currents, and  $U_{on}$  is the onshore near-bed peak orbital velocity in wave direction which, under hypothesis of regular waves, coincides with the maximum bottom orbital velocity  $U_{m0}$ .  $U_{cr}$  can be computed using equation (2.14).  $w_{s,gran}$  is the fall velocity of grains.

The equation (2.30) has been obtained considering just waves perpendicular to current: a sensitivity analysis evidences that for waves parallel to current the value of  $q_{sb,eq}$  can result about twice as large.

### Soulsby

In his book [44], Soulsby proposed a bed load transport formula based on integration over wave period of the criterion of Nielsen[29], which suggested for current-alone field

$$\frac{q_{sb,eq}}{\sqrt{(s-1)gd_{50}^3}} = 12\theta^{0.5}(\theta_m - \theta_{cr}). \quad (2.31)$$

Soulsby considered the following components:

$$\frac{q_{sb,eq,x1}}{\sqrt{(s-1)gd_{50}^3}} = 12\theta^{0.5}(\theta_m - \theta_{cr}) \quad (2.32)$$

$$\frac{q_{sb,eq,x2}}{\sqrt{(s-1)gd_{50}^3}} = 12\theta_w^{0.5}\theta_m(0.95 + 0.19\cos(2\phi)) \quad (2.33)$$

$$q_{sb,eq,x} = \max(q_{sb,eq,x1}, q_{sb,eq,x2}) \quad (2.34)$$

and

$$\frac{q_{sb,eq,y}}{\sqrt{(s-1)gd_{50}^3}} = \frac{12(0.19\theta_m\theta_w^2\sin 2\phi)}{\theta_w^{\frac{3}{2}} + 1.5\theta_m^{\frac{3}{2}}} \quad (2.35)$$

where  $\phi$  is the angle between waves and current directions  $q_{sb,eq,x}$  is the bed load in current direction and  $q_{sb,eq,y}$  the bed load perpendicular to the current, with a versus coherent with  $\phi$ .  $\theta_w$  is the Shields parameter corresponding to  $\tau_w$  and  $\theta_m$  that Shields parameter corresponding to  $\tau_m$ . Finally,  $q_{sb,eq,x} = q_{sb,eq,y} = 0$  if maximum value of Shields parameter ( $\theta_{max} = \tau_{max}/[g(s-1)d_{50}]$ ) is lesser than the critical Shields parameter.

### Soulsby and Van Rijn

The last criterion presented here has been proposed in 1997 by Soulsby and Van Rijn [44]. In his more general form, this approach considers both bed and suspended sediment transport: in this section the bed load component is described while the suspended load component will be discussed later. Soulsby and Van Rijn modified equation (2.27) following Grass approach, in order to take into account the effect of the waves.

Grass supposed that, if the total load in current-alone environment is given by

$$q_{s,eq} = A_G U^{n_{sr}}, \quad (2.36)$$

then the combined wave-current total load can be computed by the following expression:

$$q_{s,eq} = A_G U \left( U^2 + \frac{0.08}{C_D} U_{1m}^2 \right)^{(n-1)/2} \quad (2.37)$$

where  $A_G$  and  $n_{sr}$  are empirical coefficients. They thus suggested as bed load the following expression:

$$q_{sb,eq} = \frac{0.005h \left( \frac{d_{50}}{h} \right)^{1.2}}{((s-1)gd_{50})^{1.2}} U \left[ \left( U^2 + \frac{0.018}{C_D} U_{1m}^2 \right)^{0.5} - U_{cr} \right]^{2.4}. \quad (2.38)$$

This formula, with respect to Grass equation (2.37), has the advantage not to need further calibration processes by the users.

### The effect of bed slope on granular bed load

In case of non-horizontal bottom, longitudinal and transverse bed slopes have influence on the bed transport dynamics. Many different formulas have been presented in literature and some of them have been summarised by Van Rijn [60]. Generally, longitudinal and transverse slope effects are treated separately through the use of two different coefficients.

Longitudinally, resulting bed load is given by

$$q_{sb,lon} = \alpha_{lon} q_{sb} \quad (2.39)$$

where  $\alpha_{lon}$  is the longitudinal slope factor. Bagnold suggested for  $\alpha_{lon}$  the following expression:

$$\alpha_{lon} = \frac{\frac{\tan \Phi_i}{\cos \beta}}{(\tan \Phi_i - \tan \beta)} \quad (2.40)$$

where  $\Phi_i$  is sediment angle of repose and  $\beta$  is the longitudinal slope.

Transversally, the slope increases bed load giving rise to a component perpendicular to the current. Transverse bed load component is given by

$$q_{sb,trans} = \alpha_{trans} q_{sb} \quad (2.41)$$

where  $\alpha_{trans}$  is the transverse slope factor. Ikeda proposed the expression:

$$\alpha_{trans} = 1.5 * \left( \frac{\tau_{cr}}{\tau'_m} \right)^{0.5} \tan \gamma \quad (2.42)$$

where  $\gamma$  is transverse bed slope. This bed load component is of course downslope-oriented.

### 2.2.3 Suspended load

When the critical bed shear stress has been exceeded, bed sediment transport begins and particles will start rolling, sliding and jumping. Increasing the bed shear stress (and the bed velocity), the jumps (saltations) begin to be more height and long and the particles reach a level where turbulent forces are equal of greater than submerged particle weight. In this way, particles will stay in suspension, with occasional contacts with the bed and a velocity close to the flow velocity (we will assume the hypothesis of passive tracer: sediments are thus characterized by the same velocity of the flow).

In literature different curves for initiation of suspension are presented, which are analogous to the Shields Curve [59]. Bagnold (1960) studied interaction between turbulence and particles and assumed that suspension can exist when the vertical velocity component of eddies  $u'_{z,rm}$  is equal or greater than the particle fall velocity. From an analysis of the orders of magnitude, it is demonstrated that  $u'_{z,rm} \simeq u_*$  (see chapter 1) and the critical friction velocity for suspension  $u_{*,crs}$  is therefore

$$\frac{u_{*,crs}}{w_{s,gran}} = 1 \quad (2.43)$$

which can be written also as

$$\theta_{crs} = \frac{w_{s,gran}^2}{(s-1)gd_{50}} \quad (2.44)$$

where  $w_{s,gran}$  is the fall velocity for granular sediments and  $\theta_{crs}$  is the critical Shields parameter for suspension.

Van Rijn proposed an alternative formula after an experimental investigation carried out at Delft Hydraulics. The experimental results can be presented by

$$\begin{cases} \frac{u_{*,crs}}{w_{s,gran}} = \frac{4}{D_*} & 1 < D_* < 10 \\ \frac{u_{*,crs}}{w_{s,gran}} = 0.4 & D_* > 10 \end{cases} \quad (2.45)$$

Niño et al. [60] suggested a modification of 2.45, which takes in account the effect of hiding caused by rough beds, which preclude the entertainment in suspension of particles finer than rough elements. The resulting equation for critical friction velocity for suspension is

$$\begin{cases} \frac{u_{*,crs}}{w_{s,gran}} = \frac{20}{D_*^{1.7}} & 1 < D_* < 10 \\ \frac{u_{*,crs}}{w_{s,gran}} = 0.4 & D_* > 10 \end{cases} \quad (2.46)$$

The latter formula has been chosen in the model we will describe later.

The behaviour of *suspended load* is described in term of volume concentration or mass concentration. In shallow water models (depth integrated), usually depth integrated suspend load for unit width is considered, defined as

$$q_{ss} = \int_a^h u(z) c_{gran}(z) dz \quad (2.47)$$

where  $a$  is the reference level at which suspension begins: this is the limit of bed load layer and under this level sediment transport is considered to have bed transport behaviour.

It is therefore important to know the vertical velocity distribution and the vertical concentration distribution (see Figure 2.6). Moreover, in order to solve the integral in equation (2.47), the *reference concentration*  $c_a$  at level  $a$  is needed.

The evaluation of suspended load can be done using alternatively an equilibrium or a non-equilibrium approach. Equilibrium approach assumes that suspended load at each point at every instant corresponds to the maximum suspended load supported by the water flow. This required, in particular, an unlimited availability of sediments in study domain and at the boundaries. While for bed load this hypothesis can be considered easily verifiable, it is not always realistic for suspended load in real environments. The time scale of suspended sediment transport is in fact greater than that of bed load and changes in hydrodynamic conditions give rise to slower changes in sediments dynamic. Thus, for suspended load a more appreciate approach is the non-equilibrium approach. In this case, as previously discussed, suspended sediment is studied considering the horizontal distribution of the averaged volume concentration, obtained by solving a proper advective-diffusive equation.

### The vertical concentration distribution

Sediment concentration over the water depth can be described by different analytical models, which can be divided in diffusion models, energy models and stochastic models: the most commonly used in sediment transport are diffusion models [59].

Diffusion models are based on the law of Fick, which considers turbulence vertical transport proportional to the vertical concentration. In this case, the equilibrium between fall velocity and turbulence becomes

$$c_{gran} w_{s,gran} + \epsilon_s(z) \frac{dc_{gran}}{dz} = 0 \quad (2.48)$$

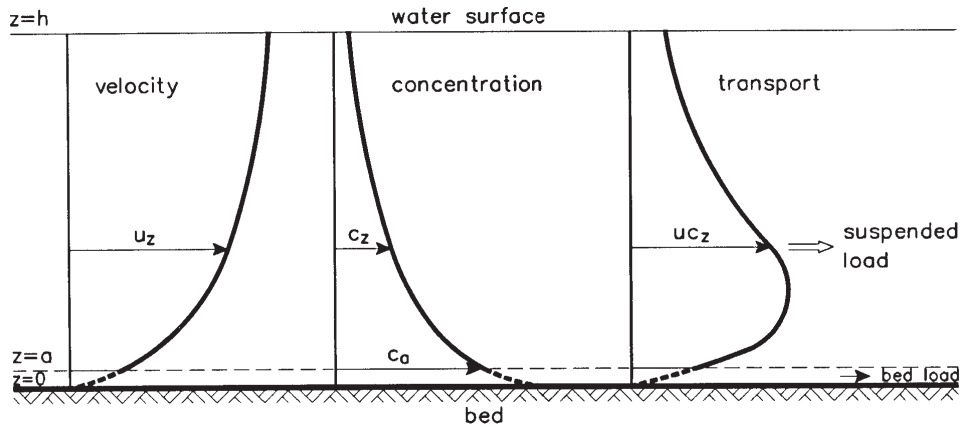


Figure 2.6: Sketch of velocity, concentration and suspended load distribution [59].

where  $\epsilon_s$  is the *mixing coefficient* at height  $z$  above bed.

Several mixing coefficient distributions are available in literature.

One of the simpler assumption is to consider mixing coefficient distribution increasing linearly with height ( $\epsilon_s = \kappa u_* z$ ). In this way a power-law distribution profile is obtained:

$$c_{gran}(z) = c_a \left(\frac{z}{a}\right)^{-b} \quad (2.49)$$

where  $b = w_{S,gran}/\kappa u_*$  is the *Rouse number*, which determines the shape of the profile.

Soulsby [44] proposed, for wave-current conditions, the use of a 2-layers power law profile. In particular he suggested

$$\begin{cases} c_{gran}(z) = c_a \left(\frac{z}{a}\right)^{-b_{max}} & a \leq z \leq \delta_w \\ c_{gran}(z) = c(\delta_w) \left(\frac{z}{\delta_w}\right)^{-b_m} & \delta_w \leq z \leq h \end{cases} \quad (2.50)$$

where  $b_m = w_{S,gran}/\kappa u_{*m}$  and corresponds to mean bed shear stress,  $b_{max} = w_{S,gran}/\kappa u_{*max}$  and corresponds to the maximum bed shear stress, as defined by Soulsby, while  $\delta_w$  is the height of the wave boundary layer.

An alternative mixing coefficient distribution is the parabolic. This is considered most satisfactory from a physical point of view, because is based on logarithmic velocity profile and linear shear stress distribution. The distribution is  $\epsilon_{s,c} = \kappa u_* z (1 - z/h)$  and gives rise to the *Rouse profile*:

$$c_{gran}(z) = c_a \left[ \frac{z h - a}{a h - z} \right]^{-b} \quad (2.51)$$

Because a similar profile has a 0-concentration at the water surface, which is not coherent with experimental observations, Van Rijn suggested a parabolic-constant mixing coefficient distribution:

$$\begin{cases} \epsilon_{s,c} = \kappa u_* z \left(1 - \frac{z}{h}\right) & a \leq z \leq \frac{h}{2} \\ \epsilon_{s,c} = 0.25 \kappa u_* h & \frac{h}{2} \leq z \leq h \end{cases} \quad (2.52)$$

In this way, he obtained the concentration profile

$$\begin{cases} c_{gran}(z) = c_a \left[ \frac{z h - a}{a h - z} \right]^{-b'} & a \leq z \leq \frac{h}{2} \\ c_{gran}(z) = c_a \left(\frac{a}{h-a}\right)^{-b'} \exp\left(-4b' \left(\frac{z}{h} - \frac{1}{2}\right)\right) & \frac{h}{2} \leq z \leq h \end{cases} \quad (2.53)$$

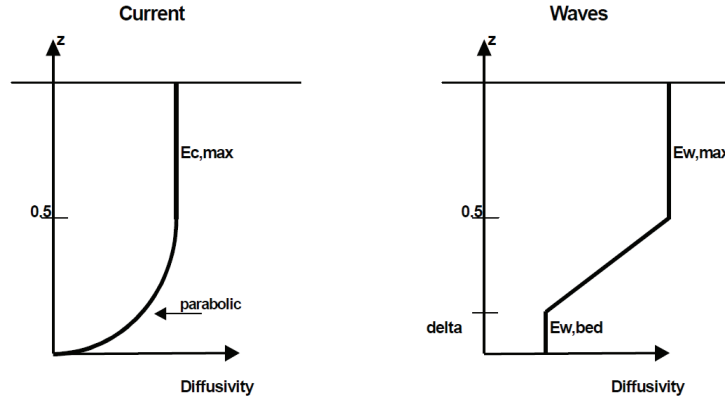


Figure 2.7: Mixing coefficients for waves and current in Van Rijn model [61].

where  $b'$  is the Rouse number corrected for the effect of the differences between mixing coefficient and fluid eddy viscosity through  $\beta_c$  and for the stratification effects through  $\psi$  :

$$b' = \frac{b}{\beta_c} + \psi \quad (2.54)$$

$$\beta_c = \min \left( 1.5, 1 + 2 \left( \frac{w_{s,gran}}{u_*} \right)^2 \right) \quad (2.55)$$

$$\psi = 2.5 \left( \frac{w_{s,gran}}{u_*} \right)^{0.8} \left( \frac{c_a}{c_{0,gran}} \right)^{0.4} \quad (2.56)$$

In the presence of waves, Van Rijn proposed a wave-related mixing coefficient, which is constant in the very first layer over the bed ( $\epsilon_{s,w,bed}$ ) and in the upper half of the water column ( $\epsilon_{s,w,max}$ ), while varies linearly between the top of the near bed sediment mixing layer and the half of the water column (see Figure 2.7). In particular, the bed and the maximum values of mixing coefficient are

$$\epsilon_{s,w,bed} = 0.018\beta_w\delta_s U_{m0} \quad (2.57)$$

$$\epsilon_{s,w,max} = \min \left( 0.05, 0.035\gamma_{br}h \frac{H_s}{T_p} \right) \quad (2.58)$$

where

$$\beta_w = \min \left( 1.5, 1 + 2 \left( \frac{w_s}{u_{*,w}} \right)^2 \right) \quad (2.59)$$

and

$$\delta_s = 2\gamma_{br}\delta_w. \quad (2.60)$$

Here,  $\gamma_{br} = 1 + (H_s/T_p - 0.4)^{0.5}$  is an empirical coefficient related to the wave breaking and  $\delta_w$  is the wave boundary layer height. The resulting mixing coefficient is given by

$$\epsilon_{s,wc} = \sqrt{\epsilon_{s,c}^2 + \epsilon_{s,w}^2} \quad (2.61)$$

### The reference concentration and the settling velocity

Two more parameters play an important role in the evaluation of concentration distribution, as it is evident from previous equations: the *reference bed concentration*  $c_a$  and the *granular fall velocity (or settling velocity)*  $w_{s,gran}$ .

The reference bed concentration  $c_a$  is the equilibrium concentration at reference level  $a$ . It is important to distinguish between two main conditions: flat bed and presence of bed forms.

In first case, the reference concentration can be considered to coincide with the bed level concentration  $c_b$ , for which Van Rijn suggested equation (2.22). In this case, the reference level  $a$  should coincide with the bed load layer thickness  $\delta_b$ , given by (2.23). Other formulas have been proposed in literature: many of them have been reviewed by Van Rijn [59] and Soulsby [44].

While flat bed condition is easily obtained in laboratory test, studying in particular the lower regime, in real domains it occurs rarely: generally hydraulic bed-forms, vegetation or other rough elements prevents the bottom to be considered flat.

In the presence of bed-forms or, more generally, of macroscopical rough elements, Van Rijn suggested an alternative formula

$$c_a = 0.015 \frac{d_{50}}{a} \frac{T^{1.5}}{D_*^{0.3}}. \quad (2.62)$$

In this particular case, the value of  $a$  should be set as

$$a = \max \left( 0.01h, \frac{\varepsilon}{2} \right). \quad (2.63)$$

It should be noticed that, being the reference concentration an equilibrium concentration, the vertical distribution obtained using 2.45 is an equilibrium concentration profile.

Finally, the velocity fall of granular particles depends on the diameter  $d$  (generally,  $d_{50}$  is considered), on  $D_*$  and on the water cinematic viscosity  $\nu$ . The physical behaviour of a spherical particle falling in a fluid has been described by Stokes:

$$w_{s,gran} = \frac{(s-1)gd}{18\nu}. \quad (2.64)$$

Many authors proposed to modify this formula in order to adapt it to natural sands, in particular for bigger diameter. Soulsby developed, for natural sands, a regression curve based on the optimization of two coefficients in a viscous environment with a drag law, against experimental data for irregular grains. He obtained the following formula:

$$w_{s,gran} = \frac{\nu}{d} \left[ (10.36^2 + 1.049D_*^3)^{0.5} - 10.36 \right]. \quad (2.65)$$

The equation is valid for all values of  $D_*$  (Figure 2.8).

### Van Rijn

Van Rijn proposed an equilibrium method for the evaluation of sediment transport, based on the above mentioned considerations, valid in case of current-alone condition [56] and wave-current condition [61].

The suspended load  $q_{ss}$  can be computed from depth averaged variable as

$$q_{ss} = q_{ss,eq} = \beta_{ragg} UC_{gran} h = FUhc_a \quad (2.66)$$

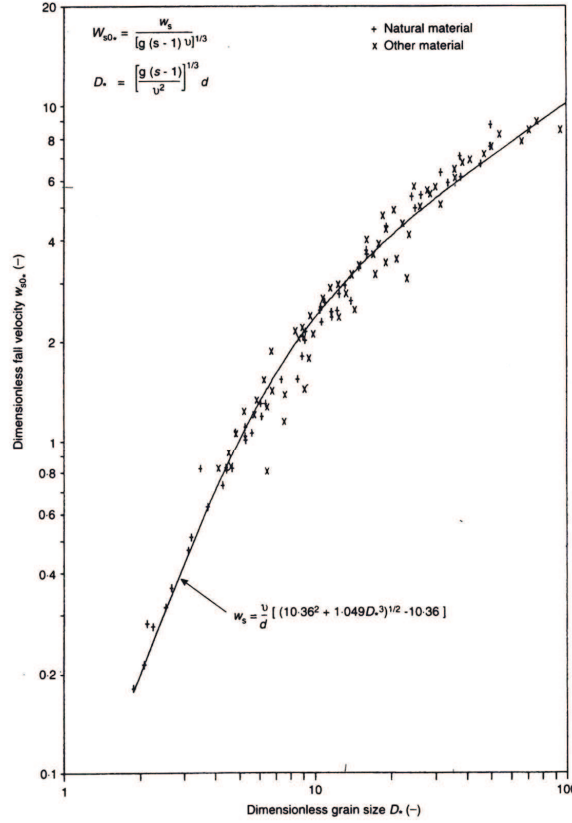


Figure 2.8: Soulsby regression formula for sands settling velocity [44].

where  $C_{gran}$  is the depth-averaged concentration and  $\beta_{ragg}$  and  $F$  analytical correction factors, which take into account concentration and velocity vertical distributions.

In its more general form,  $F = F_c + F_w$ , where  $F_c$  is the current component and  $F_w$  is the wave component.

Let us consider  $F_c$ . From the logarithmic velocity profile (1.112) and the concentration distribution (2.53) the correction factor is demonstrable to be

$$F_c = \frac{u_*}{\kappa U} \left( \frac{a}{h-a} \right)^{b'} \left[ \int_{a/h}^{0.5} \left( \frac{h-z}{z} \right)^{b'} \ln \frac{z}{z_0} d \left( \frac{z}{h} \right) + \int_{0.5}^1 e^{-4b'(\frac{z}{h}-0.5)} \ln \frac{z}{z_0} d \left( \frac{z}{h} \right) \right]. \quad (2.67)$$

$F_c$  can't be analytically solved but an approximated expression is available, valid for  $0.3 \leq b' \leq 3$  and  $0.01 \leq a/h \leq 0.1$ , given by

$$F_c = \frac{\left( \frac{a}{h} \right)^{b'} - \left( \frac{a}{h} \right)^{1.2}}{\left( 1 - \frac{a}{h} \right)^{b'} (1.2 - b')}. \quad (2.68)$$

Similarly, correction factor  $F_w$  can be obtained by the following approximated formula

$$F_w = \frac{\left( \frac{a}{h} \right)^{b_w} - \left( \frac{a}{h} \right)^{1.2}}{\left( 1 - \frac{a}{h} \right)^{b_w} (1.2 - b_w)} \quad (2.69)$$

where  $b_w = 4 \left( \frac{h}{h_{ref}} \right)^{0.6} \left( w_{s,gran} \frac{T_p}{H_s} \right)$  and  $h_{res}$  is the reference water depth ( $h_{ref} = 5\text{m}$ ).

### Soulsby and Van Rijn

The suspended load component of Soulsby and Van Rijn formula is analogous to the bed load component and is based on the same assumptions. The formula reduces to

$$q_{ss,eq} = \frac{0.012d_{50}D_*^{-0.6}}{((s-1)gd_{50})^{1.2}}U \left[ \left( U^2 + \frac{0.018}{C_D}U_{1m}^2 \right)^{0.5} - U_{cr} \right]^{2.4}. \quad (2.70)$$

The total load transport is thus given by

$$q_{s,eq} = A_s U \left[ \left( U^2 + \frac{0.018}{C_D}U_{1m}^2 \right)^{0.5} - U_{cr} \right]^{2.4}. \quad (2.71)$$

where  $A_s = A_{sb} + A_{ss}$  and  $A_{sb} = \frac{0.005h(\frac{d_{50}}{h})^{1.2}}{((s-1)gd_{50})^{1.2}}$  while  $A_{ss} = \frac{0.012d_{50}D_*^{-0.6}}{((s-1)gd_{50})^{1.2}}$ .

### Non-equilibrium approach

As previously discussed, non-equilibrium approach consists on the solution of solid mass balance by solving the sediment concentration advective-diffusive equation. For the general 3D case, we can write

$$\frac{\partial c}{\partial t} + u_x \frac{\partial c}{\partial x} + u_y \frac{\partial c}{\partial y} + u_z \frac{\partial c}{\partial z} = w_s \frac{\partial c}{\partial z} + \frac{\partial}{\partial x} \left( \epsilon_x \frac{\partial c}{\partial x} \right) + \frac{\partial}{\partial y} \left( \epsilon_y \frac{\partial c}{\partial y} \right) + \frac{\partial}{\partial z} \left( \epsilon_z \frac{\partial c}{\partial z} \right) \quad (2.72)$$

where  $c$  is a generic volume concentration and  $u_x$ ,  $u_y$  and  $u_z$  are the velocity component in  $x$ ,  $y$  and  $z$  directions,  $w_s$  is the generic fall velocity and  $\epsilon_x$ ,  $\epsilon_y$  e  $\epsilon_z$  are the diffusivity coefficients of the sediments.  $\epsilon_x$  and  $\epsilon_y$  are generally assumed equal: they correspond to the horizontal sediment diffusivity  $\epsilon_H$ .  $\epsilon_z$  is described by a proper vertical mixing coefficient distribution, as illustrated above. Mixed derivatives of diffusive problem are neglected. The solution of equation (2.72) needs adequate boundary conditions on the volume concentration. In particular, great importance is assumed by the bottom boundary condition.

If we consider the depth-averaged problem (Figure 2.9) of granular concentration, equation (2.72) reduces to

$$\frac{\partial [hC]}{\partial t} + \frac{\partial [hUC]}{\partial x} + \frac{\partial [hVC]}{\partial y} = h \left[ \frac{\partial}{\partial x} \left( \epsilon_H \frac{\partial C}{\partial x} \right) + \frac{\partial}{\partial y} \left( \epsilon_H \frac{\partial C}{\partial y} \right) \right] + ED \quad (2.73)$$

where  $C$  is the depth-averaged granular concentration and  $U$  e  $V$  the depth-averaged velocity component in  $x$  and  $y$  directions.  $ED$  is the source-sink term, which corresponds to the erosion or deposition rate. In case of suspended granular sediment transport, the problem is applied to  $C_{gran}$ , the depth-averaged granular volume concentration, while the erosion-deposition rate is  $ED_{gran}$ .

One of the first study about depth-averaged advective-diffusive model for suspended sediments has been presented by Galapatti [15]. He proposed an asymptotic solution of the problem for slowly varying flow, starting from the 0-order equilibrium solution. Under opportune hypothesis and considering 1-order solution in steady conditions, he obtained the following relation for the erosion-deposition rate  $ED_{gran}$ :

$$ED_{gran} = E_{gran} - D_{gran} = \alpha_{ED} w_{s,gran} (C_{gran} - C_{gran,eq}) \quad (2.74)$$

where  $E_{gran}$  and  $D_{gran}$  are respectively granular erosion and deposition and  $C_{gran,eq}$  is the depth-averaged equilibrium concentration, for which there are not vertical sediment fluxes along the depth.

This approach for the computation of the erosion-deposition term is widely used in morphodynamic models.

Lesser developed a 3-dimensional morphological model [25, 24], proposing also a depth-integrated version. In this case, for the calculation of  $S$ , he suggested the following expression:

$$ED_{gran} = \frac{C_{gran,eq} - C_{gran}}{T_s}. \quad (2.75)$$

$T_s$  is a time scale factor and is computed as

$$T_s = \frac{1}{w_{s,gran}} T_{sd} \quad (2.76)$$

with  $h$  is the water depth,  $w_{s,gran}$  the fall velocity and  $T_{sd}$  is the dimensionless adaptation time which is given (according to Galapatti numerical development ) by

$$T_{sd} = w_* \exp \left( \begin{array}{l} (1.547 - 20.12u_r) w_*^3 + (326.832u_r^{2.2047} - 0.2) w_*^2 \\ + (0.1385 \ln(u_r) - 6.4061) w_* + (0.5467u_r + 2.1963) \end{array} \right) \quad (2.77)$$

where  $w_* = w_{s,gran}/u_{*,c}$ ,  $u_r = u_{*,c}/U$  and  $u_{*,c}$  is current-related friction velocity.

The value of  $C_{eq,gran}$  can be computed by the use of an equilibrium suspended load formula, keeping in mind that  $C_{eq,gran} = q_{ss,eq}/(Uh)$ .

An alternative way to calculate erosion and deposition rate is to refer it not to the depth-averaged concentration but to the bottom concentration. We can consider the mass flux at the bottom as

$$ED_{gran} = w_{s,gran} (c_a - c_{gran}(a)) \quad (2.78)$$

where  $a$  is the reference height for the suspended concentration and  $c_a$  the reference concentration. Following Van Rijn method, they are calculated using equations (2.62) and (2.63).  $c_{gran}(a)$  is computed by the depth-averaged concentration  $C_{gran}$ , choosing an opportune concentration profile:

$$c_{gran}(a) = \frac{C_{gran}}{\beta_d}. \quad (2.79)$$

$\beta_d$  depends on the concentration profile and, for a power law profile in presence of current and waves (equation (2.50)), have an analytical solution which is

$$\beta_d = \frac{1}{(h-a)} \left[ \frac{1}{1-b_{max}} \left( \frac{\delta_w^{(1-b_{max})}}{a^{-b_{max}}} - a \right) + \left( \frac{z_w}{a} \right)^{-b_{max}} \frac{1}{1-b_m} \left( \frac{h^{(1-b_m)}}{\delta_w^{-b_m}} - \delta_w \right) \right]. \quad (2.80)$$

In case of current-alone condition, equation (2.80) reduces to

$$\beta_d = \frac{1}{(h-a)} \frac{1}{1-b} \left( \frac{h^{(1-b)}}{a^{-b}} - a \right). \quad (2.81)$$

Considering Van Rijn concentration distribution,  $\beta_d$  coefficient becomes

$$\beta_d = \frac{1}{h-a} \frac{\overline{\epsilon_{s,wc}}}{w_{s,gran}} \left[ 1 - \exp \left( -\frac{w_{s,gran}}{\overline{\epsilon_{s,wc}}} (h-a) \right) \right] \quad (2.82)$$

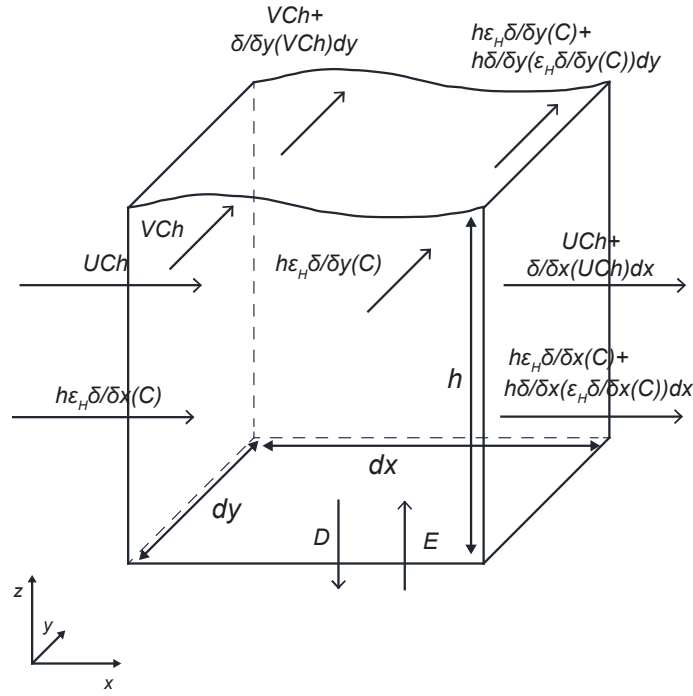


Figure 2.9: Scheme of shallow water advective-diffusive problem.

where  $\overline{\epsilon_{s,wc}}$  is depth-averaged value of  $\epsilon_{s,wc}$ , as in equation (2.61).

Finally, a really simple method for the calculation of  $c_{gran}(a)$  has been proposed by Canestrelli [48] who, citing Parker et al. [32], proposed

$$c_a = r_0 C_{gran} \quad (2.83)$$

with  $r_0 \approx 1.4$ .

In literature, a total load non-equilibrium sediment transport model has been presented too. The approach is absolutely analogous to that described here. In this case, a fictitious depth-averaged total load equivalent concentration is considered, while equilibrium depth averaged concentration is carried out by a total load equilibrium formula as

$$C_{tot,gran,eq} = \frac{q_{s,eq}}{Uh}. \quad (2.84)$$

The erosion and deposition rates are obtained by equation (2.75) or similar formulations.

## 2.3 Cohesive sediment transport

The physics of cohesive sediment transport is more complex than that of granular sediment transport, and a model able to describe all its parts would result really heavy to be applied.

For cohesive sediments, bed sediment transport characterized by salting and rolling of sediment does not exist and, therefore, the distinction between bed load and suspended load loses his sense. Cohesive sediment transport is here assumed to be suspended and no further distinctions are considered. However, behaviour of cohesive sediments is close related to the suspended concentration: in literature, different classifications for mud have been proposed [64].

Basing on european research project COSINUS and considering in particular suspended mud, Winterwerp proposed three main categories: *low-concentrated mud suspension* (LCMS), *high-concentrated mud suspension* (HCMS) and *fluid mud*.

Low-concentrated mud suspension is characterized by a mass concentration of the order of  $0.01-0.1 \text{ kg/m}^3$  and a newtonian rheology. It does not modify significantly the turbulent flow field.

High concentrated mud suspension have a mass concentration of about  $0.1-1 \text{ kg/m}^3$ : the fluid is newtonian and suspension is transported with the main flow, but interactions between mud and the turbulent flow field take place.

Finally, mud flow is characterized by a concentration above the gelling point ( $10-100 \text{ kg/m}^3$ ) and exhibits an important non-newtonian behaviour. It can be stationary or moving, with a dynamics fairly independent of the water main flow.

An alternative classification has been proposed by Soulsby, who considered *unfloculated suspension*, *flocculated suspension* and *mud flow*.

Unflocculated suspension, known also as wash load, is characterized by concentration low enough not to let the flocks collide (mass concentration  $< 0.01 \text{ kg/m}^3$ ), while in case of flocculated suspension (up to mass concentration of about  $3 \text{ kg/m}^3$ ) grains collide thought differential settling and turbulent shear. In the latter case, settling velocity can be deeply different with respect to the first case.

Fluid mud ( $C_M > 3 \text{ kg/m}^3$ ) has a concentration large enough that the gaps between flocks have dimension similar to the flocks and, thus, the flocks interact with each other. Settling velocity increases until a maximum value in the range of  $1-10 \text{ mm/s}$  (for  $3 \text{ kg/m}^3 < C_M < 10 \text{ kg/m}^3$ ), decreasing then until zero ( $C_M = 50 - 100 \text{ kg/m}^3$ ) The viscosity is much higher than that of pure water, but sufficiently low to permit the mud to be mobilized.

A very first approach for the solution of cohesive transport problem is to analyse it by solving of a proper advective-diffusion equation, similarly to the non-equilibrium approach for granular suspended sediment transport. The main difference between cohesive sediment transport and non-equilibrium granular suspended load study is the source-sink term, which represents the erosion and deposition rate. Thus, the problem is analysed by solving equation (2.73) for the cohesive depth-averaged concentration  $C_{coes}$  and considering the correspondent erosion and deposition rate  $ED_{coes}$ . The problem is here considered totally independent from granular sediment transport and, if both classes are considered, they should be solved with two different advective diffusive equations.

In case of cohesive sediment transport, a unique critical state at which both erosion and deposition take place is not generally defined. In fact, due to the presence of cohesion as additional resistance factor, the bed shear stress needed for threshold of motion is significantly higher than that at which sediment deposition begins.

Under this assumption two critical shear stress are considered, *erosion shear stress* and *deposition shear stress*, and two different equations are used for erosion and deposition rates: in this way, no simultaneous erosion and deposition can take place.

Alternative approaches are considered in literature: for example, Winterwerp [65] proposed a continuous sedimentation flux model, which seems to describe better certain experimental results. In the present study, however, only the classic approach of mutually exclusive erosion-deposition model is illustrated and discussed.

Mud flow phenomena, which can take place in the lowest part of water depth, can't be studied with a depth averaged method and won't be analysed in the model we are going to describe.

### 2.3.1 Settling velocity for cohesive sediments

As discussed above, settling velocity in case of cohesive sediments is mainly related to the concentration of the suspension and to the effect of the flocks.

Generally, settling velocity function can be divided in three main regions.

For very low concentrations, grains do not collide and do not interact significantly each other. In this case, settling velocity is related to the fall of single grains (*free settling*) and, from a theoretical point of view, it can be computed by the use of the Stokes formula, valid for spherical particles in the lower regime and in stationary conditions:

$$w_{s,coes} = \frac{(\rho_{coes} - \rho) g d_{50,coes}^2}{18\mu} \quad (2.85)$$

where  $w_{s,coes}$  is the settling velocity of the mud.

As suggested by Winterwerp et al. [65] and Mehta [26], the same formula can be applied in presence of flocks (*flocculating settling*) for concentration not enough high to let flocks hinder each other. In this case, it is assumed that there is no flow through the flocks, which is not consider a trivial hypothesis, as described by the authors. Considering flocks with a fractal structure, the excess of density with respect to the water can be computed as

$$\Delta\rho_f = \rho_f - \rho = (\rho_{coes} - \rho) \left( \frac{d_p}{d_f} \right)^{3-n_f} \quad (2.86)$$

where  $\rho_f$  is the flock density,  $d_p$  and  $d_f$  the diameters of primary particles (equals to  $d_{50,coes}$  in our case) and of the flocks, and  $n_f$  the fractal dimension.

From the balance between gravitational and drag force it is possible to write

$$w_{s,coes} = \frac{\alpha_{ws}}{18\beta_{ws}} \frac{(\rho_{coes} - \rho) g}{\mu} d_p^{3-n_f} \frac{d_f^{n_f-1}}{1 + 0.15 Re_f^{0.687}} \quad (2.87)$$

where  $Re_f = w_{s,coes} d_f / \nu$ , while  $\alpha_{ws}$  and  $\beta_{ws}$  are shape function.

For spherical ( $\alpha_{ws} = \beta_{ws} = 1$ ), euclidian ( $n_f = 3$ ) particles in lower Regime ( $Re_f \ll 1$ ), equation 2.87 reduces to 2.85 in the form

$$w_{s,coes} = \frac{(\rho_{coes} - \rho) g d_f^2}{18\mu} \quad (2.88)$$

An alternative quite simple approach for the calculation of flocculating settling for low concentrations ( $C_M < 5 - 10 \text{ kg/m}^3$ ), is the use of an empirical exponential formula:

$$w_{s,coes} = k_{ws} C_M^{m_{ws}} \quad (2.89)$$

where  $k_{ws}$  and  $m_{ws}$  are empirical coefficients. Whitehouse [64] suggested the values  $k_{ws} = 0.001$  and  $m_{ws} = 1.0$ , with  $C_M$  in  $\text{kg/m}^3$ .

For high value of concentration, settling flocks interfere with their surrounding flow and with other flocks. In this case, the *hindered settling* takes place.

In this case the fall velocity tends to decrease for the hindering process of the flocks. One of the first formulas discussed in literature has been presented by Richardson and Zaki [36]: they suggested for the hindered settling velocity the formula:

$$w_{s,coes} = w_{s,r} (1 - C_f)^{n_{ws}} \quad (2.90)$$

where  $w_{s,r}$  is the reference settling velocity, calculated by the use of equation (2.88),  $C_f = \left( \frac{\rho_{coes} - \rho}{\rho_f - \rho} \right) C_{coes} = C_M / C_{GEL}$  is flocks volume concentration and  $n_{ws} = f(Re_p)$ , with  $2.5 < n < 5.5$  and a default value  $n_{ws} = 4.65$ .

An alternative approach, suggested by Winterwerp, takes into account the effects of increased viscosity, particle buoyancy and return-flow of the fluid due to continuity as particle settle. In this case, the settling velocity is computed as

$$w_{s,coes} = w_{s,r} \frac{(1 - C_f)(1 - C_s)}{1 + 2.5C_f} \quad (2.91)$$

where  $C_s = C_M / \rho_{coes}$  is particles volume concentration.  $C_{GEL}$  is the mass concentration at gelling point, at which  $\phi_f = 1$  and flocks form a space-filling network.

A general scheme, able to compute settling velocity for every concentration and, thus, able to take into account both flocculating and hindered settling, has been proposed by Soulsby [64]. Considering a regression totally analogous to equation (2.65), he proposed the following formula:

$$w_{s,coes} = \frac{\nu}{D_f} \left\{ [10.36 + 1.049 (1 - C_f)^{4.7} D_*^3]^{1/2} - 10.36 \right\} \quad (2.92)$$

where  $D_* = d_f \left[ \frac{g(\rho_f - \rho)}{\rho \nu^2} \right]$ . For the computation of  $d_f$ , he suggested

$$d_f = l C_{coes}^{m_{ws}/2} \quad (2.93)$$

where  $m_{ws}$ , is the power of equation 2.89 and  $l$  a length scale given by

$$l = \left[ \frac{19.8 \rho \nu \rho_{coes}^{m_{ws}} k_{ws}}{g(\rho_f - \rho)} \right]^{1/2}. \quad (2.94)$$

$k_{ws}$  is the coefficient of equation 2.89.

The formula of the equation 2.92 is plotted in Figure 2.10.

## 2.3.2 Erosion

### Erosion shear stress

Different empirical formulas have been presented in literature for the calculation of erosion shear stress. Generally, it is strictly related to the bed consolidation. Because of their greatly experimental nature, such type of formulas needs an accurate calibration process.

In 1980, Thorn and Parsons suggested to relate the erosion shear stress to the bed dry density (see [64]), proposing for recently formed, partially consolidated cohesive-sediment beds the following formula

$$\tau_e = E_1 C_{M,b}^{E_2} \quad (2.95)$$

where  $C_{M,b}$  is the bed dry density, or mass concentration. They obtained for freshly deposited bed in saline water, with a range of  $30 < C_{M,b} < 200$ , the values  $E_1 = 5.42 \times 10^{-6}$  and  $E_2 = 2.28$ .

Alternative values for coefficients have been proposed by Delo and Ockenden [9]. They considered a largest dataset and obtain  $E_1 = 0.0012$  and  $E_2 = 1.2$ , valid for a range of  $30 < C_{M,b} < 400$ .

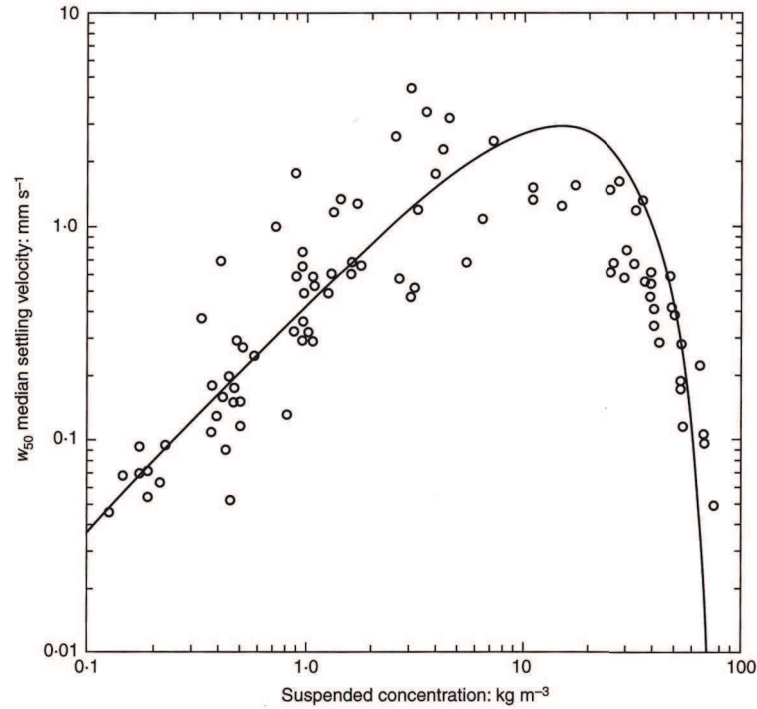


Figure 2.10: Solsby settling velocity formula for cohesive sediments [64].

In order to extend relation (2.95) considering a wider range of cohesive beds such as mixed beds and consolidated beds, Mitchener et al. [27] proposed a new relation, based on bulk density  $\rho_B$ . In particular,

$$\tau_e = E_3 (\rho_B - 1000)^{E_4} \quad (2.96)$$

where, from data fitting, they obtained  $E_3 = 0.015$  and  $E_4 = 0.71$ , as showed in Figure 2.11.

### Erosion rate

Once known the critical shear stress, erosion rate can be computed. In literature, the first to carry out experiments about erosion on marine cohesive sediments was Partheniades: the most commonly used formulas for computation of erosion rate, proposed by several authors, are based on his studies [26, 65].

In his first experiments, Partheniades [33] observed that, also for the smallest bed shear stresses applied, a non-zero erosion took place. For this reason, he assumed that no critical shear stress for erosion exists. Choosing a gaussian bed shear stress distribution, he obtained the following formula for mass erosion rate  $E_{M,coes}$ :

$$E_{M,coes} = \frac{A_E d_{50,coes} \rho_{coes}}{t(\tau_b)} \left[ 1 - \frac{1}{\sqrt{2\pi}} \int_{-\frac{co}{k_E \eta_b \bar{\tau}_b} - \frac{1}{\eta_b}}^{\frac{co}{k_E \eta_b \bar{\tau}_b} - \frac{1}{\eta_b}} \exp\left(-\frac{\omega^2}{2}\right) d\omega \right] \quad (2.97)$$

where  $A_E$  and  $k_E$  are experimental parameters,  $d_{50,coes}$  is the mean diameter for cohesive sediments,  $t(\tau_b)$  the time that the bed shear stress exceeds cohesive forces at the bed,  $co$  the cohesion,  $\bar{\tau}_b$  the mean bed shear stress and  $\eta_b \bar{\tau}_b$  its variance.

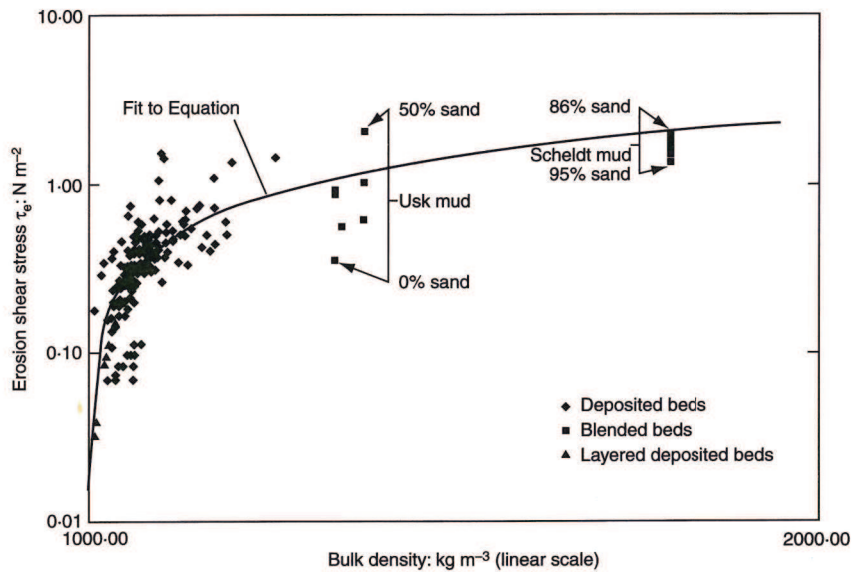


Figure 2.11: Critical shear stress for erosion: Mitchener et al. formula [64].

The simplest parametrization of Partheniades' formula has been carried out by Ariathurai, who proposed

$$E_{M,coes} = M_{par} \left( \frac{\tau_b - \tau_e}{\tau_e} \right). \quad (2.98)$$

The formula considers the existence of a threshold stress for erosion, neglecting the rate of erosion for smallest bed shear stresses (Figure 2.12).

Equation 2.98 has been generalized by different authors in the form

$$E_{M,coes} = M_{par} \left( \frac{\tau_b - \tau_e(z, t)}{\tau_e(z, t)} \right)^{n_{par}} \quad (2.99)$$

where  $\tau_e$  depends on the depth and on the time, considering thus the consolidation process of the bed.  $n_{par}$  is generally unity while the erosion parameter  $M_{par}$  is generally taken constant, in a range between  $0.01 \cdot 10^{-3} \text{ kg}/(\text{m}^2 \text{ s}) < M_{par} < 0.5 \cdot 10^{-3} \text{ kg}/(\text{m}^2 \text{ s})$ .

Equations (2.98) and (2.99) are generally applied to well-consolidated beds and describe an *unlimited* erosion. For very soft beds instead an alternative formula has been proposed by Partheniades and Mehta:

$$E_{M,coes} = E_f \exp \left\{ \alpha_{par} \left[ \frac{\tau_b - \tau_e(z, t)}{\tau_e(z, t)} \right]^{\beta_{par}} \right\} \quad (2.100)$$

where  $E_f$ ,  $\alpha_{par}$  and  $\beta_{par}$  are experimental parameters. This formula is said *depth-limited*, because describes an important decreasing of erosion increasing the depth. In the present work, only first approach has been implemented in the numerical model.

### 2.3.3 Deposition

#### Deposition rate

The most widely used model for deposition has been presented by Krone 1962 (see for details [26, 65]). He observed the settling of a suspension of fine sediments from S. Francisco

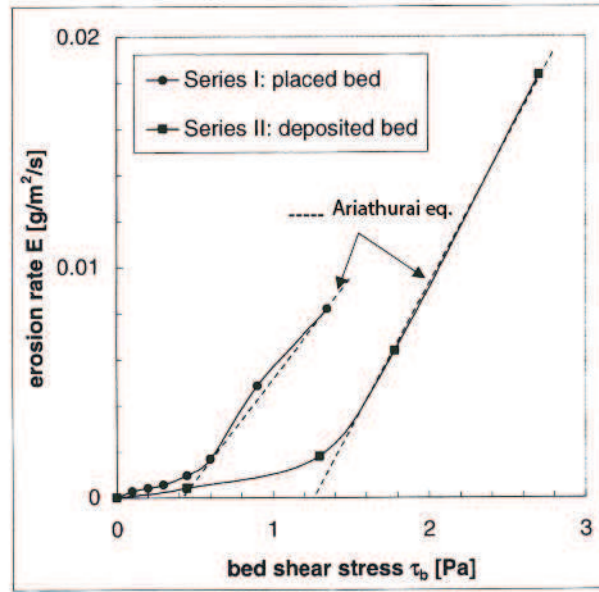


Figure 2.12: Partheniades erosion rate formula [65].

bay, mixed with sodium-chloride, in a 33m long flume. In the first phase of the experiment, a high velocity flow has been carried out in order to mix sediments, salt and fresh water. Afterwards, the flow velocity has been reduced letting the sediments settle.

The mass sediment concentration  $c_{M,coes}$  showed a logarithmic decay for  $c_{M,coes} < 300$  mg/L (Figure 2.13), which takes place when the bed shear stress is lower than the critical deposition value  $\tau_d$ . In this case, the decay is fitted by

$$\frac{c_{M,coes}}{c_{M0,coes}} = \exp \left\{ - (1 - p_{dep}) \frac{w_{s,coes} t}{h} \right\} = \exp \left\{ - \frac{w'_{s,coes} t}{h} \right\} \quad (2.101)$$

where  $c_{M0,coes}$  is the initial concentration and  $p_{dep}$  is considered to be the overall probability of resuspension of the material. Krone considered  $p_{dep}$  linearly depending on the bed shear stress  $\tau_b$ :

$$p_{dep} = \frac{\tau_b}{\tau_d} \quad (2.102)$$

where  $\tau_d$  is the critical bed shear stress for deposition.

Hence, Krone proposed the following law for deposition rate:

$$-D_{coes} = -w'_{s,coes} c_{b,coes} = -w_{s,coes} \left( 1 - \frac{\tau_b}{\tau_d} \right) c_{b,coes} \quad (2.103)$$

where  $c_{b,coes}$  is the bottom bed volume (or mass) concentration.

At present, no law for the calculation of  $\tau_d$  has been presented in literature, although Whitehouse suggested to use a value of about 0.06 – 0.1 Pa, and typically about half the value of critical shear stress for erosion.

### Vertical concentration distribution

For the computation of  $c_{b,coes}$ , a vertical concentration distribution valid for cohesive sediments is needed. The widely known Rouse distribution (equation (2.51)), is based on equilibrium between fall velocity and turbulence. Considering cohesive sediments, however,

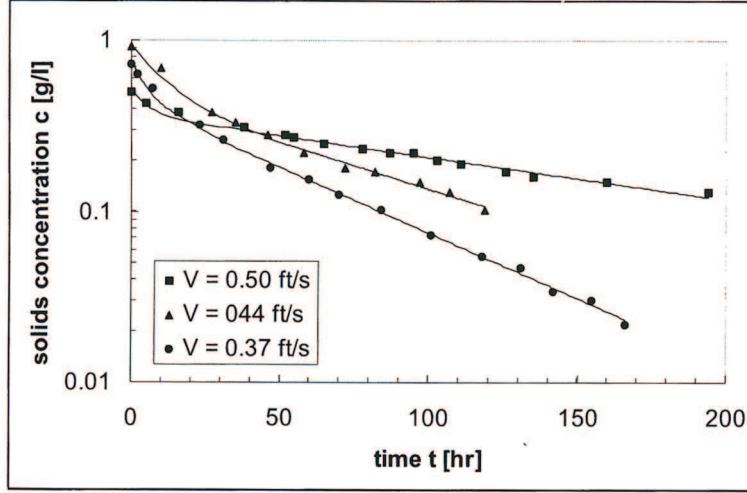


Figure 2.13: Concentration decay in Krone experiments [65].

fall velocity is generally vanishing with respect to the turbulence effect, and Rouse number  $b = w_{s,coes}/\kappa u_*$  is close to 0.

Developing in Taylor series equation (2.51) for  $b \ll 1$ , we obtain the concentration  $c_{coes}(z)$  as a function of the depth-averaged concentration  $C_{coes}$ . In particular, at height  $z$ , we have

$$c_{coes}(z) = C_{coes} \frac{\sin(\pi b)}{\pi b} \left( \frac{1-z/h}{z/h} \right)^b \quad b \ll 1 \quad (2.104)$$

When deposition and erosion rates become large, an alternative profile, described by Teeter [49], should be considered more accurate.

In order to take into account the vertical variation of suspension with a non-dimensional approach, he defined the variables  $Z = z/h$ , *non-dimensional depth*,  $T_a = w_{s,coes}/h$ , *advective time scale* and  $T_d = \epsilon_z t/h^2$ , *diffusive time scale*, where  $h$  is the water depth and  $\epsilon_z$  is the eddy diffusivity. The ratio between advective and diffusive time scale is defined as *Peclet Number*:

$$Pe = \frac{T_a}{T_d} = \frac{w_{s,coes}h}{\epsilon_z} \quad (2.105)$$

In this way, the vertical transport equation can be written as

$$\frac{\partial c_{coes}(z)}{\partial T_a} = \frac{\partial}{\partial Z} \left( c_{coes}(z) + \frac{1}{Pe} \frac{\partial c_{coes}(z)}{\partial Z} \right) \quad (2.106)$$

or

$$\frac{\partial c_{coes}(z)}{\partial T_d} = \frac{\partial}{\partial Z} \left( c_{coes}(z) Pe + \frac{\partial c_{coes}(z)}{\partial Z} \right). \quad (2.107)$$

Considering equilibrium condition, Teeter observed that, being  $\delta c_{coes}$  the concentration difference between bottom and surface and considering the depth-averaged concentration  $C_{coes}$  as a characteristic concentration, the following expression is obtained

$$Pe = \frac{\delta c_{coes}}{C_{coes}} \quad (2.108)$$

and, thus, Peclet Number becomes a suspension stratification parameter.

The solution of either (2.106) and (2.107) needs appropriate boundary conditions. With regard to the surface, no flux condition is imposed

$$\left[ w_{s,coes} c_{coes}(z) + \epsilon_z \frac{\partial c_{coes}(z)}{\partial z} \right] \Big|_{z=h} = 0. \quad (2.109)$$

Finally, at the bottom, deposition or erosion condition is considered. In the first case, the turbulence term is set to 0 and the particle settle is computed as

$$[w_{s,coes} c_{coes}(z)] \Big|_{z=0} = p_{dep} w_{s,coes} c_{b,coes}$$

where  $p_{dep}$  is the probability of deposition (e.g. in the Krone theory, described above in this subsection) (probability that a particle reaching the bed will deposit and remain in the bed). For  $p = 1$  we have free settling, while for  $p = 0$  no sediment enter or left the suspension.

In case of erosion, the bottom boundary condition is

$$w_{s,coes} c_{b,coes} + \epsilon_z \frac{\partial c_{b,coes}}{\partial z} = -E_{coes} \quad (2.110)$$

where  $E$  is the erosion rate per unit area.

Teeter solved numerically the problem, considering different values of  $Pe$  and different bed boundary conditions, in particular free settling and equilibrium conditions (Figure 2.14).

He carried out, from sensitivity analyses, also a relation able to correlate bottom concentration to the depth-averaged concentration, bed fluxes and  $Pe$ , which is

$$\frac{c_{b,coes}}{C_{coes}} = 1 + \left( \frac{Pe}{1.25 + 4.75p^{5/2}} \right). \quad (2.111)$$

Finally, Soulsby [64] proposed an alternative diffusional concentration profile valid for steady currents. He considered a eddy diffusivity  $\epsilon_z$  constant with height, given by  $\epsilon_z = 0.0025Uh$ , and a settling velocity given by equation (2.89). He obtain the following ratio between bottom and depth-averaged mass concentrations, valid for bottom mass concentration  $c_{Mb} < 3 \text{ kg/m}^3$ :

$$\frac{c_{Mb}}{C_{M,coes}} = \left[ 1 + B_{coes} \left( \frac{z}{h} \right) \right]^{-\frac{1}{m_{ws}}}$$

where  $B_{coes} = \frac{m_{ws} w_b}{0.025U}$ ,  $w_b = k_{ws} c_{bM}^{m_{ws}}$  is the settling velocity at the bottom and  $C_{M,coes}$  is cohesive depth-averaged mass concentration.

A simple alternative suggested by Soulsby is to consider the concentration varying linearly with depth. In absence of specific data, he proposed as the ration between surface and bottom concentration the value  $R_c = 3$ .

## 2.4 Bottom morphological evolution

The analysis of sediment transport is fundamental for the comprehension of morphological evolution of the studied domain: this is in fact one of the main scopes of morphodynamic modeling. Thus, it is important to understand the correlation between sediment transport and bottom evolution, which are strictly related by the sediment continuity equation. Coherently with previous considerations, morphological change is split in two different contributes given respectively by granular and cohesive sediment transport.

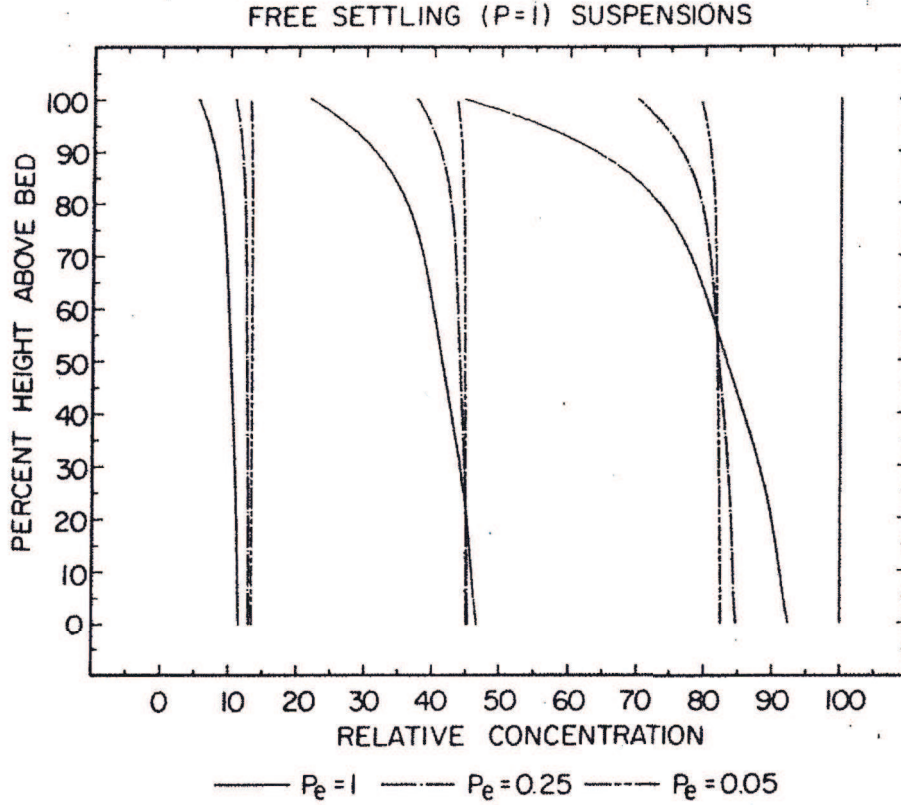


Figure 2.14: Teeter profiles in settling conditions for  $T_A = 0, 0.2, 0.8, 2$  [49].

Consider the 1D control volume in Figure 2.15. For the mass conservation, it is possible to write

$$\frac{\partial m_s}{\partial t} = m_{s,e} - m_{s,u} \quad (2.112)$$

where  $m_s = \rho_s C A_s ds$  is the total solid mass,  $m_{s,e} = \rho_s q_{s,e}$  is the mass sediment inflow and  $m_{s,u} = \rho_s q_{s,u}$  is the mass sediment outflow. In particular,  $A_s = Bh$  is the cross section and  $B$  is the volume control width and  $q_s = q_{ss} + q_{st}$  is the total sediment transport rate.

The time derivative at first term of equation (2.112) can be developed as

$$\frac{\partial m_s}{\partial t} = \rho_s \frac{\partial (C A_s)}{\partial t} ds + (1 - n_{por}) \rho_s \frac{\partial z_b}{\partial t} B ds \quad (2.113)$$

where  $n_{por}$  is the bed porosity (valid for granular sediments) and  $z_b$  is the bottom level.

Substituting in equation (2.112), we obtain

$$\rho_s \frac{\partial (C A_s)}{\partial t} ds + (1 - n_{por}) \rho_s \frac{\partial z_b}{\partial t} B ds = \rho_s q_{s,e} - \rho_s q_{s,u} = \rho_s q_{s,e} - \left( \rho_s q_{s,e} + \frac{\partial (\rho_s q_s)}{\partial s} ds \right). \quad (2.114)$$

With regards to granular sediment transport, the equilibrium approach considers inertial term of sediment transport vanishing with respect to other terms. Thus, we can write

$$O\left(\frac{\partial (C_{gran} A_s)}{\partial t}\right) \ll O\left(\frac{\partial q_s}{\partial s}\right) \sim O\left(\frac{\partial z_f}{\partial t} B_w\right)_{gran} \quad (2.115)$$

obtaining the widely known Exner Equation:

$$\left(\frac{\partial z_b}{\partial t}\right)_{gran} = -\frac{1}{B(1 - n_{por})} \left(\frac{\partial q_s}{\partial s}\right) \quad (2.116)$$

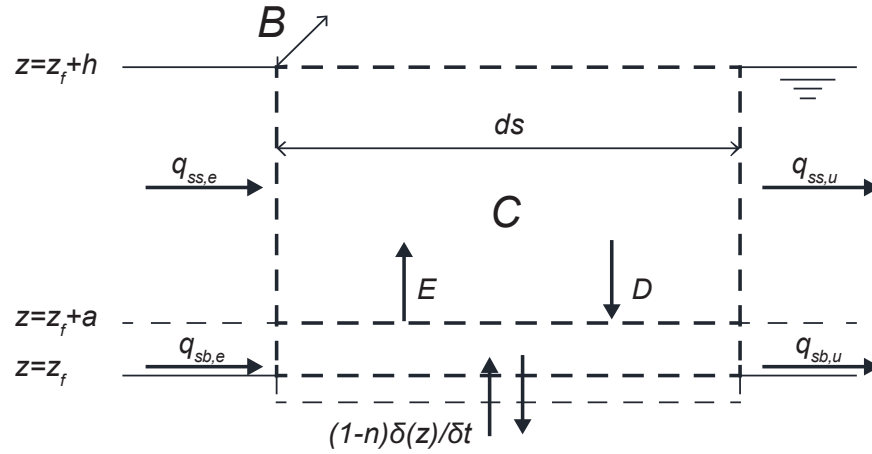


Figure 2.15: Vertical schematisation of sediment exchange at the bottom (modified from [59]).

which is valid if equilibrium approach is used for both suspended and bed loads.

If non-equilibrium approach for suspended load is considered, the control volume should be reduced to the lowest layer of the water volume, where bed sediment transport takes place, and to the bottom. In fact, suspended sediment conservation on the upper water volume is described by the advective diffusive equation (e.g. Section 2.2.3). In this case, the inertial term  $\frac{\partial(C_{gran}A_s)}{\partial t}$  corresponds to the  $ED_{gran}$  term of suspended sediment A-D equation. Thus, the mass continuity equation can be rewritten as

$$\left(\frac{\partial z_b}{\partial t}\right)_{gran} = -\frac{1}{B(1-n_{por})} \left(\frac{\partial q_{sb}}{\partial s} + ED_{gran}\right). \quad (2.117)$$

where  $q_{sb}$  is the bed sediment transport load (computed with an equilibrium approach).

For cohesive sediments, porosity loses its meaning. In this case, erosion and deposition rates take into account implicitly bed sediment density. Moreover, no bed load is considered. Thus bottom continuity equation reduces to

$$\left(\frac{\partial z_b}{\partial t}\right)_{coes} = -\frac{1}{B} (ED_{coes}). \quad (2.118)$$

Finally, assuming granular and cohesive contributes independent, it is possible to solve the global morphological problem:

$$\frac{\partial z_b}{\partial t} = \left(\frac{\partial z_b}{\partial t}\right)_{gran} + \left(\frac{\partial z_b}{\partial t}\right)_{coes}. \quad (2.119)$$



## Chapter 3

# The morphodynamic model

Morphodynamic models are numerical models able to couple the hydrodynamic problem to the sediment transport analysis (how sediments are transported by the water flow) and to the morphological evolution (how the bottom changes due to sediment transport). They are considered among the most powerful instruments available in hydraulic and morphological studies, resulting particularly useful in comprehending and predicting the sediment movement and the morphological response in rivers, estuaries or coastal environments. For this reason, their use is becoming more common in support of water environments management and decision-making.

In the literature, a great number of different models have been presented and discussed, which differ for example in the number of problem dimensions, in the used equations and in their discretization technique (numerical scheme).

Models which seem to be more suited for application in coastal areas are 2DH models (2-dimensional horizontal models). In this case, hydrodynamic problem is generally based on *De Saint Venant Equations*, which describe depth-average conservations of mass and momentum into a bi-dimensional domain. De Saint Venant equations are not analytically solvable, except for very simple theoretical cases.

For this reason, they require to be adequately discretised and can be solved on a finite number of points into the domain, which is generally divided into simple polygonal sub-volumes, called *cells*. Cells are characterized by a plane bottom and here the problem is assumed to be uniform or uniformly varied: equations can be applied to cells and a cell-centred solution is obtained. Alternative approaches give the solution at vertex nodes of the cells.

With regard to sediment transport problem, as previously described different approaches are available.

In case non-equilibrium transport is analysed (e.g. for suspended load or for cohesive sediments), a depth-averaged advective-diffusive equation must be associated to De Saint Venant Equations and similarly discretised. Moreover, when different non-equilibrium problems are simultaneously considered (e.g. different sediment classes or both granular and cohesive sediment transport), more independent depth-averaged advective-diffusive equations are generally imposed.

If the equilibrium approach is chosen, otherwise, sediment loads are directly computed on cells with simple empirical formulas, as described in chapter 2.

Once solved hydrodynamic and sediment transport problem, bottom continuity equation permits to solve the morphological evolution.

In last years, 3D modelling has been deeply developed too, but generally 3D-models are

computationally heavy and thus they can difficultly be applied in complex wide domains.

The most used numerical schemes in morphodynamic modelling are *finite volume method (FVM)* and *finite element method (FEM)*, which guarantee more stability than *finite difference method (FDM)*.

Here, a new FVM 2DH morphodynamic model, called DAM\_SED, is presented: it based on the hydrodynamic model developed by University of Udine Hydraulics Laboratory, of which I am a member. In particular, sediment transport and morphological modules will be deeply described and discussed.

DAM\_SED is able to take into account the effect of the wave field, which can be alternatively imposed by the user (e.g. for easy laboratory tests) or obtained by coupling the morphodynamic model with SWAN, an open-source spectral model edited by TU Delft: in this way, both wave motion and morphological evolution can influence each other.

A very simple flowchart of DAM\_SED is illustrated in Figure 3.1. The model is divided into three main modules: hydrodynamic module, sediment transport module and morphological module. As previously discussed, in case of non-equilibrium granular transport or cohesive transport, the corresponding advective-diffusive equations are solved together with the hydrodynamic system, as scalar transport equations.

The development of a new morphodynamic model has three main purposes.

At first, the model has been studied in order to reduce, as much as possible, the number of calibration parameters. Indeed, the model should be suited to applications in real cases, where the availability of experimental data and monitoring networks is generally poor.

Secondly, a large number of different theories and approaches has been implemented, in order to compare them and focus on that which seems to be more appropriate in each single study-case.

Finally, the present morphodynamic model is based on an accurate shock-capturing scheme, able to describe properly phenomena like dam break or wet-dry propagation in complex areas. The latter is typical of coastal environments like lagoons, where salt marshes are regularly flooded by tides. Many of the most commonly used open-source and commercial models are in fact based on gradually varied hypothesis and, thus, are not easily suited to similar situations.

## 3.1 The hydrodynamic module

The hydrodynamic model here used is called DAM\_HYD: it is a Finite Volume shallow water model, able to solve the problem on a quadrangular irregular mesh. The scheme is I-order in space and in time and is shock capturing, being mathematical and physical conservative. Moreover, it respects the C-property, as we will discuss later.

A number of physical parameters and modelling options are required, which involve water physical properties, turbulence characteristics, bottom roughness and the bed shear stress computation, boundary and initial conditions and external forcing, like Coriolis force, wind or waves. Most of them are imposed in a proper modelling setting file, which will be described in Appendix.

### 3.1.1 The mathematical scheme

The hydrodynamic module is a 2D finite volume shallow water model based on De Saint Venant equations. In particular, three equations are involved: continuity equation, momen-

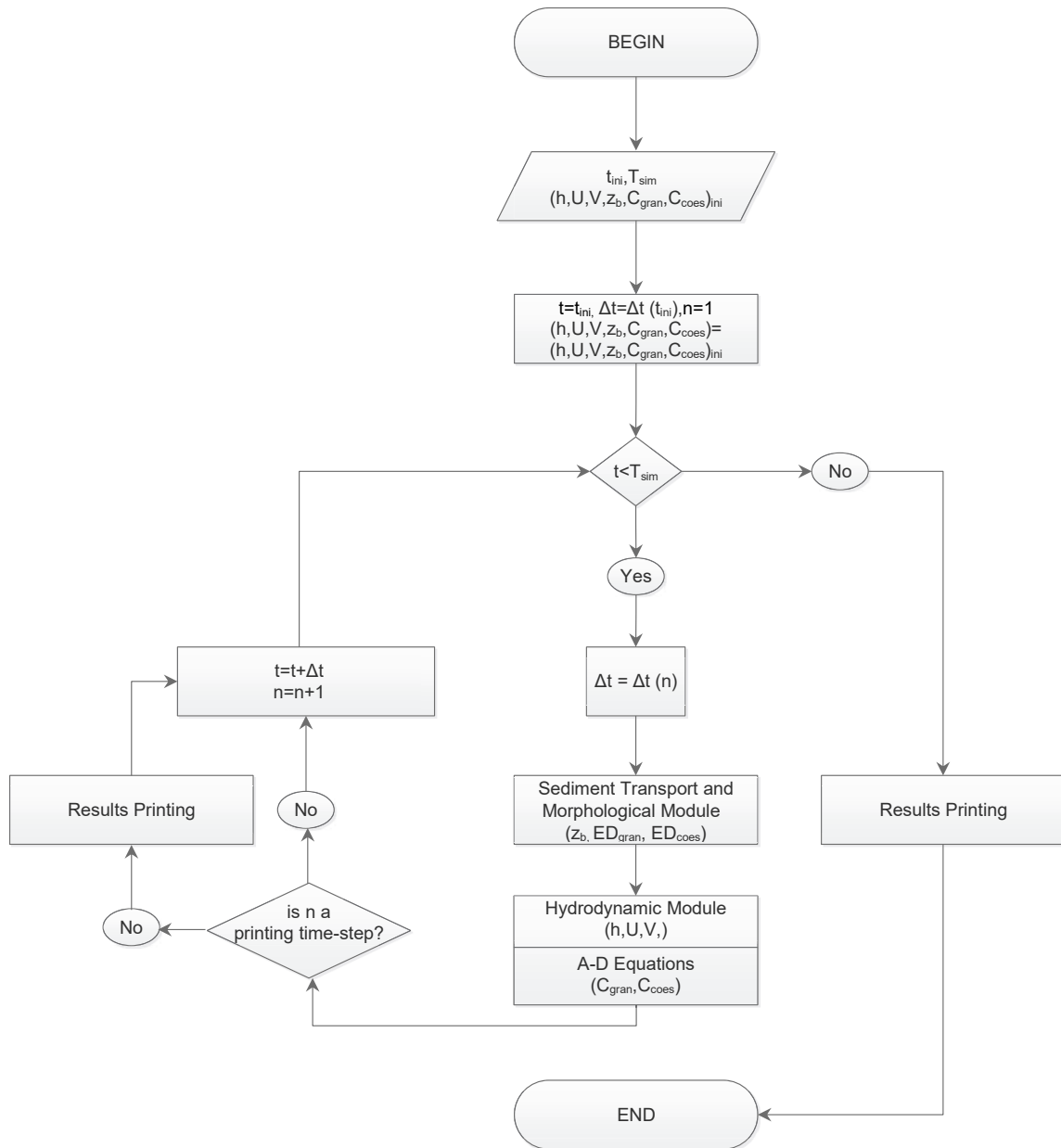


Figure 3.1: Flowchart of the model DAM\_SED.

tum equation in  $x$ -direction and momentum equation in  $y$ -direction. It can be useful write them in matrix notation:

$$\frac{\partial \mathbf{U}}{\partial t} + \frac{\partial (\mathbf{F}_c + \mathbf{F}_v)}{\partial x} + \frac{\partial (\mathbf{G}_c + \mathbf{G}_v)}{\partial y} = \mathbf{S} \quad (3.1)$$

where, in particular,

$$\mathbf{U} = \begin{pmatrix} h \\ Uh \\ Vh \end{pmatrix} \quad (3.2)$$

$$\mathbf{F}_c = \begin{pmatrix} Uh \\ U^2h + g\frac{h^2}{2} \\ UVh \end{pmatrix} \quad \mathbf{F}_v = \begin{pmatrix} 0 \\ 2\nu_T h \frac{\partial U}{\partial x} \\ \nu_T h \left( \frac{\partial U}{\partial y} + \frac{\partial V}{\partial x} \right) \end{pmatrix}, \quad (3.3)$$

$$\mathbf{G}_c = \begin{pmatrix} Vh \\ UVh \\ V^2h + g\frac{h^2}{2} \end{pmatrix} \quad \mathbf{G}_v = \begin{pmatrix} 0 \\ \nu_T h \left( \frac{\partial U}{\partial y} + \frac{\partial V}{\partial x} \right) \\ 2\nu_T h \frac{\partial V}{\partial y} \end{pmatrix} \quad (3.4)$$

and

$$\mathbf{S} = \begin{pmatrix} 0 \\ -gh \frac{\partial z_b}{\partial x} - \frac{\tau_{bx}}{\rho} + \frac{f_{rsx}}{\rho} + S'_x \\ -gh \frac{\partial z_b}{\partial y} - \frac{\tau_{by}}{\rho} + \frac{f_{rsy}}{\rho} + S'_y \end{pmatrix}. \quad (3.5)$$

Here,  $U$  and  $V$  are the  $x$ - and  $y$ - components of depth-averaged velocity vector,  $h$  is the water depth,  $\nu_T$  is the eddy viscosity, which is considered horizontally isotropic and constant in each cell,  $z_b$  the bottom elevation while  $\tau_{bi}$  and  $f_{rsi}$ , with  $i = x, y$ , are respectively the bed shear stress and the wave radiation stress forcing components.  $S'_i$  take finally into account the effect of wind and Coriolis force. In this notation,  $\mathbf{U}$  is the variables vector,  $\mathbf{F}_c$  and  $\mathbf{G}_c$  are convective flux terms vector,  $\mathbf{F}_v$  and  $\mathbf{G}_v$  are viscous and turbulent flux terms vector and  $\mathbf{S}$  is the source terms vector.

Under current-alone condition, the bed shear stress  $\tau_b$  corresponds to the current bed shear stress  $\tau_c$  and is here computed using the Manning formula (1.96) as

$$\tau_{bx} = \tau_{bcx} = \rho g n^2 \frac{U \sqrt{U^2 + V^2}}{h^{1/3}} \quad (3.6)$$

$$\tau_{by} = \tau_{bcy} = \rho g n^2 \frac{V \sqrt{U^2 + V^2}}{h^{1/3}}. \quad (3.7)$$

If wave motion effect are taken into account (e.g. coupling DAM\_HYD with SWAN), wave field characteristics are provided in each cell. In particular significant wave height  $H_s$ , significant wave period  $T_{ws}$ , maximum bottom orbital velocity  $U_{m0}$  and wave direction  $\phi$  are required. Moreover, radiation stress gradient effect can be considered and, in case, its forcing should be imposed.

From an hydrodynamic point of view, wave-current bed shear stress and stress due to radiation stress can be thus taken into account.

In case of presence of waves, Soulsby approach is here implemented for the calculation of bed shear stress. Hydrodynamics is considered to be influenced by mean bed shear stress value  $\tau_m$ , which is characterized by the same direction of flow velocity. The maximum bed

shear stress is instead important for sediment dynamics. Thus, by the use of equations (1.170), wave-current mean bed shear stress components become

$$\tau_{bx} = \tau_{mx} = \tau_{bcx} \left( 1 + b_s \left( \frac{\tau_{bc}}{\tau_{bc} + \tau_{bw}} \right)^{p_s} \left( \frac{\tau_{bw}}{\tau_c + \tau_w} \right)^{q_s} \right) \quad (3.8)$$

$$\tau_{by} = \tau_{my} = \tau_{bcy} \left( 1 + b_s \left( \frac{\tau_{bc}}{\tau_{bc} + \tau_{bw}} \right)^{p_s} \left( \frac{\tau_{bw}}{\tau_{bc} + \tau_{bw}} \right)^{q_s} \right) \quad (3.9)$$

Where  $b_s$ ,  $p_s$  and  $q_s$  are Soulsby parameters, described in Subsection 1.3.5. Maximum bed shear stress is finally computed using equation (1.171):

$$\tau_{max} = (\tau_{bc} + \tau_{bw}) \left[ 1 + a_s \left( \frac{\tau_{bc}}{\tau_{bc} + \tau_{bw}} \right)^{m_s} \left( \frac{\tau_{bw}}{\tau_{bc} + \tau_{bw}} \right)^{n_s} \right] \quad (3.10)$$

where  $a_s$ ,  $m_s$  and  $n_s$  are Soulsby parameters, described in Subsection 1.3.5. In the particular cases of DATA2 or DATA13 Soulsby formulations, the maximum bed shear stress is computed as the vectorial addition between  $\tau_m$  and  $\tau_{bw}$ .

In this way, the following theories can be chosen:

- Bijker
- Grant and Madsen
- Fredsøe
- Huyng-Thahn and Temperville
- Myrhaug and Slaattelid
- Soulsby DATA 13
- Soulsby DATA 2.

Coherently with Soulsby approach, the wave friction factor used for wave bed shear stress computation depends on the chosen wave-current bed shear stress model (further details in [45, 44]). As discussed in Subsection 1.2.2, this is anyway related to the global roughness  $\varepsilon$ , which can be either computed from Manning coefficient or imposed by the operator after a calibration process.

In the first case, from current bed shear stress a drag coefficient  $C_D$  is obtained using equation (1.91):

$$C_D = \frac{\tau_c}{\rho(U^2 + V^2)} = \frac{gn^2}{h^{1/3}} \quad (3.11)$$

The correspondent bed roughness is hence obtained inverting equation (1.92):

$$\varepsilon = 30h \exp \left( \frac{\kappa}{\sqrt{C_D}} - 1 \right) \quad (3.12)$$

where  $\kappa$  is the Von Karman constant. The maximum wave bed shear stress  $\tau_{bw}$  is thus obtained as

$$\tau_{bw} = \frac{1}{2} f_w \rho U_{1m}^2 \quad (3.13)$$

where the wave friction factor  $f_w = f_w(\varepsilon, h)$ .

Considering radiation stress effects, SWAN is able to compute in each cell the radiation stress forcing  $f_{rsx}$  and  $f_{rsy}$  as:

$$f_{rsx} = -\frac{\partial S_{rs,xx}}{\partial x} - \frac{\partial S_{rs,xy}}{\partial y} \quad (3.14)$$

$$f_{rsy} = -\frac{\partial S_{rs,xy}}{\partial x} - \frac{\partial S_{rs,yy}}{\partial y}. \quad (3.15)$$

Here,  $S_{rs,ij}$ , with  $i, j = x, y, z$ , are the radiation stress tensor components (see [19] for details).

With regard to the computation of the eddy viscosity, four main approaches have been implemented:

- **NO TURBULENCE:** in this case turbulence terms are not considered;
- **ELDER MODEL [12]:** this is a depth averaged parabolic eddy viscosity model. The expression chosen for  $\nu_T$  is:

$$\nu_T = \alpha_T u_* h \quad (3.16)$$

where  $\alpha_T$  is an empirical coefficient and  $u_*$  the friction velocity. It is generally assumed that  $\alpha_T$  is related to the ratio between flow width and depth and typical values are in the range  $\alpha_T = 0.3 \div 1$ ;

- **SMAGORINSKY MODEL:** the model considers the eddy viscosity dependent on the rate of strain and supposes to represent subgrid turbulence [42]. In particular Smagorinsky proposed

$$\nu_T = (C_S^2 l_S^2) \sqrt{\left(\frac{\partial U}{\partial x}\right)^2 + \frac{1}{2} \left(\frac{\partial U}{\partial y}\right) \left(\frac{\partial V}{\partial x}\right) + \left(\frac{\partial V}{\partial y}\right)^2} \quad (3.17)$$

where  $C_S$  is Smagorinsky coefficient and  $l_S$  is the grid elements length scale. In the present model, this latter parameter is imposed by the user, although a good approximation of it is [10]

$$l_S = \sqrt{\Omega} \quad (3.18)$$

where  $\Omega$  is the horizontal area of considered cell. More generally,  $l_S$  can be considered as the turbulent length scale that the model considers.

- **CONSTANT EDDY VISCOSITY,** can be imposed by the operator. In this case it is thus independent from hydrodynamic conditions.

Manning coefficient  $n$ , eddy viscosity  $\nu_T$  and, if used, wave-related bed roughness  $\varepsilon$ , are unique hydrodynamic calibration coefficients and are thus used to suite the model to real hydraulics data, for example mareometer records.

### 3.1.2 The numerical solution

DAM\_HYD is a finite volume model, able to solve the hydrodynamic problem on irregular meshes with quadrangular elements. The model satisfies C-property.

The aim of finite volume technique is to discretise the differential equation system at each cell directly in the physical space. For this reason, particular importance is given to the computation of the so called *intercell fluxes*.

Consider the Euler 1D problem on horizontal bottom

$$\frac{\partial \mathbf{U}'}{\partial t} + \frac{\partial \mathbf{F}'}{\partial x} = 0 \quad (3.19)$$

with  $\mathbf{U}' = \begin{pmatrix} h \\ Uh \end{pmatrix}$ ,  $\mathbf{F}' = \begin{pmatrix} Uh \\ U^2h + gh^2/2 \end{pmatrix}$ .

Given a domain  $i$  with a control volume  $L_i = [x_{i-\frac{1}{2}}, x_{i+\frac{1}{2}}]$  (cell  $i$ , see Figure 3.2), equation (3.19) can be integrated in the cell as

$$\int_{x_{i-\frac{1}{2}}}^{x_{i+\frac{1}{2}}} \frac{\partial \mathbf{U}'}{\partial t} dx + \int_{x_{i-\frac{1}{2}}}^{x_{i+\frac{1}{2}}} \frac{\partial \mathbf{F}'}{\partial x} dx = 0 \quad (3.20)$$

Let us define the integral averaged quantities

$$\mathbf{U}_i = \check{\mathbf{U}}_i = \frac{1}{x_{i+\frac{1}{2}} - x_{i-\frac{1}{2}}} \int_{x_{i-\frac{1}{2}}}^{x_{i+\frac{1}{2}}} \frac{\partial \mathbf{U}'}{\partial t} dx$$

where in particular  $\check{\cdot}$  operator is the space integral average into the domain.

Equation (3.20) can thus be rewritten as

$$\frac{\partial \mathbf{U}_i}{\partial t} + \frac{1}{(x_{i+\frac{1}{2}} - x_{i-\frac{1}{2}})} \left( \mathbf{F}'_{i+\frac{1}{2}} - \mathbf{F}'_{i-\frac{1}{2}} \right) = 0 \quad (3.21)$$

where  $\mathbf{F}'_{i+\frac{1}{2}}$  and  $\mathbf{F}'_{i-\frac{1}{2}}$  are fluxes vectors at intercells  $i + \frac{1}{2}$  and  $i - \frac{1}{2}$ .

Knowing variables at time  $t^n$ , time derivative in equation (3.21) can be discretised by the use a Taylor series. In this way, the equation becomes for example

$$\mathbf{U}_i^{n+1} = \mathbf{U}_i^n - \frac{\Delta t}{(x_{i+\frac{1}{2}} - x_{i-\frac{1}{2}})} \left( \mathbf{F}'_{i+\frac{1}{2}}^n - \mathbf{F}'_{i-\frac{1}{2}}^n \right) \quad (3.22)$$

where  $\mathbf{U}_i^{n+1}$  is the averaged variables vector in the cell  $i$  at instant  $t^{n+1} = t^n + \Delta t$ .

Equation (3.22) represents a typical example of I-order discretisation by finite volume method. Known the variables vector  $\mathbf{U}_i^n$  at time  $t^n$ , the main problem is the computation of intercell fluxes  $\mathbf{F}'_{i+\frac{1}{2}}$  and  $\mathbf{F}'_{i-\frac{1}{2}}$ : afterwards solution at instant  $t^{n+1}$  is immediately available.

Advective intercell fluxes computation can be done solving the so called *Riemann Problem*. In particular, Riemann problem let to study discontinuity propagation between two different steady states for inviscid fluid on an horizontal bottom. The problem has an analytical solution but, in numerical modelling, approximated method are often preferred because computationally lighter.

Source terms and viscosity effects, which cannot be taken into account in Riemann problem, are computed separately. For this reason, the time derivative in the 1D hydrodynamic problem (3.1) is solved splitting the resolution of the homogeneous system (3.19) and the effect of viscous fluxes and source terms.

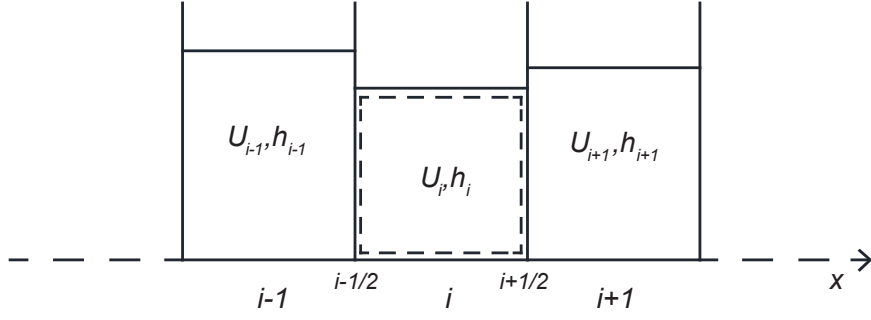


Figure 3.2: 1D Scheme for Finite Volume Method.

### The 2-dimensional problem

In order to solve the 2D hydrodynamic problem with Finite Volume Method, we consider two dimensional Euler equation on horizontal bottom

$$\frac{\partial \mathbf{U}}{\partial t} + \frac{\partial (\mathbf{F}_c)}{\partial x} + \frac{\partial (\mathbf{G}_c)}{\partial y} = 0 \quad (3.23)$$

Let us integrate equation (3.23) in a 2D domain  $\Omega$  (Figure 3.3):

$$\int_{\Omega} \frac{\partial \mathbf{U}}{\partial t} d\Omega + \int_{\Omega} \frac{\partial (\mathbf{F}_c)}{\partial x} d\Omega + \int_{\Omega} \frac{\partial (\mathbf{G}_c)}{\partial y} d\Omega = 0 \quad (3.24)$$

Defining  $\mathbf{H} = [\mathbf{F}_c \ \mathbf{G}_c]$ , by the use of divergence theorem, second and third terms of equation (3.24) can be computed as a linear integral of the flux over the boundary of the cell. In particular, we obtain

$$\int_{\Omega} \frac{\partial \mathbf{U}}{\partial t} d\Omega + \oint_{\partial \Omega} (\mathbf{H} \cdot \vec{n}) ds = 0 \quad (3.25)$$

where  $\vec{n} = (n_x, n_y) = (\cos \theta_n, \sin \theta_n)$ . As discussed by Toro [51], equation 3.23 satisfies the rotational invariance. Thus, defining the rotation matrix  $\mathbf{T}$  as

$$\mathbf{T} = \begin{bmatrix} 1 & 0 & 0 \\ 0 & \cos \theta_n & \sin \theta_n \\ 0 & -\sin \theta_n & \cos \theta_n \end{bmatrix} \quad (3.26)$$

and its inverse  $\mathbf{T}^{-1}$

$$\mathbf{T}^{-1} = \begin{bmatrix} 1 & 0 & 0 \\ 0 & \cos \theta_n & -\sin \theta_n \\ 0 & \sin \theta_n & \cos \theta_n \end{bmatrix}, \quad (3.27)$$

for each angle  $\theta$  and variables vector  $\mathbf{U}$  we can write

$$\mathbf{H} \cdot \vec{n} = \mathbf{T}^{-1} \mathbf{F}_c (\mathbf{T} \mathbf{U}) = \mathbf{T}^{-1} \mathbf{F}_c (\hat{\mathbf{U}}). \quad (3.28)$$

Let us note that if  $\Omega$  is a  $N$ -sided polygon, integral at second term of (3.25) can be thus replaced by the sum

$$\oint_{\partial \Omega} (\mathbf{H} \cdot \vec{n}) ds = \sum_{k=1}^N \int_{\Delta l_k} \mathbf{T}_k^{-1} dl \mathbf{F}_c (\hat{\mathbf{U}}_k) = \sum_{k=1}^N \mathbf{T}_k^{-1} \mathbf{F}_{ck} \Delta l_k \quad (3.29)$$

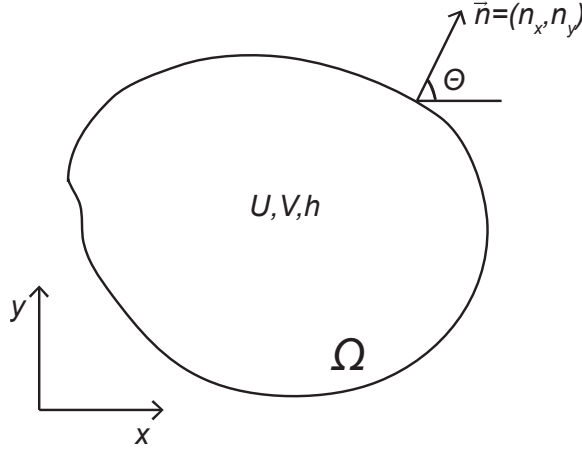


Figure 3.3: 2D generic domain.

where

$$\mathbf{F}_{ck} = \check{\mathbf{F}}_c(\hat{\mathbf{U}}_k) = \frac{1}{\Delta l_k} \int_{\Delta l_k} \mathbf{F}_c(\hat{\mathbf{U}}_k) dl \quad (3.30)$$

2-dimensional problem is thus reduced to the computation of 1-dimensional fluxes term  $\mathbf{F}_{ck}$ . Because the system is composed by three equations (and for this reason it is not a real 1D problem), it is said *1D-augmented*, while the approach here described is said *x-splitting*.

Consider a quadrangular cell  $\Omega_i$  (Figure 3.4). Using previously discussed concepts, a simple FVM discretisation of equation (3.23), is thus:

$$\mathbf{U}_i^{n+1} = \mathbf{U}_i^n - \Delta t \left( \sum_{k=1}^4 \mathbf{T}_{i,k}^{-1} [\mathbf{F}_{ck}^n] \Delta l_{k,i} \right). \quad (3.31)$$

Viscous flux contribution  $\mathbf{F}_v$  can be treated in a similar way: in fact, viscous terms do not remove rotational invariance. Similarly to the 1D case, this term and the source terms are split from the homogeneous problem and treated separately for the time derivative computation.

### Computation of intercell advective fluxes: the solution of Riemann problem

The Riemann problem is an initial value problem based on a linear advective equation and on an initial condition with a single discontinuity. In this particular case, we refer to Euler equation.

Let us write Riemann problem for the 1D-augmented case. We have

$$\begin{cases} \frac{\partial \mathbf{U}}{\partial t} + \frac{\partial \mathbf{F}_c}{\partial x} = 0 \\ \mathbf{U}(x, 0) = \mathbf{U}_0 = \begin{cases} \mathbf{U}_L & x < 0 \\ \mathbf{U}_R & x > 0 \end{cases} \end{cases} \quad (3.32)$$

where  $\mathbf{U}_L$  and  $\mathbf{U}_R$  are constant values (Figure 3.5). Euler equation can be rewritten in the form

$$\frac{\partial \mathbf{U}}{\partial t} + \frac{\partial \mathbf{F}_c}{\partial \mathbf{U}} \frac{\partial \mathbf{U}}{\partial x} = 0 \quad (3.33)$$

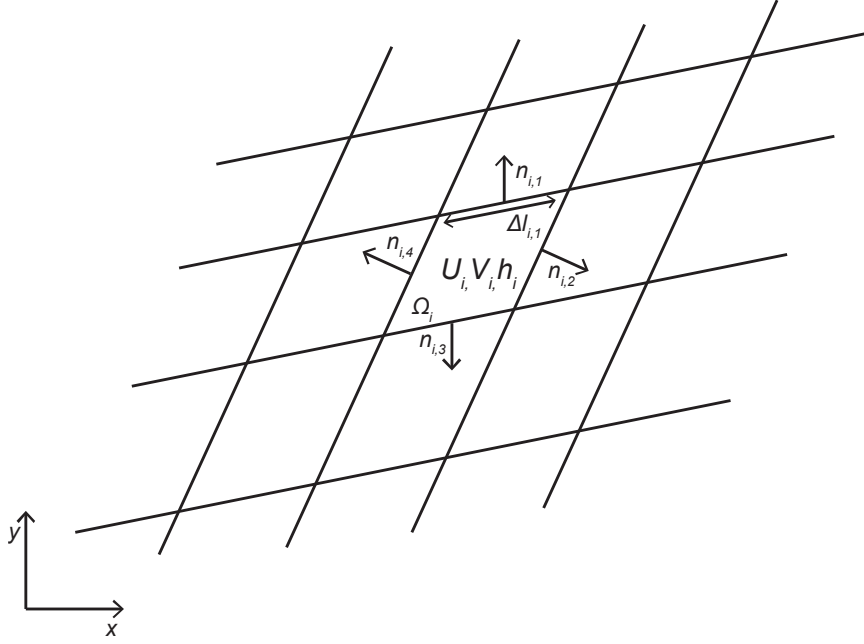


Figure 3.4: Quadrangular cell scheme.

where Jacobian matrix  $\frac{\partial \mathbf{F}_c}{\partial \mathbf{U}}$  is easily demonstrable to be

$$\frac{\partial \mathbf{F}_c}{\partial \mathbf{U}} = \begin{bmatrix} 0 & 1 & 0 \\ gh - U^2 & 2U & 0 \\ -UV & V & U \end{bmatrix}. \quad (3.34)$$

In order to reduce (3.33) to a linear form, we consider the system evolution in a limited interval close to the instant  $t_0$ : in particular we consider the time domain  $t_0 \leq t \leq t_0 + \Delta t$ . In this way, general Jacobian matrix can be substituted with its value at time  $t = t_0$ :

$$\frac{\partial \mathbf{U}}{\partial t} + \frac{\partial \mathbf{F}_c}{\partial \mathbf{U}} \Big|_{t=t_0} \frac{\partial \mathbf{U}}{\partial x} = 0. \quad (3.35)$$

For  $t > t_0$ , this equation is quasi-linear.

Equation (3.35) is hyperbolic: in fact, it is characterized by three real eigenvalues, which are

$$\begin{aligned} \lambda_1 &= U - \sqrt{gh} \\ \lambda_2 &= U \\ \lambda_3 &= U + \sqrt{gh} \end{aligned} \quad (3.36)$$

where  $\lambda_i, i = 1, 2, 3$  are the eigenvalues of the jacobian matrix  $\frac{\partial \mathbf{F}_c}{\partial \mathbf{U}} \Big|_{t=t_0}$ .

Eigenvalues  $\lambda_i$  are demonstrable to be the *characteristic speeds* of the problem, which are the speeds of informations (and small perturbations) propagation.

On  $(x, t)$  plane, Riemann problem is schematised in Figure 3.6. Three waves, associated to characteristic speeds  $\lambda_i$ , are generated by the propagation of initial condition in (3.32). These can be of three different type: *shock waves*, *rarefaction waves* or *shear waves*.

Shock and rarefaction waves are associated to eigenvalues  $\lambda = U \pm \sqrt{gh}$ . In the first case, discontinuity is concentrated into a single jump, while in the second case two different states are connected through a smooth transition. Shock and rarefaction waves always

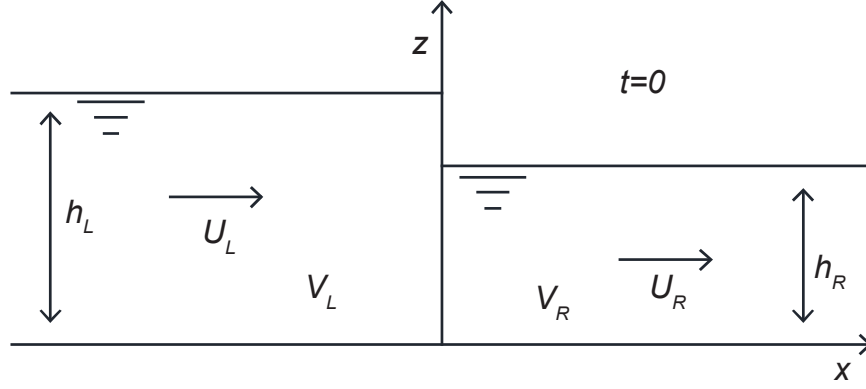


Figure 3.5: Riemann Problem.

corresponds to the physical limits of perturbation propagation. Their analytical solution can be easily obtained using the characteristic method.

Shear waves are shear discontinuities across which tangential velocity  $V$  jumps discontinuously. They are associated to the eigenvalue  $\lambda = U$ . Shear waves are of particular interest in case of passive scalar transport like, for example, sediment concentration, which behaves as a tangential velocity. All waves are characterized by their celerity, which are respectively called  $S_L$  and/or  $S_R$  for shock and rarefaction waves and  $\tilde{S}$  for shear waves.

Finally, considering hyperbolic system with a discontinuous solution between two states  $L$  and  $R$ , Rankine-Hugoniot condition can be demonstrated. In particular, the following relation is valid:

$$\mathbf{F}_c(\mathbf{U}_R) - \mathbf{F}_c(\mathbf{U}_L) = S_{cel}(\mathbf{U}_R - \mathbf{U}_L) \quad (3.37)$$

where  $S_{cel}$  is the propagation celerity of the considered wave.

Riemann analytical solution has been presented by Godunov and is widely discussed in literature (see [18, 51, 52]): an example of Riemann solution is illustrated in Figure 3.7). In particular, considering waves associated to  $\lambda = U \pm \sqrt{gh}$ , several combinations are possible, depending on initial right and left states: there can be two rarefactions, two shock or a rarefaction and a shock waves, alternatively at right or at left. Computation of intercell fluxes corresponds to the solution of Riemann problem at  $x = 0$ .

Godunov solution is generally considered computationally heavy because of its influence on computational time, in particular for wide domains.

Thus, alternative Riemann solutors have been proposed in literature, which give an approximated solution of the intercell fluxes. They result to be more efficient and their solution is considered acceptable in hydrodynamic modelling.

In the present model, Riemann problem is solved with HLLC solver.

Consider the Riemann problem in Figure 3.6. HLLC solver considers on  $(x, t)$  plane four main regions, divided by discontinuity waves: *left region* and *right region*, (where the discontinuity has not yet influence), and *star-left* and *star-right regions* (which are involved in the discontinuity propagation).

We consider left wave moving with celerity  $S_L$ , right wave moving with celerity  $S_R$  and the shear wave moving with celerity  $\tilde{S}$ . HLLC considers a constant state inside each

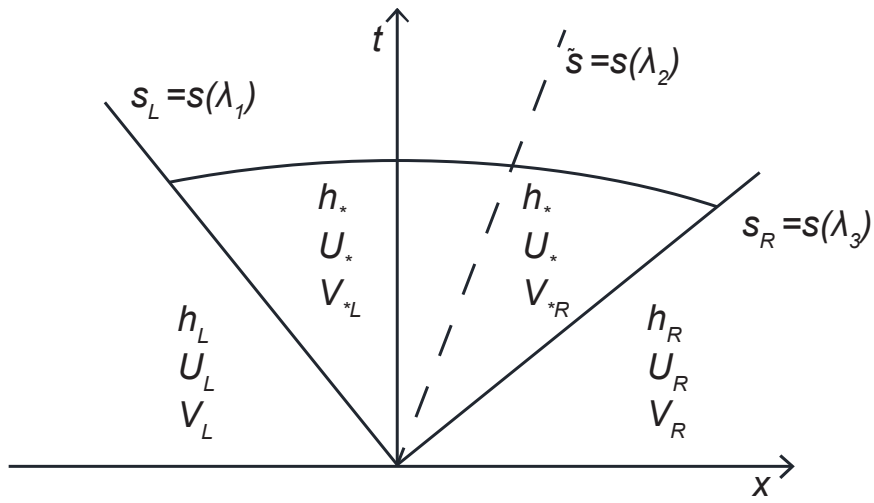


Figure 3.6: Riemann Problem sketch on  $(x, t)$  plane (modified from [34]).

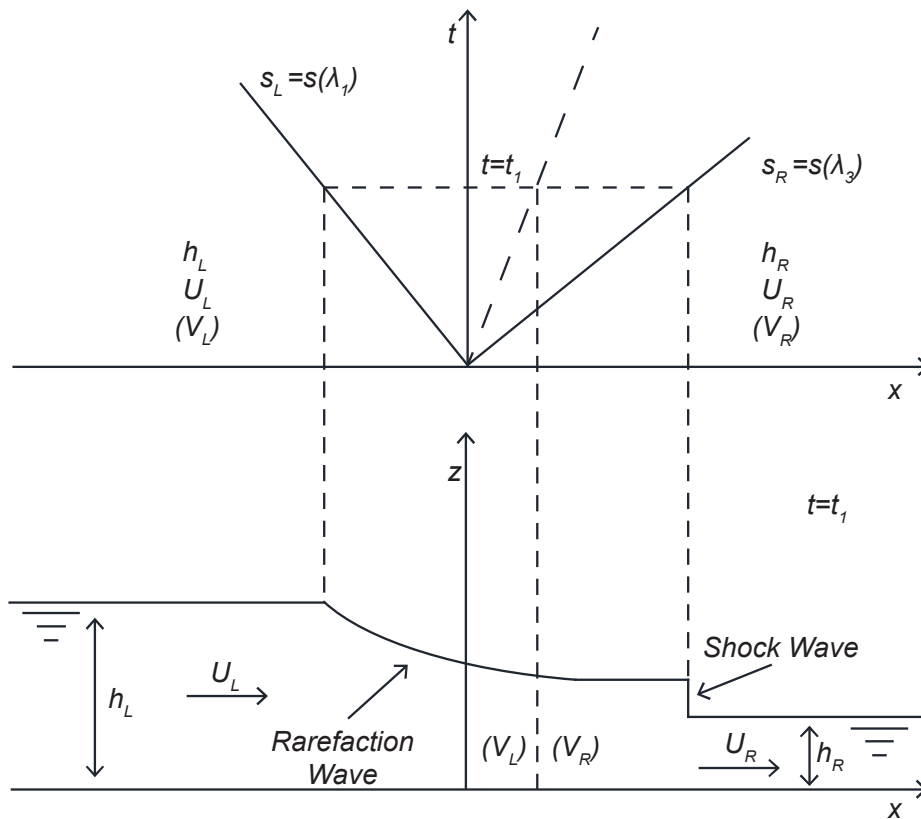


Figure 3.7: Graphical example of the solution of a generic Riemann problem at  $t = t_1$  (modified from [34]).

region. In particular, intercell flux can be alternatively

$$\mathbf{U}^{hllc} = \begin{cases} \mathbf{U}_L & 0 \leq S_L \\ \mathbf{U}_{*L}^{hllc} & S_L \leq 0 \leq \tilde{S} \\ \mathbf{U}_{*R}^{hllc} & \tilde{S} \leq 0 \leq S_R \\ \mathbf{U}_R & 0 \geq S_R. \end{cases} \quad (3.38)$$

It should be noted that star-left and star-right regions are separated by a shear waves and for this reason their state differs only for the third component: shear velocity  $V$  can be thus either  $V_L$  or  $V_R$ . We can write

$$\mathbf{U}_{*L}^{hllc} = \begin{pmatrix} h_* \\ U_* h_* \\ V_L h_* \end{pmatrix} \quad (3.39)$$

and

$$\mathbf{U}_{*R}^{hllc} = \begin{pmatrix} h_* \\ U_* h_* \\ V_R h_* \end{pmatrix} \quad (3.40)$$

Therefore, intercell flux can be alternatively

$$\mathbf{F}_c^{hllc} = \begin{cases} \mathbf{F}_L & 0 \leq S_L \\ \mathbf{F}_{*L}^{hllc} & S_L \leq 0 \leq \tilde{S} \\ \mathbf{F}_{*R}^{hllc} & \tilde{S} \leq 0 \leq S_R \\ \mathbf{F}_R & 0 \geq S_R \end{cases} \quad (3.41)$$

The solution proposed by HLLC method is obtained by integration Euler equation in  $(x, t)$  plane.

From equation (3.37), Fluxes in left-star and right-star regions are written as

$$\begin{cases} \mathbf{F}_{*L}^{hllc} = \mathbf{F}_L + S_L (\mathbf{U}_{*L}^{hllc} - \mathbf{U}_L) \\ \mathbf{F}_{*R}^{hllc} = \mathbf{F}_R + S_R (\mathbf{U}_{*R}^{hllc} - \mathbf{U}_R) \end{cases} \quad (3.42)$$

We consider for hypothesis  $\tilde{S} = U_*$  and we develop first component of equations (3.42). In this way,  $h^*$  is obtained and for each  $K = L, R$  the variable vector  $\mathbf{U}_{*K}^{hllc}$  becomes:

$$\mathbf{U}_{*K}^{hllc} = \begin{pmatrix} h_* = h_K \frac{(S_K - U_K)}{S_K - \tilde{S}} \\ U_* h_* = h_K \frac{(S_K - U_K)}{S_K - \tilde{S}} \tilde{S} \\ V_K h_* = h_K \frac{(S_K - U_K)}{S_K - \tilde{S}} V_K \end{pmatrix} \quad (3.43)$$

Fluxes  $\mathbf{F}_{*K}^{hllc}$  are thus computed substituting (3.43) into 3.42.

An approximated formula has been proposed for the calculation of  $\tilde{S}$ :

$$\tilde{S} = \frac{S_L h_R (U_R - S_R) - S_R h_L (U_L - S_L)}{h_R (U_R - S_R) - h_L (U_L - S_L)}. \quad (3.44)$$

$S_L$  and  $S_R$  propagation velocities are finally computed using Godunov analytical theory. In particular, he demonstrated that

$$S_R = \begin{cases} U_R + \sqrt{g\bar{h}} \sqrt{\frac{h_*(h_R + h_*)}{2h_R^2}} & h_* > h_R \quad (\text{shock}) \\ U_R + \sqrt{g\bar{h}} & h_* < h_R \quad (\text{rarefaction}) \end{cases} \quad (3.45)$$

and

$$S_L = \begin{cases} U_L - \sqrt{gh} \sqrt{\frac{h_*(h_L+h_*)}{2h_L^2}} & h_* > h_L \quad (\text{shock}) \\ U_L - \sqrt{gh} & h_* < h_L \quad (\text{rarefaction}) \end{cases}. \quad (3.46)$$

In case of dry-bed Riemann problem (said Ritter problem), a rarefaction wave propagates upstream with typical rarefaction celerity, while a so called *contact discontinuity* moves along the dry bed with celerity  $S_{0K}$ . We distinguish right and left dry-bed. In case of right dry-bed, celerities are demonstrated to be

$$\begin{aligned} S_L &= U_L - \sqrt{gh_L} \\ S_R &= U_L + 2\sqrt{gh_L} \end{aligned}. \quad (3.47)$$

Otherwise, in case of left dry-bed propagation we have

$$\begin{aligned} S_{0L} &= U_R - 2\sqrt{gh_R} \\ S_R &= U_R + \sqrt{gh_R} \end{aligned}. \quad (3.48)$$

The Riemann problem is solved for each side of the considered cell. *Left* state corresponds to the cell state, while *Right* state corresponds, for each side, to the respective adjacent cell state at a considered time-step.

### Correction scheme for the Conservation-property

A scheme satisfies the *Conservation-property* (C-property) regarding the stationary solution of a fluid at rest if it is able to describe it exactly (or with a proper accuracy) when applied [63].

As previously discussed, Riemann problem considers inviscid fluid on horizontal bottom: thus, both the presence of resistance and the bottom slope causes the solution not to be exact. In particular, in presence of bed slope the classic approach to the Riemann problem gives rise to spurious flows which are not compensated by the slope effect component in the source term. Thus, bed slope does not allow the scheme to respect the C-property.

Consider the problem in Figure 3.8. The water is at rest and the solution of the problem in each cell is given in term of  $h$  (while  $Uh = Vh = 0$ ). The bed slope is interpreted by the numerical scheme as a step between region  $L$  and region  $R$ : cell-averaged data are in fact considered.

Solving the Riemann problem between  $L$  and  $R$  states comparing water depths, the difference between  $h_L$  and  $h_R$  is interpreted as a difference in water level, causing the propagation of a wave rightward: this is of course meaningless because for hypothesis we have

$$\eta_L = \eta_R = \eta \quad (3.49)$$

and the water level is horizontal.

Thus, a fictitious flux is generated from cell  $L$  to cell  $R$ . The numerical scheme corrects this analytical solution by the effect of the source term  $gh \frac{\partial z_b}{\partial x}$ , which is however not able to totally offset the effect of such flux. The balance is thus guaranteed by a consequent water level increase in  $R$  and the solution of the water at rest is not respected.

In order to solve this particular problem, Audusse et al. proposed an alternative scheme which considers an interface hydrostatic reconstruction [2].

Let us focus on the intercell between  $L$  and  $R$  in Figure 3.9. We consider the bottom at intercell ( $z_{i+\frac{1}{2}}$ ) to be

$$z_{i+\frac{1}{2}} = \max(z_L, z_R). \quad (3.50)$$

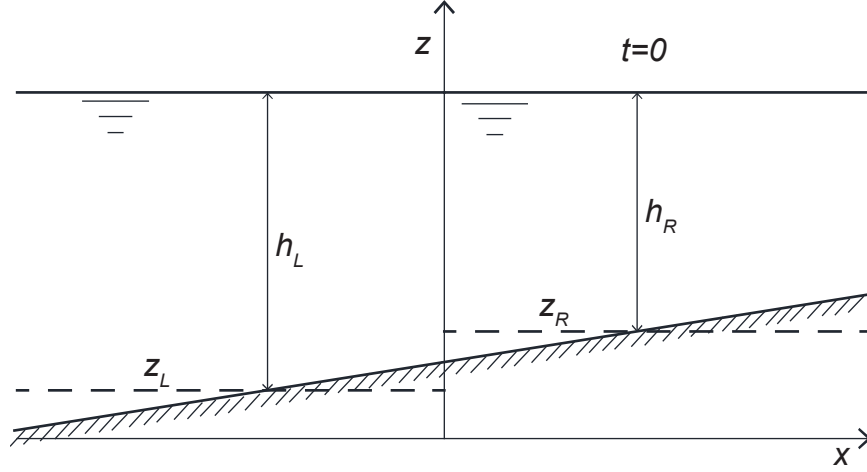


Figure 3.8: Riemann problem at rest on non-horizontal bottom.

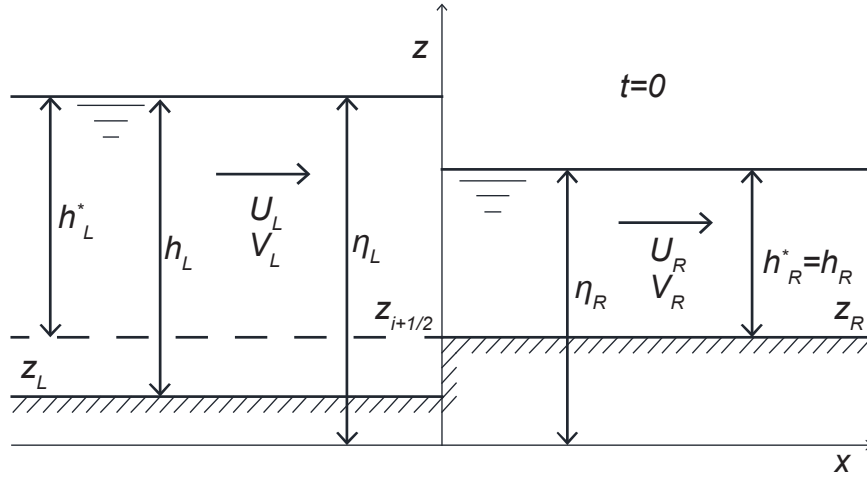


Figure 3.9: C-property correction scheme in case of non-horizontal bottom.

The water depth is then calculated from the water level. In particular for  $L$  and  $R$  states we have

$$h_L^* = \max\left(\eta_L - z_{i+\frac{1}{2}}, 0\right) \quad (3.51)$$

$$h_R^* = \max\left(\eta_R - z_{i+\frac{1}{2}}, 0\right) \quad (3.52)$$

where  $\eta_L = z_L + h_L$  and  $\eta_R = z_R + h_R$ . Thus, fluxes become  $Uh_L^*$  and  $Uh_R^*$ .

The Riemann problem is hence solved using corrected left and right states

$$L^* = (\eta_L, h_L^*, U_L, Uh_L^*, V_L) \quad (3.53)$$

and

$$R^* = (\eta_R, h_R^*, U_R, Uh_R^*, V_R). \quad (3.54)$$

The fluxes  $\mathbf{F}_{c, i+\frac{1}{2}}^*$  are thus obtained by  $L^*$  and  $R^*$  using HLLC solutor as discussed above.

In order to guarantee coherence with this approach, the slope effect should be considered in intercell fluxes computation. Thus, Audusse et al. proposed to correct them with a

proper correction of the flux term which takes into account the hydrostatic pressure on the bottom step. The second term of  $\mathbf{F}_{c_{i+\frac{1}{2}}}$  becomes

$$\mathbf{F}_{c_{i+\frac{1}{2},2}} = \mathbf{F}_{c_{i+\frac{1}{2},2}}^* - \frac{g}{2} (h_L^{*2} - h_L^2). \quad (3.55)$$

Applying the scheme to the stationary solution at rest in Figure 3.8, the left and right water depth  $h^*$  at intercell become

$$h_L^* = h_R^* = h_R. \quad (3.56)$$

The advective flux at intercell is thus

$$\mathbf{F}_{c_{i+\frac{1}{2}}}^* = \begin{pmatrix} 0 \\ g \frac{h_R^2}{2} \\ 0 \end{pmatrix} \quad (3.57)$$

and, considering the slope effect, it is corrected as

$$\mathbf{F}_{c_{i+\frac{1}{2}}} = \begin{pmatrix} 0 \\ g \frac{h_L^2}{2} \\ 0 \end{pmatrix} \quad (3.58)$$

Computing the advective flux in a similar way at each intercell of  $L$ , the hydrostatic pressure results at each side equal to  $g \frac{h_L^2}{2}$  and the water at rest condition is thus respected.

### Computation of intercell viscous fluxes

As written above, the viscous fluxes are characterised by rotational invariance. Thus, also turbulence terms can be studied using the 1D-augmented approach. In particular, given a quadrangular cell, integrating the  $x$  and  $y$  derivatives of viscous fluxes we obtain:

$$\int_{\Omega} \frac{\partial (\mathbf{F}_v)}{\partial x} d\Omega + \int_{\Omega} \frac{\partial (\mathbf{G}_v)}{\partial y} d\Omega = \oint_{\partial\Omega} (\mathbf{H}_v \cdot \vec{n}) ds = \sum_{k=1}^N \mathbf{T}_k^{-1} \mathbf{F}_{vk} \Delta l_k \quad (3.59)$$

where  $\mathbf{H}_v = [\mathbf{F}_v, \mathbf{G}_v]$  and  $\mathbf{F}_{vk} = \check{\mathbf{F}}_{vk} (\hat{\mathbf{U}}_k)$  is the integral averaged viscous flux on side  $k$  in local coordinates:

$$\mathbf{F}_{vk} = \begin{pmatrix} 0 \\ 2\nu_T h \frac{\partial \hat{U}_k}{\partial \hat{x}} \\ \nu_T h \left( \frac{\partial \hat{U}_k}{\partial \hat{y}} + \frac{\partial \hat{V}_k}{\partial \hat{x}} \right) \end{pmatrix} \quad (3.60)$$

where  $(\hat{x}, \hat{y}, \hat{z}) = \mathbf{T}_k(x, y, z)$  is the local coordinates system and  $\mathbf{T}_k$  is the rotational matrix relative to side  $k$  of the considered cell.  $\hat{U}_k$  and  $\hat{V}_k$  are then  $\hat{x}$  and  $\hat{y}$  components of the depth-averaged velocity vector. Finally, the eddy viscosity  $\nu_T$  is constant on the cell.

The computation of derivatives in viscous fluxes vector is here obtained with a finite difference scheme. In particular, let us consider the simplified problem in Figure 3.10. The  $\hat{y}$ -derivative is assumed vanish, being particularly difficult to be evaluated at cell sides. The  $\hat{x}$ -derivatives are computed by I-order finite difference scheme, involving the adjacent

cell along  $k$  side. Considering cell  $i$  and the adjacent  $k$ -sided cell  $i+1$ , the derivative at correspondent intercell is:

$$\frac{\partial \hat{U}_k}{\partial \hat{x}_{i,k}} = \frac{\hat{U}_{i+1,k} - \hat{U}_{i,k}}{\Delta x_{i,k}} \quad (3.61)$$

$$\frac{\partial \hat{V}_k}{\partial \hat{x}_{i,k}} = \frac{\hat{V}_{i+1,k} - \hat{V}_{i,k}}{\Delta x_{i,k}} \quad (3.62)$$

where  $\hat{U}_{i,k}$  and  $\hat{V}_{i,k}$  are local-system components of the flow on cell  $i$ ,  $\hat{U}_{i+1,k}$  and  $\hat{V}_{i+1,k}$  are local system components of the flow on cell  $i+1$  and  $\Delta x_{i,k}$  is the distance between  $i$  and  $i+1$  cell centres.

The depth-averaged  $h$  is computed as the average value between  $h_i$  and  $h_{i+1}$ .

The eddy viscosity is finally computed for each cell as discussed above.

In case Smagorinsky model is used for the computation of  $\nu_T$ , a simplified scheme has been implemented for the computation of central velocity vector derivatives is here used. Consider a cell  $i$ . We assume  $i$  and its neighbouring cells to be rectangular. In this way, two orthogonal axis can be defined connecting cell centres (Figure 3.11). Thus, a local Cartesian system, cell-oriented, is obtained. In particular, if sides of cell  $i$  are numbered from 1 to 4, let us consider as  $\check{x}$ -axis, the line which connects the centre of cell  $i$  with centres of adjacent cells at first and third sides, and as  $\check{y}$ -axis, the line which connects the centre of cell  $i$  with centres of adjacent cells at second and fourth sides. Velocity vector  $\bar{U}_i$  is thus rotate becoming

$$\check{U}_i = \mathbf{T}'_i \bar{U}_i \quad (3.63)$$

where  $\mathbf{T}'$  is the correspondent rotation matrix. Being  $i-1$  and  $i+1$  neighbour cells along  $\check{x}$ ,  $j+1$  and  $j-1$  neighbour cells along  $\check{y}$  and  $dl_{i,k}$  the distances between centers of cells  $i$  and  $k$ , derivatives of  $\check{U}$  can be computed as

$$\left. \frac{\partial \check{U}}{\partial x} \right|_i = 0.5 \left( \frac{\check{U}_{i+1} - \check{U}_i}{dl_{i,i+1}} + \frac{\check{U}_i - \check{U}_{i-1}}{dl_{i,i-1}} \right) \quad (3.64)$$

$$\left. \frac{\partial \check{U}}{\partial y} \right|_i = 0.5 \left( \frac{\check{U}_{j+1} - \check{U}_i}{dl_{i,j+1}} + \frac{\check{U}_i - \check{U}_{j-1}}{dl_{i,j-1}} \right) \quad (3.65)$$

$$\left. \frac{\partial \check{V}}{\partial x} \right|_i = 0.5 \left( \frac{\check{V}_{i+1} - \check{V}_i}{dl_{i,i+1}} + \frac{\check{V}_i - \check{V}_{i-1}}{dl_{i,i-1}} \right) \quad (3.66)$$

$$\left. \frac{\partial \check{V}}{\partial y} \right|_i = 0.5 \left( \frac{\check{V}_{j+1} - \check{V}_i}{dl_{i,j+1}} + \frac{\check{V}_i - \check{V}_{j-1}}{dl_{i,j-1}} \right) \quad (3.67)$$

In case of rectangular cells, this scheme is II-order accurate in space.

In case of irregular quadrangular cells, a different rotation matrix  $\mathbf{T}'$  is used for each considered side, correspondent to the  $k$ -sided rotation matrix  $\mathbf{T}_{i,k}$  (as defined in equation (3.26)): we thus approximate the local coordinate velocity vector as

$$\check{U}_i = 0.5 (\mathbf{T}_{i,1} \bar{U}_i - \mathbf{T}_{i,3} \bar{U}_i) = 0.5 (\hat{U}_{i,1} - \hat{U}_{i,3}) \quad (3.68)$$

for computation of  $\check{x}$ -derivatives and as

$$\check{U}_i = 0.5 (\mathbf{T}_{i,2} \bar{U}_i - \mathbf{T}_{i,4} \bar{U}_i) = 0.5 (\hat{U}_{i,2} - \hat{U}_{i,4}) \quad (3.69)$$

for  $\check{y}$ -derivatives.

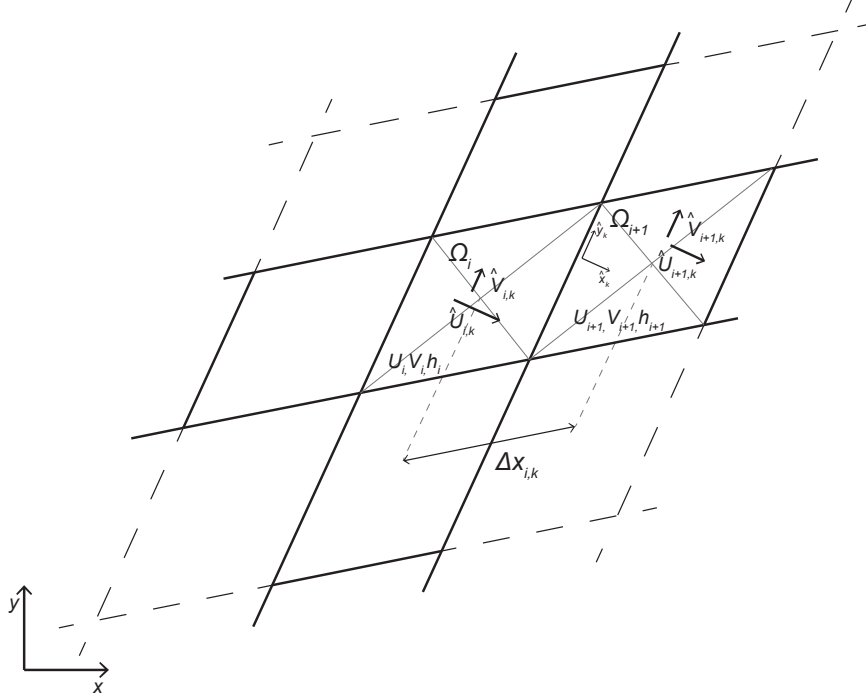


Figure 3.10: Viscous fluxes computation sketch.

Velocity derivatives are finally computed as

$$\left. \frac{\partial \check{U}}{\partial x} \right|_i = 0.5 \left( \frac{\hat{U}_{i+1,1} - \hat{U}_{i,1}}{dl_{i,i+1}} + \frac{\hat{U}_{i-1,3} - \hat{U}_{i,3}}{dl_{i,i-1}} \right) \quad (3.70)$$

$$\left. \frac{\partial \check{U}}{\partial y} \right|_i = 0.5 \left( \frac{\hat{V}_{j+1,2} - \hat{V}_{i,2}}{dl_{i,j+1}} + \frac{\hat{V}_{j-1,4} - \hat{V}_{j,4}}{dl_{i,j-1}} \right) \quad (3.71)$$

$$\left. \frac{\partial \check{V}}{\partial x} \right|_i = 0.5 \left( \frac{\hat{V}_{i+1,1} - \hat{V}_{i,1}}{dl_{i,i+1}} + \frac{\hat{V}_{i-1,3} - \hat{V}_{i,3}}{dl_{i,i-1}} \right) \quad (3.72)$$

$$\left. \frac{\partial \check{V}}{\partial y} \right|_i = 0.5 \left( \frac{\hat{U}_{j+1,2} - \hat{U}_{i,2}}{dl_{i,j+1}} + \frac{\hat{U}_{j-1,4} - \hat{U}_{j,4}}{dl_{i,j-1}} \right) \quad (3.73)$$

where  $\hat{U}_{i,k} = \mathbf{T}_{i,k} \bar{U}_i$ . In should here be noticed that verse of  $\hat{U}_{i,k}$ , for definition of  $\mathbf{T}_{i,k}$ , is outgoing respect to the cell.

Although this scheme is not rigorous, it seems to give good results, as we will observe in validation tests. The same scheme here described is used for the computation of velocity vector derivatives for the calculation of Smagorinskii eddy viscosity.

Secondary flow effects on suspended sediments are here not considered: in fact, they are strictly related to the secondary flow vertical velocity distribution, which can't be approximated by a depth-averaged value.

### The time derivative and the source term

Riemann problem does not involve source terms, which are computed separately and inserted in the solution of time derivative.

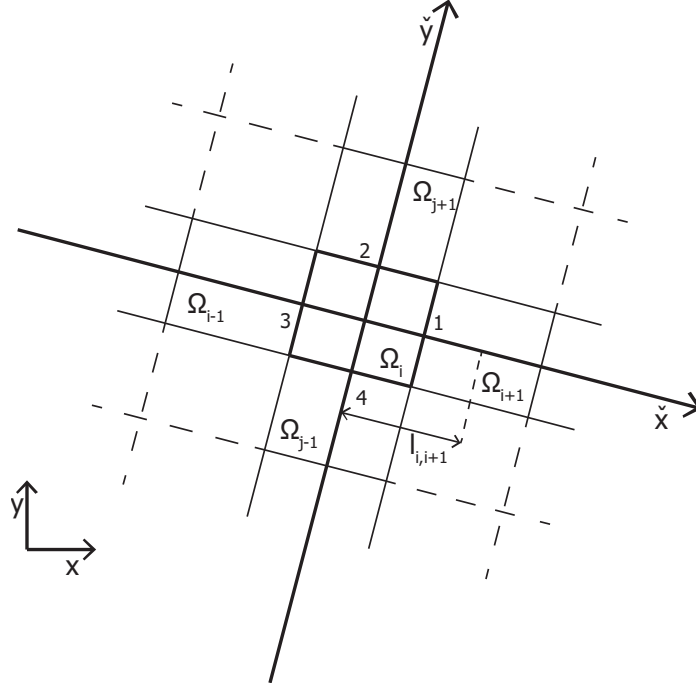


Figure 3.11: Simplified scheme for the computation of velocity derivatives in secondary currents algorithm.

In the present model *Strang Splitting* technique is used, with a I-order in time accurate scheme. The following steps are done:

1. 
$$\begin{cases} \frac{\partial \check{U}}{\partial t} + \frac{\partial \check{F}}{\partial x} = 0 \\ \check{U}(x, t_n) = U^n \end{cases} \xrightarrow{\Delta t} U^{adv} \quad (3.74)$$

2. 
$$\begin{cases} \frac{d\check{U}}{dt} = \check{S}(\check{U}) \\ \check{U}(x, t_n) = U^{adv} \end{cases} \xrightarrow{\Delta t} \check{U}^{n+1}. \quad (3.75)$$

Let us consider a cell  $i$  with solution  $U_i^n$  at time-step  $n$ . We consider cell-averaged variables  $U_i^n = \check{U}(\Omega_i, t_n)$ .

The solution of DAM\_HYD model in cell  $i$  at time-step  $n+1$  is then:

$$\begin{aligned} U_i^{adv} &= U_i^n - \Delta t \left\{ \sum_{k=1}^4 T_{k,i}^{-1} [F_{v_k}^n + F_{v_k}^n] \Delta l_{k,i} \right\} \\ U_i^{n+1} &= U_i^{adv} + \Delta t S(U_i^{adv}) \end{aligned} \quad (3.76)$$

where  $\Delta t$  is the time-step.

The scheme here proposed is explicit, and, from stability analysis of Riemann problem, it is demonstrated to be stable only if Courant Friedrichs Lewy condition is satisfied [18].

Courant Friedrichs Lewy condition (CFL) requires that, in each cell, the wave propagation speed is lower than so called *grid speed* ( $l/\Delta t$ ). In particular, we refers to Courant

number  $C_{CFL}$ , defined as

$$C_{CFL} = \frac{\lambda_{CFL} \Delta t}{l_c} \quad (3.77)$$

where  $\lambda_{CFL}$  is the maximum wave propagation speed and  $l$  is the characteristic length of the cell (for example,  $l_c = \sqrt{\Omega}$ ). CFL condition is respected if

$$C_{CFL} \leq 1. \quad (3.78)$$

A more adequate range for the Courant number, able to guarantee stability in presence of turbulence or in case of morphodynamic computations, is  $C_{CFL} = 0.4 \div 0.8$ .

### Initial and boundary Conditions

In order to solve the hydrodynamic problem, initial and boundary conditions have to be set.

Initial conditions have to be imposed in the whole domain. Hydrodynamic initial conditions corresponds to the values of  $h_i$ ,  $U_i$  and  $V_i$  in each  $i$ -cell at initial instant.

Boundary conditions are needed at the boundaries of the domain. Boundary conditions work as *ghost cells* bounded to the boundary cells. Ghost cells behave as normal cells and permits the computation of intercell fluxes at the boundary. Different conditions have been developed in the DAM\_HYD, which are suited for coastal areas. In particular they are:

- WALL CONDITION: no flux across the boundary is permitted;
- CINEMATIC CONDITION: the water level and the velocity of the ghost cell are equal to those of correspondent boundary cell. In this way, free outflow is guaranteed;
- IMPOSED WATER FLOW CONDITION: the water flow ( $q = [q_x, q_y] = [Uh, Vh]$ ) is imposed in the ghost cell. Water level is obtained by uniform flow law;
- TIDAL BOUNDARY CONDITION: tidal effect are simulated at the boundary. Water level is imposed, while flow is obtained by characteristics method, as proposed by Sleigh et al. [41].

Moreover, all forcing terms must be set at each cell at each time-step: in particular, in the more general case, the following data are given:

- THE WIND FIELD AND THE CORRESPONDENT DRAG FACTOR (if wind is considered);
- THE WAVE FIELD (if waves are considered);
- THE WAVE RADIATION STRESS FIELD (if waves and radiation stress are considered).

They can be alternatively constant or variable in time.

## 3.2 The sediment transport module

In the sediment transport module, bed and suspended granular sediment transport and cohesive sediment transport are computed.

As widely discussed in Chapter 2, two main approaches can be chosen: the use of equilibrium formulas, which are available for granular bed and suspended load, and the solution of an advective-diffusive equation, which is needed for cohesive sediment transport and is

preferred for granular suspended load too. Finally, morphological evolution is obtained by the solution of the sediment balance at the bottom in each cell.

The module is based on FVM scheme, coherently with hydrodynamic solution: in each time-step, sediment transport and morphological computations are based on hydrodynamic solution at previous time-step.

Cohesive and granular sediment transport are considered totally independent either in the advective-diffusive problem and in the bottom evolution problem.

In order to compute both equilibrium sediment transport load and erosion and deposition terms in advective-diffusive equations at cell  $i$  and time-step  $n+1$ , the vector  $U_i^n$  is required: sediment load and erosion-deposition rates are cell-centred and are considered constant in each cell. In presence of waves, for each cell four more variables are taken into account: the bottom orbital wave velocity  $U_{1m,i}^n$ , the (significant) wave height  $H_i^n$ , the (significant) wave period  $T_{w,i}^n$  and the wave direction  $\Theta_i^n$ .

The module is divided in three stages:

- computation of granular sediment transport;
- computation of cohesive sediment transport;
- solution of bed continuity equation.

As we will discuss later, a proper *morphological factor* is available, which amplifies morphological evolution and let to preview middle and long term evolution with short-period simulations.

Moreover, *secondary flow* and *avalanching* effects can be taken into account.

Secondary flows are given by the vortex motion of water in circular motion. Secondary flow can have great influence in presence of bents and meanders. Because of their nature, depth averaged models can't describe the 3-dimensional structure of a vortex motion, however theories about resulting bed shear stress have been presented in literature and can be useful, in particular for bed load computation.

Avalanching is a geotechnical phenomena related to the slope instability. Generally, lateral slopes can't have an excessive steepness and sediments begin to avalanche when the slope is greater than sediment repose angle, as defined in Section 2.1. For cohesive sediments, presence of cohesion causes the process to be more complicate, and deep studies about slope stability should be required. However, a simple avalanching algorithm, based on an equivalent repose angle, is here presented.

In next subsections, equilibrium and non-equilibrium sediment loads computation and morphological evolution computations are described, with particular regard to the numerical implementation.

### 3.2.1 Computation of granular sediment transport

Granular sediment transport modelling is divided into bed load and suspend load computation. For bed load several equilibrium formulas are available, while for suspended load alternatively equilibrium formulas use or advective-diffusion equation resolution can be used.

A little data are required for the description of considered granular sediments, regarding the grains property ( grain diameter  $d_{50}$  and grain density  $\rho_s$ ) and the bed characteristics ( bed friction angle  $\Phi_i$  and bed porosity  $n_{por}$ ).

In order to solve granular sediment transport problem, particular attention is given to the computation of bed shear stress. In fact, as discussed in Chapter 2, granular sediment transport is not associated to the global bed shear stress, computed in hydrodynamic module, but to grain-related bed shear stress. Thus, both current-alone and wave-alone bed shear stresses are here computed from the grain-related roughness  $\varepsilon'$ , which is considered to be equal to  $2.5 d_{50}$ , as proposed by Nielsen (see Subsection 2.2.1). Grain-related bed shear stress does not require a new Manning coefficient:  $\tau'_{bc}$  is in fact computed using equation

$$\tau'_{bc} = \rho C'_D \sqrt{U^2 + V^2} \quad (3.79)$$

where drag coefficient  $C'_D$  is obtained by  $\varepsilon'$  as

$$C'_D = \left[ \frac{\kappa}{1 + \ln(\varepsilon' / (30h))} \right]^2. \quad (3.80)$$

Moreover, in presence of waves, Soulsby method is applied for the computation of grain-related wave-current bed shear stress, using the same theory applied in the hydrodynamic module.

Critical Shields parameter is obtained in each cell by equation (2.13), proposed by Soulsby and Whitehouse, and slope influence is taken into account considering Schoktlitsch and Leiner factors (equations (2.15) and (2.16)), respectively for slopes parallel and perpendicular to the flow.

Grain-related fall velocity is dependent on grain diameter and is thus constant for the whole domain and simulation duration. In the present model, Soulsby fall velocity formula (2.65) is implemented.

The use of equilibrium formulas in 2D models needs some considerations. Such theories, in fact, have been generally carried out from flume experiments and, thus, are essentially 1D. In the present model, they are considered to represent the sediment load towards the flow velocity direction. The resulting load is thus decomposed in  $x$  and  $y$  directions using flow velocity versors.

## Bed load

Considering bed load, 7 different theories have been implemented. Particular attention is given to approaches which consider both current and wave effects, as discussed in Subsection 2.2.2. Theories considered are:

- **NO BED LOAD:** in this case the term is not taken into account.
- **MEYER-PETER AND MÜLLER.** The theory is the result of one of first studies on current-alone sediment transport and generally imposes the value of critical Shields parameter ( $\theta_{crit} = 0.047$ , see equation (2.21)). Here, the possibility of using computed Shields parameter is also given.
- **VAN RIJN FOR CURRENT (1984).** The original formula proposed by Van Rijn. As for Meyer-Peter and Müller formula, no waves are considered (see equation (2.25)). However, mean bed shear stress  $\tau_m$  is used for computation of the dimensionless bed-shear stress parameter  $T$  and, thus, wave effect is anyway taken into account.
- **VAN RIJN FOR WAVE AND CURRENT (1993).** The second Van Rijn's formula is derived from the previous one and is considered valid also in presence of waves (equation (2.28)).

- VAN RIJN APPROXIMATED METHODS (2001). Two more formulas proposed from Van Rijn are available, valid respectively for instantaneous and mean wave-current bed load (equations (2.29) and (2.30)). In the present model, only mean wave field is considered and both these formulas are applied to the mean bed shear stress.
- VAN RIJN AND SOULSBY (1997). One more considered criterion is that of Van Rijn and Soulsby, which is derived from Grass original approach and pretends to consider both wave and current effects (equation (2.38)).
- SOULSBY (1997). The last criterion uses Soulsby formula for bed load transport (equations (2.33) and (2.35)).

Bed load, as discussed in previous chapter, involves mainly heavy sediments and it is important for large diameter sediment class. In coastal areas,  $d_{50}$  is generally quite small (0.060 ÷ 0.300 mm) and the bed load have small influence on general sediment transport dynamics. However, the choice of criterion can have a significant influence on the final result of simulations, as evident in the test illustrated in Figure 3.12. Here, different bed load formulas are compared in describing the evolution of a trench under an imposed current ( $U = 0.5$  m/s,  $h = 0.39$  m,  $d_{50} = 0.3$  mm) after 5 hours of simulation. Changing methods, the migration effect of upstream slope results to be quite different: Soulsby formula, for example, appears to magnify the migration of the trench and the erosion of the downstream slope with respect to Meyer-Peter and Müller and Van Rijn formulas.

### Suspended load

Computation of suspended load can be done using alternatively an equilibrium approach or a non-equilibrium approach.

In the first case, two methods are here implemented. As for bed load formulas, such theories are generally 1D and are considered valid for flow-directed suspended load.

In the second case, an advective-diffusive equation is coupled to the hydrodynamic problem.

All models here cited are illustrated in Chapter 2: the following possibilities are thus available:

- NO SUSPENDED LOAD: in this case the term is not taken into account;
- VAN RIJN FORMULA FOR WAVE AND CURRENT (2001): the formula is the adaptation to wave and current case of the original Van Rijn criterion [56]. Equilibrium Rouse concentration profile is considered, with a vertical sediment diffusivity able to comprehend current and wave effects (see equation (2.66));
- VAN RIJN AND SOULSBY (1997): Van Rijn and Soulsby formula for suspended load is analogous to that one for bed load, as discussed in Chapter 2 (equation (2.70));
- NON-EQUILIBRIUM APPROACH: horizontal depth-averaged concentration distribution is studied and different methods for erosion-deposition rate computation are proposed.

The choice of using an equilibrium or a non-equilibrium method for the computation of suspended load has a great influence in simulation results. As previously discussed, non-equilibrium methods are able to describe the concentration fluxes into the domain and generally are considered more accurate. In order to understand the different behaviour between

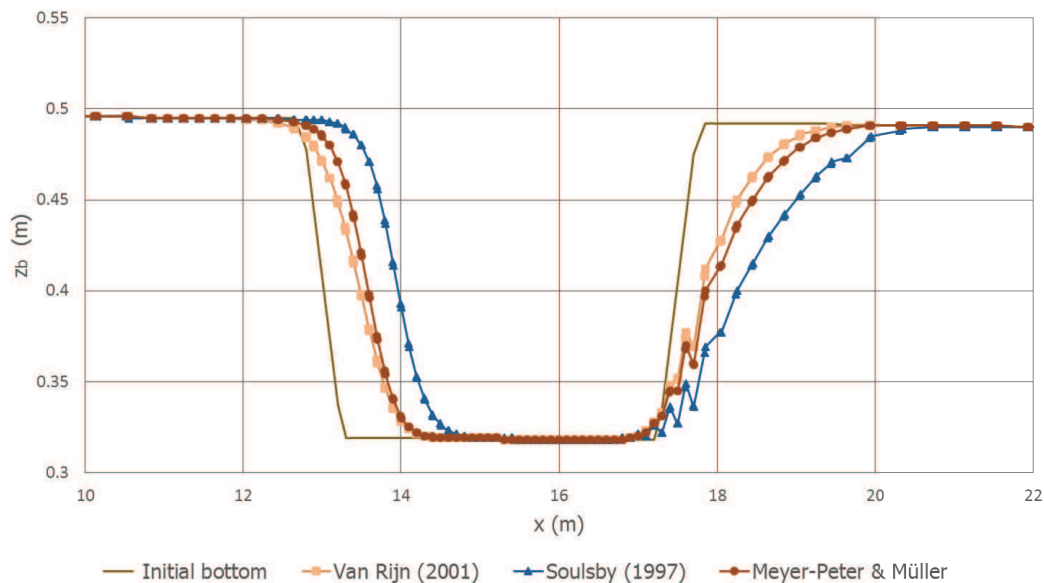


Figure 3.12: Comparison of different bed load formulas in a trench under steady current ( $T_{sim} = 5$  h,  $d_{50} = 0.3$  mm,  $U = 0.5$  m/s,  $h = 0.39$  m): no suspended load considered.

these approaches, consider the test illustrated in Figure 3.13, similar to the previous one. In this graphic, Van Rijn equilibrium formula is compared with non-equilibrium approach. You should note the differences in the shape of sediment deposit: because of the adaptation length needed by advective diffusive equation to reach a concentration equilibrium, the migration effect seems to be less evident, while the trench has been gradually infilled. As we will discuss in next chapters, this is coherent with experimental results.

### Reference level and reference concentration

As pointed out in Chapter 2, the reference level  $a$  is the level at which suspended sediment volume begin. It is thus particularly important for the computation of equilibrium or non-equilibrium suspended load.

Theoretical concentration distributions have in fact an asymptotic behaviour close to the bottom and, changing  $a$ , the total volume of involved sediment in each cell totally changes. In particular, the smaller is  $a$ , the quicker the morphological evolution tends to be.

In the present model different methods for the computation of  $a$  are proposed:

- $a$  AS AN IMPOSED PERCENTILE OF THE WATER DEPTH:  $a = a_{\%} h$  where  $a_{\%}$  is a percentile imposed by the user;
- $a$  AS THE GLOBAL ROUGHNESS:  $a = \max(\varepsilon, 0.02)$ , where the lower limit is suggested by Van Rijn [61];
- $a$  AS A FRACTION OF THE BEDFORMS HEIGHT: proposed by Van Rijn in order to take into account the effects of current and wave ripples. Further details in [44, 59];
- $a$  IMPOSED BY THE OPERATOR:  $a = a_{val}$ .

The first three cases associate  $a$  to hydrodynamic conditions: in this way, the influence of operator choice is limited. However, great attention is needed in setting  $a$  and a calibration process is often required. Consider, from a qualitatively point of view, trench test in

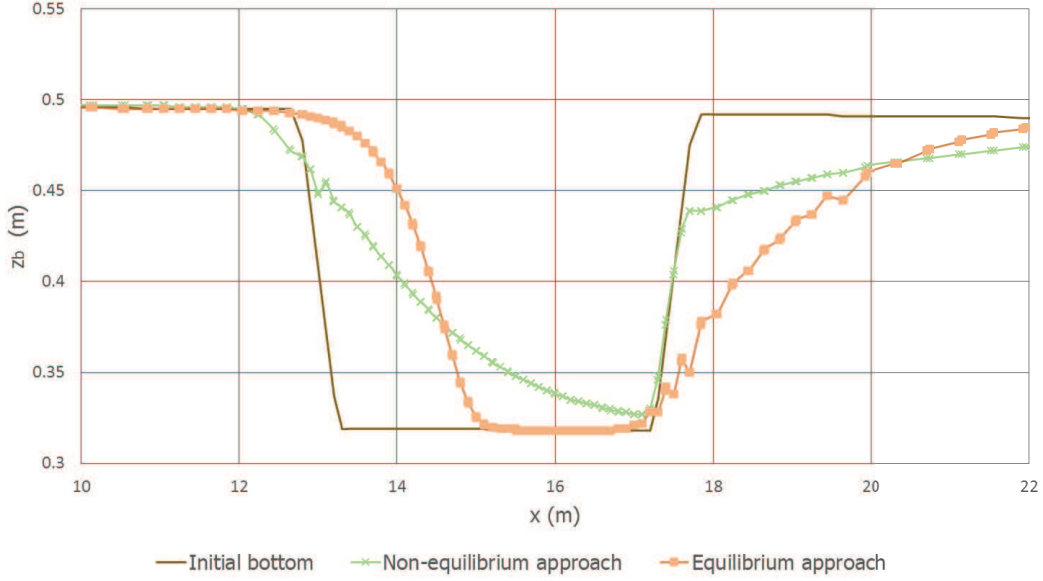


Figure 3.13: Comparison of equilibrium and non-equilibrium approaches in suspended load computation. Trench under steady current ( $T_{sim} = 5$  h,  $d_{50} = 0.160$  mm,  $U = 0.5$  m/s,  $h = 0.39$  m,  $a = 0.025$  m): no bed load considered.

Figure 3.14. The test compares different values of  $a$  for the computation of a trench evolution under steady current: changing  $a$ , the effects on the trench profile given by the same morphological problem is more or less magnified: in fact, the smallest is  $a$ , the most amplified is morphological evolution. For this reason,  $a$  is considered one of the most sensible calibration factors in sediment transport problems.

The reference concentration  $c_a$  is here computed with the widely known Van Rijn formula (equation (2.62)), with a higher limit imposed as  $c_a = 0.05$ .

### Advective-diffusive equation

Advective-diffusive equation is solved with the same FVM, I-order method used for hydrodynamic module (see equation (3.76)). Consider the depth-averaged concentration advective-diffusive equation:

$$\frac{\partial Ch}{\partial t} + \frac{\partial UCh}{\partial x} + \frac{\partial VCh}{\partial y} - \epsilon_H h \left[ \frac{\partial}{\partial x} \left( \frac{\partial C}{\partial x} \right) + \frac{\partial}{\partial y} \left( \frac{\partial C}{\partial y} \right) \right] + ED. \quad (3.81)$$

Here, the depth-averaged concentration is a scalar transported by water flow. It can thus be considered as the fourth equation of system (3.1). Considering in particular  $C_{gran}$ , for a cell  $i$  at instant  $n$ , equation (2.73) is discretized as

$$(C_{gran}h)_i^{adv} = (C_{gran}h)_i^{n+\frac{1}{2}} - \Delta t \left\{ \sum_{k=1}^4 \mathbf{T}_{k,i}^{-1} \left[ \left( \hat{U} C_{gran} h \right)_{i,k}^{n+\frac{1}{2}} + \epsilon_{H,i} h \left( \frac{\partial (C_{gran})_k}{\partial \hat{x}} \right)_{i,k} \right] \Delta l_{k,i} \right\} \quad (3.82)$$

$$(C_{gran}h)_i^{n+1} = (C_{gran}h)_i^{adv} + \Delta t ED_{gran} (C_{gran})$$

where  $(C_{gran})_i$  is the granular depth-averaged concentration of cell  $i$ ,  $ED_{gran}$  is the granular erosion and deposition rate and  $\epsilon_{H,i}$  is the concentration horizontal diffusivity. In order

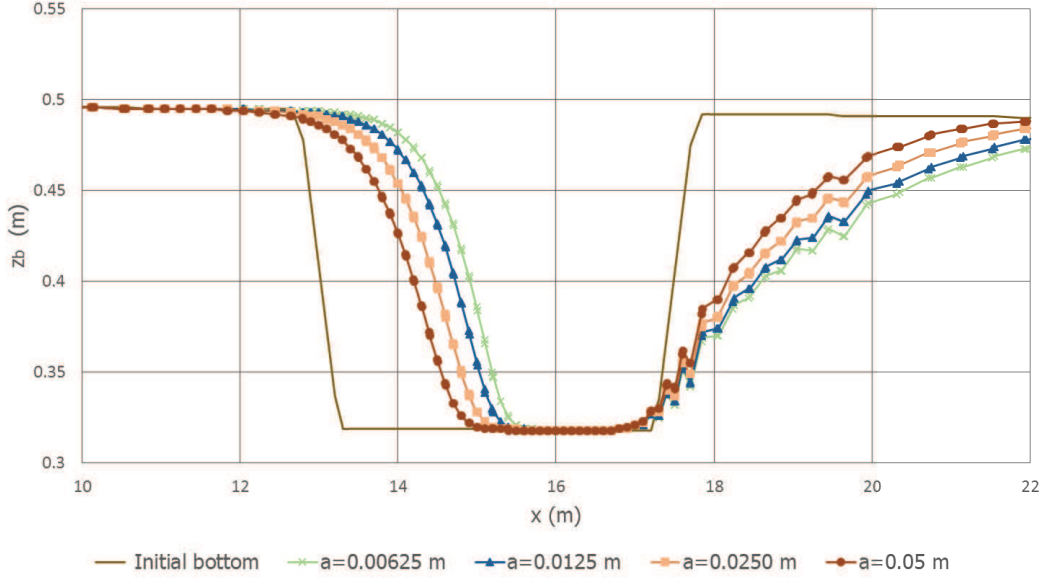


Figure 3.14: Comparison of different values of reference height  $a$  in a trench test under steady current: suspended load formula of Van Rijn [61] ( $T_{sim} = 5$  h,  $d_{50} = 0.160$  mm,  $U = 0.5$  m/s,  $h = 0.39$  m): no bed load considered.

to obtain intercell concentration  $(C_{gran})_{i,k}$ , a proper Riemann problem is solved using HLLC solutor. As discussed above, propagation wave associated to scalar transport is the shear wave and the solutor scheme is thus analogous to that used for the third equation of the hydrodynamic system. In particular, considering Figure 3.6, the depth-averaged concentration at intercell is

$$(C_{gran})_{i+\frac{1}{2}} = \begin{cases} C_L & \tilde{S} > 0 \\ C_R & \tilde{S} < 0 \end{cases} \quad (3.83)$$

where  $C_L$  is the granular concentration in Left region, while  $C_R$  is the granular concentration in Right region.

With regard to the horizontal diffusivity  $\epsilon_H$ , there are three different options available:

- **NO DIFFUSION:** in this case the diffusivity is not considered;
- **DIFFUSIVITY EQUAL TO EDDY VISCOSITY:** this is the default option. Generally no much information about sediment diffusivity are available and it is assumed that it is generated mainly by turbulence.
- **DIFFUSIVITY IMPOSED BY OPERATOR:** in this case horizontal sediment diffusivity is used as a calibration factor.

Finally, particular importance is given to the erosion-deposition rate and its computation. As discussed in Chapter 2, the term is generally proportional to the difference between equilibrium and instantaneous concentrations. In literature, two main approaches have been presented. In the first case, bottom concentration is considered for the computation of  $ED_{gran}$  (equation (2.78)) while in the last case depth averaged concentration is used (equation (2.74)).

In both cases, vertical concentration distribution has important influence in the final result. In order to solve  $ED_{gran}$  term, 4 possibilities have been implemented, three consid-

ering bottom concentration and the last one considering depth averaged concentration. In particular, the following options are available:

- **BOTTOM CONCENTRATION WITH VAN RIJN DISTRIBUTION:** in this case, the ratio  $\beta_d$  between depth averaged and bottom concentrations is based on Van Rijn vertical concentration profile. The solution is given by equation (2.82). In order to get  $\overline{\epsilon_{s,cw}}$ , each cell is divided in 40 sub-layers and  $\epsilon_{s,cw}$  is computed in each of them ;
- **BOTTOM CONCENTRATION WITH POWER LAW CURRENT-ALONE DISTRIBUTION:** in this case,  $\beta_d$  is based on analytical solution based on power law concentration profile under current alone condition. It is given by equation (2.81);
- **BOTTOM CONCENTRATION WITH POWER LAW WAVE AND CURRENT DISTRIBUTION:** similar to the previous one, this option supposes to describe in a better way the wave and current condition.  $\beta_d$  is given by equation (2.80).
- **EQUILIBRIUM DEPTH-AVERAGED CONCENTRATION WITH VAN RIJN DISTRIBUTION:** in the last case, equilibrium suspended load is computed solving Rouse equation along the water depth, with an easy finite difference scheme. Depth-averaged suspended load and depth-averaged concentration are then obtained. In order to compute  $ED_{gran}$ , Galapatti adimensional adaptation time has been used (equation (2.77)).

Power law distributions seem to give the best results in validation tests, as we will describe in next Chapter.

### 3.2.2 Computation of cohesive sediment transport

Cohesive sediment transport problem is here quite simplified. Sediments are supposed not to have influence on hydrodynamic and the problem is schematised by an advective-diffusive equation on the depth-averaged cohesive concentration  $C_{coes}$ , analogous to that used for suspended load sediment in case of non-equilibrium approach. In particular, equations (3.82) and (3.83) are applied to  $(C_{coes})_i$  and  $ED_{coes}$  is used as source term.

Thus, if cohesive sediment transport is considered, one more advective-diffusive equation is imposed, independent from that used for solving granular suspended load. As discussed in previous Chapter, the main differences between the two problems are the settling velocity computation, which depends on the instantaneous depth-averaged concentration and erosion and deposition rates. Moreover, cohesive vertical concentration distributions have a different shape. As horizontal diffusivity, the same value used for granular suspended load is applied.

For the computation of cohesive sediment transport, the different parameters are required, involving cohesive sediment properties (the sediment density  $\rho_{coes}$ , the particle diameter  $d_{50,coes}$  and the gel-point concentration  $C_{GEL}$ ), bed properties (the bulk density  $\rho_{soil}$  and the bed dry density  $C_M$ ) and experimental coefficients for the computation of settling velocity  $w_{s,coes}$  and erosional and depositional critical bed shear stress  $\tau_e$  and  $\tau_d$ .

Because of the lack of strong theories for cohesive sediment transport, an important number of coefficients and parameters is generally needed. It should be noted that although cohesive sediment transport modelling is a useful instrument for comprehending morphological evolution in coastal areas, the number of independent factors acting on the phenomena is really high and similar models should be used with particular care.

### Settling velocity

Settling velocity can be computed using different approaches, described in Subsection 2.3.1. In particular, the following method have been considered:

- **SETTLING VELOCITY IMPOSED BY THE USER:**  $w_{s,coes} = w_{s,val}$ . In this case, the user set the cohesive settling velocity as input parameter.
- **SOULSBY FORMULA FOR COHESIVE SEDIMENTS:** the regression formula proposed by Soulsby [64] is here used. Refer in particular to equation (2.92).
- **STOKES FORMULA FOR SPHERICAL PARTICLES:** classic analytical Stokes formula, valid for free settling, is used (equation (2.85)).

Settling velocity influences directly deposition rate and is thus important to obtain realistic values of it. Soulsby formula is here considered the more appropriate to describe cohesive dynamics, because it is able to consider the effect of concentration on settling, which has great influence on the phenomena. For low concentrations, a lower limit is imposed, correspondent to free settling velocity.

### Erosional critical bed shear stress and erosion rate

Erosion rate depends on two main factors: the computation of erosional critical bed shear stress and the calibration of Partheniades formula for erosion process.

With regard to the erosional critical bed shear stress, as previously discussed, two main formulas are here proposed, the first one depends on the bed dry density while the last one on the bed bulk density. The following options are thus possible:

- **MITCHENER ET AL. FORMULA:** this formula (equation (2.96)) is valid for a wide range of cohesive beds;
- **THORN AND PARSONS FORMULA:** the first important criterion presented in literature (equation (2.95)), depending on bed dry density;
- **EROSIONAL CRITICAL STRESS IMPOSED BY THE USER.**

In case Mitchener experimental formulas is used, values of  $E_3$  and  $E_4$  of formula (2.96) are required. Otherwise, if Thorne and Parsons model is considered,  $E_1$  and  $E_2$  coefficients of formula (2.95) should be set. Although these parameters are freely imposed by an operator, as discussed in Subsection 2.3.2 authors suggests optimized values, which are recommended if no experimental data are available.

Because of the variability of critical bed shear stress and the lack of data for a proper evaluation of it, the possibility of manually setting its value permits to calibrate and adapt it to the different possible situations (marsh salts, vegetation, etc).

Finally the Partheniades model is here used for erosion rate (equation (2.99)). Setting of experimental parameters  $M_{par}$  and  $n_{par}$  of equation (2.99) is thus required, and a range of values for both of them has been suggested by the author (see Subsection 2.3.2)

### Vertical concentration distribution and deposition rate

Deposition rate depends on settling velocity, on instantaneous bed shear stress, on depositional critical bed shear stress and on bottom concentration.

Due to the absence of empirical models for the evaluation of depositional bed shear stress, this parameter is evaluated by the operator. Several range of values are available in literature and, as previously discussed, it is generally between 0.06 and 0.1 Pa. In order to obtain bottom concentration, vertical concentration distribution is needed. In the present model, three different profiles are available:

- **CONSTANT PROFILE:** in this case, the bottom concentration corresponds to depth-averaged concentration. This assumption is not trivial because vertical profiles for cohesive sediments tend to be much more uniform than those valid for granular sediments;
- **LINEAR PROFILE:** in this case the ratio between surface and bottom concentration  $R_c$  is required;
- **TEETER PROFILE:** Teeter profile is used, as discussed in Subsection 2.3.3, which corresponds to equation (2.111).

### 3.2.3 Some consideration about input parameters in DAM\_SED

Although one of the main aim of DAM\_SED is to reduce the number calibration parameters with respect to other similar models, morphodynamic modelling requires a conspicuous amount of independent variables, which are not always easily available.

By the experience of Hydraulics Laboratory group of University of Udine, not all required data or parameters have the same influence on final solution and some of them are particularly significant in model calibration. For this reason, a list of such parameters is here reported, with some comment about their influence.

- $n$ : the Manning coefficient describes roughness in the whole studied area: it can be constant or, more often, variable into the domain. In the present model, Manning coefficient should take into account of all different macrological-roughness elements present at the bottom, such as vegetation, grains, bedforms, etc. Generally, once identified different roughness regions, Manning coefficient is set in order to respect hydraulic experimental data. A typical example is given by tide propagation, which should be well described by the model with the proper set of Manning coefficients.
- $\varepsilon$ : bottom roughness, if not related to Manning coefficient, have strong influence on wave bed shear stress and on reference height. In particular, maximum bed shear stress can significantly change and both granular suspended load and cohesive sediment transport are directly affected.
- $\nu_T$ : eddy viscosity can have great influence where advective fluxes result to be less important. In closed basin like lagoons, for example, an eddy viscosity change corresponds to significant variation on hydrodynamic field. Otherwise, in river hydrodynamic eddy viscosity model is generally less important, except for the river mouth, which is a typical example of water plane jet and is strongly influenced by turbulence field.

- $d_{50}$ : in granular sediment transport, mean grain diameter is one of the most important input parameters. In fact, it influences almost all main factors, such as critical shear stress, bed load, reference concentration and suspended load. Moreover, the bigger is the grain diameter, the more important is bed load with respect to suspended load. The choice of  $d_{50}$  should not take into account of finest diameters, which have not a granular behaviour.
- $a$ : the reference level, as previously discussed, have influence on the magnification of suspended load effect. It is generally suggested to relate it to the bottom roughness, as proposed by Van Rijn. In this way, complex domains can be easily analyzed taking implicitly into account the effect of bed geometry on suspended load.
- $\beta_d$ : the ratio between depth-averaged and reference concentration have a strong influence on suspended load. Power law formulas seem to well describe laboratory tests, as we will discuss in next chapter. However further investigations on all available concentration profiles are suggested.
- $\tau_e$ : the erosional critical bed shear stress for cohesive sediments is particularly important for the computation of the erosion rate and the source term  $ED_{coes}$ . In literature, a really large range of possible values for  $\tau_e$  is available and it is strictly related to the bed layer geotechnical history and characteristics, often not available. Thus, its evaluation should be done with particular care and remains a matter of judgment of the operator.

### 3.3 The morphological module

Once computed in each cell the sediment transport load and/or granular and cohesive erosion and deposition rates, the morphological evolution can be studied. In order to do this, sediment continuity equation at the bottom is solved at each time-step, considering both granular and cohesive influence.

In particular, bi-dimensional form of equations (2.117) and (2.118) are considered and discretised. The two contributes are treated independently.

With regard to granular sediment transport, a FVM 1D-augmented I-order in time and space scheme is here used. In particular, the change of the bottom level is computed as

$$(\Delta z_{b,gran})_i^n = -\frac{\Delta t^n}{1 - n_{por}} f_{MOR} \left[ \frac{1}{\Omega_i} \left( \sum_{k=1}^4 \hat{q}_{s,i,k}^n \Delta l_{i,k} \right) + (ED_{gran})_i^n \right] \quad (3.84)$$

where  $\Delta z_{b,gran}$  is the change of the bottom level due to granular sediment transport,  $\hat{q}_{s,i,k}^n$  is the total equilibrium load (bed load and, in case, suspended load) crossing perpendicularly  $k$ -side.  $n_{por}$  is the bottom porosity and  $f_{MOR}$  is a morphological factor, which will be described in next Subsection. The evaluation of sediment transport load at  $k$ -side intercell is obtained by the averaging the total load of the two involved cells (cell  $i$  and the  $k$ -sided adjacent cell, e.g.  $i + 1$ ):

$$\hat{q}_{s,i,k}^n = T_{i,k} \left( \frac{q_{s,i}^n + q_{s,i+1}^n}{2} \right) \quad (3.85)$$

Cohesive sediment transport model considers the following simpler scheme:

$$(\Delta z_{b,coes})_i^n = -\Delta t^n f_{MOR} (ED_{coes})_i^n \quad (3.86)$$

where  $\Delta z_{b,coes}$  is the change of the bottom level for cohesive sediment transport.

The total bottom level change is thus given by

$$(\Delta z_b)_i^n = (\Delta z_{b,gran})_i^n + (\Delta z_{b,coes})_i^n \quad (3.87)$$

In order to guarantee sediment balance, sediment supply must be checked. In particular, depositional rate must be less equal to the suspended sediment available in the cell

$$(ED_{gran})_i^n \geq -C_{gran,i}^n \Delta t^n \quad (3.88)$$

and

$$(ED_{coes})_i^n \geq -C_{coes,i} \Delta t^n. \quad (3.89)$$

At the bottom, bedrock level  $z_{br}$  and initial ratio between granular and cohesive sediments  $R_{g-c}$  must be set at each cell. Bedrock can't be eroded and the granular and cohesive sediment availability (respectively,  $\Delta_{z,disp,gran}$  and  $\Delta_{z,disp,coes}$ ) are computed as

$$(\Delta_{z,disp,gran})_i^n = (z_{b,i}^n - z_{br,i}) R_{g-c,i}^n \quad (3.90)$$

and

$$(\Delta_{z,disp,coes})_i^n = (z_{b,i}^n - z_{br,i}) (1 - R_{g-c,i}^n). \quad (3.91)$$

In order to respect non-erodibility condition, erosion rate can't be greater than sediment availability:

$$(ED_{gran})_i^n \leq (\Delta_{z,disp})_{gran,i}^n \frac{1 - n_{por}}{\Delta t^n - f_{MOR}} - \frac{1}{\Omega_i} \left( \sum_{k=1}^4 \hat{q}_{s,i,k}^n \Delta l_{i,k} \right) \quad (3.92)$$

and

$$(ED_{coes})_i^n \leq (\Delta_{z,disp})_{coes,i}^n \frac{1}{\Delta t^n - f_{MOR}}. \quad (3.93)$$

### 3.3.1 The Morphological factor

One of the most relevant problems in morphodynamic and morphological modelling is the time scale of morphological evolution.

In fact, considering coastal environments, evaluation of morphological trends needs simulations of months or, most probably, years of morphological evolution.

This is difficult to be done for two main reason: the computational time and the cumulative error.

With regards to computational time, it should be noted that hydrodynamic and morphodynamic modelings are computationally heavy. The adequate number of cells in real environments studies, such as estuaries or lagoons, is of the order of 50.000 - 250.000, if not higher. Moreover, as discussed above the model is explicit and Courant Friedrichs Lewy condition is required, which limits the magnitude of time-steps.

In order to optimize the algorithm, parallel OMP technique has been used, which lets the morphodynamic problem to be solved by all available processor cores at each time-step. In this way, computational time is significantly reduced. Despite of it, simulation time and computational time in similar models can be of similar order of magnitude (in a single last generation multi-core workstation), and set up long period simulations can thus result quite difficult.

The second problem regarding long period simulations is the cumulative error: a numerical model is characterized by a certain accuracy order, depending on the discretisation technique, and the mathematically exact solution can't be reached. For this reason, for a really high time-steps number, model accuracy is reduced and a not reliable can be difficultly obtained.

A way of solving similar problems is to reduce the simulation time by the use of an adequate morphodynamic evolution technique.

An interesting review over different morphological updating strategies has been presented by Roelvink [37], which compares some of the most common methods.

In the present model, so called "Online approach with morphological factor" is used. The technique corresponds to a simple increasing of depth change rates at each time-step by the use of an amplifier factor, which is here  $f_{MOR}$ . The "online" method, in comparison with other techniques which upload the bottom with less frequency, has the advantage to reduce all flow-morphology interactions at time-step level. In this way, amplified shock phenomena like wet-dry excursion can be taken into account more easily.

Morphological factor has been widely used in morphodynamic modelling. More application examples are given in Lesser et al. [25], who have implemented morphological factor in 3D-morphodynamic model Delft 3D.

As similar techniques, "Online" methods imposes limits on the morphological factor, depending on characteristics of modelled location: in fact, the idea is that hydrodynamics is not significantly influenced by sediment transport in a single time-step, even if multiplied by  $f_{MOR}$ . For this reason, an accurate calibration of morphological factor is needed, and its more appropriate value remains a matter of judgment of the operator, as pointed out also by Lesser [25].

## 3.4 Secondary factors for morphological evolution

Depth-averaged approach for morphodynamic and morphological studies can't be able to describe all the morphological changes which take place in a real environment: a great number of different phenomena, whether natural or anthropogenic, have influence on it and some of them are particularly important. For this reason, two more phenomena are considered in the present model: the secondary flows and the avalanching.

Secondary flows take place in river bents. They are caused by an imbalance of centripetal force acting on the fluid, which generates an outwards motion near the surface and an inwards motion at the bottom perpendicularly to the main flow. Thus, bents are characterized by a resulting helical flow. For inertia effect, the helical flow will born with a certain lag behind the change in topography.

Avalanching is a typical slope stability phenomenon. It is related to granular sediments: when slope angle is larger than repose angle, bed material will slide forming a new slope. A recursive algorithm based on Larson model [22] is here used. In this way, slope steepness is limited to repose angle, which results to be two more input parameters.

### 3.4.1 Secondary flow

As widely demonstrated in literature, secondary flows have an important influence on bed topography in bents and in curved flows. Helical flow has obviously a 3D structure, and a depth-averaged model can't describe it accurately.

However, it is relatively easy to compute the change in bed shear stress direction caused by secondary flow effects, which have important influence on bed load.

The algorithm here implemented is based on Rozovskii theory [39], which considers the bed shear stress direction in presence of secondary flow as

$$\tan \delta_s = -\beta \frac{h}{R_s} \quad (3.94)$$

where  $\delta_s$  is the angle between main flow and resulting shear stress,  $R_s$  is the radius of curvature of flow stream line and  $\beta_{sc}$  is a parameter defined as

$$\beta_{sc} = \alpha_{sc} \frac{2}{\kappa^2} \left( 1 - \frac{\sqrt{g}}{\kappa C_{chez}} \right) \quad (3.95)$$

where  $\alpha_{sc}$  is a calibration parameter (its default value is 1),  $\kappa$  Von Karman coefficient and  $C_{chez}$  the Chezy coefficient.

Secondary flow causes thus a further bed load component transverse to the flow given by

$$q_{sb,sc} = q_{sb} \tan \delta. \quad (3.96)$$

This component is thus added to the transverse component caused by the slope effect (equation (2.41)).

In regions where streamline curvature changes, secondary flow will adapt gradually, with different length scales  $\lambda_{sf}$  near the bed and at the surface. Such length is a function of  $h$  and  $\chi$  (a-dimensional Chezy coefficient). Scientific Documentation of DHI - MIKE21 model [10], whose secondary flow approach has been considered here as reference, suggests the following differential length scale:

$$\lambda_{sc} = \frac{1.2h\chi}{\sqrt{g}}. \quad (3.97)$$

The direction of bed shear stress for continuously varied curvature is thus computed along the streamline as

$$\lambda_{sc} \frac{\partial (\tan \delta_s)}{\partial s_s} + \tan \delta_s = -\beta_{sc} \frac{h}{R_s} \quad (3.98)$$

where  $s_s$  is stream-wise coordinate along streamline. In Cartesian coordinates equation (3.98) becomes

$$\frac{\partial x}{\partial s_s} \frac{\partial (\tan \delta_s)}{\partial x} + \frac{\partial y}{\partial s_s} \frac{\partial (\tan \delta_s)}{\partial y} + \frac{\tan \delta_s + \beta_{sc} \frac{h}{R_s}}{\lambda_{sc}} = 0. \quad (3.99)$$

We consider  $\frac{\partial x}{\partial s_s} = \frac{U}{\sqrt{U^2+V^2}}$  and  $\frac{\partial y}{\partial s_s} = \frac{V}{\sqrt{U^2+V^2}}$ . Rearranging equation (3.99) and including the unsteady term we obtain

$$\frac{\partial (\tan \delta_s)}{\partial t} + U \frac{\partial (\tan \delta_s)}{\partial x} + V \frac{\partial (\tan \delta_s)}{\partial y} + \frac{\sqrt{U^2+V^2}}{\lambda_{sc}} \left( \tan \delta_s + \beta_{sc} \frac{h}{R_s} \right) = 0. \quad (3.100)$$

The radius of curvature is defined as

$$\frac{1}{R_s} = \frac{|\overline{U} \times \overline{U}_T|}{|\overline{U}|^3} \quad (3.101)$$

where  $\bar{U} = (U, V)$  is the velocity vector and  $\bar{U}_T = \left(\frac{dU}{dt}, \frac{dV}{dt}\right)$  is the acceleration vector. Assuming quasi-steady conditions, the components of acceleration vector are computed as

$$\frac{dU}{dt} = U \frac{\partial U}{\partial x} + V \frac{\partial U}{\partial y} \quad (3.102)$$

$$\frac{dV}{dt} = U \frac{\partial V}{\partial x} + V \frac{\partial V}{\partial y}. \quad (3.103)$$

Thus, developing (3.101)  $R_s$  is obtained as

$$\frac{1}{R_s} = \frac{U^2 \frac{\partial V}{\partial x} + UV \left( \frac{\partial V}{\partial y} - \frac{\partial U}{\partial x} \right) - V^2 \frac{\partial U}{\partial y}}{\sqrt{U^2 + V^2}}. \quad (3.104)$$

$R_s$  is calculated with a sign. In particular, it is positive if the flow is bending to the left, while is negative if the flow is bending to the right.

The velocity derivatives in equation (3.104) are computed using the same simplified approach proposed for Smagorinsky turbulence model at Subsection 3.1.2, while equation (3.100) is solved using the same finite volume technique adopted for the concentration advective-diffusion equation.

### 3.4.2 Avalanching

Avalanching occurs if bottom slope exceeds the critical bottom slopes. In order to consider this phenomena, the model permits to do, with a given frequency, a control of bottom slope into the whole domain. In cells where such condition occurs, avalanching algorithm takes place.

The present algorithm is inspired by Larson [23] which considers two different limit profile slopes, coherently with Allen description of concept of avalanching [1]: the angle of repose  $\Phi_i$  ( or angle of initial yield) and the residual angle after shearing  $\Phi_r$ . In particular, when slope exceeds angle of repose, the material is redistributed and a new slope is reached, which corresponds to the residual angle.

In order to guarantee the sediment balance, the following conditions are required:

$$\begin{cases} \sum_{i=1}^N \Omega_i \Delta z_i = 0 \\ \Delta z_i = z'_i - z_i \end{cases} \quad (3.105)$$

where  $z'_i$  is the bottom level after avalanching. Moreover, at the end of avalanching we should have

$$\left| \frac{z_i - z_{i+1}}{\Delta l} \right| = \tan(\Phi_r) \quad (3.106)$$

where  $i$  and  $i + 1$  are two adjacent cells for which avalanching takes place and  $\Delta l$  is the distance between cell centres.

Developing equations (3.105) and (3.106) and assuming, without losing generality, that  $h_i > h_{i+1}$ , the following expressions for bed levels  $i$  and  $i+1$  are obtained:

$$z'_{i+1} = \frac{(z_{i+1} \Omega_{i+1} + z_i \Omega_i - \tan(\Phi_r) \Delta l \Omega_i)}{\Omega_i + \Omega_{i+1}} \quad (3.107)$$

$$z'_i = z'_{i+1} + \tan(\Phi_r) \Delta l. \quad (3.108)$$

In order to give physically correct results, cells are checked in sorted from the higher to the lower. A merge-sort sorting algorithm is used to this purpose. In case avalanching takes place, the level correction is recursive, until all cells adjacent to the first corrected cells are stable.

This algorithm is computationally heavy and, thus, the activation of avalanching check at each time-step is not advised. However, the time scale of morphological evolution is much bigger than that of hydrodynamic problem, which directly limits the time-step period: for this reason, avalanching control can be done with a lesser frequency without losing validity.

In Figure 3.15, the flowchart of avalanching algorithm used in the presented model is illustrated.

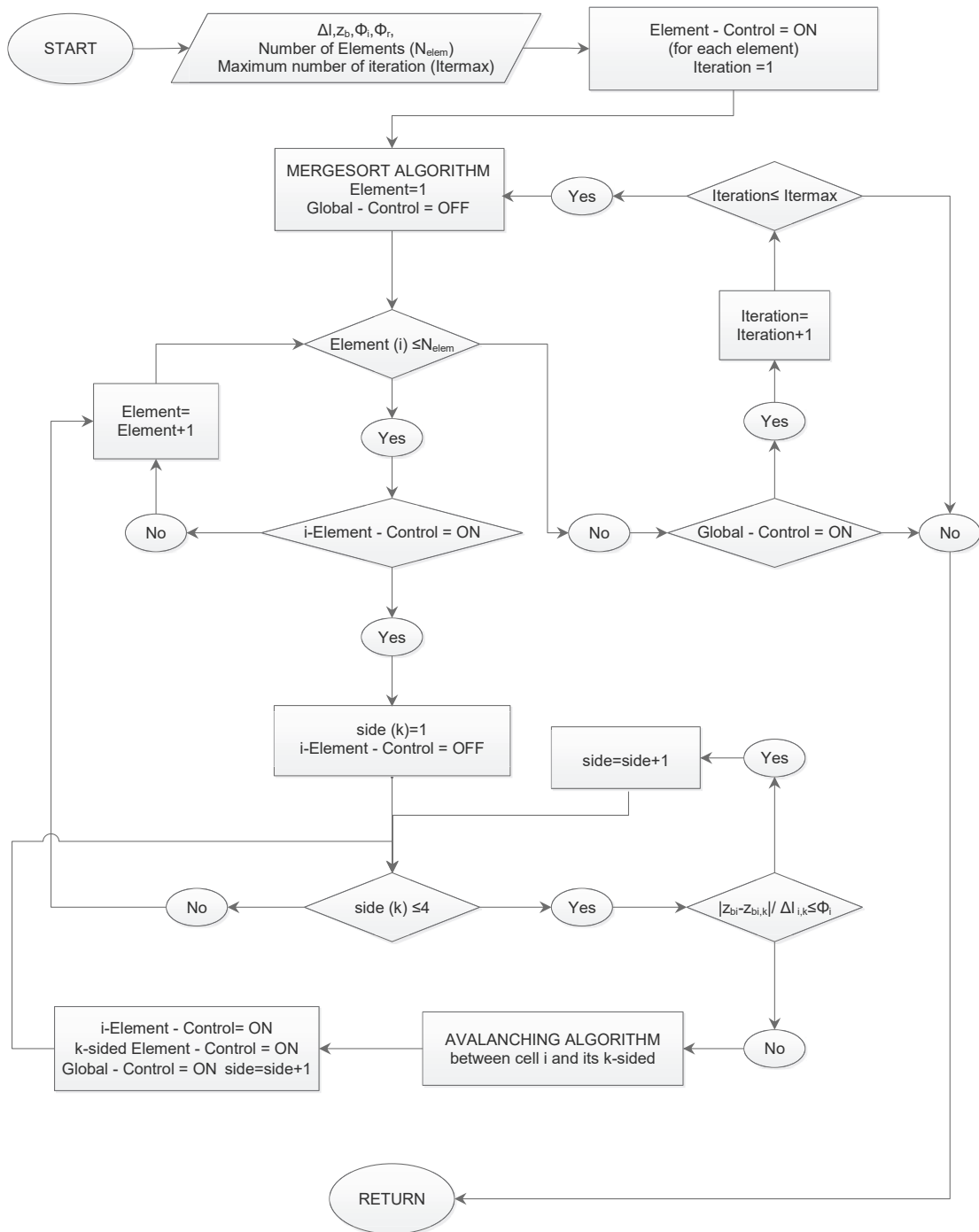


Figure 3.15: Flowchart of avalanching algorithm in DAM\_SED. *Global Control* and *Element Control* are logical variables useful to optimise the control. In this way, if somewhere, during the first iteration, avalanching takes place, only involved cells are considered in the following iterations. For each cell  $i$ , slope is checked along each of its 4 side (corresponding to  $k$  from 1 to 4).

# Chapter 4

## Model validation: laboratory tests

Validation process is fundamental in order to verify and ensure the reliability of a numerical model. Considering complex real domains, the availability of environmental monitoring networks is generally scarce and, if present, data are often inadequate or wrong. In this case, the quality of simulation results is difficultly verifiable: only the experience and the judgment of modellers can guarantee their accuracy.

For this reason, application of numerical models to some analytical or experimental tests, considered as benchmarks, is advised. These tests are generally designed for focusing on a reduce number of the numerical model skills, and let the users to appreciate how the model describe particular phenomena.

In morphodynamic and morphological modelling, different benchmark experimental tests are available in literature which consider mainly granular sediment transport and can be either 1-dimensional and 2-dimensional: some of them are here described and applied.

One of the most important tests used in morphodynamics is trench migration test, a typical 1-dimensional test proposed first by Van Rijn [58, 62]. As we will discuss later in the present chapter, trench tests study the evolution of a trench, with known width and lateral slopes, in a flume. Several settings of this test have been proposed and studied, which differs for example for sediment dimension, hydrodynamic condition (e.g. with or without wave field) or slopes steepness.

Soarez-Frazão et al. [43] proposed an another test, able to check the behaviour of shock-capturing morphological models: it consists on the study of the evolution of a mobile-bed during a dam-break test. Experimental data have been compared with a wide number of different numerical models, as discussed in their article.

Application of Van Rijn and Soarez-Frazão tests to the presented model have been discussed also by Bosa et al. in several conferences [5, 6].

Another type of laboratory test widely used in model validation studies morphological evolution in meanders and bend, where helicoidal flow plays an important role. Amongst other, two important tests are that proposed by Odgaard and Bergs [31], which considers steady-state morphological evolution, and that proposed by Yen and Lee [66], which analyses a channel bend evolution under unsteady current. Similar tests are useful for the evaluation secondary flow algorithm.

In next sections, above mentioned tests will be described and discussed.

## 4.1 Migration of a trench in a flume

Trench migration experiments consist on measuring of flow velocity profiles, sediment concentration profiles and bed level change of a trench in a flume. The trench is excavated in a sediment bed, which is movable. Several configurations of the test have been performed and, in particular, two main conditions have been studied:

- TRENCH MIGRATION UNDER STEADY CURRENT;
- TRENCH MIGRATION UNDER CURRENT AND WAVES (with parallel directions);

### 4.1.1 Trench Migration under steady current

#### Laboratory Experiment

The first series of tests have been carried out by Van Rijn in 1980, as discussed in [58], who considered trench evolution under steady current. Here, a flume 30 long, 0.5 m wide and 0.7 m deep has been used.

This test was characterized by a water depth upstream of the trench  $h_0 = 0.39$  m and a correspondent velocity flow  $U_0 = 0.51$  m/s, while the trench was 0.175 m deep and 5 m long. Van Rijn studied three different side slope: 1:3, 1:7 and 1:10.

The characteristic diameters of the sediment were  $d_{50} = 160$   $\mu\text{m}$  and  $d_{90} = 200$   $\mu\text{m}$ . Finally, grain density  $\rho_s$  was  $2650$   $\text{kg}/\text{m}^3$ .

During the experiment, an equilibrium sediment transport load has been guaranteed at upstream of the trench: basing on velocity and concentration measurements, equilibrium suspended load is supposed to be about  $0.03$   $\text{kg}/(\text{sm})$  (with a relative error of about 25%) while total inflow sediment transport rate was  $0.04$   $\text{kg}/(\text{sm})$ . For this reason, a bed load rate of about  $0.01$   $\text{kg}/(\text{sm})$  was supposed to be present. Moreover, analysis of suspended sediment samples, performed by Van Rijn, evidenced that suspended sediment particles was  $120$   $\mu\text{m}$  near the water surface and  $160$   $\mu\text{m}$  near the bottom. During the experiment, ripples were measured upstream of the trench, characterized by a length of about  $0.10 - 0.25$  m and a height of  $0.015 - 0.035$  m. Thus, bed roughness was evaluated to be  $0.025$  m.

In Figure 4.1, Van Rijn experiment geometry and hydraulic conditions are illustrated.

#### Numerical Settings and Results

In the numerical test, the computational domain is rectangular, 30 m long and 0.5 m wide. This flume is characterized by a bed slope of 0.4‰ and, centrally, a trench is inserted. The trench has the same dimensions used in laboratory and a lateral slope of 1:3, which is considered the hardest to be modelled. The mesh has rectangular elements, which are 0.1 m long inside the trench and along the slopes, 0.2 m close the trench (for 2 m from the trench slopes) and 0.4 m outside this area. All cells have a width of 0.15 m.

In order to guarantee experimental hydrodynamic conditions, an inflow of  $0.1989$   $\text{m}^2/\text{s}$  was set, while the Manning coefficient was  $0.02$   $\text{s}/\text{m}^{1/3}$ . In Figure 4.2, geometry of the domain, characteristics of the mesh and used hydrodynamic conditions for the test are illustrated. Initial hydrodynamic conditions are illustrated in Figure 4.3: in the trench, water flow is not able to maintain in suspension grains.

Different computation methods for bed and suspended loads have been considered and compared.

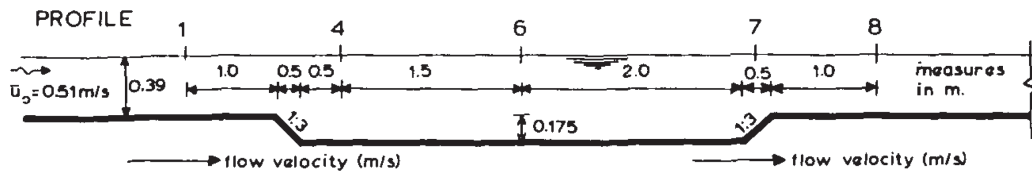


Figure 4.1: Trench profile in 1987 Van Rijn's experiment (Van Rijn [58]).

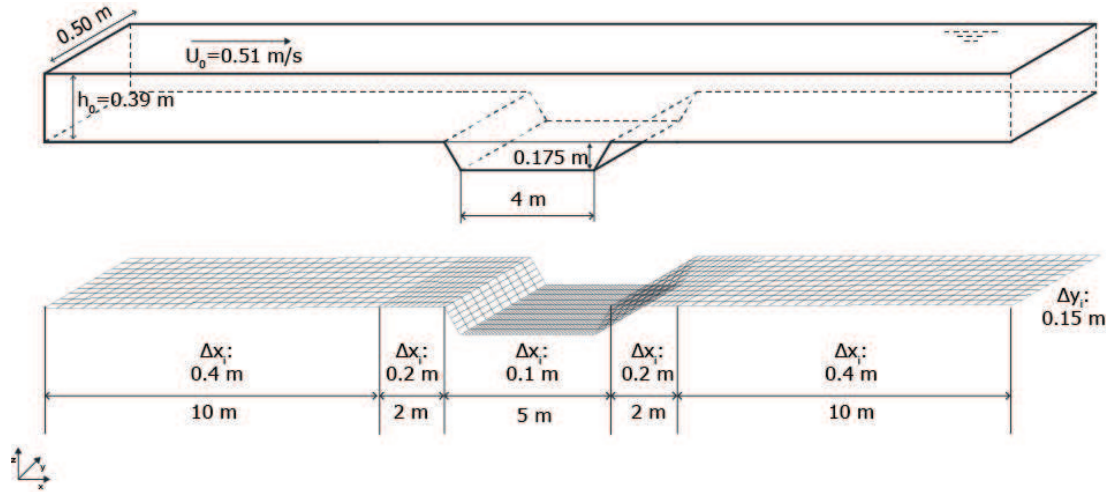


Figure 4.2: Trench migration under steady current [58]: geometry and hydrodynamic conditions in the numerical model.

Suspended load has been studied analyzing both equilibrium and non equilibrium approaches (considering different concentration distribution) have been used. In particular, we used Van Rijn formula for equilibrium suspended load (equation (2.28)) and Van Rijn (equation (2.53)) and Soulsby (equation (2.49)) vertical concentration distributions for the resolution of advective-diffusive equation in non-equilibrium approach.

With regard to the bed load, three formulas are here considered: Van Rijn (2.28), Soulsby (2.33) and Meyer-Peter and Müller (2.21).

As sediment inflow boundary condition, an equilibrium suspended load was imposed, obtained by a calibration process: in this way, no scour nor deposition occur close to the inflow and along the upstream channel. A mean grain diameter  $d_{50} = 160 \mu\text{m}$  is imposed while the reference height  $a$  is imposed to be 0.0250 m, coherently with ripples height. Results of the numerical simulation and the experimental data along central longitudinal section have been compared after 7.5 h and 15 h.

As evident by the bed and suspended loads ratio in Van Rijn experiment, the main factor in trench evolution of this particular experiment is the suspended load. Consider Figure 4.4: here, initial suspended sediment load using the three illustrated methods has been compared with Van Rijn bed load. At inflow, Van Rijn equilibrium load and Soulsby profile for non-equilibrium load give the better results, with a sediment rate of  $0.024 - 0.025 \text{ kg}/(\text{sm})$ , which is comparable with experimental data. Van Rijn profile for non-equilibrium approach seems to slightly overestimate suspended load ( $0.04 \text{ kg}/(\text{sm})$ ). Also the ratio between suspended and bed load appears to be closer to the first two cases than the last one.

With regard to the trend of suspended load, we can observe an important difference between equilibrium and non-equilibrium approaches behaviours. In the first case (as for the equilibrium bed load), a sudden change of the suspended load takes place at the lat-

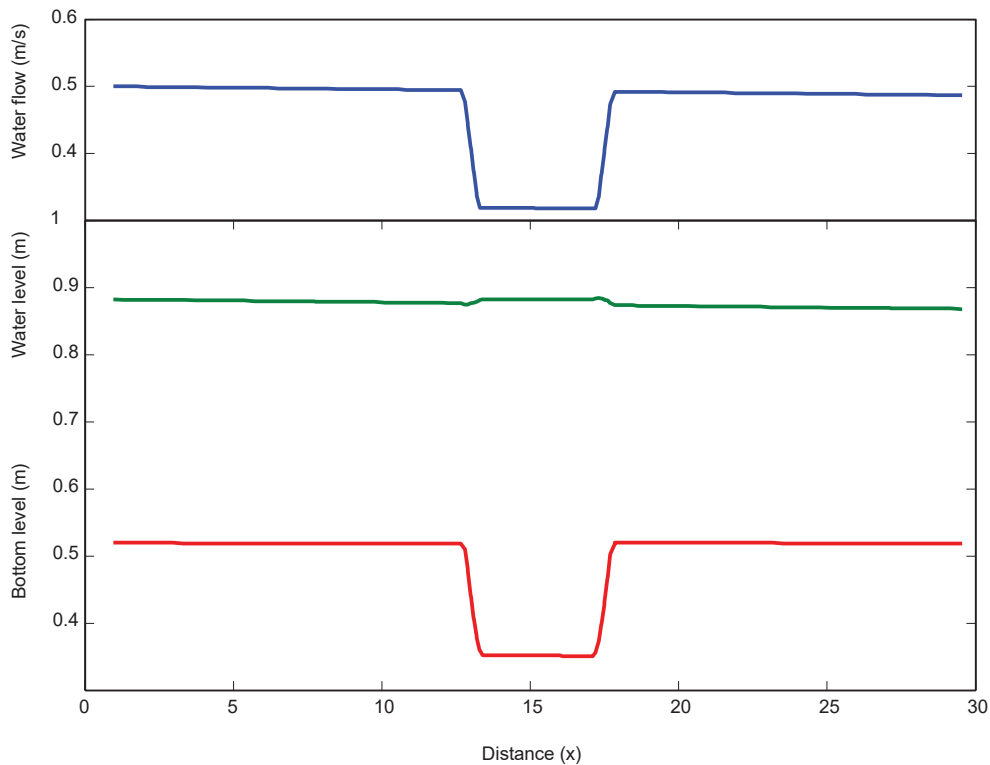


Figure 4.3: Initial hydrodynamic conditions: steady flow on a fixed bed.

eral slopes, while it remains constant at inflow and outflow channel and inside the trench. Conversely, in case of non-equilibrium approach, a gradual change of the load takes place across the trench and along the first part of the outflow channel.

During the experiment, the upstream slope of the trench advances while the trench bottom gradually fills. Instead, the downstream slope is eroded, beginning from the upper side. This particular morphological behaviour is better described by the non-equilibrium approach, chosen here.

Let us consider the comparison in Figure 4.6: experimental results are compared with numerical results using the different above mentioned approaches for suspended load.

Equilibrium approach tends to overestimate trench migration, while filling process is actually underestimated. In this case, upstream trench slope results to be advanced much more than that measured. Also downstream slope has advanced more than in experiment, while outflow channel is generally more eroded. After 15 h, the trench is thus located downstream and results to be deeper than in experimental results.

In case of non-equilibrium approach, trench shape is not strongly influenced by the choice of the concentration distribution. The slopes migration is in fact more gradual in both considered cases, while the entire trench is progressively smoothed and filled. The trench morphology in these cases is in better agreement with experimental data. However, using the Van Rijn vertical concentration profile, infilling process is generally quicker. This is coherent with Figure 4.4: suspended load is higher than in the latter case and more material tends to be deposited in the trench due to the hydrodynamic changes.

For these reasons, the best method for suspended load computation in this particular test appears to be the non-equilibrium approach with the use of Soulsby concentration profile.

In this case, upstream slope is advanced of about 1.5 m after 7.5 h, and of about 4 m

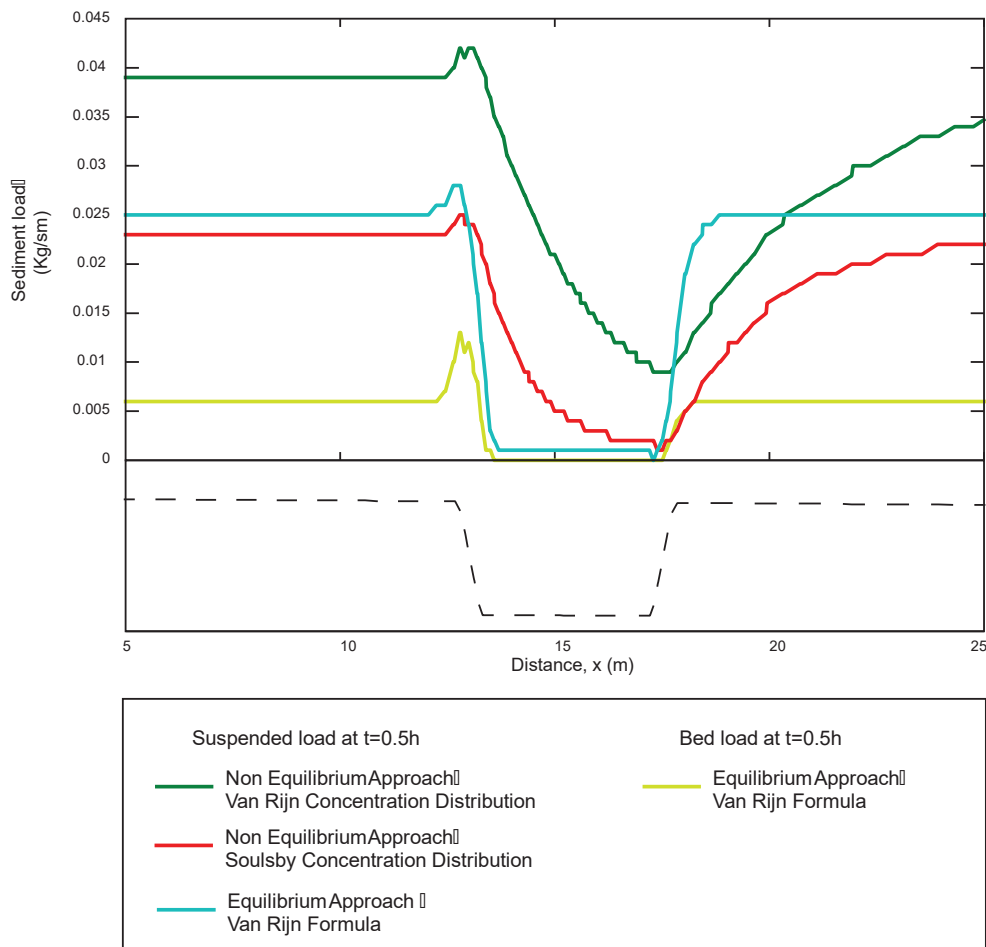


Figure 4.4: Comparison of bed and suspended sediment load using different suspended load computation methods: non-equilibrium approach with Van Rijn concentration distribution (2.61), non-equilibrium approach with Soulsby concentration distribution (2.49), Van Rijn equilibrium formula (2.66).

after 15 h, which is in agreement with experimental profile. The upstream steepness is gradually reduced and simulated profile appears to be parallel to the experimental data. Also the computed trench filling process is coherent with experimental data: after 15 h the simulated bed appears a few higher: however, this error is relatively small and the trench lowest section is the same in both cases.

The erosion process of downstream slope is finally adequately modeled too: the erosion involves all the downstream channel and the two profiles are close and parallel.

The different bed load formulas cited above have been compared in Figure 4.6. In this case, the non-equilibrium approach has been chosen for suspended load, assuming the Soulsby's power law concentration distribution.

The bed load has less influence than suspended load in trench evolution and, changing formula, the differences between computed profiles involves mainly the migration process.

Van Rijn and Meyer Peter and Müller formulas result to be in better agreement with experimental data: in these cases both filling process and upstream slope position are coherent with them. however, Van Rijn appears to describe slightly better the upstream trench slope.

Soulsby formula gives less accurate results. In this case, the trench appears to be less

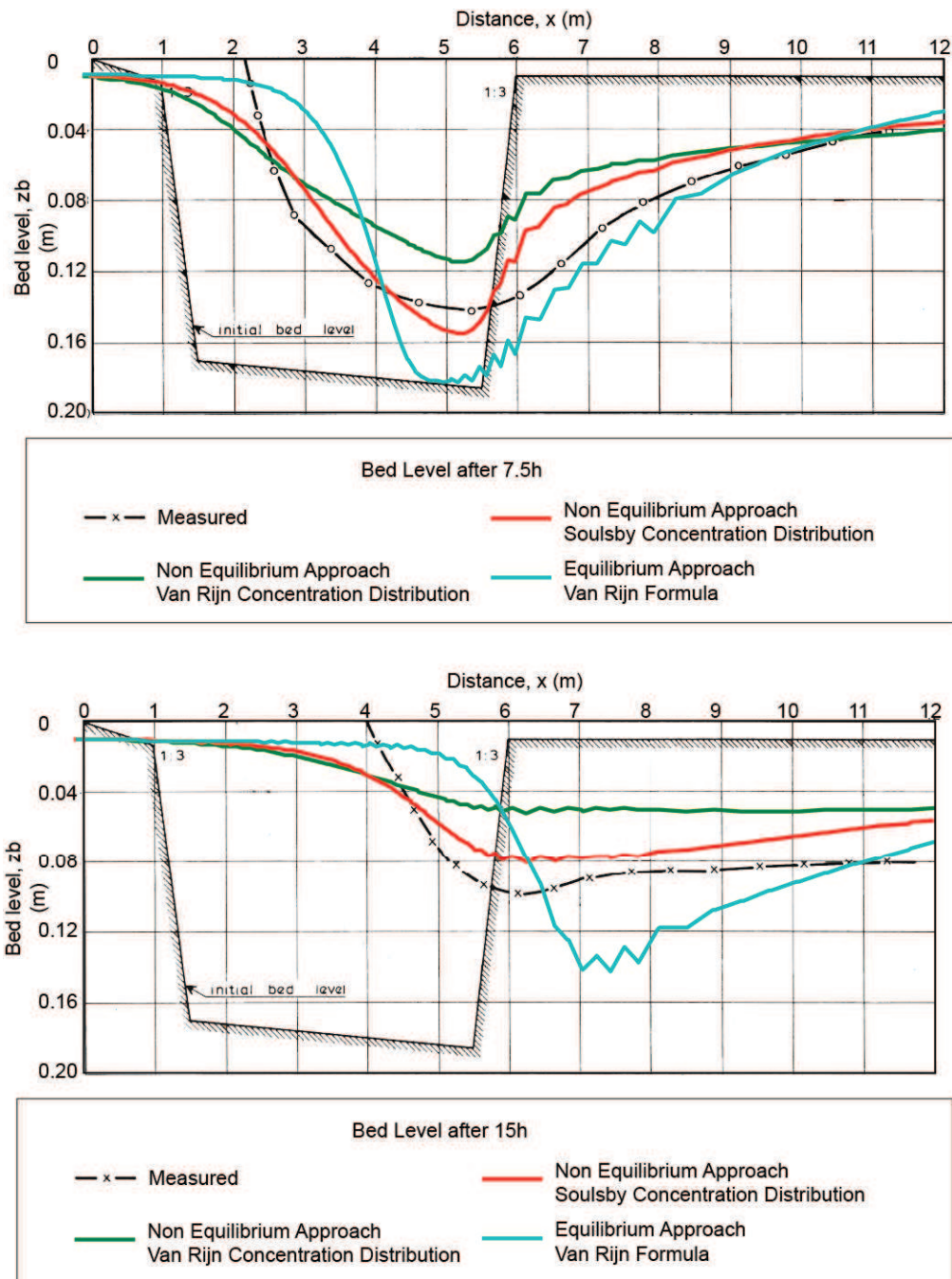


Figure 4.5: Comparison of trench evolution using different suspended load computation methods: non-equilibrium approach with Van Rijn concentration distribution (2.61), non-equilibrium approach with Soulsby concentration distribution (2.49), Van Rijn equilibrium formula (2.66).

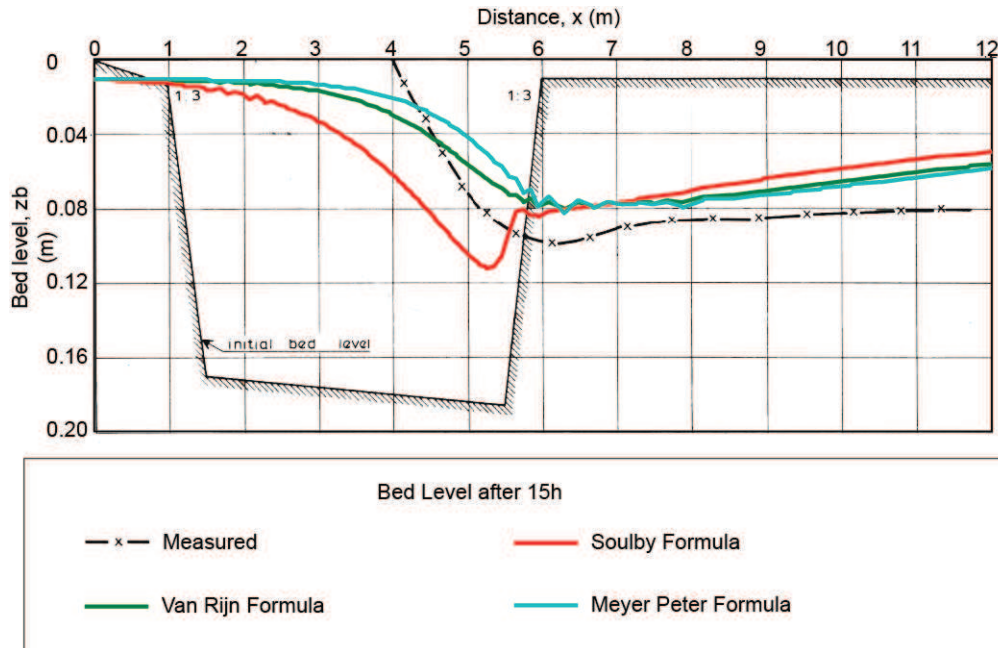


Figure 4.6: Comparison of trench evolution using different bed load equilibrium formulas: Van Rijn (2.28), Soudby (1.170), Meyer Peter (2.21).

filled and the upstream slope less migrated with respect to the initial condition. Thus, Van Rijn formula for bed load seems to better describe the test.

For these reasons, the numerical model reveals a good agreement with trench behaviour. In particular, the use of Van Rijn formula for bed load and the chose of non-equilibrium approach for suspended load, (considering Soulsby concentration profile) result to be the best approach for the analysis of this test.

#### 4.1.2 Trench Migration under Current and waves

##### Laboratory experiment

The second trench test is based on Van Rijn's 1986's experiment at Delft Hydraulics [62]: it is similar to the previous one and evaluates the migration of a trench perpendicular to a current under the influence of a regular wave field in a flume (length 17 m, width 0.3 m, depth 0.5 m).

Upstream of the trench, a water depth of 0.255 m and a flow velocity of 0.18 m/s were maintained constant. A simple wave paddle generated regular waves with a period of 1.5 s and a height of 0.08 m (measured upstream of the trench). The trench was 1.5 m long and 0.125 m deep, with side slope of 1:10.

Bed material used was sand, with characteristic diameters  $d_{50} = 100 \mu\text{m}$  and  $d_{90} = 130 \mu\text{m}$ ; grain density was  $2650 \text{ kg/m}^3$ . In order to guarantee an equilibrium sediment load at inflow, a constant rate of  $0.0167 \text{ kg/(sm)}$  was maintained. No bed load measures are available, however suspended load particle size was in the range of  $80 - 110 \mu\text{m}$ . During the test, ripples were generated, with a height of 0.01-0.02 m and a length of about 0.05-0.08 m. In Figure 4.7, Van Rijn experiment set-up is shown.

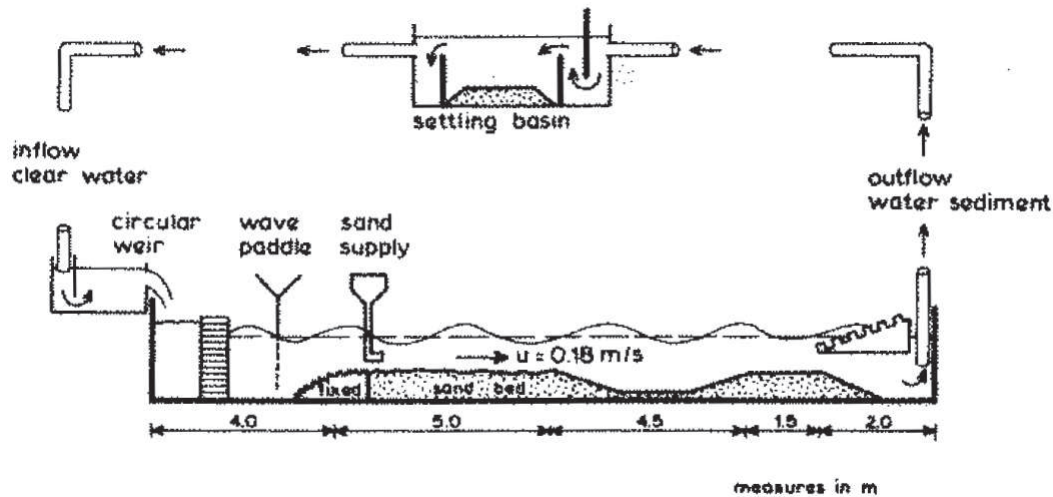


Figure 4.7: Trench migration under waves and current [62]: experiment set-up.

### Numerical Settings and Results

The computational grid is characterized by uniform square cells of side 0.05 m long. The flume has a global slope of about 0.018‰, with a Manning coefficient of  $0.025 \text{ s/m}^{1/3}$ : in this way, experimental current-alone flow characteristics are respected.

The trench is positioned at the centre of the flume, with a geometry analogous to that designed by Van Rijn. Inflow and outflow sections are located about 6.25 m from the trench.

At inflow section, a steady flow of  $0.0459 \text{ m}^2/\text{s}$  is set, while a cinematic outflow boundary condition is imposed.

With regard to wave field, a regular wave with period  $T_w = 1.5 \text{ s}$  and height  $H = 0.08 \text{ m}$  is imposed on the domain. Soulsby DATA2 formulas (1.174) and (1.175) are used for the calculation of mean and maximum wave-current bed shear stresses. Mean grain diameter is  $d_{50} = 100 \mu\text{m}$ , while bottom porosity is 0.4, as declared by Van Rijn for the experimental conditions. The reference height  $a$  is set equal to 0.01 m, coherently with ripples height.

Considering sediment transport computation, three approaches for suspended sediment transport have been compared: non-equilibrium approach with Van Rijn concentration distribution (equation (2.53)), non-equilibrium approach with Soulsby concentration distribution for waves and current (equation (2.50)) and equilibrium approach using Van Rijn formula (equation (2.28)).

Bed load Van Rijn equilibrium formula is here considered (equation (2.28)), although no bed load takes place during simulation under considered hydrodynamic conditions (mean bed shear stress is not strong enough to let the current move grains on the bottom).

As morphodynamic boundary conditions, equilibrium suspended load at inflow and cinematic condition at outflow are imposed.

In Figure 4.8, test geometry and setup are shown.

The evolution of the trench, using the above mentioned different theories, has been compared with experimental data after 10 h (Figure 4.9).

With regard to non-equilibrium approach, the two considered concentration profiles give similar results: differences are much less evident than in trench migration under steady current experiment. In this test, sediment suspension is guaranteed only by wave field and the effects of different hypothesis for current vertical mixing coefficient are thus negligible.

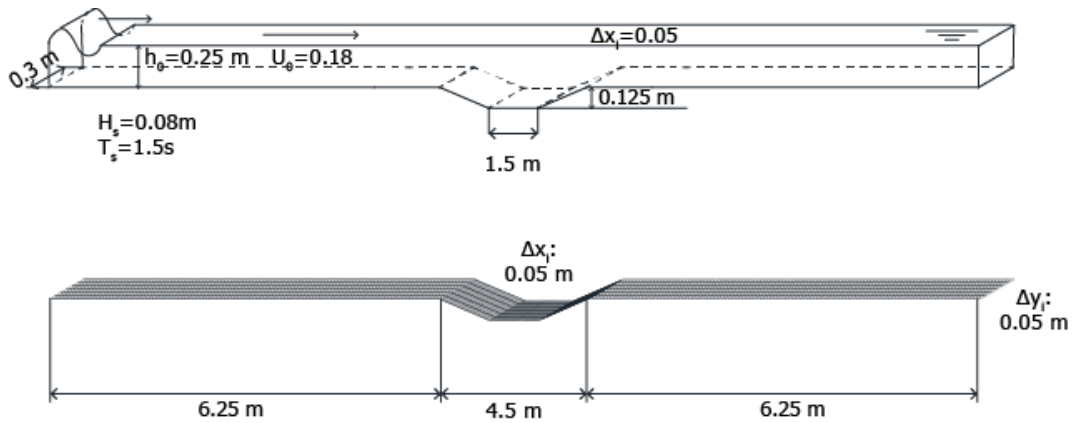


Figure 4.8: Trench migration under waves and current [62]: geometry and hydrodynamic conditions in the numerical model.

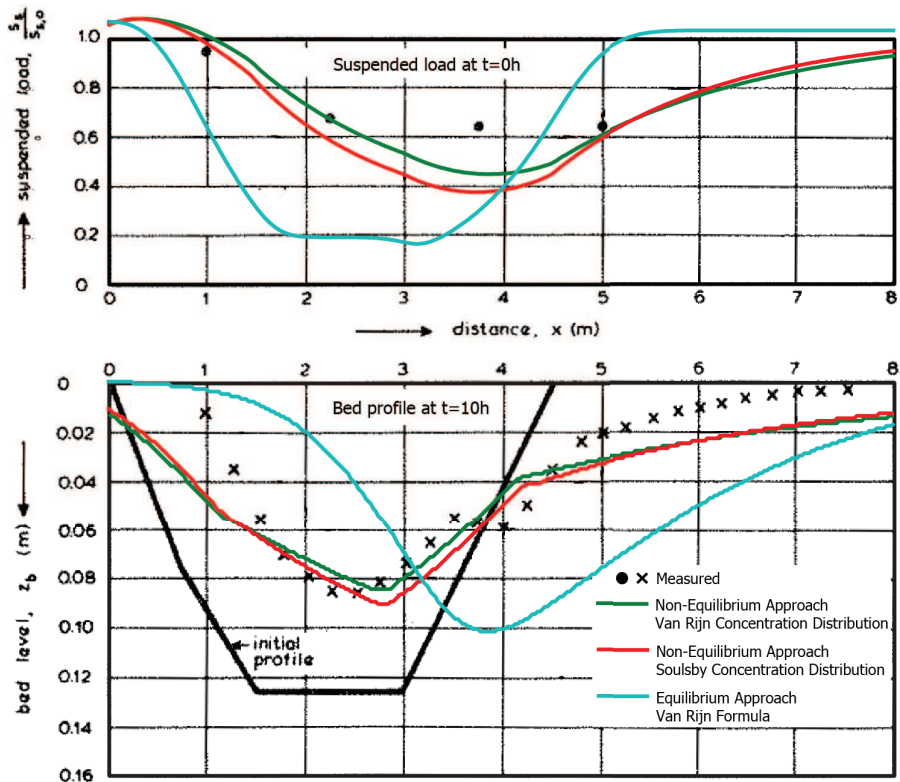


Figure 4.9: Trench migration under waves and current [62]: experimental and computed data after 10 h.

Model	Inflow Suspended Sediment [ $kg/m^3$ ]
Bijker (1967)	0.017
Fredøe (1984)	0.008
Grant and Madsen (1979)	0.012
Myrhaug and Slaattelid (1990)	0.009
Huyngh-Thahn and Temperville (1991)	0.009
Soulsby DATA2 (1997)	0.009

Table 4.1: Equilibrium inflow suspended load for each bed shear stress theory.

The migration of upstream trench slope results less evident in numerical simulation than in experimental data. This fact is probably caused by the absence of bed load influence on the numerical simulation, which is generally one of the main responsible for trench migration. Anyway, Van Rijn gave no informations about bed load in his experiment: if present, probably the declared mean diameter  $d_{50}$  would result to be no representative for the bed load. The filling process is adequately simulated by the model: the profile is close to experimental data in central part of the trench and at the downstream slope. Downstream to the trench, the flume in numerical model is slightly more eroded, but the profile is anyway parallel to experimental data and coherent with them.

The equilibrium suspended load at inflow has been obtained by a calibration process: it corresponds to  $0.0113 \text{ kg}/(sm)$  for Van Rijn concentration distribution and to  $0.0093 \text{ kg}/(sm)$  for Soulsby concentration distribution. In both cases sediment load is slightly inferior to experimental data, although Van Rijn did not declare the measurement error. Anyway, suspended sediment rate at inflow can be considered comparable with experimental data using both hypothesis on concentration distribution.

Considering variations of suspended load in Figure 4.9, it seems to represent adequately laboratory test, except for the downstream slope, where suspended load appears to be slightly underestimated. The trend is anyway coherent with the original test.

Also in this case, trench evolution is not well described by equilibrium approach. In fact, in this case trench migration is really overestimated, while the trench results to be less filled than in experimental measurements.

Inflow suspended load is closer to the value declared by Van Rijn. Otherwise, across the trench, suspended load fall quickly down, being reduced by about 80%, which is not coherent with the test.

For these reasons, trench migration test under waves and current can be considered well simulated by the numerical model using non equilibrium approach (with both considered concentration distribution), while equilibrium approach seems to give less accurate results.

### Comparison of different wave-current bed shear stress theories

Soulsby scheme for bed shear stress permits to choose between different wave-current bed shear stress theories. In order to better understand, from a practical point of view, the differences between them, Van Rijn trench test under waves and current has been simulated using different approaches. In this case, a unique sediment transport computation method has been considered. In particular, for suspended load, non-equilibrium approach, using Soulsby concentration profile, is here used.

The following mathematical models for the computation of wave current bed shear stress has been compared:

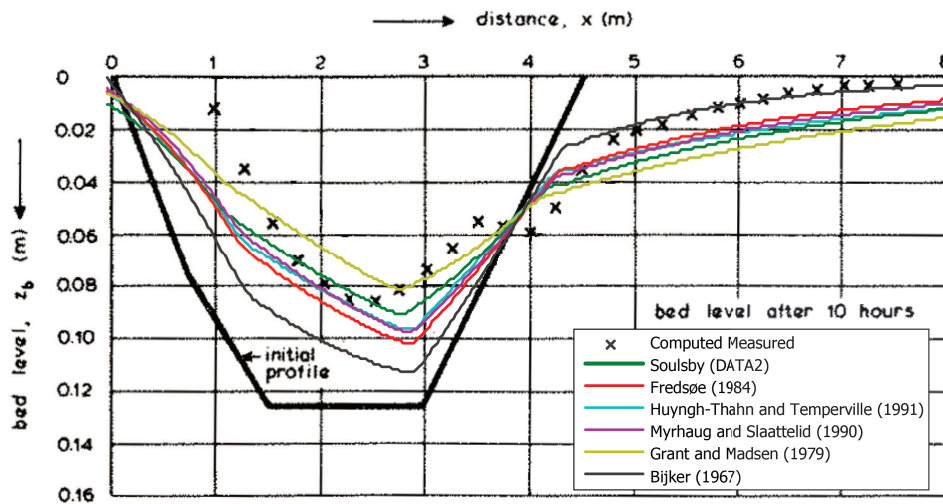


Figure 4.10: Trench migration under waves and current[62]: comparison of different wave-current bed shear stress theories.

- Bijker;
- Fredsøe;
- Grant and Madsen;
- Myrhaug and Slaattelid;
- Huyng-Thahn and Temperville;
- Soulsby (DATA2).

Using all these theories, hydrodynamics (measured under current-alone conditions) and wave field are coherent with experimental data illustrated above. Moreover, for each theory the equilibrium inflow concentration has been carried out by a calibration process. In Table 4.1, equilibrium suspended load at inflow for each theory is summarized.

All models, with exception of Bijker, are characterized by a similar equilibrium inflow load. Bijker model seems to overestimate, with respect to the others, suspended load, but it anyway results comparable with experimental data.

The trench profile after 10h using different mathematical theories is illustrated in Figure 4.10.

Considering filling process, Bijker model results to be the less accurate than others with respect to experimental data: after the simulation, in fact, the trench has not been successfully filled and, in its lower level, filled layer results less than half thick than that observed. Also in Fredsøe, Myrhaug and Slaattelid and Huyng-Thahn and Temperville models the simulated trench appears to be slightly less filled than experimental data. Conversely, Grant and Madsen model overestimates the process: the trench bottom in this case is slightly higher.

With regard to the migration process, all models underestimate the upstream trench slope progression, while trench bottom is a bit ahead with respect to experimental results.

The downstream channel appears slightly more eroded, but anyway coherent with experimental data, for each model.

From the present comparison, DATA2 formula seems to better describe the physical process. However, all formulas give results in fairly agreement with experimental data.

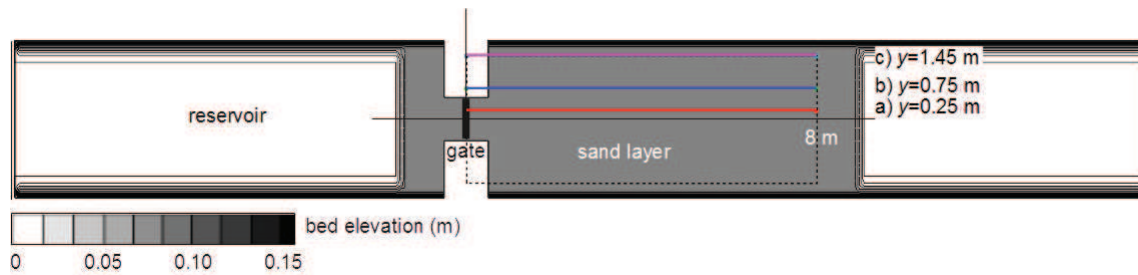


Figure 4.11: Bi-dimensional dam-break over an erodible bed [43]: experiment set up.

## 4.2 Bi-dimensional dam-break over an erodible bed

### Laboratory experiment

In order to compare different morphodynamic numerical models on fast transient flow, Soares-Frazão et al. [43] developed a new benchmark laboratory test. It consisted in a two-dimensional dam-break flow over a sand bed in a 3.6 m wide and 36 m long laboratory channel. A localized obstruction of the flume section, with a 1 m wide gate, created an upstream reservoir that gave rise to a dam-break as soon as the gate was removed.

The flume had a fixed bed, which was covered by an 85-mm thick layer of sand for 9 m downstream of the gate and 1.5 m upstream of it, as illustrated in Figure 4.11.

Manning coefficients for the sand and the fixed bed were declared as 0.0165 and 0.010  $s/m^{1/3}$  respectively. Grain size ( $d_{50}$ ) was 1.61 mm, specific density and porosity were 2.63 and 0.42, respectively.

As physical boundary conditions, a closed wall limits upstream the reservoir, while a sediment trapping has been disposed at downstream channel end.

Two different test conditions has been considered, Case 1 and Case 2: in the first case, water level corresponds to the bottom level while in the latter it corresponds to a water depth of 0.15 m. In both cases, the initial sand layer thickness was saturated.

Considering in particular Case 1, which has been studied and discussed in the present work, the general hydrodynamic behaviour is similar to that of a dam-break over a dry-bed. The initial water depth upstream the gate was set to 0.47 m.

The opening time of the gate has been found to be 0.23 s and the process can be considered instantaneous. Further details on the experimental set-up are provided in the original paper [43].

In Figure 4.12, final bed topography for Case 1 is reconstructed [43]: as study domain, the dotted area of Figure 4.11 has been considered.

### Numerical Settings and Results

The mesh adopted is square shaped, with a cell side of 0.1 m. The same initial condition illustrated for physical Case 1 test has been applied, i.e. water depth of 0.47 m in the reservoir and water level corresponding to the bottom height downstream of the gate.

Because of the dimension of sand grains, bed load is absolutely predominant in the test, while suspended load has not great influence. For this reason, the latter has not been considered. A uniform Manning coefficient of 0.0165.

The test has been carried out using three different bed sediment transport formulations:

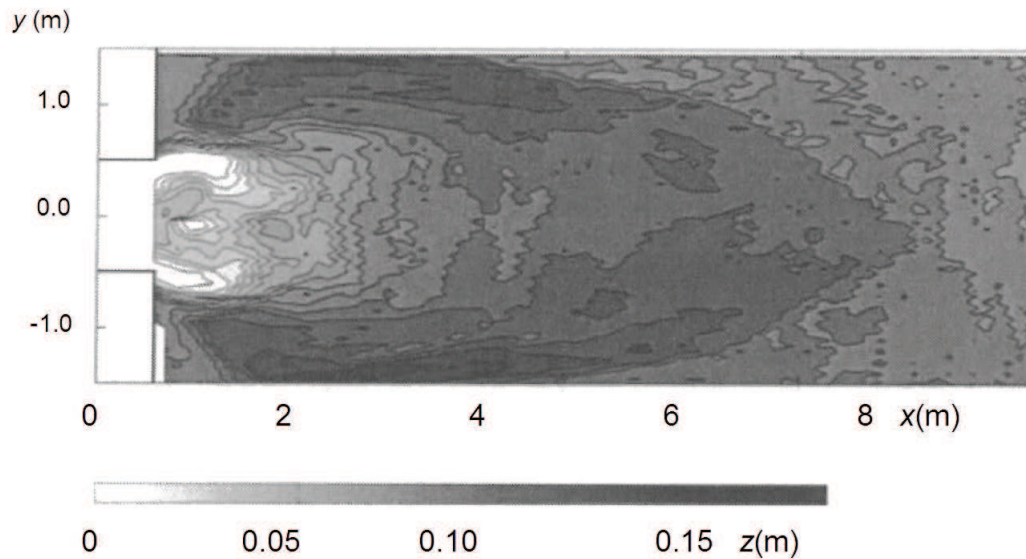


Figure 4.12: Bi-dimensional dam-break over an erodible bed [43]: experimental bottom level after 20 s.

Van Rijn (equation (2.25)), Soulsby (equation(2.32)) and Meyer-Peter and Müller (equation(2.21)).

The results after 20 s are shown in Figure 4.13 as bed elevation in the whole domain and in Figure 4.14 as a comparison between numerical and experimental bottom height on the longitudinal profiles depicted in Figure 4.11. The models describes accurately the scour process at the flume enlargement, and the development of a sandbar along the study domain, with its typical ogival shape.

The model seems to describe the phenomenon in a proper way, even if the results obtained by Meyer-Peter and Müller formulation are less accurate in predicting the occurrence of both the central scour and the deposition area, with less accentuate erosion and deposition. On the other hand, the results obtained by the Van Rijn and Soulsby formulations are almost in agreement with each other. The agreement with the experimental data is better in the central part of the flume (longitudinal profile located at  $y = 0.20$  m, section a of Figure 4.14) and it differs more when moving apart (longitudinal profile located at  $y = 1.45$  m, section c of Figs. 7-9). Nevertheless, Soares-Frazão et al. [43] show that this is a difficulty common among numerical models.

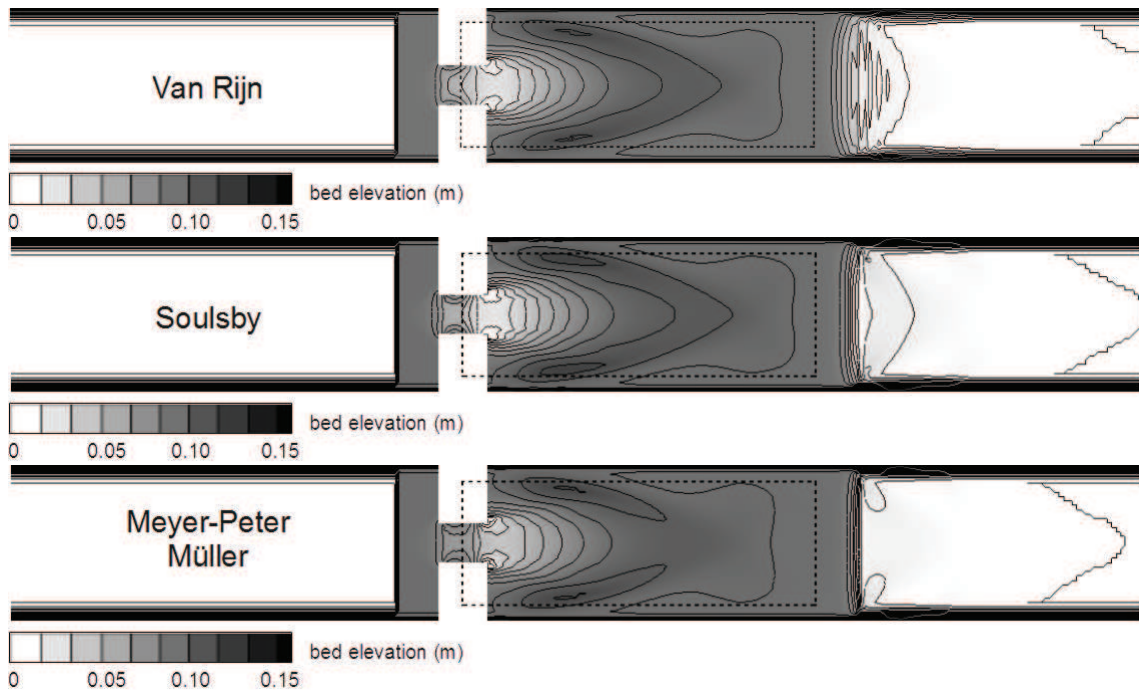


Figure 4.13: Bi-dimensional dam-break over an erodible bed [43]: bed elevation after 20 s using different bed load equilibrium formulas.

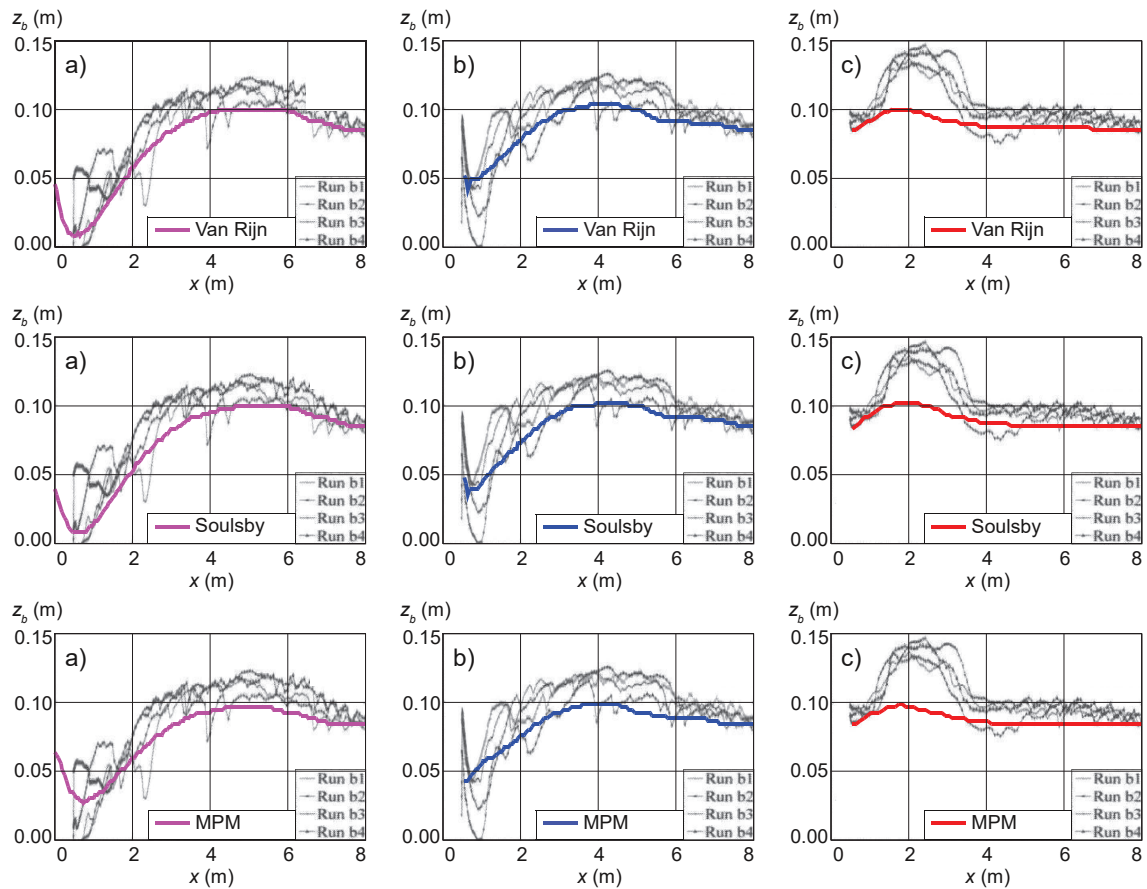


Figure 4.14: Bi-dimensional dam-break over an erodible bed [43]: bed elevation after 20 s on the longitudinal profiles in Figure (4.11). Bed load formula of Van Rijn, Soulsby and Meyer-Peter and Müller.

## 4.3 Hydrodynamics of a curved channel under steady flow

Due to the effect of secondary flow, the sediment dynamics of a channel bend results to be much more complex than that of a straight channel. In particular, as discussed in subsection 3.4.1, the presence of an helicoidal flow generates an additional component to the bed load, normal to the water flow, which transports grain material to the inner channel bank (or wall). In this way, the bottom results to be higher in the inner part and lower in the outer part. Consequently, a transverse slope takes place and a more bed load transverse component is generated by the slope effects. Thus, if the bed load plays an important role in morphodynamics, bend morphology is the result of mutual effects of longitudinal current, transverse slope and secondary flow.

### Laboratory Experiment

The first test proposed here has been presented in literature by Odgaard and Bergs [31]. They used an U-channel, 80 m long and 2.44 m wide: it is composed by an inflow and an outflow straight channels, 20 m long, and a 180° bend. The mean radius was 13.11 m. The channel had trapezoidal section and a 23-cm-thick layer of sand formed the bed, as illustrated in Figure 4.15. Sand had a mean diameter  $d_{50}$  of 0.3 mm and a standard deviation of 1.45.

An inflow discharge of  $0.153 \text{ m}^3/\text{s}$  has been maintained constant during the test: under this condition, authors measured a centre line average flow velocity of 0.45 m/s, water depth of 0.15 m and longitudinal free surface slope of 0.00116. With regard to sediment transport, a bed load rate of about  $0.006 \text{ kg}/\text{m}^3$  has been measured at inflow and outflow.

In their article, steady-state morphodynamic evolution is studied, with particular attention to hydrodynamic field (in terms of velocity and water depth).

The test, considered a benchmark test, has been used by several authors for the evaluation of their morphodynamic models. Among others, Duc et al. [11] and Begnudelli et al. [3] validated their numerical models studying the present experiment: both of them take into account secondary flow effects in their algorithms.

### Numerical Settings and Results

The mesh reproduces Odgaard's U-channel with 25020 approximately rectangular elements. In particular, they are perfectly rectangular in inflow and outflow straight channels, about 0.1 m long and 0.076 m wide, while in the bend they are lightly trapezoidal, with similar dimension. In this way, they fit the bend remaining parallel to the water flow. The initial longitudinal slope corresponds to the free surface slope measured in laboratory ( $i_f = 0.00116$ , Figure 4.15). The section is characterized by a trapezoidal bedrock with a 23 cm mobile bed layer, as describe for the laboratory experiment. An inflow, a constant discharge of  $0.153 \text{ m}^3/\text{s}$  is imposed, while free flow cinematic boundary condition has been set at outflow section. Lateral boundaries are treated as wall boundary condition.

The model takes into account turbulence effects using Smagorinsky approach. Coherently with Petti et al. [35], imposed turbulent length scale  $l_S$  is the half width of the channel (about 0.72 m), while the empirical coefficient  $C_S$  is set to 0.3.

The Manning coefficient is  $0.0214 \text{ m}^{1/3}\text{s}^{-1}$ , as suggested by Begnudelli et al. [3], which corresponds to laboratory conditions described above. The morphodynamic model starts from steady-flow hydrodynamic conditions on fixed bed.

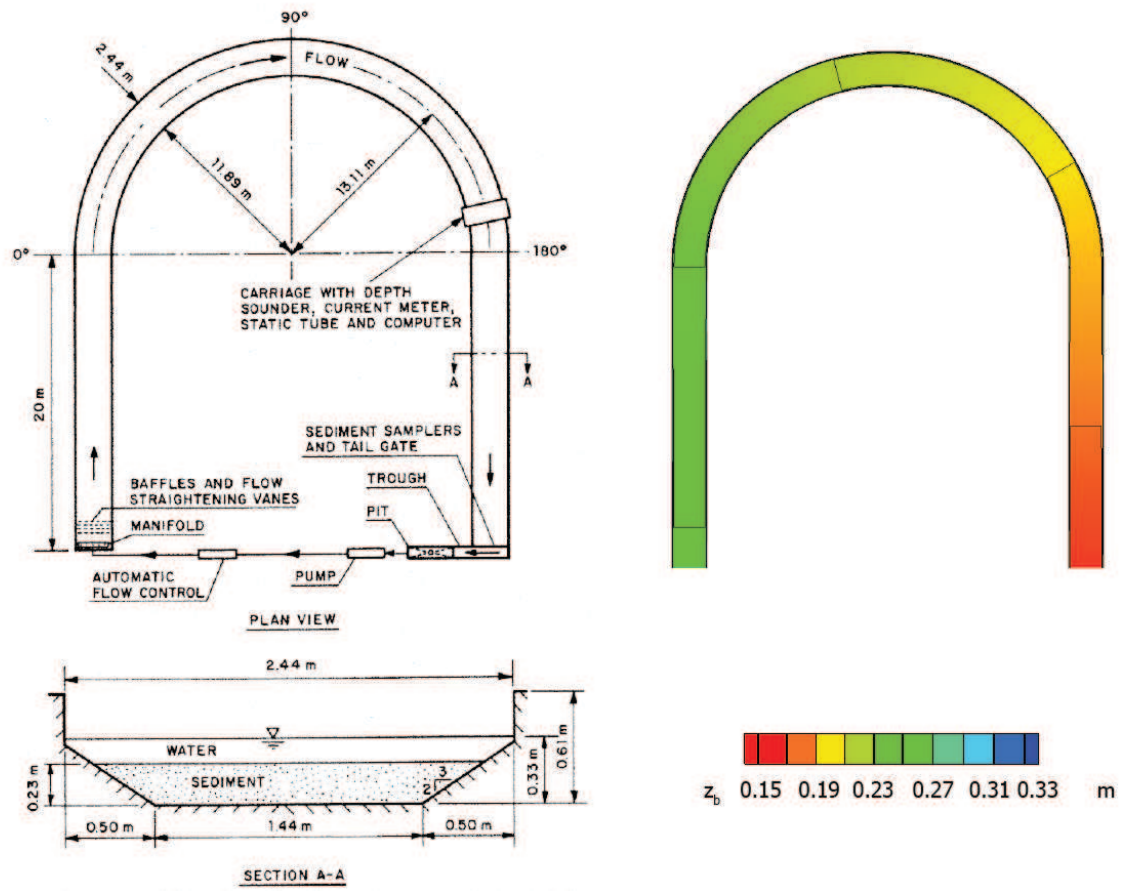


Figure 4.15: Odgaard and Bergs U-flume laboratory geometry [31] and model geometry.

In order to reach morphodynamic steady-state conditions, the model simulates 5 h of bed evolution using a morphological factor of 10: in this way, the evolution after 50 h is described, which corresponds to an equilibrium morphology. Moreover, equilibrium approach has been used for describing both bed and suspended load. Van Rijn formulas are here chosen.

In Figure 4.16, the bottom evolution without taking into account secondary flow effect is compared with an analogous simulation which considers them. Under the effects of secondary flows, bend bottom evolution change significantly: due to the transverse bed load, in fact, in the inner part of the bend an important deposition area takes place, while the erosion process, limited by fixed bed presence, influences the outer bend slope.

Laboratory test and numerical model steady solutions are illustrated in Figure 4.17, where velocity and water depth fields are compared. General behaviour of the model is in agreement with laboratory test. Water depth is maximum at the beginning and at the end of the bend, close to the outer slope. Moreover, velocity is higher at the outer bend side too, in particular in the final part of the bend.

However, there are some relevant differences between numerical results and laboratory test: considering velocity, maximum velocity in the central part of the bend is lower in numerical simulation than in laboratory experiment. At the end of the bend, moreover, simulated velocity appears to be higher than experimental data. Finally, maximum water depth is lower in numerical model than in laboratory test.

Such differences are caused by sediment transport approach chosen for the bed load in this test and, more generally, in the presented numerical model : the equilibrium approach.

Generally, hypothesis of equilibrium load is coherent with bed load dynamics, but the hypothesis of unlimited sediment availability is required. In this particular case, fixed bed plays an important role, limiting erosion at the outer lateral slope. For this reasons, this is a typical non-equilibrium problem and the use of equilibrium load for the transverse bed load, which is responsible of bend evolution, loses its sense. Other authors who consider the present test use non-equilibrium approach (Duc et al. [11]) or consider exclusively the central part of the channel, treating lateral slope as wall (Begnudelli et al. [3]). Further development of the numerical model are thus required for a better description of similar non-equilibrium situations.

Anyway, it should be noticed that, despite these model limitations, the secondary flow effects are globally well described. Considering bends or meanders, their evolution is strictly related to the behaviour of such phenomenon, particularly for granular sediment transport. Thus, if secondary flow problem is not properly considered in numerical modelling, final results can significantly differ from real measurements.

## 4.4 Channel bend evolution under unsteady flow

### Laboratory Experiment

The second test proposed here for the evaluation of secondary flow effects has been developed by Yen and Lee [66]. In particular, they studied the effect of an unsteady flow on the morphological evolution of a laboratory channel bend. Different hydrodynamic conditions have been considered and studied. The aim of this test is thus the evaluation of morphodynamic model ability to describe bottom evolution in presence of a varied curvilinear flow, where, another time, secondary flow and transverse slope play an important role.

Yen and Lee proposed a set of experiments in a 180° channel bend, with a mean radius

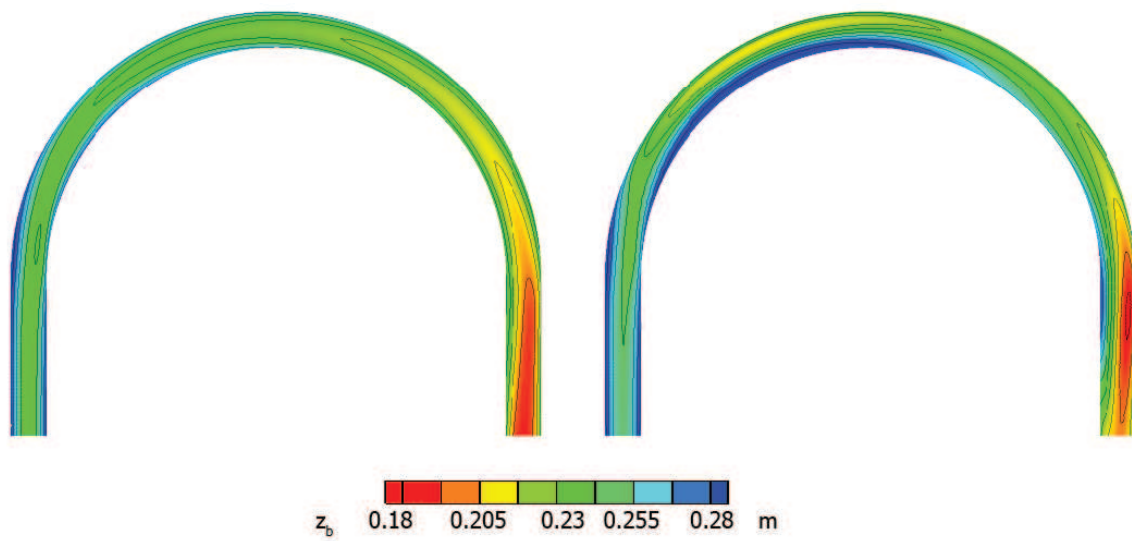


Figure 4.16: Odgaard and Bergs test: bottom evolution not considering and considering secondary flow effects.

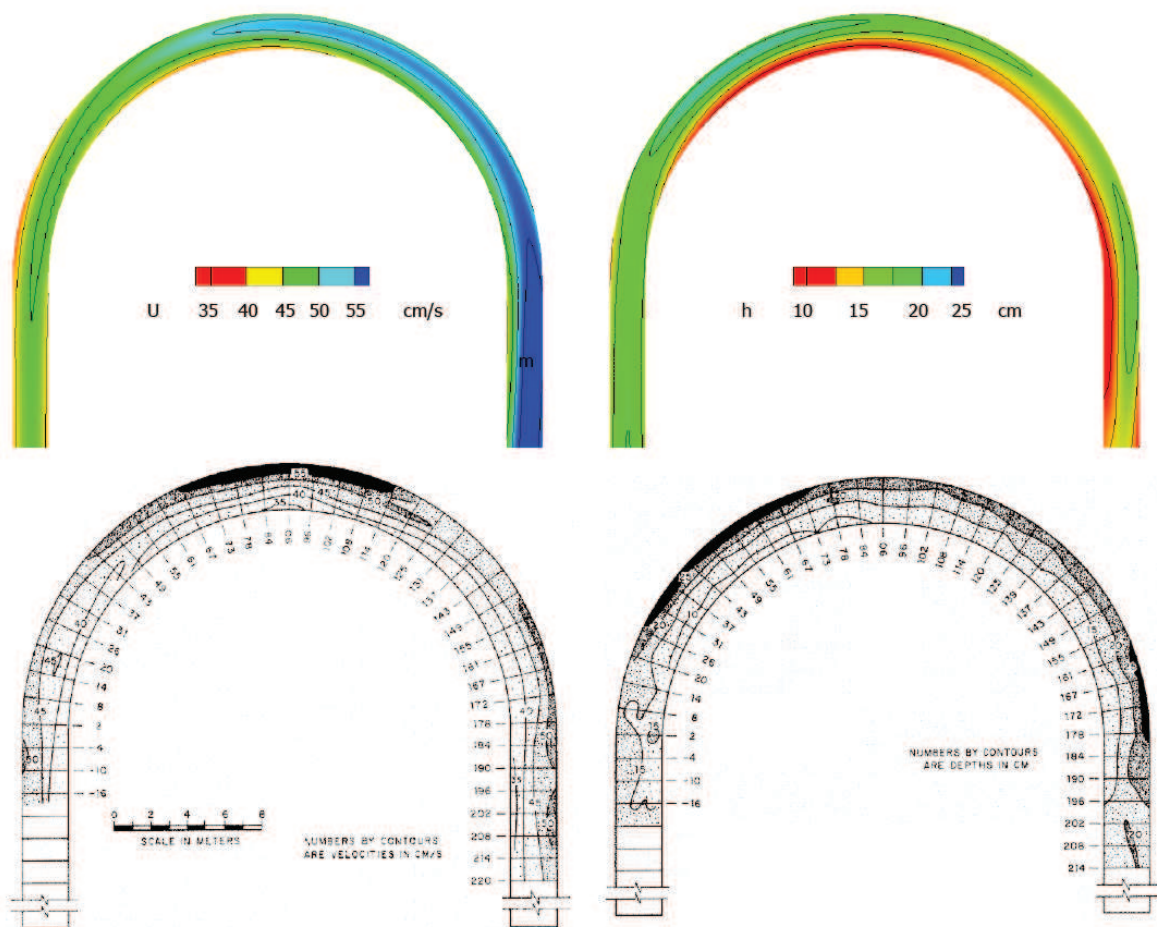


Figure 4.17: Odgaard and Bergs test [31]: comparison between experimental (above) and numerical (below) results.

Run	Peak flow $Q_p$ ( $m^3/s$ )	Peak flow depth $h_p$ (m)	Duration $t_d$ (s)
1	0.0750	0.129	180
2	0.0685	0.121	204
3	0.0613	0.113	240
4	0.0530	0.103	300
5	0.0436	0.091	420

Table 4.2: Characteristics of hydrographs employed (Yen and Lee [66]).

$r_c = 4$  m and a width  $B = 1$  m. Upstream and downstream the bend, two straight channel 11.5 m long guaranteed, respectively, inflow and outflow. The longitudinal slope  $i_f$  was 0.002.

A layer of sand around 20 cm thick, with a mean grain diameter of  $d_{50} = 1$  mm and a variance of 2.5 mm, has been placed on the bed before each experiment began.

The base flow  $Q_0$  was set at  $0.02 m^3/s$ , which corresponds to the incipient motion condition for a grain diameter of 1.0 mm: under this condition, a mean water depth  $h_0 = 0.0544$  cm characterized the inflow strain channel. Five experiments, with different inflow hydrographs, have been analysed: each hydrograph was triangular, with the peak imposed at the first third of each test duration.

The tests, numbered from *Run 1* to *Run 5*, are characterized by a gradually increased duration and decreased peak flow. *Run 1* hydrograph has thus the maximum peak flow,  $0.075 m^3/s$ , which corresponds to the maximum possible value to avoid the generation of undesirable cross waves.

In Table 4.2 are summarized hydrodynamic conditions of each test.

In the first part of their article, Yen and Lee studied the morphological evolution of the bend considering in particular the adimensional variable  $\Delta z_b/h_0$ , which is here considered for the comparison between experimental and numerical results.

### Numerical Settings and Results

The same geometry for the U-shape channel used by Yen and Lee has been considered and discretized in the model. The mesh is characterized by square elements with cell side of 0.1 m in the straight inflow and outflow channels, and by approximately square element of the same dimension in the bend. The same longitudinal slope has been used and, coherently with hydrodynamic conditions measured for initial inflow, Manning coefficient  $n$  has been set at 0.0174.

At inflow, the hydrograph of the corresponding Run has been imposed: the same five different *Runs*, with hydrographs summarized in Table 4.2, have been studied. As outflow boundary condition, free flow (cinematic condition) has been set.

Channel lateral walls have been modelled using wall boundary conditions: the effect of the wall roughness on the flow is not here considered. The model has not considered horizontal turbulence.

Coherently with the mean diameter, only bed load has been studied: suspended load is in fact not relevant under these hydrodynamic conditions. As a first approach, Van Rijn bed load formula of equation (2.28) is here used.

Finally, the model takes into account the effect of secondary flow on the bed load, as discussed in Chapter 3.

During simulations, typical evolution of bend channel takes place. Due to the bed load deviation under the combined effect of secondary flow and consequent transverse slope,

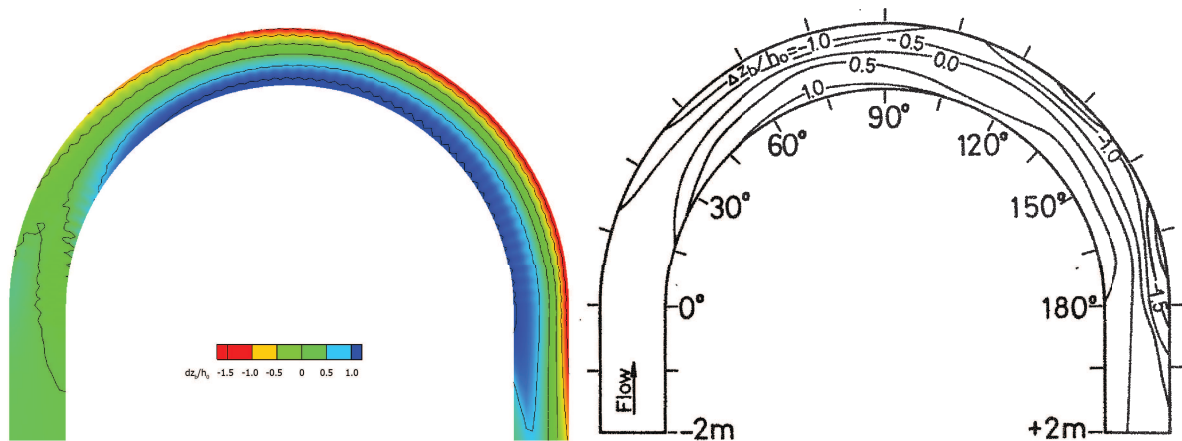


Figure 4.18: Comparison in bed evolution of the channel bend: Run1.

deposition is concentrated at the inner wall, being maximum in the first part of the bend. Similarly, scour phenomena is concentrated at the outer wall, where bed material is gradually eroded and transported in the inner areas. Maximum scour is located in the final part of the bend. At the end of each simulation, the bend is characterized by a transverse slope fairly constant, which however increases in maximum scour areas.

In Figures from 4.18 to 4.22  $\Delta z_b/h_0$  contours of numerical simulation and isolines of experimental data are compared: maximum erosion, maximum deposition and the general morphology obtained by numerical simulation are in fairly agreement with experimental data.

Yen and Lee observed that maximum deposition occurred near the inner bank at 75° section from the beginning of the bend, while maximum scour took place near the outlet bank at 165° section from the bend beginning. In Figure 4.23, the comparison between experimental data and numerical result at these sections is illustrated for each Run. In the first section, the transverse slope appears to be less sensible to the hydrograph in numerical model than in physical experiment. In particular for Run 1, transverse slope seems to be slightly underestimated. However, mean transverse slope (of the five Runs) seems to be in good agreement with experimental data. In section 2, deposition rate in Run 1, Run 2 and Run 3 is well described by the numerical model, although erosion rate is underestimated. In Run 4 and Run 5, both scour end deposition rates are higher in numerical simulations than in measured data. It should be considered that Yen and Lee used a sand mixture with a significant variance, which has probably a relevant effect on the bend morphology. Moreover, in the numerical model no turbulence effect and wall roughness influence are considered.

In order to obtain a comparison of different bed load formulas for the description of bend morphodynamics, some more simulations have been considered using Soulby (equation (2.33)) and Meyer-Peter and Müller (equation (2.21)) formulas.

In particular, two Runs are here reported, the first one (Run 1) and the last one (Run 5): they are in fact considered to represent the two extreme configurations.

In Figure 4.24, maximum deposition and scour sections, using different bed load computation methods, are compared in terms of adimensional variable  $\Delta z_b/h_0$  with measured data.

Van Rijn and Meyer-Peter and Müller formulas give similar results: in Run 1, scour is slightly underestimated while in Run 5 both scour and deposition seem to be more accentuate. Anyway, in both sections the transverse slope is in fairly good agreement with

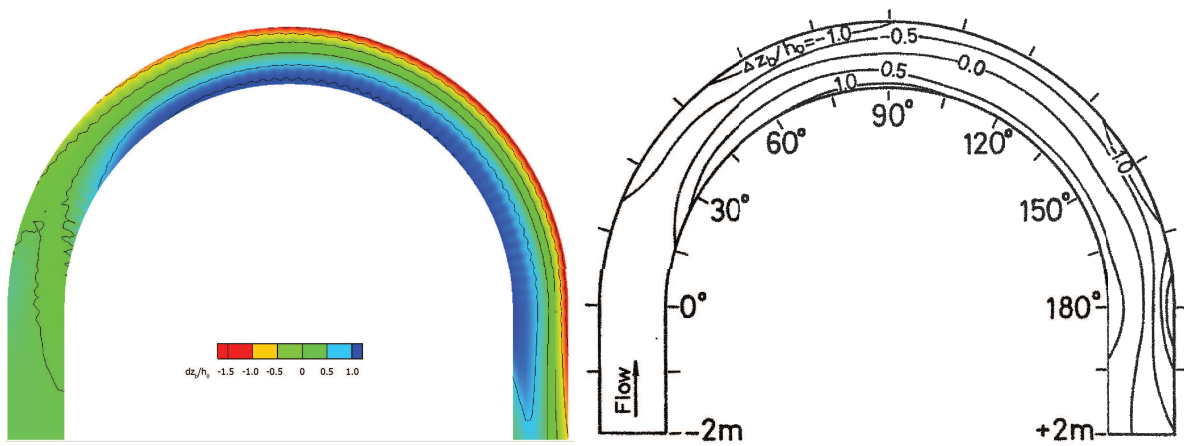


Figure 4.19: Comparison in bed evolution of the channel bend: Run2.

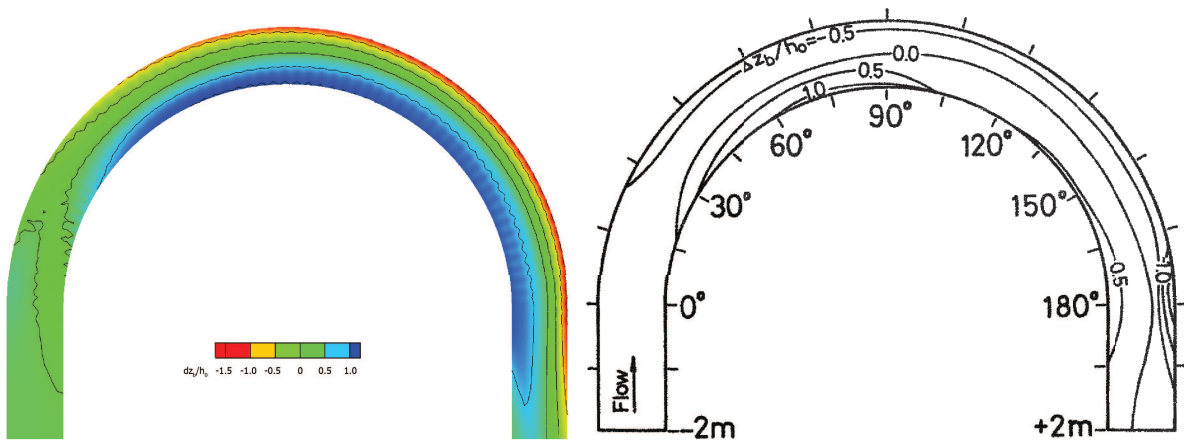


Figure 4.20: Comparison in bed evolution of the channel bend: Run3.

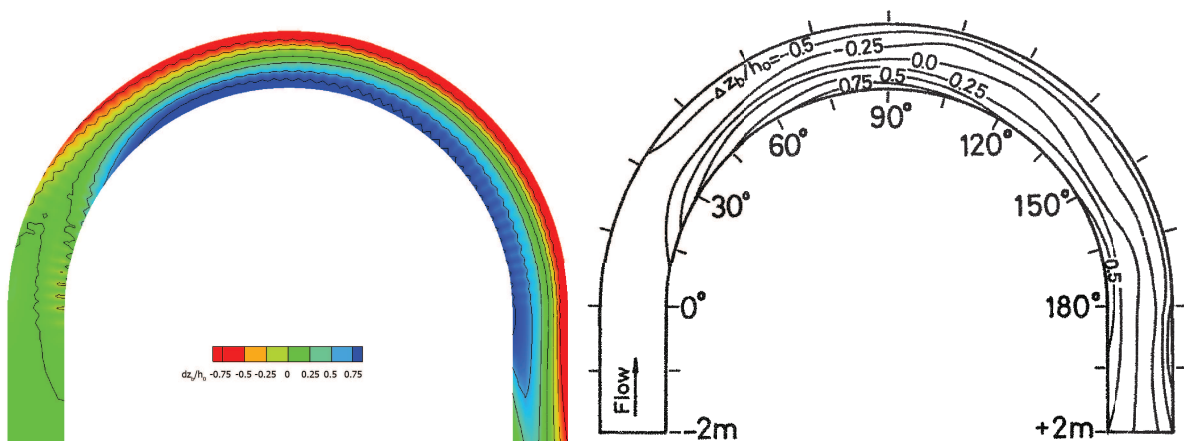


Figure 4.21: Comparison in bed evolution of the channel bend: Run4.

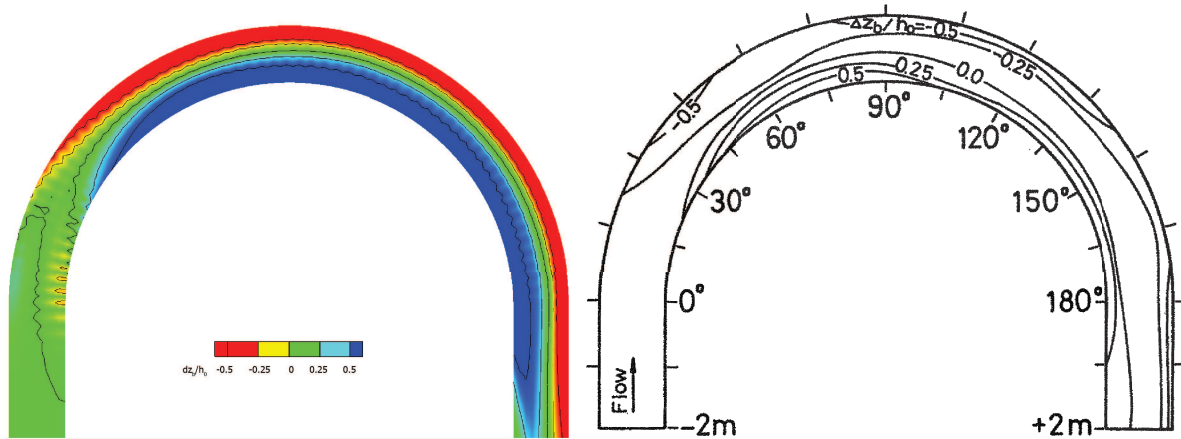


Figure 4.22: Comparison in bed evolution of the channel bend: Run5.

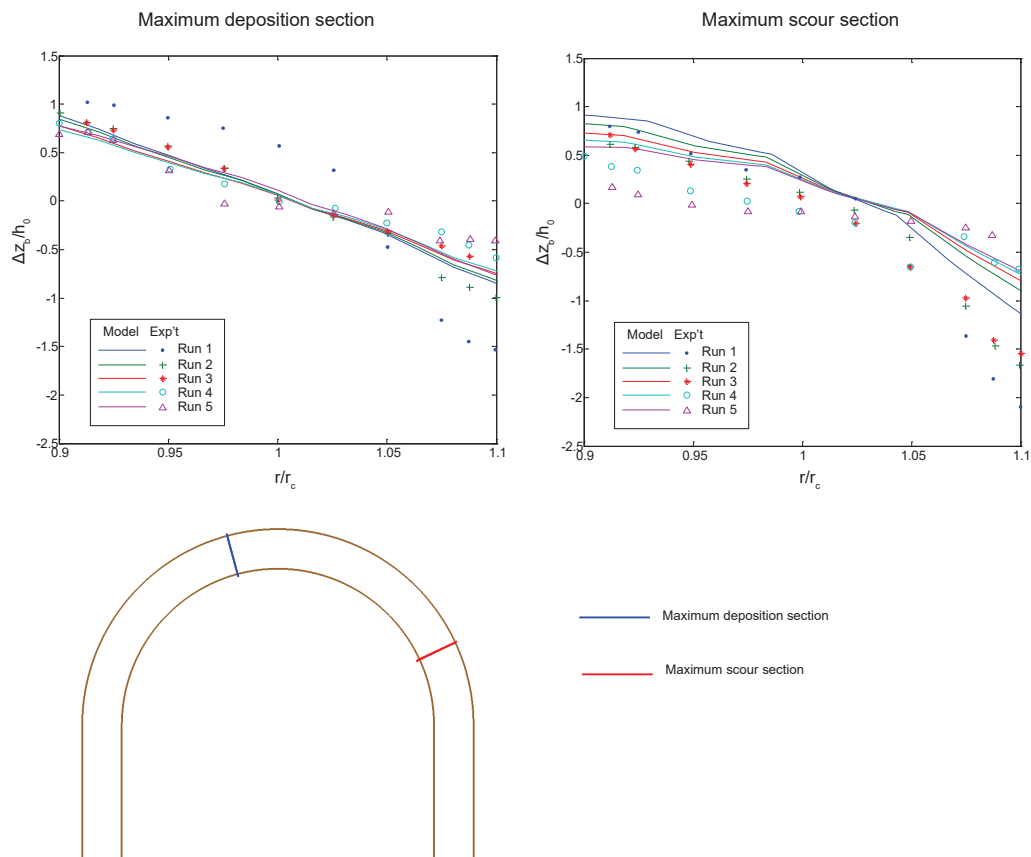


Figure 4.23: Maximum scour and erosion sections: comparison between numerical model and experimental data.

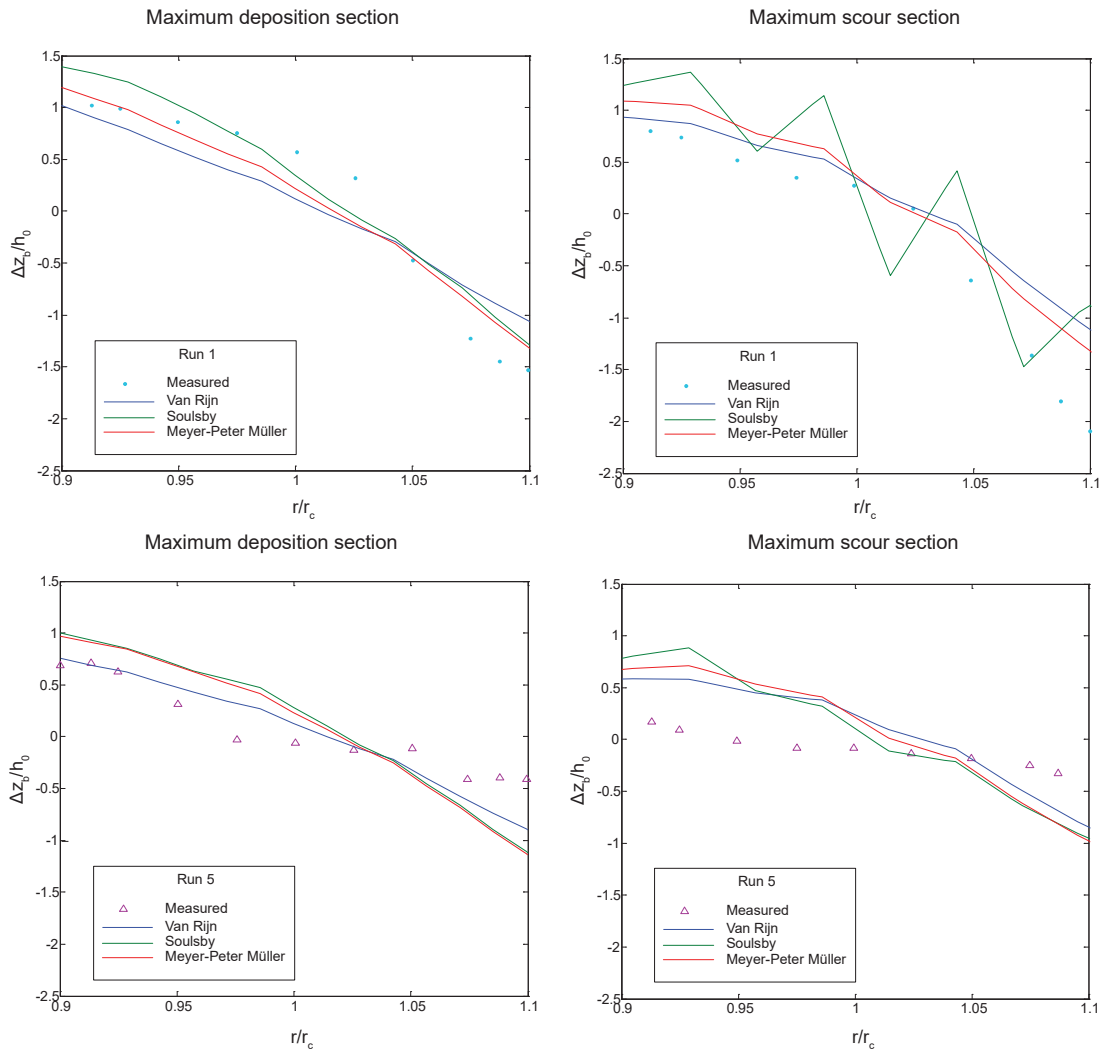


Figure 4.24: Maximum scour and erosion sections: comparison between different bed load formulas.

measured data.

Conversely, Soulsby formula gets less accurate results. In fact, although in Run 5  $\Delta z_b/h_0$  is coherent with other simulations, in Run 1 maximum scour section is characterized by numerical instabilities, as evident in Figure 4.24.

For these reasons, the model can be considered to describe adequately the morphological evolution of the bend under unsteady conditions. Van Rin and Meyer-Peter and Müller formulas for bed load computation seem to give better results than Soulsby method.



# Conclusions

In the present thesis bed shear stress computation and sediment transport problem have been discussed and a new 2-dimensional depth-averaged morphodynamic model has been presented and validated.

With regard to bed shear stress, current-alone and waves-alone bed shear stress is based on a few analytical theories, generally shared, while many analytical and practical theories are available for wave-current bed shear stress.

Soulsby DATA2 formula has been compared with other mathematical models, resulting to be in good agreement with them for mean bed shear stress. However, such match evidenced as it tends to underestimate maximum bed shear stress. Anyway, due to its simplicity, Soulsby formula DATA2 has been here considered as the reference technique, coherently with many other morphodynamic models.

With regard to sediment transport problem, granular and cohesive sediments dynamic have been distinguished.

Dynamics of granular sediments depends on grains characteristics and hydrodynamic conditions. Grains can be transported either rolling and jumping on the bed (bed load) or they can involve all the water volume, maintained in suspension by the water flow (suspended load). Two main approaches, available for their computation, have been presented: equilibrium and non equilibrium approach.

Equilibrium approach is generally valid for bed load, where length and time scales of sediment dynamics are small enough and transient terms can be considered negligible. In this case, equilibrium experimental formulas are thus applied.

Conversely, suspended load is characterized by greater time and length scales: here non-equilibrium approach gives generally more accurate results. Such approach has been obtained by solving a proper advective-diffusion equation.

Considering cohesive sediments, single grains are small enough to interact each other by electrochemical forces (cohesion), forming flocks. In this case, sediment transport mainly depends on sediment concentration and mud bed soil properties.

For computation of cohesive sediment transport, one more advective-diffusive equation has been here used, as proposed in literature.

The morphodynamic model presented here is a depth-average 2D finite volume model.

The hydrodynamic module solves Saint Venant equations, taking in account Coriolis forces, wind forces, radiation stress forcing and turbulence effect. With regard to bed shear stress, in presence of waves, mean wave-current bed shear stress has been adopted.

The hydrodynamic model, previously developed by Hydraulics Laboratory of University of Udine, is based on 1D augmented scheme and HLLC Riemann solver has been used. The model guarantees C-property.

Sediment transport model has been coupled with hydrodynamic model and treats independently granular and cohesive problems. The advective-diffusive equation needed for the non-equilibrium approach for granular sediment transport has been solved using the

same finite volume scheme proposed for hydrodynamic problem. In an analogous manner cohesive sediment transport has been treated.

The morphological evolution has been obtained by solving sediment continuity equation at the bottom, taking into account bed load, erosion and deposition rates due to suspended load and erosion and deposition rates due to cohesive sediment transport.

In order to reduce computational time, which is bonded to Courant Friedrichs Lewy condition, a morphological factor has been implemented: in this way, at each time-step morphological changes are amplified by such factor, accelerating evolution process.

Finally, the model is able to take into account two secondary factors: avalanching process, which occurs if lateral slope steepness exceeds critical value, and secondary currents, which take place in meander or bends and give rise to an additional bed load component normal to the flow.

Validation process has been done and has been presented in this thesis: it proves that morphodynamic model is in good agreement with experimental data.

In particular, validation considered different tests: trench migration under steady current, trench migration under waves parallel to the current, dam-break over erodible bed, steady-state hydrodynamic in a channel bend and bottom evolution of a channel bend under unsteady current.

All tests have been properly described by the model. Considering trench evolution, non-equilibrium approach evidences a better behaviour than equilibrium approach. Moreover, using Soulsby vertical concentration profile numerical results fit better experimental data than using Van Rijn vertical concentration profile. In presence of waves, different wave-current bed shear stress computation models, simulated using Soulsby technique, have been compared. Results evidence that DATA2 Soulsby model suites better than others the experimental data.

With regard to dam-break over erodible bed, the test has demonstrated that the model is able to well reproduce shock problems. The solution is coherent with other morphodynamic models, whose results are presented and discussed in [43]. The several bed load formulas used here have given similar morphological results.

The model has described in a proper manner also the two tests proposed here for bend morphodynamics. However, the first test has evidenced major differences with respect to experimental data. In this case, bedrock interacts significantly with morphological evolution and, thus, hypothesis of unlimited sediment availability, required by the use of equilibrium approach, is not guaranteed. For this reason, the model tends to underestimate erosional process. The use of non-equilibrium approach for bed load would probably solve such problem.

Finally, in all tests Van Rijn formula for bed load computation gives good results. For this reason, it demonstrates to be adequate for the description of bed load dynamic in different morphological and morphodynamic situations. Conversely, other formulas, like Soulsby formula, demonstrated to describe less accurately several tests.

The presented model has to be considered as a “work in progress” project. As discussed above, the development of a non-equilibrium algorithm for bed load can be useful under particular situations, which however can occur in real study cases. Moreover, cohesive sediment transport is here very simplified: in particular, it does not consider several factors such as mud flow or soil consolidation, which play a fundamental role in erosion process.

Also model efficiency needs to be improved. At present, the model requires important computation power in real applications. This is mainly caused by the explicit approach, which significantly reduces time-step dimension. Further developments are thus necessary

in order to optimize the present code, reducing time cost and improving model applicability in long period morphological studies.



# Symbols

$(x, y, z)$  Cartesian space

$(\hat{x}, \hat{y}, \hat{z})$  Local cartesian system:  $\mathbf{T}(x, y, z)$

$\vec{a}$  Generic vectorial variable  $a$

$a_i$  i-component of vector  $\vec{a}$

$\langle a \rangle$  Moving average of variable  $a$

$a'$  Fluctuating component of variable  $a$

$\Delta l_k$  length of k-side of considered polygon

$\acute{a}$  Phase average of variable  $a$

$\check{a}$  Space integral average into the domain of variable  $a$

$\hat{a}$  Vector  $a$  in local reference system

$a_L$  Left solution of variable  $a$

$a_i^n$  Variable  $a$  in cell  $i$  at instant  $n$

$\tilde{a}$  Periodic component of variable  $a$

$\alpha$  Generic integrating constant

$\alpha_1, \alpha_2$  Numerical coefficients

$\alpha_{ED}$  Erosion and deposition parameter

$\alpha_{lon}$  Longitudinal slope bed load correction coefficient

$\alpha_{sc}, \beta_{sc}$  secondary flow parameters

$\alpha_{trans}$  Transverse slope bed load correction coefficient

$\alpha_T$  Elder empirical coefficient

$\alpha_{ws}, \beta_{ws}$	Shape functions for cohesive settling velocity
$\bar{\tau}_b$	Mean bed shear stress
$\beta_M$	Ratio between depth-averaged square velocity and integral averaged square velocity
$\beta$	Generic integrating constant
$\beta$	[Chapter 2] Longitudinal slope angle
$\beta_c, \psi$	Van Rijn coefficients for the correction of $b$
$\beta_d$	Ratio between depth $a$ level and depth-averaged concentration
$\beta_F$	Fredsøe parameter
$\beta_{ragg}$	Correction factor
$\beta_w, \delta_s, \gamma_{br}$	Van Rijn's parameters for the wave mixing coefficient computation
$\chi$	Adimensional Chezy coefficient
$\delta c_{coes}$	Concentration difference between bottom and surface
$\Delta t$	Timestep
$\delta$	Boundary layer thickness
$\delta_b$	Bed layer thickness
$\delta_m$	Mean boundary layer thickness
$\delta_s$	Secondary flow deviation angle
$\delta_w$	Wave boundary layer thickness
$\Delta_{z,disp,coes}$	Bottom cohesive sediment availability
$\Delta_{z,disp,gran}$	Bottom granular sediment availability
$\dot{\gamma}$	Shear strain angle
$\epsilon_H$	Horizontal diffusivity coefficients
$\epsilon_{s,c}$	Sediment mixing coefficient due to current
$\epsilon_{s,w,bed}$	Sediment mixing coefficient due to waves at the bed
$\epsilon_{s,w,max}$	Maximum sediment mixing coefficient due to waves
$\epsilon_{s,w}$	Sediment mixing coefficient due to waves
$\epsilon_x, \epsilon_y, \epsilon_z$	$x, y, z$ diffusivity coefficients
$\eta$	Water level
$\eta_a$	Adimensional variable $z/h$

$\eta_b \bar{\tau}_b$	Bed shear stress variance
$\gamma$	Resulting bed shear stress direction with respect to the current (Fredsoe)
$\gamma$	[Chapter 2] Transverse slope angle
$\gamma_w$	Water volume weight
$\kappa$	Von Karaman constant
$\Lambda$	Darcy-Weissbach friction factor
$\lambda_1, \lambda_2, \lambda_3$	Eigenvalues of Riemann problem
$\lambda_{CFL}$	Maximum wave propagation speed
$\lambda_{sc}$	Secondary flow differential length scale
$\lambda_{wc}$	Wave-current Darcy-Weissbach-form friction factor
$\mu$	Water dynamic viscosity
$\nu$	Water cinematic viscosity
$\nu_T$	Eddy cinematic viscosity
$\Omega$	Volume control horizontal area
$\omega$	Wave frequency
$\overline{\epsilon_{s,wc}}$	Depth-averaged wave-current mixing coefficient
$\phi$	Wave direction with respect to the current
$\phi'$	Wave front direction with respect to the current
$\phi_b$	Bed shear stress adimensional function
$\Phi_i$	Angle of repose
$\Phi_r$	Residual angle
$\rho$	Water density
$\rho_b$	Bulk density
$\rho_{coes}$	Density of cohesive particles
$\rho_f$	Flock density
$\rho_s$	Granular sediment density
$\sigma_{ij}$	Normal stress generic component, $i,j=x,y,z$
$\tau_{b,cr,o}$	Critical bed shear stress on horizontal bed
$\tau_{b,cr}$	Critical bed shear stress

$\tau_{bc}$	Current bed shear stress
$\tau'_{bc}$	Skin-friction current bed shear stress
$\tau_{bw}$	Maximum wave bed shear stress
$\tau_b$	Bed shear stress
$\tau''_b$	Form-related bed shear stress
$\tau'_b$	Skin-friction (grain-related) bed shear stress
$\tau_d$	Critical bed shear stress for deposition (cohesive sediments)
$\tau_e$	ritical bed shear stress for erosion (cohesive sediments)
$\tau_{ij}$	Shear stress generic component, $i,j=x,y,z$
$\tau_{ij}^{Re}$	Reynold stress generic component, $i,j=x,y,z$
$\tau_{lam}$	Laminar shear stress
$\tau_{max}$	Maximum bed shear stress
$\tau_m$	Mean bed shear stress
$\tau_{par}$	Enforcing component of flow-parallel bed shear stress due to $\tau_w$
$\tau_{per}$	Enforcing component of flow-perpendicular bed shear stress due to $\tau_w$
$\tau_{threshold}$	Threshold shear stress for fluid strain (rheology)
$\tau_{wc}$	Wave-current bed shear stress
$\tau'_{wc}$	Grain-related wave current bed shear stress
$\theta$	Mobility Shields parameter
$\theta_{cr}$	Critical mobility Shields parameter
$\theta_{max}$	Maximum mobility Shields parameter
$\theta_m$	Mean mobility Shields parameter
$\theta_n$	Outgoing surface-normal versor direction
$\theta_w$	Wave mobility Shields parameter
$v'$	Order of magnitude of fluctuating velocity
$\varepsilon$	Roughness height
$\varepsilon''$	Form-related roughness
$\varepsilon'$	Grain-related roughness

$\varepsilon_a$	Apparent roughness
$\vec{n}$	Outgoing surface-normal versor
$\xi$	Bijker model parameter
$a$	Reference level at which suspension begins
$A_{1m}$	Bottom semi-orbital excursion for regular wave
$a_1, a_2, a_3, a_4, a_s, I, p_s, q_s$	[Chapter1] Soulsby parameters for mean bed shear stress
$a_1, a_2, a_3, b_1, b_2, \alpha_1, \alpha_2, \alpha_3, \alpha_4$	[Chapter 2] Shields theory parameters
$a\%, a_{val}$	Imposed percentil and value of reference level $a$
$a_b, b_b, c_b$	Bijker model parameters
$A_E, k_E$	Experimental parameters for cohesive erosion rate
$A_G$	Empirical coefficient
$A_s$	Cross section area
$A_s, A_{sb}, A_{ss}$	Soulsby and Van Rijn Total load coefficients
$B$	Wetted perimeter
$b$	Rouse number
$b'$	Corrected Rouse number
$b_1, b_2, b_3, b_4, b_s, J, m_s, n_s$	[Chapter 1] Soulsby parameters for maximum bed shear stress
$B_{coes}$	Analitical coefficient for Soulsby cohesive concentration profile
$b_{max}$	Maximum wave-current Rouse number
$b_m$	Mean wave-current Rouse number
$b_w$	Wave-related Rouse number
$c_{0,gran}$	Maximum volume concentration
$c_a$	Reference concentration
$c_{b,coes}$	Cohesive bottom bed volume concentration
$c_{b,eq}$	Bottom equilibrium volume concentration
$c_{b,gran}$	Granular bottom volume concentration
$c_b$	Bottom volume concentration
$C_{chez}$	Dimensional Chezy coefficient

$C_{CLF}$	Courant Friedrichs Lewy Number
$c_{coes}$	Cohesive volume concentration
$C_D$	Drag coefficient
$C'_D$	Skin-friction drag coefficient
$C_f$	Flock volume concentration
$C_{GEL}$	Mass concentration at gelling point
$C_{gran,eq}$	Granular depth-averaged equilibrium concentration
$C_{gran}$	Granular depth-averaged volume concentration
$c_{gran}$	Granular volume concentration
$C_{M,b}$	Bed dry density
$c_{M,coes}$	Cohesive mass concentration
$c_{M,gran}$	Granular mass concentration
$c_{M0,coes}$	Initial cohesive mass concentration
$c_{Mb}$	Bottom mass concentration
$C_M$	Depth-averaged mass concentration
$C_S$	Smagorinsky coefficient
$C_s$	Particle volume concentration
$c_{xz}$	Correlation coefficient between $u'_x$ and $u'_z$
$d$	Sediment diameter
$D_*$	Dimensionless particle diameter
$d_{50,coes}$	Cohesive mean particle diameter
$d_{50}$	50-percentile sediment diameter
$d_{90}$	90-percentile grain diameter
$D_{coes}$	Cohesive deposition rate
$d_f$	Flock diameter
$D_{gran}$	Granular deposition rate
$d_n$	n-percentile grain diameter
$E_1, E_2, E_3, E_4$	Empirical coefficients for cohesive critical bed shear stress
$E_f, \alpha_{par}, \beta_{par}$	Experimental parameters for cohesive erosion rate

$E_{gran}$	Granular erosion rate
$E_{M,coes}$	Cohesive mass erosion rate
$ED$	Erosion and deposition rate
$ED_{coes}$	Cohesive erosion and deposition rate
$ED_{gran}$	Granular erosion and deposition rate
$F$	Correction factor
$F_c$	Current-related component of $F$
$f_c$	Current friction factor
$F_{D,cr,\beta}$	Drag force on sloping bed
$F_{D,cr,\gamma}$	Drag force on transversely sloping bed
$F_{D,cr,o}$	Drag force on horizontal bed
$F_D$	Drag force
$f_i$	Generic function, $i=1-5$
$F_L$	Lift force
$f_{MOR}$	Morphological factor
$f_{rs}$	Wave radiation stress forcing
$F_R$	Friction force
$f_{wc}$	Wave-current friction factor
$F_w$	Wave-related component of $F$
$f_w$	Wave friction factor
$G$	[Chapter 2] Submerged wight
$g$	Gravity acceleration
$g_x, g_y, G, V_2, K, \alpha_{gm}, l_{gm}, \xi_0$	Grant and Madsen model functions and parameters
$H$	Wave height
$h$	Water depth
$h^*$	C-property corrected water depth
$h_*, U_*$	Water depth and depth-averaged velocity in the star region
$h_p$	Piezometric load
$H_s$	Significant wave height

$i_f$	Bed slope
$j$	Grade of total load
$k$	Wave number
$k_\beta$	Scholitsch factor
$k_\gamma$	Leiner factor
$k_s$	Gauckler-Strickler roughness parameter
$k_{ws}, m_{ws}$	Empirical coefficients for cohesive settling velocity computation
$l$	Mixing length
$L^*, R^*$	C-property corrected left and right states
$l_c$	Cell characteristic length
$l_S$	Turbulence length scale
$M$	Momentum per unit volume
$M_{par}, n_{par}$	Erosion power and erosion parameter for cohesive erosion rate
$m_{s,e}$	Mass sediment inflow
$m_{s,u}$	Mass sediment outflow
$m_s$	Solid mass
$n$	Manning coefficient
$n_f$	Fractal dimension
$n_{por}$	Bed porosity
$n_{sr}$	Empirical coefficient
$n_{ws}$	Power for hindering settling velocity law
$O$	Order of magnitude
$p$	Isotropic pressure
$p_b$	Ratio between $U_{1m}$ and $U_{bw}$
$p_{dep}$	Probability of material resuspension
$Pe$	Peclet number
$q_{s,eq}$	Equilibrium sediment transport load
$q_{sb,eq}$	Equilibrium bed transport load

$q_{sb,lon}$	Longitudinal resulting bed load component
$q_{sb,sc}$	Bed load transverse component due to secondary flow
$q_{sb,trans}$	Transverse resulting bed load component
$q_{sb}$	Bed transport load
$q_{ss,eq}$	Equilibrium suspended transport load
$q_{ss}$	Suspended transport load
$q_s$	Sediment transport load
$R$	Hydraulic radius
$r_0$	Parker proportional coefficient
$R_c$	Ratio between surface and bottom concentration
$R_s$	Flow radius of curvature
$Re$	Reynolds number
$Re_*$	Friction velocity Reynolds number
$Re_l$	l-referred Reynolds number
$s$	Relative density ( $\frac{\rho_s}{\rho}$ )
$S_{ij}$	ij-component of strain tensor
$S_L, S_R, \tilde{S}, S_{cel}$	Propagation celerities
$S_{rs}$	Radiation stress tensor
$S'_x$	Generic source terms in x direction
$S'_y$	Generic source terms in y direction
$T$	Dimensionless bed shear stress parameter
$t$	Time
$t^{\tau_b}$	Time that the bed shear stress exceeds cohesive forces at the bed
$T_a$	Advective time scale
$T_d$	Diffusive time scale
$T_m$	Moving average period
$T_{sd}$	Dimensionless adaptation time
$T_s$	Galapatti time scale factor
$T_{turb}$	Fluctuations time scale

$T_{ws}$	Significant wave period
$T_w$	Oscillatory (wave) period
$U$	Depth-averaged x-velocity
$u_{*,crs}$	Critical friction velocity for suspension
$u_{*,cr}$	Critical friction velocity
$u_{*0}$	Boundary layer friction velocity (Fredsoe)
$u_{*c}$	Current related friction velocity
$u_{*res}$	Fictitious friction velocity (Fredsoe)
$u_{*wc}$	Wave-current related friction velocity
$u_*$	Friction velocity
$u_*$	Friction velocity
$u'_*$	Skin-friction (grain-related) friction velocity
$u_{0max}$	Maximum bottom velocity outside boundary layer
$u_0$	Bottom velocity outside boundary layer
$U_{1m}$	Maximum bottom velocity amplitude for regular wave
$U_{bc}$	Current velocity at $z = z'$
$U_{bw}$	Wave velocity at $z = z'$
$U_b$	Velocity at $z = z'$
$u_b$	Bottom particles velocity
$U_{cr}$	Critical depth-averaged velocity
$U_{eff}$	Effective velocity due to waves and current
$u_i$	i-component of velocity, i=x,y,z
$U_{on}$	Onshore near peak orbital velocity
$u_{xc}$	x-direction current velocity in
$u_{xh}$	Mean velocity at the free surface in x-direction
$u'_{irm}$	i-direction root mean square fluctuating velocity, i=x,y,z
$V$	Depth-averaged y-velocity

$w$	Scaling velocity for Reynolds stresses
$w_*, u_r$	Galapatti parameters
$w_{s,coes}$	Cohesive settling velocity
$w_{s,gran}$	Granular fall velocity
$w_{s,val}$	Imposed value of cohesive settling velocity
$Z$	non-dimensional depth
$z^+$	Adimensional variable $\frac{u_* z}{\nu}$
$z'$	Limit between viscous sublayer and turbulent core
$z_0$	0-velocity level
$z_b$	Bottom level
$Z_F$	Adimensional Fredsøe function
$\mathbf{F}'$	1D advective flux terms vector
$\mathbf{F}_c^*$	C-property corrected convective fluxes vector
$\mathbf{F}_c$	Convective flux term vector [x-direction]
$\mathbf{F}_v$	Viscous flux term vector [x-direction]
$\mathbf{F}_{*L}, \mathbf{F}_{*R}$	HLLC fluxes in left-star and right-star regions
$\mathbf{G}_c$	Convective flux term vector [y-direction]
$\mathbf{G}_v$	Viscous flux term vector [y-direction]
$\mathbf{H}_v$	$[\mathbf{F}_v, \mathbf{G}_v]$
$\mathbf{H}$	$[\mathbf{F}_c, \mathbf{G}_c]$
$\mathbf{S}$	Source terms vector
$\mathbf{T}'$	Simplified derivative computation rotation matrix
$\mathbf{T}_{i,k}$	Rotational matrix relative to side $k$ of cell $i$
$\mathbf{T}$	Rotational matrix relative to the local outgoing surface-normal versor
$\mathbf{U}'$	1D variable vector
$\mathbf{U}$	Variable vector
$\mathbf{U}^{adv}$	Advanced solution in Strang splitting
$\mathbf{U}_{*L}, \mathbf{U}_{*R}$	HLLC solution for variables vector in the star region
$\bar{\mathbf{U}}$	Depth-averaged velocity vector



# Bibliography

- [1] JRL Allen. The avalanching of granular solids on dune and similar slopes. *The Journal of Geology*, pages 326–351, 1970.
- [2] Emmanuel Audusse, François Bouchut, Marie-Odile Bristeau, Rupert Klein, and Benoît Perthame. A fast and stable well-balanced scheme with hydrostatic reconstruction for shallow water flows. *SIAM Journal on Scientific Computing*, 25(6):2050–2065, 2004.
- [3] Lorenzo Begnudelli, Alessandro Valiani, and Brett F Sanders. A balanced treatment of secondary currents, turbulence and dispersion in a depth-integrated hydrodynamic and bed deformation model for channel bends. *Advances in Water Resources*, 33(1):17–33, 2010.
- [4] Eco W Bijker. Some considerations about scales for coastal models with movable bed, 1967.
- [5] Silvia Bosa, Marco Petti, Francesco Lubrano, and Sara Pascolo. A comparison of different sediment transport numerical models useful to applications in lagoons. In Civil-Comp Press, editor, *Proceedings of the Fifteenth International Conference on Civil, Structural and Environmental Engineering Computing*, 2015. Paper 272.
- [6] Silvia Bosa, Marco Petti, Francesco Lubrano, and Sara Pascolo. Finite volume morphodynamic model useful in coastal environment. *Procedia Engineering*, 161(C):1887–1892, 2016. In press.
- [7] John B Christoffersen and Ivar G Jonsson. Bed friction and dissipation in a combined current and wave motion. *Ocean Engineering*, 12(5):387–423, 1985.
- [8] Alan G Davies, Richard L Soulsby, and HL King. A numerical model of the combined wave and current bottom boundary layer. *Journal of Geophysical Research: Oceans*, 93(C1):491–508, 1988.
- [9] E Delo and MC Ockenden. Estuarine muds manual. Technical report, HR Wallingford Ltd, 1992.
- [10] DHI, Agern Allé,5,DK-2970,Hørsholm,Danemark. *MIKE 21 I& MIKE 3 Flow Model FM - Sand Transport Module - Scientific Documentation*, 2011.
- [11] Bui Minh Duc, Thomas Wenka, and Wolfgang Rodi. Numerical modeling of bed deformation in laboratory channels. *Journal of Hydraulic Engineering*, 130(9):894–904, 2004.
- [12] JW Elder. The dispersion of marked fluid in turbulent shear flow. *Journal of fluid mechanics*, 5(04):544–560, 1959.

- [13] Jørgen Fredsøe. Turbulent boundary layer in wave-current motion. *Journal of Hydraulic Engineering*, 110(8):1103–1120, 1984.
- [14] Jørgen Fredsøe and Rolf Deigaard. *Mechanics of coastal sediment transport*, volume 3. World scientific, 1992.
- [15] R Galapatti. A depth-integrated model for suspended transports, report 83-7. faculty of civil engineering. Technical report, Delft University of Technology. Delft. The Netherlands, 1983.
- [16] William D Grant and Ole S Madsen. Combined wave and current interaction with a rough bottom. *Journal of Geophysical Research: Oceans*, 84(C4):1797–1808, 1979.
- [17] Jean-Michel Hervouet. Telemac modelling system: an overview. *Hydrological Processes*, 14(13):2209–2210, 2000.
- [18] Charles Hirsch. Numerical computation of internal & external flows: fundamentals of numerical discretization. 1988.
- [19] Leo H Holthuijsen. *Waves in oceanic and coastal waters*. Cambridge University Press, 2010.
- [20] Son Huyng-Thanh and Andre Temperville. A numerical model of the rough turbulent boundary layer in combined wave and current interaction. *Coastal Engineering Proceedings*, 1(22), 1990.
- [21] Ivar G Jonsson. Wave boundary layers and friction factors. *Coastal Engineering Proceedings*, 1(10):127–148, 1966.
- [22] Magnus Larson and Nicholas C Kraus. Sbeach: numerical model for simulating storm-induced beach change. report 1. empirical foundation and model development. Technical report, DTIC Document, 1989.
- [23] Magnus Larson, Nicholas C Kraus, and Mark R Byrnes. Sbeach: Numerical model for simulating storm-induced beach change. report 2. numerical formulation and model tests. Technical report, DTIC Document, 1990.
- [24] Giles R Lesser. *An approach to medium-term coastal morphological modelling*. UNESCO-IHE, Institute for Water Education, 2009.
- [25] GR Lesser, Dano JA Roelvink, JATM Van Kester, and GS Stelling. Development and validation of a three-dimensional morphological model. *Coastal engineering*, 51(8):883–915, 2004.
- [26] Ashish J Mehta. *An introduction to hydraulics of fine sediment transport*. World scientific, 2014.
- [27] Helen Mitchener and Hilde Torfs. Erosion of mud/sand mixtures. *Coastal engineering*, 29(1):1–25, 1996.
- [28] Day Myrhaug and Olav H Slaattelid. A rational approach to wave-current friction coefficients for rough, smooth and transitional turbulent flow. *Coastal Engineering*, 14(3):265–293, 1990.

- [29] Peter Nielsem. *Coastal Bottom Boundary Layers and Sediment Transport*. World Scientific, Singapore, 1992. Re-Printings : 1994,2005.
- [30] Peter E Nielsen. *Coastal and estuarine processes*. World Scientific, Singapore, 2009.
- [31] A Jacob Odgaard and Mary A Bergs. Flow processes in a curved alluvial channel. *Water Resources Research*, 24(1):45–56, 1988.
- [32] Gary Parker, M Garcia, Y Fukushima, and Wrn Yu. Experiments on turbidity currents over an erodible bed. *Journal of Hydraulic Research*, 25(1):123–147, 1987.
- [33] Emmanuel Partheniades. Erosion and deposition of cohesive soils. *Journal of the Hydraulics Division*, 91(1):105–139, 1965.
- [34] Marco Petti. *Lezioni di idraulica ambientale*. Ordinario di Idraulica presso l'Università Degli Studi di Udine, 2006.
- [35] Marco Petti, Silvia Bosa, Sara Pascolo, and Francesco Lubrano. Hydrodynamic wave effects on the river delta: an efficient 2dh numerical model. In Civil-Comp Press, editor, *Proceedings of the Fifteenth International Conference on Civil, Structural and Environmental Engineering Computing*, 2015. Paper 271.
- [36] JF Richardson and WN Zaki. The sedimentation of a suspension of uniform spheres under conditions of viscous flow. *Chemical Engineering Science*, 3(2):65–73, 1954.
- [37] JA Roelvink. Coastal morphodynamic evolution techniques. *Coastal Engineering*, 53(2):277–287, 2006.
- [38] Hunter Rouse. *Engineering hydraulics*. In *Hydraulics Conference IOWA Institute of Hydraulic Research*. John Wiley & Sons, 1949.
- [39] Izrail' L'vovich Rozovskiĭ. *Flow of water in bends of open channels*. Academy of Sciences of the Ukrainian SSR, 1957.
- [40] Albert Shields. *Anwendung der aehnlichkeitsmechanik und der turbulenzforschung auf die geschiebebewegung*. Technical report, Preussischen Versuchsanstalt für Wasserbau, 1936.
- [41] PA Sleigh, PH Gaskell, Martin Berzins, and NG Wright. An unstructured finite-volume algorithm for predicting flow in rivers and estuaries. *Computers & Fluids*, 27(4):479–508, 1998.
- [42] Joseph Smagorinsky. General circulation experiments with the primitive equations: I. the basic experiment\*. *Monthly weather review*, 91(3):99–164, 1963.
- [43] Sandra Soares-Frazão, Ricardo Canelas, Zhixian Cao, Luis Cea, Hanif M Chaudhry, Andres Die Moran, Kamal El Kadi, Rui Ferreira, Ignacio Fraga Cadórniga, Noemi Gonzalez-Ramirez, et al. Dam-break flows over mobile beds: experiments and benchmark tests for numerical models. *Journal of Hydraulic Research*, 50(4):364–375, 2012.
- [44] Richard L Soulsby. *Dynamics of marine sands: a manual for practical applications*. Thomas Telford, 1997.

- [45] Richard L Soulsby, Luc Hamm, Gert Klopman, Dag Myrhaug, Richard R Simons, and Gareth P Thomas. Wave-current interaction within and outside the bottom boundary layer. *Coastal engineering*, 21(1-3):41–69, 1993.
- [46] RL Soulsby, RJS Whitehouse, et al. Threshold of sediment motion in coastal environments. In *Pacific Coasts and Ports' 97: Proceedings of the 13th Australasian Coastal and Ocean Engineering Conference and the 6th Australasian Port and Harbour Conference; Volume 1*, page 145. Centre for Advanced Engineering, University of Canterbury, 1997.
- [47] Dirk H Swart. *Offshore sediment transport and equilibrium beach profiles*. PhD thesis, TU Delft, Delft University of Technology, 1974.
- [48] N Tambroni, C Ferrarin, and A Canestrelli. Benchmark on the numerical simulations of the hydrodynamic and morphodynamic evolution of tidal channels and tidal inlets. *Continental Shelf Research*, 30(8):963–983, 2010.
- [49] Allen M Teeter. Vertical transport in fine-grained suspension and newly-deposited sediment. In *Estuarine cohesive sediment dynamics*, pages 170–191. Springer, 1986.
- [50] Hendrik Tennekes and John L Lumley. *A first course in turbulence*. M.I.T. Press, Cambridge (Mass.), London, 1972. Re-Printings : 1981, 1985, 1987, 1994, 1997, 2001,2008.
- [51] Eleuterio F TORO. Riemann solvers and numerical methods for fluid dynamics-a practical introduction. 1999.
- [52] Eleuterio F Toro. Shock-capturing methods for free-surface shallow flows. 2001.
- [53] Walther GM Van Kesteren and WT Bakker. Near bottom velocities in waves with a current; analytical and numerical computations. *Coastal Engineering Proceedings*, 1(19), 1984.
- [54] Mathijs van Ledden. *Sand-mud segregation in estuaries and tidal basins*. TU Delft, Delft University of Technology, 2003.
- [55] Leo C Van Rijn. Sediment transport, part i: bed load transport. *Journal of hydraulic engineering*, 110(10):1431–1456, 1984.
- [56] Leo C Van Rijn. Sediment transport, part ii: suspended load transport. *Journal of hydraulic engineering*, 110(11):1613–1641, 1984.
- [57] Leo C Van Rijn. Sediment transport, part iii: bed forms and alluvial roughness. *Journal of hydraulic engineering*, 110(12):1733–1754, 1984.
- [58] Leo C Van Rijn. *Mathematical modelling of morphological processes in the case of suspended sediment transport*. Waterloopkundig Laboratorium Delft, 1987.
- [59] Leo C Van Rijn. *Principles of sediment transport in rivers, estuaries and coastal seas*, volume 1006. Aqua publications Amsterdam, 1993.
- [60] Leo C Van Rijn. *Principles of sediment transport in rivers, estuaries and coastal seas. Part II: supplement 2006*. Aqua publications Amsterdam, 2006.

- [61] Leo C Van Rijn, Dano JA Roelvink, and W ter Horst. Approximation formulae for sand transport by currents and waves and implementation in delft-mor. Technical report, Deltares (WL), 2001.
- [62] Leo Cn Van Rijn. Sedimentation of dredged channels by currents and waves. *Journal of Waterway, Port, Coastal, and Ocean Engineering*, 112(5):541–559, 1986.
- [63] Maria Elena Vázquez-Cendón. Improved treatment of source terms in upwind schemes for the shallow water equations in channels with irregular geometry. *Journal of Computational Physics*, 148(2):497–526, 1999.
- [64] Richard JS Whitehouse, Richard L Soulsby, William Roberts, and Helen J Mitchener. Dynamics of estuarine muds. 2000.
- [65] Johan C Winterwerp and Walther GM Van Kesteren. *Introduction to the physics of cohesive sediment dynamics in the marine environment*, volume 56. Elsevier, 2004.
- [66] Chin-lien Yen and Kwan Tun Lee. Bed topography and sediment sorting in channel bend with unsteady flow. *Journal of Hydraulic Engineering*, 121(8):591–599, 1995.